CELAL BAYAR ÜNİVERSİTESİ
FEN BİLİMLERİ DERGİSİ

CELAL BAYAR UNIVERSITY
JOURNAL OF SCIENCE

CELAL BAYAR
ÜNİVERSİTESİ

"CBU Journal of Science is indexed by ULAKBIM-TUBITAK TR-DIZIN"

Celal Bayar University Journal of Science

CBU Journal of Science

Celal Bayar University Journal of Science (CBUJOS) covers scientific studies in the fields of Engineering and Science and publishes accounts of original research articles concerned with all aspects of experimental and theoretical studies. CBU Journal of Science is a refereed scientific journal published four times annually (March, June, September and December) by Institute of Natural and Applied Sciences of Manisa Celal Bayar University. CBU Journal of Science considers the original research articles written in English for evaluation.

CBU Journal of Science is indexed by TUBİTAK ULAKBIM TR-DIZIN, and also is included in DOAJ, Cite Factor, Journal TOCS, Advanced Science Index and OAJI databases. Digital Object Identifier (DOI) number will be assigned for all the articles being published in CBU Journal of Science.

Instructions for Authors and Article Template can be found on the main page of MCBU Institute of Natural and Applied Sciences (http://fbe.cbu.edu.tr)

Vol: 18, Issue: 3, Year: 2022

Contents
Research Article   **Pages**

Celal Bayar University Journal of Science

Formation of Calcium Phosphate Minerals in the Presence of Fetuin-A

Şeniz Uçar[1]* iD

[1] Department of Chemical Engineering, Norwegian University of Science and Technology, Trondheim, Norway
*seniz.ucar@ntnu.no
*Orcid: 0000-0002-5549-6061

Abstract

Mineral formation is regulated by molecular based promoters or inhibitors in biological systems. Among serum proteins, fetuin-A can effectively inhibit unwanted calcification *in vivo* via forming fetuin-mineral complexes called calciprotein particles (CPPs). Here, the formation and phase transformation mechanisms of CPPs are investigated in detail by combining *in situ* potentiometric measurements and solid phase characterization. It is found that fetuin-A inhibits mineral formation via affecting both thermodynamic and kinetic factors of precipitation. A better understanding of the reaction pathway as well as the interactions between the mineral and protein counterparts can potentially inform the development of *in vitro* model systems of biomineralization and pave the way for the development of new therapies to treat ectopic calcification.

Keywords: Biomineralization, calcium phosphate, fetuin-A, mineral formation

1. Introduction

Mineral formation *in vivo* is a complex process that involves organic phases, which regulate the nucleation, growth, morphology and organization of biogenic minerals that form the major solid inorganic component of hard tissues in many different organisms [1]. This intricate and well-regulated process results in composite materials with exceptional features that are exploited by the organisms for a variety of purposes and through active control mechanisms on mineral formation, their biophysical properties are optimized for specific functions. The key control mechanisms that involve the regulation of chemistry, structure and morphology to direct the skeletal biomineralization processes also play significant roles in the prevention of pathological calcification [2]. The blood serum in humans is supersaturated with respect to multiple calcium phosphate (CaP) phases, meaning that mineral deposition is possible in all compartments with extracellular fluid [3]. However, ectopic mineralization is regulated in body via a variety of control mechanisms and failure to prevent extraosseous calcification is commonly observed with chronic kidney and inflammatory diseases, or aging [4].

Control of mineral nucleation and growth by utilizing molecular based promoters or inhibitors is a common strategy in biological systems [5]. Among serum

proteins, fetuin-A is shown to be one of the most efficient inhibitors of unwanted calcification [6]. Fetuin-A, also known as α_2-Heremans Schmidt glycoprotein in humans, is an acidic glycoprotein circulating in the serum at a concentration range of 0.3-1.0 mg mL^{-1} in healthy individuals [7]. It shows high affinity to calcium ions via the aspartic and glutamic acid rich residues that are mostly negatively charged at physiological conditions [8]. Moreover, the distance between these residues are compatible with the lattice constant of basic calcium phosphates such as octacalcium phosphate and apatite, which explains the high affinity of fetuin-A to bone minerals [9]. The significance of fetuin-A as a mineralization inhibitor has been well documented with both *in vitro* and *in vivo* studies [10, 11]. It is hypothesized that via formation and stabilization of a fetuin-mineral complex (also called calciprotein particles, CPPs), the spontaneous precipitation of calcium phosphate minerals is inhibited in the serum [12]. Previous studies investigating the formation of these complexes suggested that the initial CPPs, CPP-1, are composed of fetuin-A coated amorphous calcium phosphate (ACP) particles, where the lifetime of the highly transient amorphous phase is prolonged by surface stabilization with the protein [13, 14]. Overtime, CPP-1 develops crystallinity and transforms into the secondary CPP, CPP-2, that constitutes an octacalcium phosphate (OCP) or hydroxyapatite (HA) core [15]. Extensive work on the fetuin-CaP system agrees on the

2-step mechanism and has unraveled the features of these mineral-protein complexes [4]. However, the precise function of fetuin-A during the initial stage of the fetuin-mineral complex formation and phase transformation remain obscure. This is mainly due to the poorly understood mechanism of ACP formation even without the additives, and investigation of fetuin-CaP systems in complex biological media where it is difficult to decouple the interactions between fetuin and mineral phase. Therefore, this work pursues to gain more insight on the modes of interaction between the organic and inorganic phases that form CPPs at different stages of mineralization and generate a comprehensive understanding of the interactions between fetuin-A and CaP minerals.

In this work, detailed investigations of solution chemistry are employed via *in situ* monitoring of the reaction media and coupled with characterization of the solid phase. A better understanding of the reaction pathway as well as the interactions between the mineral and protein counterparts can potentially inform the development of *in vitro* model systems of biomineralization and pave the way for the development of new therapies to treat ectopic calcification.

2. Materials and Methods
2.1. Materials

All chemical reagents were purchased from Sigma-Aldrich. Lyophilized bovine fetuin-A (Sigma F3385) was used as received. Ultrapure deionized water (resistivity 18.2 MΩ cm at 25°C) was used to prepare all aqueous solutions.

2.2. Methods

All experiments were carried out in a magnetically stirred 0.5 L double-walled glass reactor. Two baffles were attached to the lid to ensure homogeneous mixing in the reaction medium. Temperature was controlled by a water bath at 25°C for all experiments. This temperature was chosen to minimize the fluctuations during product collection via filtration. In order to prevent intrusion of atmospheric carbon dioxide, nitrogen gas, saturated with water, was constantly bubbled into solutions 2 h prior to and during the experiments. The chemical speciation and activity-based supersaturation, S, were determined by the thermodynamic calculation programs PHREEQC Interactive 3.1 (U.S. Geological Survey, Reston, VA, USA) and Visual Minteq 3.0 (KTH, Royal Institute of Technology, Stockholm, Sweden), using the Minteq v4 database. All equilibrium constants used for calculations of solution speciation are provided in the supplementary information (supplementary information, section A and Table S1). Supersaturation with respect to different calcium phosphate phases were calculated according to Equation 1, where the multiplication of the activities of precursor ions are divided by the solubility product, K_{sp}, for a given phase.

$$S_{CaP} = \left(\frac{a_{Ca}^{x} \cdot a_{PO4}^{y} \cdot a_{OH}^{z}}{K_{sp,CaP}} \right)^{\frac{1}{x+y+z}} \qquad \textbf{(Eq.1)}$$

The pH was measured with 2 s intervals via a combined glass electrode and calcium ion activity was monitored online via a calcium ion specific electrode. Both measurements were continuously recorded with Tiamo software (Metrohm AG, Herisau, Switzerland). Both electrodes were calibrated daily (supplementary information, section B). Spontaneous precipitation of calcium phosphate was induced in semi-batch experiments by allowing precipitation to occur from supersaturated solutions (S_{HA}= 25.6) under constant stirring (300 rpm), as described elsewhere [16]. Briefly, 2.4 mM KH_2PO_4 solution containing 50 mM KNO_3 for ionic strength adjustment and KOH to adjust the final pH to 7.40 ± 0.02, was prepared in a total volume of 250 mL. 50 mM and 20 mL $Ca(NO_3)_2.4H_2O$ solution was then added in the reaction medium at a rate of 0.4 mL min^{-1} via an automated dosing unit (907 Titrando, Metrohm AG, Herisau, Switzerland).

The concentrations of the precursor solutions were set to evoke a multistep precipitation pathway within a reasonable experimental time and with sufficient product. In experiments with fetuin-A, the corresponding amount of protein solution that will give a total of 5 or 10 mg of fetuin-A in the reaction medium, was added in the phosphate solution. Fresh solutions were prepared for each experiment and filtered through 0.22 μm sterile vacuum filtration systems prior to experiments. Minimum 2 parallel experiments were conducted for each experimental condition.

Solid phases collected at different stages of the reactions were characterized via powder X-ray Diffraction (XRD) (D8 Advance, Bruker AXS GmBH) in the 2θ range of 4-75° with a step size of 0.013° and a step time of 0.67 s. Fourier transform infrared (FTIR) (Tensor, Bruker AXS GmBH) spectra of powder samples were collected between 4000-550 cm^{-1} by averaging 75 scans. Scanning electron microscopy (SEM) (Apreo, FEI) was performed at an accelerating voltage of 2-5 kV. Prior to imaging samples were coated with gold.

3. Results and Discussion
3.1. Two-step precipitation pathway

Calcium phosphate (CaP) mineralization was achieved by establishing supersaturation in the reaction medium via slow titration of calcium solution, and allowing the spontaneous precipitation to occur. During the course of the reaction, solution pH was continuously monitored and succeeding steps of the reaction were identified via the distinct drops in the monitored signal (Figure 1).
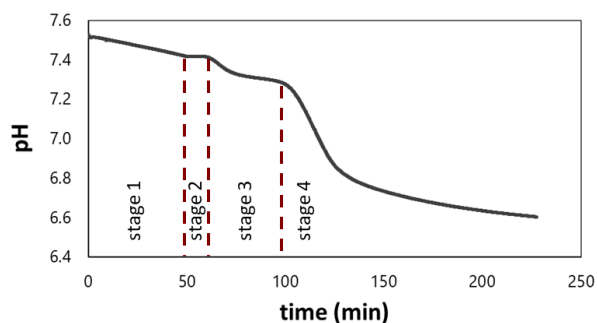
Figure 1. pH of the solution during the precipitation reaction in time, and the succeeding stages of the reaction determined by the distinct changes in the signal profile.

Experiments were initiated by slow titration of 20 mL calcium solution into the reaction medium that contained the phosphate solution. This duration is marked as stage 1, and lasts for 50 min. A linear decrease in solution pH was observed during stage 1. Calculations of solution chemistry via Visual MINTEQ showed that the pH drop was due to the formation of ion pairs between calcium ions and phosphate species, which increased the ratio of free acidic phosphate species (supplementary information, section C and Table S2) [16]. When the titration of calcium solution was complete, solution pH showed a stable value during stage 2, corresponding to the metastable supersaturated solution. The first discernible drop in pH remarked the appearance of the first new phase in the solution and the start of stage 3. Observations of the pH change was accompanied by visual changes in solution turbidity shortly after, verifying precipitation. Characterization of the solid phase at stage 3 by FTIR showed broad PO_4^{3-} bands near 1040 cm^{-1}, and a weak band at 875 cm^{-1} associated with HPO_4^{2-}. XRD analysis showed no diffraction peaks, which together with FTIR data indicated presence of an amorphous calcium phosphate phase (ACP) (Figure 2). The drop in pH at stage 3 was followed by a short plateau, which can be interpreted as the solution reaching a steady state, in equilibrium with the ACP. Accordingly, the second drop of pH was interpreted as the emergence of a second phase in the system and determined the onset of stage 4. Characterization of precipitates by XRD showed diffraction peaks associated with poorly crystalline apatite and the distinguishing peak for octacalcium phosphate (OCP) was observed at 2 theta 4.7° (Figure 2b). FTIR data supported the crystal formation via sharp PO_4^{3-} peaks at 1025 and 962 cm^{-1} and splitting of the v_4 bending of PO_4^{3-} at 600 and 560 cm^{-1}, indicating apatite crystallization [17]. SEM images of samples collected at stage 3 and stage 4 showed aggregated spherical ACP particles and flake-like apatite precipitates, respectively (Figure 3).

The two-step precipitation pathway observed here is common when the initial solution is supersaturated with respect to ACP, due to its fast precipitation kinetics.

Since the solution was still supersaturated with respect to crystalline phases of calcium phosphate after ACP precipitation at stage 3, nucleation of a new phase was probable and initiated the phase transformation in the system towards the more stable product. In the presence of macromolecular additives, both the precipitation pathway and the kinetics of each precipitation step can be affected, which could give insights on the interaction modes between the organic and inorganic components [18, 19]. Correspondingly, the effects of fetuin-A on mineralization of CaP were investigated.
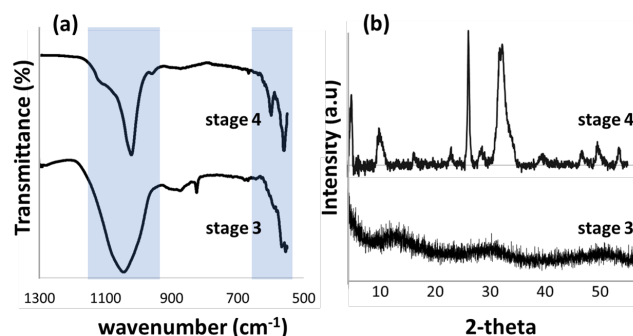
Figure 2. (a) FTIR and (b) XRD spectra of precipitates collected at stage 3 (bottom) and stage 4 at the end of experiments (top). The areas shaded in blue in FTIR spectra highlight the changes in the peak widths and positions.
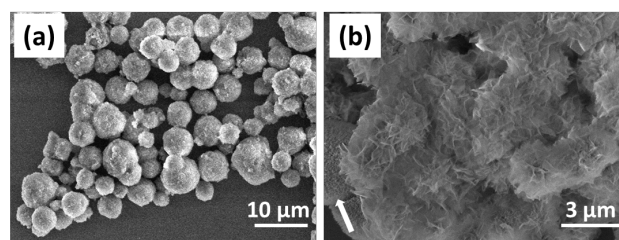
Figure 3. SEM images of the particles collected at (a) stage 3 and (b) stage 4. The arrow in (b) shows a remaining spherical particle showing incomplete phase transformation.

3.1.1. Effect of Fetuin-A on mineral formation

The precipitation experiments were repeated in the presence of varying concentrations of fetuin-A. The pH curves showed the same characteristic 2-step behavior with plateaus observed at comparable values for all experimental conditions and similar pH change during titration of calcium solution during stage 1, but with drastic changes in the duration of subsequent stages (Figure 4). The pH data revealed that the presence of fetuin-A did not induce a change in the precipitation pathway, which was secondarily supported by the SEM images of precipitates collected during the subsequent stages of the reaction in the presence of the highest fetuin-A concentration (supplementary the information, section D). It was shown that succeeding stages of the reaction were associated with typical morphologies of
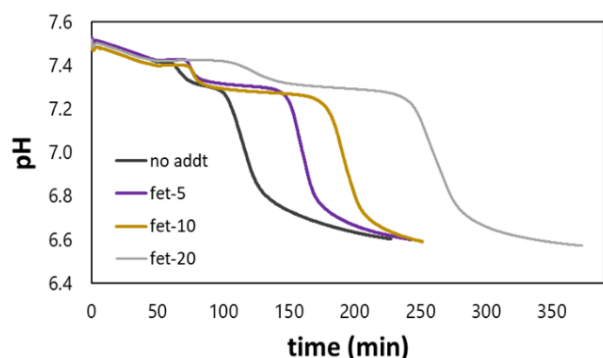
Figure 4. pH curves without additive and with varying concentrations of fetuin-A as a function of time.

amorphous spheres at stage 3 and formation of crystalline flakes at stage 4. However, fetuin-A greatly affected the kinetics of the precipitation reactions. The lifetime of the metastable solution prior to precipitation (duration of stage 2) and lifetime of ACP phase (duration of stage 3) were investigated as a function of fetuin-A concentration (Figure 5). Data showed significant prolongation in stage 2, with a parabolic dependence on protein concentration. The delay in the formation of ACP in the presence of molecular additives could be related to (i) an effective drop in the calcium activity due to protein binding, thus lowering of supersaturation, and/or (ii) interruption of fetuin-A with kinetics of mineral formation [20, 21]. Supersaturation, constituting the thermodynamic driving force for precipitation, affects both the nucleation and growth rates of solids. In-situ measurements of calcium activity during the titration of calcium solution (stage 1) showed that in the presence of fetuin-A, the calcium activity was lowered in a concentration dependent manner, reaching a 12% reduction at the highest concentration of the additive (fet-20) (Figure 6). In the absence of protein, the calcium activity measurements matched very closely with the thermodynamically calculated values shown by blue dots on Figure 5, which takes into account the amount of calcium added to the system and the ion association complexes it would form with phosphate species. However, when fetuin-A is present in the reaction medium, calcium activity was measured at lower values indicating binding of calcium by the protein via its high affinity aspartic and glutamic acid rich residues [8]. Thermodynamic calculations with the lowest calcium activity measured at fet-20 conditions showed that initial solution supersaturation was lowered to $S_{HA}= 23.9$. When the kinetic factors of nucleation are considered, presence of fetuin-A can decrease the nucleation rate by interfering with the incoming flux of monomers to the nuclei surface or block the nucleation sites, as commonly observed in precipitation systems in the presence of additives [22]. Thus, it was concluded that the presence of fetuin-A could inhibit ACP formation via both thermodynamic and kinetic effects.

The lifetime of ACP, specified by the duration of stage 3, was also prolonged and showed a linear dependence to the fetuin-A concentration. Earlier work suggested that such a dependance on additive concentration signals to adsorption of additives on the surface of the metastable phase [17, 23]. They can then hinder the phase transition either via inhibition of heterogeneous nucleation of the new phase on the metastable precursor, or via slowing down the dissolution process of the metastable phase, which consequently hinders the availability of constituent ions for the new phase formation.
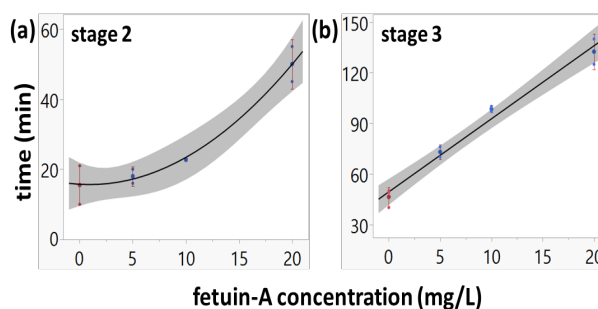
Figure 5. The duration of (a) stage 2 and (b) stage 3 as a function of fetuin-A concentration. The grey shaded area marks the 95% confidence interval.
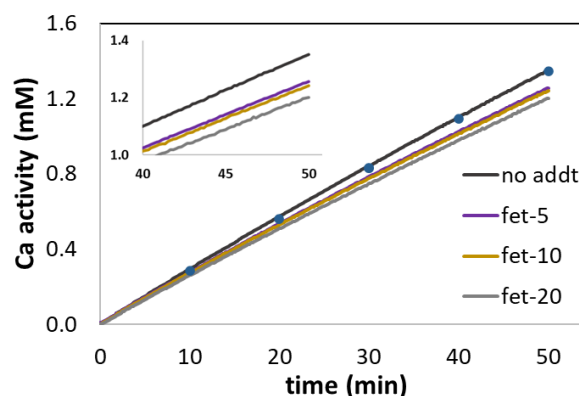
Figure 6. In situ measurements of calcium ion activity during the titration of calcium solution without and with varying concentration of fetuin-A. Blue dots denote the theoretically calculated values of activity, showing a close match with additive-free experiments.

Yet, we cannot differentiate between the active inhibition mechanism of the fetuin-A within the scope of this work. In order to make such deductions, quantitative analysis of adsorbed protein as a function of initial additive concentration would be required in combination with high resolution *in situ* or cryogenic methods such as TEM, to follow the mode of nucleation for the emerging phase.

The characterization of final precipitates with XRD showed that in the presence of lower concentrations of fetuin-A, the final precipitates were not altered (Figure 7). However, with the fetuin-A concentration of 20 mg in the reaction medium, the final precipitate was composed of HA only, as shown by the absence of OCP peak in the XRD spectrum. The change in composition could be induced by the prolonged reaction time, where the thermodynamically more stable HA dominates the final composition. OCP could still have precipitated in the system and phase transformed to HA completely during the course of the reaction. Yet, without further time-resolved analysis, this hypothesis cannot be confirmed. SEM images of final precipitates showed structural changes with the flake-like structures being composed of thicker plates at highest fetuin-A concentration (Figure 8).
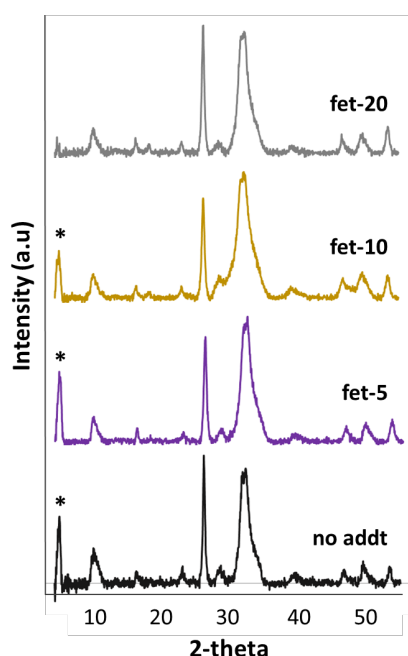
Figure 7. XRD spectra of final precipitates with asterisk marking the distinguishing OCP peak.
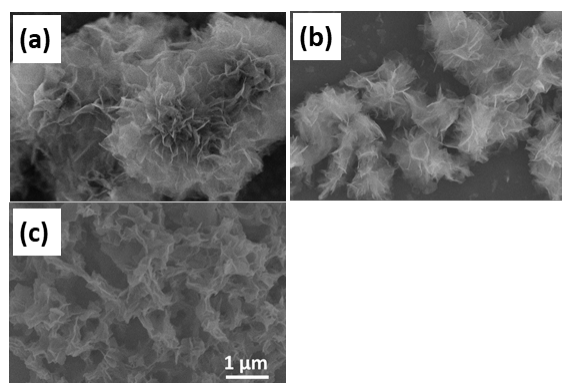
Figure 8. SEM images of precipitates collected at the end of experiments with fetuin-A additive in concentrations of (a) 5, (b) 10 and (c) 20 mg.

4. Conclusion

The role of fetuin-A in inhibition of mineral formation was investigated in a two-step precipitation pathway. It was shown that the presence of fetuin-A lowers the calcium ion activity through binding of ions and prolong the precipitation time for ACP. Yet, after its formation ACP was stabilized by the protein against phase transformation, most likely via surface adsorption. We anticipate the findings in this study will improve the understanding of mineralization inhibition mechanisms by the additives, and, in turn contribute to the design of enhanced treatment methods towards ectopic mineralization.

Acknowledgement

Author's Contributions

Şeniz Uçar: Conceptualized the study, performed the experiments and analyses of result, drafted and wrote the manuscript.

Ethics

There are no ethical issues after the publication of this manuscript.

References

[1]. Mann, S., 1988, Molecular recognition in biomineralization. *Nature*, 332(6160): p. 119-124.

[2]. Meldrum, F.C. and H. Cölfen, 2008, Controlling Mineral Morphologies and Structures in Biological and Synthetic Systems. *Chemical Reviews*, 108(11): p. 4332-4432.

[3]. Eidelman, N., L.C. Chow, and W.E. Brown, 1987, Calcium phosphate saturation levels in ultrafiltered serum. *Calcified Tissue International*, 40(2): p. 71-78.

[4]. Cai, M.M., E.R. Smith, and S.G. Holt, 2015, The role of fetuin-A in mineral trafficking and deposition. *Bonekey Rep*, 4: p. 672.

[5]. Xu, A.-W., Y. Ma, and H. Cölfen, 2007, Biomimetic mineralization. *Journal of Materials Chemistry*, 17(5): p. 415-449.

[6]. Gelli, R., F. Ridi, and P. Baglioni, 2019, The importance of being amorphous: calcium and magnesium phosphates in the human body. *Advances in Colloid and Interface Science*, 269: p. 219-235.

[7]. Trepanowski, J.F., J. Mey, and K.A. Varady, 2015, Fetuin-A: a novel link between obesity and related complications. *International Journal of Obesity*, 39(5): p. 734-741.

[8]. Heiss, A., et al., 2003, Structural basis of calcification inhibition by α2-HS glycoprotein/fetuin-A: Formation of colloidal calciprotein particles. *Journal of Biological Chemistry*, 278(15): p. 13333-13341.

[9]. Brylka, L. and W. Jahnen-Dechent, 2013, The Role of Fetuin-A in Physiological and Pathological Mineralization. *Calcified Tissue International*, 93(4): p. 355-364.

[10]. Schinke, T., et al., 1996, The serum protein α2-HS glycoprotein/fetuin inhibits apatite formation in vitro and in mineralizing calvaria cells. A possible role in mineralization and calcium homeostasis. *Journal of Biological Chemistry*, 271(34): p. 20789-20796.

[11]. Seto, J., et al., 2012, Accelerated Growth Plate Mineralization and Foreshortened Proximal Limb Bones in Fetuin-A Knockout Mice. *PLoS ONE*, 7(10).

[12]. Price, P.A. and J.E. Lim, 2003, The inhibition of calcium phosphate precipitation by fetuin is accompanied by the formation of a fetuin-mineral complex. *Journal of Biological Chemistry*, 278(24): p. 22144-22152.

[13]. Rochette, C.N., et al., 2009, A shielding topology stabilizes the early stage protein-mineral complexes of fetuin-A and calcium phosphate: A time-resolved small-angle x-ray study. *ChemBioChem*, 10(4): p. 735-740.

[14]. Pasch, A., et al., 2012, Nanoparticle-Based Test Measures Overall Propensity for Calcification in Serum. *Journal of the American Society of Nephrology*, 23(10): p. 1744-1752.

[15]. Heiss, A., et al., 2007, Structural dynamics of a colloidal protein-mineral complex bestowing on calcium phosphate a high solubility in biological fluids. *Biointerphases*, 2(1): p. 16-20.

[16]. Ucar, S., et al., 2019, Formation of Hydroxyapatite via Transformation of Amorphous Calcium Phosphate in the Presence of Alginate Additives. *Crystal Growth and Design*, 19(12): p. 7077-7087.

[17]. Chen, Y., et al., 2014, Stabilizing amorphous calcium phosphate phase by citrate adsorption. *CrystEngComm*, 16(10): p. 1864-1867.

[18]. Fang, W., et al., 2016, Hydroxyapatite Crystal Formation in the Presence of Polysaccharide. *Crystal Growth & Design*, 16(3): p. 1247-1255.

[19]. Hu, Q., et al., 2012, The thermodynamics of calcite nucleation at organic interfaces: Classical vs. non-classical pathways. *Faraday Discussions*, 159: p. 509-523.

[20]. Zou, Z., et al., 2018, Additives influence the phase behavior of calcium carbonate solution by a cooperative ion-association process. *Journal of Materials Chemistry B*, 6(3): p. 449-457.

[21]. Ibsen, C.J.S., D. Gebauer, and H. Birkedal, 2016, Osteopontin Stabilizes Metastable States Prior to Nucleation during Apatite Formation. *Chemistry of Materials*, 28(23): p. 8550-8555.

[22]. Westin, K.J. and Å.C. Rasmuson, 2005, Nucleation of calcium carbonate in presence of citric acid, DTPA, EDTA and pyromellitic acid. *Journal of Colloid and Interface Science*, 282(2): p. 370-379.

[23]. Ding, H., et al., 2014, Toward a Detailed Understanding of Magnesium Ions on Hydroxyapatite Crystallization Inhibition. *Crystal Growth & Design*, 14(2): p. 763-769.

Boron Adsorption on Lime Soil and Phytoremediation of Lime Soil by Potato Plant (Solanum Tuberosum L.)

Mustafa Korkmaz[1*] ⓘⅮ, Cengiz Özmetin[1] ⓘⅮ, Yeliz Süzen[1] ⓘⅮ, Atilla Mutlu[1] ⓘⅮ

[1]Balıkesir University, Faculty of Engineering, Department of Environmental Engineering,Çağış Campus,Balıkesir, Türkiye
*korkmazm@balikesir.edu.tr
*Orcid:0000-0001-8424-6339

Abstract

Boron adsorption onto lime soil from Balıkesir University campus was studied to evaluate the effects of irrigation water cations (Ca^{2+}, Mg^{2+}, K^+ and Na^+) and soil clays (kaolinite, montmorillonite, clinoptilolite clays). The concentrations for cations and boron were in the range of 0-1,450 mg/L and 0-700 mg/L, respectively. The experimental maximum boron capacity for cation effect was 0.764 mg/g and this value was seen to obtain at high cation (Ca^{2+}=500 mg/L, Mg^{2+}=550 mg/L, K^+=1,450 mg/L and Na^+=550 mg/L) and middle boron concentration (300 mg/L). This capacity of cations effect in optimization graph were obtained as (Ca^{2+}=1,419.38 mg/L, Mg^{2+}=1,450 mg/L, K^+=1,450 mg/L and Na^+=1,438.59 mg/L) and middle boron concentration (304.49 mg/L). The maximum experimental boron capacity for clay effect was 1.08 mg/g and this value was obtained from experimental parameters of 0.16 g clinoptilolite, 0.38 g montmorillonite, 38 g kaolinite. This 1.08 mg/g capacity value was obtained from optimization graph at 0.5828 g clinoptilolite, 0.1936 g montmorillonite, 0.5852 g kaolinite amounts.These complexities in optimization and experimental parameters for cation and clay effect were due to near values of adsorption capacities. The borated-soil samples were successfully phytoremediated with potato plant and maximum intake of boron by the potato plant was 2,304.8 mg/kg plant.The studied soil concentrations for phytoremediation were 3.56, 13.56, 23.56, 33.56, 43.56, 53.56, 103.56, 203.56, 303.56, and 403.56 mg/kg boron.The plant dry weights decreased by increasing soil boron concentration and the green side of potato plants did not grow at 203.56, 303.56, 403.56 mg/kg boron concentrations exhibiting toxicity to seeds.

Keywords: Boron adsorption, Lime soil, RSM optimization, Phytoremediation, Potato plant

1. Introduction

The soils originate from the mother material on the Earth crust. The soils are classified as sandy, silty, clay, loamy, peaty and chalky. The components of the healthy soil are calcium, manganese, potassium, sulfur, carbon, nitrogen, phosphorus, organic matter, water, soil air and microorganism. The main boron types found in the soil are monoborate ($B(OH)_4^-$) and boric acid (H_3BO_3) [1]. The soils irrigated with domestic wastewater and sea water may contain toxic levels of boron. The soil boron concentration passing to irrigation water is generally 7-80 µg/g [1]. Boron adsorption onto soils is affected from pH, temperature, calcium carbonate content, organic matter, clay amount, metal oxides and ionic strength [2]. The soil texture is based on factors like clay content, organic matter content or particle size and the boron adsorption on soils in different regions shows changing

capacity values because boron interaction has a complex mechanism based on texture. Some of the complex mechanisms are boron fixation with soil clay, fulvic or humic acids [2]. Generally, boron binding onto soils increases with pH raise to the alkaline pHs (7-9.5) due to the increasing of monoborate anion fraction at partially low hydroxyl ion competition [2]. The boron adsorption onto soils is an endothermic or exothermic process [2].

In this study, boron adsorption onto lime soil was studied under the effect of solution cations and soil clays. The boron concentration was selected from 0 to 700 mg/L for cation effect and as 500 mg/L for clay effect. The reason of selection of high boron concentration was that the boron concentration in sea waters, boron-containing lake waters, geothermal waters used for irrigation would cause to more boron

accumulation in soils after repeated irrigation. We aimed to saturate the soil against boron at one time by applying high boron concentration. Also, irrigation waters contain cations.

The phytoremediation can be defined as the accumulation of soil pollutants in hyper-accumulator plants. The phytoremediation is a low-cost method and easy for application. The types of plant treatment of soils are phytoremediation, rhizofiltration, phytostabilization, rhizodegradation, phytodegradation, phytovolatilization, organic pumps, phytoextraction [3]. Some preliminary literature reviews aiming boron adsorption onto soils and phytoremediation of boron from soils by plants are given as follows. Alleoni and coworkers reported that the soil aluminum oxide and clay content increased the boron adsorption [4]. In other study, it was reported that boron adsorption onto soil increased with concentration, clay amount, organic matter and cation exchange capacity increase. In the same study, the sand amount of soil increased to desorption of soil boron, probably sand adsorbs the boron physically [5]. The boron intake by plants is based on clays, humidity, organic matter, aluminum and iron oxides, magnesium hydroxide in soil [6]. In a thesis study, it was studied the boron phytoremediation from soils by vetiver grass (Chrysopogon zizanioides L.)and above 40 mg/kg boron concentration, the plant dead occurred and dry weight and height of vetiver plant decreased with increasing boron concentration. The application of EDTA and DTPA extractants was determined as more effective before harvest compared with before planting [7]. Böcük and coworkers used various plants to study the phytoremediation of boron from soils and Puccinella distans subsp. distans (Poaceae) and Gypsophila perfoliata subsp. perfoliata (Caryophyllaceae) showed both the greatest tolerance and greatest B accumulation ratios [8]. Rees et al. studied boron removal from soil contaminated with borax by black poplar and hybrid poplar trees [9]. In the pot experiments made with black poplar and hybrid poplar, the boron pollution in the soil was kept in the range of 13-280 mg/kg. It has been reported that poplar trees were not affected by pollution up to a concentration of 93 mg/kg boron. It was also reported that growth in poplar decreased with the increase in the concentration of soil samples within 168-230 mg/kg boron pollution. The mean boron concentration in the poplar leaves was 3,500 mg/kg but this value was calculated to reach 7,000 mg/kg in leaf stains [9]. In this study, boron adsorption onto lime soil under irrigation water cation and clay type effects by central composite experimental design were studied and the borated lime soil was phytoremediated with potato plant. The use of potato plant for phytoremediation of soils is dense in heavy metal uptake and potato is a new alternative for boron uptake from lime soils by phytoremediation.The central composite experimental design tool of response surface method (RSM) was used in optimization.

2. Materials and Methods
2.1 The used chemicals and equipments

The lime-solid was used for cation, clay effects and potato phytoremediation experiments. The polyetilene 100 mL sample bottles were used to fill boron solutions for cation effect experiments. The solutions for cation and clay effect experiments were prepared on a magnetic stirrer (Hot Stirrer MS-300HS). The solution taking was done by automatic pipets (1, 5 mL) (Vitlab product). An incubator shaker was used for boron adsorption experiments on soil (JSR product). A pH meter was immersed into solutions for pH measurement and adjustment (WTW Multi 340i, Germany). A centrifuge was used for seperation of soil particles from boron solutions. Boric acid (Merck product) was used for preparation of boron solutions and borated soils. The special name of planted potato was not decided and purchated from market. The used clay minerals are belonging to Balıkesir city in Turkey. The typical XRF (X-ray Fluoroscence) analysis results of Balıkesir montmorillonite [10], clinoptilolite [11] and kaolinite [12] were reported by given references. The calcium, magnesium, potassium and sodium chloride salts were used for cation solutions preparation (Merck products).

2.1 Boron adsorption experiments for lime soil

The soil sample was supplied from Balıkesir University campus in Turkey. A volume of 50 mL solution with 0-700 mg/L boron concentration and 0-1,450 mg/L cation concentration transferred to 100 mL polyethylene bottles and 5 g soil was added for cation effect experiments. The cations were calcium, magnesium, sodium and potassium. Cation effects were studied at 0-1,450 mg/L concentration interval. The boron solution was treated with soil (5 g) during 24 hours at 200 rpm agitation speed in an incubator shaker. The water temperature during the experiments was 30 °C.The soil sample was sieved below 800 µm sieve fraction before addition to boron solutions for cation and clay effect. After reaction, the solutions were centrifuged at 5,000 rpm speed and the boron analysis of supernatant was carried by potentiometric titration. The procedure was as follows [13]: A volume of 5 mL boron solution was transferred to the 100 mL baker and 50 mL pure water was added and the pH of the solution was fixed to 7.6. D-mannitol was added up to constant pH value and then boron solution again titrated with 0.02 N KOH up to pH became 7.6. The boron concentration was determined from the base consumption. 1 mL of 0.02 N KOH solution is equal to 0.6964 mg B_2O_3. The used base solution was standardized against 500 mg/L boron solution daily. The clay effect was studied with clinoptilolite, montmorillonite and kaolinite clays as a mixture with soil at total 2.5 g soil-clay mixture weight. The studied boron concentration for clay type effect was constant 500 mg/L. The clays had 90-180 µm particle size. The clay effect was studied at 2.5 g mixture-to-25

solution ratio. The experiments for clay effect and cation effect were carried according to experimental matrix determined by central composite experimental design tool of respose surface method. Boron concentration and adsorption capacity were calculated by using the following equations.

$$Boron(mg/L) = \frac{(V_1 - V_2) \times 0.21627 \times 1,000 \times Sf}{V_3} \quad (1)$$

Here, V_1 is volume of consumed base during titration (mL), Sf is standardization factor, V_2 is base consumption for pure water at absence of boron (about 0.2 mL), and V_3 is the volume of boron solution taking after centrifugation (mL).

$$Qe = \frac{(C_0 - Ce)}{m} \times V \quad (2)$$

Here, Qe is the adsorption capacity (mg/g), C_0 is initial concentration (mg/L), Ce is the equilibrium concentration (mg/L), m is the soil amount (g) and V is the solution volume (L).

2.2 Characterization of soil sample

The pH and conductivity values of the soil sample were measured by treating 50 g soil with 500 mL pure water during about 48 hours at room temperature (Multi parameter pH Meter). The phosphorus and boron contents of the soil were measured by treating 50 g soil with 500 mL pure water during about 72 hours at room temperature and phosphorus was measured with stanneous chloride and boron was measured with carmine method due to its low concentration sensivity [14]. The organic matter and lime contents of the soil were gently measured by Ataturk University Agricultural Engineering Department

2.3 Phytoremediation experiments

The potato plants were growth and harvested at date of 02/05/2018 (potato planting) and 02/08/2018 (harvest), respectively. The air temperature, air humidity and irrigation of the plant were as follow: (avarage temperature 17.9-25.5 ^{o}C for mounts, air humidity 50-90% and irrigation at per 14 days as 250 mL pure water/3 kg soil). Pure water was used as irrigation water. 3 kg samples of soil were treated with different concentrations of boron solutions and the solutions were prepared from boric acid (Merck product). The soil boron concentrations were prepared as 10, 20, 30, 40, 50, 100, 200, 300 and 400 mg/kg.Addition to these concentrations, orginal soil sample had 3.56 mg/kg boron concentration. Ten pieces of water bucked were filled with 3 kg borated soil sample separately and potatoes were seeded in the soil and the potato plants were regularly irrigated during 3 months. The potatoes were planted during 3 months and the potatoes vegetable under roots did not grow. Upper side the

plants dried during 3 months at room temperature. The 0.5 g dried green potato plant was dissolved in concentrated nitric acid (50 mL) and boron analysis was done in ICP-OES instrument. Before analysis of boron by ICP-OES instrument, boron solutions were diluted at 100 fold. The characterization of soil is given in Table 1. Cation exchange capacity was measured by acetic acid method [15].

Table 1: Characterization of the soil sample.

Parameter	Value
pH	7.69
Total lime (% CaCO$_3$)	15.58
Organic matter (%)	2.66
Phosphorus (mg/g)	0.00185
Plant available boron (mg/g)	0.00356
Conductivity (μSc/cm)	175.8
Cation exchange capacity (mmol$_c$/kg)	3.872
Particle size (cation and clay effect experiments)(μm)	<800

3. Results and Discussion
3.1 RSM optimization for boron adsorption on soil

The response surface methodology was firstly defined by Box and Wilson [16]. They exposed to experimental matrix giving the optimum response by means of a very low experimental run. Generally, the RSM analysis is formed from three stages, namely the elimination study provides the low run, Anova analysis of the factor for regression model development, the analysis of factor levels to obtain the optimum conditions which are sometimes different from the investigated experimental matrix conditions. The general model in central composite design analysis was obtained by regression analysis. Model equation is Y=f(X1,X2,X3,……,Xn) + έ. Here, the Y equation is the response variable and f is the quantitative variable and έ is random error term [16]. A general regression model is as follow:

Capacity (mg/g) =b+b$_1$X$_1$ + b$_2$X$_2$ + b$_3$X$_3$ + b$_4$X$_1$X$_1$ + b$_5$X$_2$ X$_2$ + b$_6$X$_3$X$_3$ + b$_7$X$_1$X$_2$ + b$_8$X$_1$X$_3$ + b$_9$X$_2$X$_3$ + b$_{10}$X$_1$X$_2$X$_3$ + έ   (3)

In this study, central composite experimental design (CCED) tool of response surface analysis method was applied. The central composite design analysis is formed from these stages: Firstly, selection of parameter number, selection of alpha (fold between parameter levels, i.e 2 for this study) and center point number, entering of parameter levels as low and high values, entering of confidence level (95%, i.e. 0.05 for this study), and optimization of response by selecting targed value in optimization tool in programme analysis.

The optimization of solution cations effect on boron adsorption by lime soil was studied by CCED analysis. The experimental matrix is given in Table2. The boron capacity values were in the range of 0-0.764 mg/g. The

Anova analysis (student-t test and confidence factors, p) was performed and is given in Table 3. The confidence limit value (p) for main and interaction effects of parameters was selected as 95% ($p<0.05$). The P values (probability constants) were used as a control parameter to check the reliability of the developed statistical model, individual and interaction effects of the parameters. In general, the larger the magnitude of t and the smaller the value of P, the more significant is the corresponding coefficient term [17]. The constant term, magnesium, potassium-potassium, sodium-boron terms were found as statistically important. It can be seen that the cations have a very low effect on boron adsorption.The surface plots of the cation effect on boron adsorption onto lime soil are given in Figure 1.The experimental matrix for clay effect is given in Table 4. The Anova analysis for clay-soil mixture (clay amount in 2.5 g mixture) is given in Table 5. The boron adsorption capacity was in the range of 0.297-1.08 mg/g for the clays of kaolinite, montmorillonite and clinoptilolite at 2.5 g/25 mL soil-clay mixture dosage. The Anova analysis of factors for clay-soil mixture showed that the all factors p values were under confidence level ($p<0.05$). The presentation of clay type effects is given in Figure 2. The boron adsorption increased with kaolinite increase and montmorillonite decrease. Also, the adsorption capacity decreased with clinoptilolite decrease and middle kaolinite amount. The capacity increased with clinoptilolite decrease and montmorillonite middle value. The optimizer graphs of the cation effect and clay effect are given in Figure 3-4. The targeted maximum boron adsorption value of cation effect (0.764 mg/g) was obtained for 1419.3814 mg/L calcium, 1438.5952 mg/L sodium, 1450 mg/L potassium,1450 mg/L magnesium, and 304.4906 mg/L boron. The reason of 304.4906 mg/L boron was probably due to boric acid-polyborate equilibrium because above 0.25 M boron concentration, polyborates increase.The targeted maximum boron adsorption value of clay effect (1.08 mg/g) was obtained for 0.5828 g clinoptilolite, 0.1936 g montmorillonite, 0.5852 g kaolinite. The experimental matrix for cation effect in maximum boron adsorption was formed from 550 mg/L calcium, 550 mg/L sodium, 1450 mg/L potassium, 550 mg/L magnesium and 300 mg/L boron for reaching 0.764 mgB/g targeted capacity. The experimental targeted value (1.08 mg/g) for clay effect was obtained at 0.16 g zeolite, 0.38 g montmorillonite and 0.38 g kaolinite in the matrix.The difference between experimental and optimization values were due to data proximity in experimental results (Table 6). The soils generally contain clay minerals as constituent and the clays have boron binding property that causes to unusable boron fraction by plants in the soil body. The clay minerals have positive sites like silisium and aluminum at broken edge on the frame work adsorbing specifically the boric acid and monoborate anion.

Also the hydroxilated aluminum and silisium sites complex the boron. The solution cations in soil-solution medium cause the positive surface charge development with cation adsorption onto soil surface and thus much more boron adsorbed on to soil due to increasing zeta potential.

Table 2: Cation effect on boron adsorption (Temperature 30 ^{o}C, 200 rpm, Natural pH, Total soil weight 5 g, Solution volume 50 mL, concentration units of cations and boron are in mg/L)(a: 0 mg/L concentration).

Run	Ca^{2+}	Na$^+$	K$^+$	Mg^{2+}	B	Capacity (mg/g)
1	100	100	100	100	500	0,284552
2	1000	100	100	100	100	0,491870
3	100	1000	100	100	100	0,369919
4	1000	1000	100	100	500	0,487804
5	100	100	1000	100	100	0,512195
6	1000	100	1000	100	500	0,325203
7	100	1000	1000	100	500	0,487804
8	1000	1000	1000	100	100	0,004065
9	100	100	100	1000	100	0,349593
10	1000	100	100	1000	500	0,345528
11	100	1000	100	1000	500	0,345528
12	1000	1000	100	1000	100	0,004065
13	100	100	1000	1000	500	0,528455
14	1000	100	1000	1000	100	0,105691
15	100	1000	1000	1000	100	0,308943
16	1000	1000	1000	1000	500	0,569105
17	-350^a	550	550	550	300	0,317073
18	1450	550	550	550	300	0,235772
19	550	-350^a	550	550	300	0,215447
20	550	1450	550	550	300	0,317073
21	550	550	-350^a	550	300	0,235772
22	550	550	1450	550	300	0,764227
23	550	550	550	-350^a	300	0,357723
24	550	550	550	1450	300	0,520325
25	550	550	550	550	-100^ε	0,000000
26	550	550	550	550	700	0,455284
27	550	550	550	550	300	0,195122
28	550	550	550	550	300	0,296748
29	550	550	550	550	300	0,032520
30	550	550	550	550	300	0,276422
31	550	550	550	550	300	0,296748
32	550	550	550	550	300	0,276422
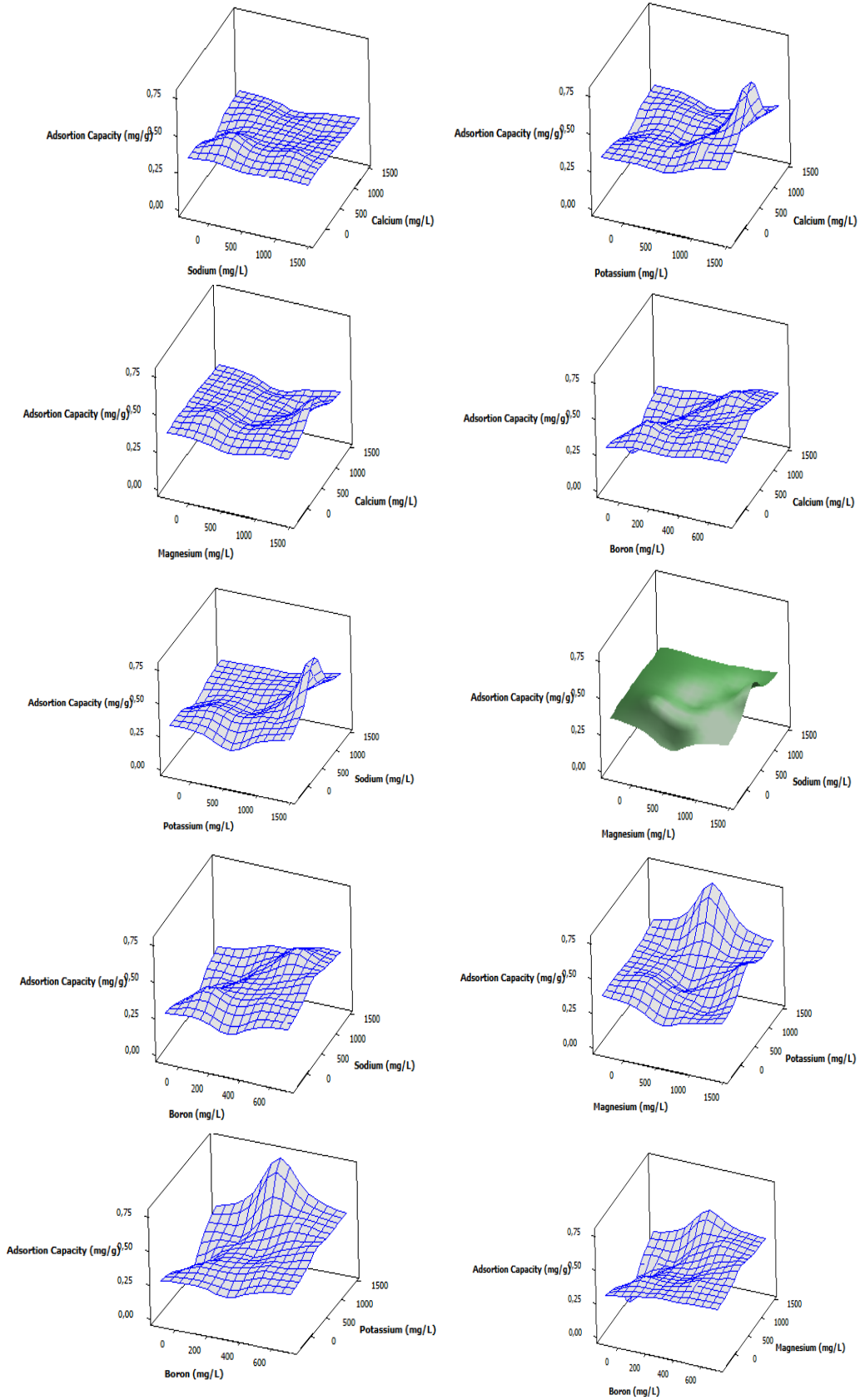
Figure 1: Surface plots for cation effect.

Table 3: Anova analysis results for cation effect.

Term	Constant	t-value	p-value
Constant	0.71112	3.664	**0,004**
Ca	-0.000173	-0.737	0.477
Na	-0.000335	-1.426	0.182
K	-0.000403	-1.719	0.114
Mg	-0,000568	-2.421	**0.034**
Boron	-0.000910	-1.654	0.126
Ca*Ca	0.000000	0.305	0.766
Na*Na	0.000000	0.199	0.846
K*K	0.000000	2.644	**0.023**
Mg*Mg	0.000000	2.006	0.070
Boron* Boron	-0.000000	-0.205	0.841
Ca*Na	-0.000000	-0.079	0.939
Ca*K	-0.000000	-1.570	0.145
Ca*Mg	-0.000000	-0.314	0.759
Ca*Boron	0.000001	1.963	0.075
Na*K	0.000000	0.314	0.759
Na*Mg	0.000000	0.314	0.759
Na*Boron	0.000001	2.277	**0.044**
K*Mg	0.000000	1.492	0.164
K*Boron	0.000001	1.413	0.185
Mg*Boron	0.000001	1.570	0.145

Table 4: Soil-clay mixture effect (Temperature 30 ^{o}C, 200 rpm, Natural pH, Total soil-clay mixture weight 2.5 g, volume 25 mL, Boron 500 mg/L).

Run	Clinoptilolite (g)	Montmorillonite (g)	Kaolinite (g)	Experimental Capacity (mg/g)
1	0.25	0.25	0.50	0.86865
2	0.38	0.38	0.38	0.29661
3	0.38	0.16	0.38	0.63559
4	0.38	0.38	0.38	0.50848
5	0.16	0.38	0.38	1.08051
6	0.38	0.38	0.38	0.86865
7	0.25	0.50	0.50	0.44492
8	0.38	0.59	0.38	0.84746
9	0.38	0.38	0.38	0.46610
10	0.38	0.38	0.59	0.84746
11	0.50	0.50	0.25	0.80509
12	0.38	0.38	0.38	0.46610
13	0.50	0.25	0.25	0.46610
14	0.38	0.38	0.16	0.63559
15	0.25	0.50	0.25	0.76271
16	0.50	0.50	0.50	0.67797
17	0.38	0.38	0.38	0.88983
18	0.59	0.38	0.38	0.63559
19	0.50	0.25	0.50	0.76271
20	0.25	0.25	0.25	0.72034

Table 5: Anova analysis for clay-soil mixture.

Constant	Constant	t-value	p-value
Constant	2.0375	1.435	0,182
Clinop.	-6.9253	-1.983	0.076
Montm.	-0.8328	-0.238	0.816
Kaol.	0.1357	0.039	0.970
Clinop*Clinop	4.7264	1.434	0.182
Montm*Montm	2.2688	0.688	0.507
Kaol.*Kaol.	2.2760	0.690	0.506
Clinop.*Montm.	5.0349	1.102	0.296
Clinop.*Kaol.	2.6464	0.579	0.575
Montm.*Kaol.	-6.9640	-1.524	0.158
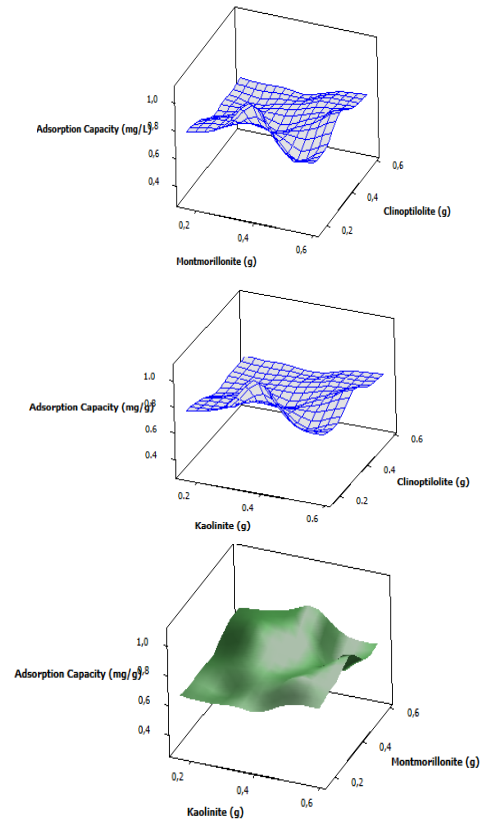
Figure 2: Surface plots for clay effect.
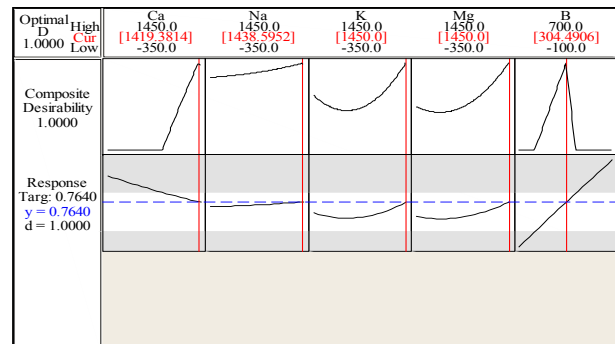
Figure 3: Optimizer graph of irrigation water cations.
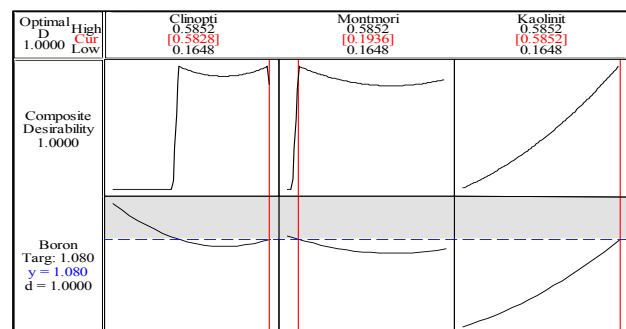
Figure 4: Optimizer graph of clay effect.

M. Korkmaz

The regression models for cation effect and clay effect were given as follows:

Capacity (mg/g) (Cation effect)= 0.71112-0.000173*Ca– 0.000335*Na– 0.000403*K-0,000568*Mg– 0.000910* Boron+0.000000*Ca*Ca+0.000000*Na*Na+0.000000* K*K+0.000000*Mg*Mg-0.000000*Boron*Boron-0.000000*Ca*Na-0.000000*Ca*K-0.000000*Ca*Mg+0,000001*Ca*Boron+0.000000*Na*K+0.0 00000*Na*Mg+0.000001*Na*Boron+0.000000*K*Mg+0.00 0001* K*Boron + 0.000001*Mg*Boron

Capacity (mg/g) (Clay effect)=2.0375–6.9253*Clinop-0.8328*Montm + 0.1357*Kaol + 4.7264*Clinop*Clinop + 2.2688*Montm*Montm + 2.2760*Kaol*Kaol + 5.0349*Clinop*Montm + 2.6464*Clinop*Kaol– 6.9640*Montm*Kaol

The comparison of model and experimental values were given in Table 6 and estimations were distorted some degree.

Table 6: Comparison of experimental and model responses.

Run	Cation Exp. Value (mg/g)	Cation Model Value (mg/g)	Clay Exp. Value (mg/g)	Clay Model Value (mg/g)
1	0.284552	0.30822	0.86865	0.947006
2	0.491870	0.44652	0.29661	0.583327
3	0.369919	0.30072	0.63559	0.658283
4	0.487804	0.75102	0.50848	0.583327
5	0.512195	0.23952	1.08051	0.90324
6	0.325203	0.68982	0.86865	0.583327
7	0.487804	0.54402	0.44492	0.608388
8	0.004065	-0.03768	0.84746	0.716652
9	0.349593	0.09102	0.46610	0.583327
10	0.345528	0.54132	0.84746	0.730901
11	0.345528	0.39552	0.80509	0.80245
12	0.004065	-0.18618	0.46610	0.583327
13	0.528455	0.33432	0.46610	0.391138
14	0.105691	-0.24738	0.63559	0.644036
15	0.308943	-0.39318	0.76271	0.852813
16	0.569105	0.77712	0.67797	0.723425
17	0.317073	0.17037	0.88983	0.583327
18	0.235772	0.39897	0.63559	0.70475
19	0.215447	0.31617	0.76271	0.747363
20	0.317073	0.25317	0.72034	0.756181
21	0.235772	0.37737		
22	0.764227	0.19197		
23	0.357723	0.52587		
24	0.520325	0.04347		
25	0.000000	-0.23133		
26	0.455284	0.80067		
27	0.195122	0.28467		
28	0.296748	0.28467		
29	0.032520	0.28467		
30	0.276422	0.28467		
31	0.296748	0.28467		
32	0.276422	0.28467		

3.2 Phytoremediation of boron from lime soil by potato plant

Boron phytoremediation from borated-lime soils containing 3.56, 13.56, 23.56, 33.56, 43.56, 53.56, 103.56, 203.56, 303.56, and 403.56 mg/kg boron was studied using potato plant growing May, June and July months in the 2018 year. Generally, the potato plants remained short at high concentration and the plantation did not occur at high concentrations (203.56, 303.56, 403.56 mg/kg concentrations). The boron uptake profile of potato plant is given in Figure 5. As can be seen in Figure 5, the maximum boron uptake was obtained at 103.56 mg/kg concentration as 2,304.8 mg/kg plant. The boron uptake capacities of plants were 406.5, 952.8, 729.5, 241.3, 180.2, 2058.8, 2304.8 mg/kg plant for 3.56, 13.56, 23.56, 33.56, 43.56, 53.56, 103.56 mg/kg soil boron concentrations. The raw soil had 3.56 mg/kg boron concentration. The dry weights of potato plants were 5.78, 3.60, 6.34, 4.94, 4.88, 2.86, 2.92 g for 3.56, 13.56, 23.56, 33.56, 43.56, 53.56, 103.56 mg/kg soil boron concentrations. The dried weights of the green potato plants were given in Figure 6. The borated potato plants were dried during three months at room temperature at subsequent months after plant dieing and the plants were retended in bucket for drying.
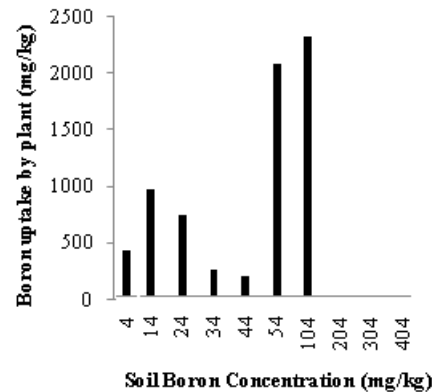
Figure 5: Boron phytoremediation by potato plant.
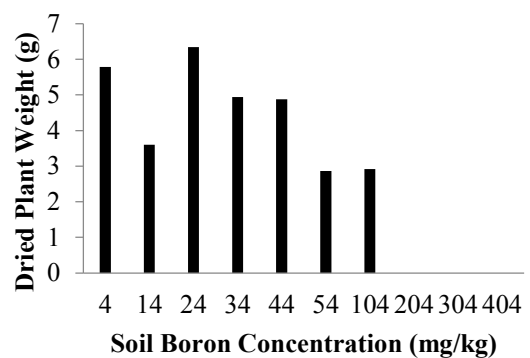
Figure 6: Dry weights of potato plants after phytoremediation.

4. Conculusions

Boron adsorption from solution onto lime soil under cations effect and soil clay effect was studied. The cations were calcium, magnesium, sodium and potassium. The clays mixed with soil were montmorillonite, clinoptilolite and kaolinite. Also, the borated soils were phytoremediated with potato plant. The results of the study can be summarized as follows. Boron adsorption onto soil under cation effect increased with increasing cation concentration and moderate boron concentration (around 300 mg/L). Maximum boron adsorption capacity of the soil under cation effect was calculated as 0.764 mg/g. The reason of the increase of soil boron capacity was increasing surface zeta potential of soil at high cation effects. The optimum clay amounts for 1.08 mg/g boron adsorption were calculated from optimizer graph as 0.5828 g clinoptilolite, 0.1936 g montmorillonite, 0.5852 g kaolinite for 2.5 g soil-clay mixture. The targeted value of cation effect (0.764 mg/g) from optimization graph was obtained for 1419.3814 mg/L calcium, 1438.5952 mg/L sodium, 1450 mg/L potassium,1450 mg/L magnesium, and 304.4906 mg/L boron. The phytoremediation studies by potato plant were carried out at 3.56, 13.56, 23.56, 33.56, 43.56, 53.56, 103.56, 203.56, 303.56, 403.56 mg/kg boron concentration. The raw soil had 3.56 mg/kg boron concentration. The boron uptake capacities of plants were 406.5, 952.8, 729.5, 241.3, 180.2, 2058.8, 2304.8 mg/kg plant for 3.56, 13.56, 23.56, 33.56, 43.56, 53.56, 103.56, mg/kg soil boron concentrations. The dry weights of potato plants were 5.78, 3.60, 6.34, 4.94, 4.88, 2.86, 2.92 g for 3.56, 13.56, 23.56, 33.56, 43.56, 53.56, 103.56 mg/kg soil boron concentrations. The potato plant did not grow at 203.56, 303.56, 403.56 mg/kg boron concentrations. The potato plant was found as effective for phytoremediation of boron from lime soils. The plant dry weights decreased by increasing soil boron concentration and the potato plants did not grow at 203.56, 303.56, 403.56 mg/kg boron concentrations exhibiting toxic effects for potato plant.

Acknowledgement

Author's Contributions

Mustafa Korkmaz: Performed the experiments, result analysis and manuscript preparation.
Cengiz Özmetin: Helped in result analysis.
Yeliz Süzen: Helped in result analysis.
Atilla Mutlu: Helped in experimental starting.

Ethics

There are no ethical issues after the publication of this manuscript.

References

[1] Tariq, M, and Mott, C.J.B. 2007. The significance of boron in plant nutrition and environment-a review. *Journal of Agronomy*; 6 (1):1-10.

[2] Chaudhary, D.R, Shukla, L.M, and Gupta, A. 2005. Boron equilibria in soil-a review. *Agricultural Reviews*; 26(4):288-294.

[3] Başcı, N. 2009. Cr (VI) iyonunun süs bitkileri kullanarak topraktan gideriminin araştırılması. Çukurova Universitesi, Yüksek Lisans Tezi, Adana, Turkiye (In Turkish).

[4] Reynaldo, L, Alleoni, F, Antonio Decamargo, O. 2000. Boron adsorption in soils from the state of sao Paulo, Brazil. *Pesquisa Agropecuária Brasileira*; (35) 2:413-421.

[5] Arora, S, Chahal, D.S. 2010. Effect of soil properties on boron adsorption and release in arid and semi-arid benchmark soils. *Communications in Soil Science and Plant Analysis*; 41:2532–2544.

[6] Goldberg, S. 1997. Reactions of boron with soils. *Plant and Soil*; 193:35–48.

[7] Memişoğlu, B.A. 2008. Bor ile kirletilmiş toprakların yeşil ıslah (Phytoremediation) yöntemi ile arıtılması. . Ataturk Üniversitesi, Doktora Tezi, Erzurum,Turkey (In Turkish).

[8] Böcük, H, Türe, C. 2014. Phytoremediation possibilities of boron contaminated environments by wild plants growing on boron reserve areas in Turkey. *Communications in Soil Science and Plant Analysis*; 45:1784–1798.

[9] Rees, R, Robinson, B.H, Menon, M, Lehmann, E, Guunthardt-Goerg, M.S, and Schulin R. 2011. Boron accumulation and toxicity in hybrid poplar (Populus nigra euramericana). *Environmental Science and Technology*; 45:10538–10543.

[10] Fil, B.A. 2007. Montmorillonitin tekstil boyar maddesi (metilen mavisi) gideriminde kullanımının araştırılması, Balıkesir Universitesi, Yüksek Lisans Tezi, Balıkesir, Turkey (In Turkish).

[11] Korkmaz, M, Özmetin, C, Fil, B.A, Özmetin, E,Yaşar, Y. 2013. Methyl violete dye adsorption onto clinoptilolite (natural zeolite): isotherm and kinetic study. *Fresenius Environmental Bulletin*; 22: 1524-1533.

[12] Bayülken, S, Başçetin, E, Güçlü, K, Apak, R. 2011. Investigation and modeling of cesium(I) adsorption by Turkish clays: Bentonite, zeolite, sepiolite, and kaolinite. *Environmental Progress & Sustainable Energy*; 30:70-80.

[13] Korkmaz, M, Özmetin, C, Özmetin, E, Süzen, Y. 2020. Modelling of boron removal from solutions by ion exchange for column reactor design in boron mine wastewater treatment. *Desalination and Water Treatment*; 179:63–74.

[14] Clesceri, F.S, Greenberg, A.E, Eaton, A.D. 1999.Standard Methods for the Examination of Water and Wastewater, 20th edition, Water Environment Federation: American Water Works Association, Washington, DC, USA.

[15] Aprile, F, Lorandi, R. 2012. Evaluation of cation exchange capacity (CEC) in tropical soils using four different analytical methods. *Journal of Agricultural Science*; 4(6):278-289.

[16] Turan, M.D, Altundoğan, H.S, 2011. Hidrometallurjik araştırmalarda yanıt yüzey yöntemlerinin (YYY) kullanımı. Madencilik; 50 (3): 11–23 (In Turkish).

[17] Korkmaz, M, Fil, B.A, Özmetin, C, Yaşar, Y. 2014. Full factorial design of experiments for boron removal from colemanite mine wastewater using Purolite S 108 resin. *Bulgarian Chemical Communucation*; 46:594–601.

Celal Bayar University Journal of Science

Effects of Thin Film Morphology of Polymer Hole Transfer Material on Photovoltaic Performance of Perovskite Solar Cells

Oğuz Çiçek[1] , Burak Gültekin[1*]

Ege University Solar Energy Institute, 35100 Bornova İzmir, Türkiye
*burak.gultekin@ege.edu.tr
* Orcid: 0000-0002-8804-7844

Abstract

In the present study, the effects of chain length variation of Poly(3-hexyl) thiophene polymer, which is one of the appropriate alternatives of Spiro-O-MeTAD used as a hole transfer layer (HTL) in perovskite-based solar cells (PSC), on thin-film morphology and device performance were investigated. Furthermore, nanowires of long (UZ) and short-chain (KZ) P3HT were obtained in the solution phase and then comparative photovoltaic performance analyses were carried out by fabricating PSC devices. As a result, it was determined that the morphological changes resulting from the polymer chain length directly affect the charge transfer between the active layer and HTL. KZ-P3HT presented better performance than both standard P3HT (5.99) and UZ-P3HT (2.68) polymers with a power conversion efficiency (PCE) of 7.74%. It was demonstrated that the main reason for this is that the fringed structure, detected by AFM images, increases the contact ratio at the perovskite/HTM interface. In addition, thanks to the morphological improvements in nano-wire studies, it was observed that the photovoltaic performance of the PSC device containing UZ-P3HT increased by 5.51%. Contrary to UZ-P3HT, it was determined that after the conversion of KZ-P3HT to the nanowire, the fringed structure on the surface disappeared and therefore the efficiency decreased to 5.81%.

Keywords: Nanowire, Perovskite, Polymer Semiconductors, Solar Cell, Surface Characterization, Thin film morphology

1. Introduction

Solar energy is one of the most important and promising types of renewable energy sources. Today, a power conversion efficiency (PCE) of 26.1% has been achieved with silicon-based solar cells that convert solar energy into electrical energy and dominate the market commercially [1]. New photovoltaic (PV) technologies need to be developed because of the high energy consumption during the production of silicon-based solar cells and their rigid structure, making them unsuitable for some energy applications [2],[3]. Perovskite solar cells, which are among the photovoltaic technologies defined as third generation or emerging technologies, have reached an energy conversion efficiency of 25.5% with the structural development they have demonstrated in recent years [1].

Planar multi-junction perovskite solar cells (PSC) have great potential in the production of high-efficiency, low-cost and flexible photovoltaic devices [4]. Planar PSCs have a perovskite active layer placed between the hole and electron transfer layers. Interlayers that provide

charge transfer play an important role in charge collection, extraction and transport. Small molecules and polymeric structures that can be used at these interfaces offer advantages such as being able to prepare solutions at low temperatures, thanks to their adjustable chemical and electronic structures [5]. In addition, high-performance PSCs have obvious advantages over other devices with their electrical and optical properties such as wide carrier diffusion length, direct Bandgap, high absorption coefficient in the visible near-infrared region, and high charge carrier mobility. PSCs can be produced with n-i-p or p-i-n (inverted) device structures. Vapor phase deposition techniques, vapor assisted solution treatment and annealing procedures have made significant progress in the improvement of the perovskite film [3], [6], [7]. High-efficiency PSCs use mesoporous or compact metal oxides as the electron conduction layer (ETL) under the perovskite layer. Among these materials, semiconductor oxides such as TiO_2 and SnO_2 are the most well-known and used ones in PSC devices [8], [9]. The stable structure and sufficient electron mobility of TiO_2 provide advantages for PSC applications [10]–[12]. On the other hand, the

hole transfer layer (HTL) acts as a barrier, preventing electron transfer between the anode and the perovskite layer. It is an effective method to increase the efficiency of the hole transport process, improve the V_{OC} value, and to prevent possible degradation at the perovskite-contact interface [13]. By using HTMs with high hole mobility, high efficiencies can be achieved with compatible ionization potentials (or energy levels), high thermal stability, and resistance to external degradation factors (such as oxygen and moisture) [14]–[16]. Spiro-O-MeTAD is the most widely used molecular structure in the literature as HTM. Thanks to its three-dimensional structure, it covers the perovskite surface very well. In addition, it fills the cracks on the surface and reduces the load trapping at the interfaces [17]. Despite its important advantages, The high cost due to the multi-step and complexity of the synthesis procedure of Spiro-O-MeTAD is still an important issue to be overcome. In addition, the necessity of doping to increase its low hole mobility and low conductivity complicates the device manufacturing process. Therefore, the HTM layer becomes an important problem for the commercialization of PSC devices [18]. In the doping process of the HTM layer, lithium bis(trifluoromethane sulfonyl)imide (Li-TFSI) increases the majority of charge carriers by oxidation and thereby increases the conductivity of the HTM layer. In addition, tert-butyl pyridine (TBP) regulates the morphology by reorganizing Spiro-O-MeTAD molecules oxidized with Li-TFSI and helps to adjust the energy levels with its basic character [17]. Despite the record yields achieved by doping, using additives is a factor that increases the difficulty level of cell production and the total cost. From these points of view, developing new types of HTMs, which can be synthesized easily and do not need to be doped, have a relatively low cost, high operating stability is an important subject for studying.

In the literature, there are studies on the use of semiconductor small molecules or polymers, which are already tried in many opto-electronic applications, without using chemical doping. In those investigations, the solvent engineering method was used to adjust the morphological properties of the HTM layer for efficient charge transfer [19]. The regioregular isomer of poly(3-hexyl)thiophene (P3HT) has been extensively used as a standard in the active layer in organic solar cells (OSC). In addition to this, P3HT has been involved in the PSC applications as the HTM layer. It is well known in the literature that the chain length of P3HT has significant effects on film morphology [20]–[22]. It has been reported that a smooth morphology is obtained with chain lengths over 85,000D used in the active layer in OSC applications, while the morphology is impaired and the charge transport decreases with shorter chain lengths [20], [23]. For PSC applications where P3HT is used as HTM, studies on PCE changes depending on chain length have been carried out, and it has been

reported that higher yields are achieved with an increase in chain length [24]. On the other hand, to increase the charge carrying capacity of P3HT, which has mobility of 0.1 $cm^2V^{-1}s^{-1}$, and to extend the absorption band, converting it into a nanowire is a method used in the literature. In OSC applications with nanowire P3HTs, which were grown by optimizing solvent polarity, temperature and time parameters, a mobility of 1.44 $m^2V^{-1}s^{-1}$ and a PCE of 2.40% were achieved [24].

In the presented article, two fractions of P3HT with short (KZ) and long-chain (UZ) lengths and nanowire structures of these fractions were used as HTM in PSC and PV performance comparisons of these polymers were carried out. In addition, both Spiro-O-MeTAD and mixed P3HT were used as standard. Furthermore, morphological properties of both perovskite and HTM thin film have been investigated by SEM and AFM analyses in order to express the photovoltaic performance changes of PSC devices.

2. Materials and Methods
2.1 Materials

Glasses with fluorine-doped tin oxide (FTO) as the conductive oxide layer were supplied from Pilkington company in 2.5 cm x 2.5 cm dimensions. The surface resistivity levels are 13 Ω/sq and the FTO layer thickness is 450nm. The materials used for the triple cation Perovskite active layer solution were obtained from different companies: lead iodide (PbI_2) from TCI, methyl ammonium bromide ($MABr_2$) from Lumtec, cesium iodide (CsI) from Acros, lead bromide ($PbBr_2$) from Aldrich tan and formamidinium iodide (FAI) were purchased from Lumtec.

The starting material, titanium isopropoxy ($TiOPr_4$) used for the compact titanium dioxide (TiO_2) layer solution as the electron transfer material was obtained from Aldrich company. Hollow carrier materials, Spiro-O-MeTAD and poly(3-hexyl) thiophene (P3HT) were obtained from Lumtec. In addition, Lithium bis(trifluoromethanesulfonyl)imide (Li-TFSI) was purchased from Lumtec and 4-t-butyl pyridine (4-TBP) was purchased from Aldrich companies. Contact material silver, locally sourced. Zinc (Zn) powder and hydrochloric acid (HCl) used for etching the FTO from the glass substrate surface were obtained from VWR companies. Solvents used in the experiments were purchased from different companies: hexane from Fisher, isopropyl alcohol (IPA), acetone and chlorobenzene from Sigma-Aldrich, acetonitrile from Riedel, dimethyl sulfoxide (DMSO) from Merck, and dimethylformamide (DMF) from Sigma. Pure water, on the other hand, was used from the GFL brand ultrapure water device within the institute.

2.2 Device preparation

FTO glasses were used as both the substrate and the anode of the solar cell. In accordance with the geometry of the solar cell, one side of the FTO (~1.2 cm wide) was etched. The process was carried out by applying zinc (Zn) powder and 4 M HCl (hydrochloric) acid solution to the FTO. Afterwards, purified water, acetone, and isopropyl alcohol (IPA) were used for cleaning, respectively. The glasses were placed on the glass cleaning rack and sonicated in an ultrasonic bath for 5 minutes in those solvents. In the final stage of the cleaning process, substrates were dried with a nitrogen gun and exposed to oxygen plasma for 7 minutes to get rid of organic impurities on the surface and activate the surface. Compact TiO_2 was used as the electron transfer layer. The preparation of compact TiO_2 solution was carried out in two steps. In the first step, mixtures of IPA (2.53 ml)-HCl acid (35 μl) and IPA (2.53 ml)-TiOPr4 (0.369 ml) were placed in two separate vials. A compact TiO_2 solution was prepared by adding the solution containing TiOPr4 to the other solution. The substrates, whose surfaces were cleaned of organic residues with oxygen plasma, were coated with compact TiO_2. The coating process was carried out in the spin coater at 2000 rpm in 20 seconds. Then this layer was sintered at 460 ºC for 1 hour.

Triple cation perovskite was used as the active layer. During the preparation of triple cation Perovskite (Cs0.15 FA0.81 MA0.14 PbI2.53 Br0.45) solution, PbI2 (470 mg), PbBr2 (66 mg), MABr2 (18.81 mg), FAI (167 mg) and CsI (15 mg) was mixed stoichiometrically into 1 mL of DMF:DMSO in a 4:1 ratio [2]. During the coating process of the perovskite active layer, 80 μL of the mixture was used and the process was carried out at 2000-4000 rpm (10-20 seconds). Washing was performed with 100 μL of chlorobenzene in the last 10 seconds of the coating process. Finally, in order for the perovskite active layer to crystallize and get rid of chlorobenzene (1 hour at 100 ºC), annealing was applied. Spiro-O-MeTAD and P3HT were used as hole transfer layer for standard devices. The P3HT polymer was used both as purchased without any pre-treatment and after it was separated into two fractions as high molecular weight and low molecular weight by preparative high-performance liquid chromatography (P-HPLC) system.
A chlorobenzene solution of Spiro-O-MeTAD (76 mg/ml) was prepared for the films obtained with the spin coating system. 16 μL of 4-TBP and 30 μL of Li-TFSI were added to the mixture prepared for doping the HTM layer. During the Spiro-O-MeTAD coating, 60 μL of the solution was used for each device and the coating process was carried out with a program consisting of 20 s rotation at 4000 rpm. For the coating of P3HT HTMs, solutions of 10 mg/mL in chlorobenzene were prepared without adding any additives. In these mixtures, 80 μL was taken for each film, and the coating process was

carried out at a rotational speed of 2000 rpm for 20 s of rotation. P3HT coated films were then dried (5 min at 80 ºC) [25]. After the HTM layers were coated, silver (Ag) contacts were coated on the FTO/compact TiO2/ABX3/HTM structure. By using suitable masks, evaporation process was carried out with a thermal evaporation system in a pressure environment of ~ 4x10-6 mbar so that contact can be made from both FTO and HTM. Ag contact thickness was determined as 100 nm. Another hole transfer layer application is the P3HT nanowire application. P3HT nanowires were formed by adding KZ and UZ-P3HT materials obtained from P-HPLC to 10 mg/ml chlorobenzene: hexane (ratio: 6:4) solution and then keeping those solutions at room temperature for 1 h without stirring. The resulting solutions were filmed with the same coating and drying process as P3HT mixtures [26].

2.3 Analysis Methods
2.3.1 Characterization of Materials

X-ray diffraction (XRD) technique (Rigaku Ultima IV multi-mode XRD, $Cu_{K\alpha}$,1.54 Å) was used for the structural characterization of the triple cation perovskite active layer. All XRD analyses were performed using the CBO (cross-beam-optics) multilayer mirror system as a monochromator, with tube voltage and current of 40 V and 40 mA, respectively, from 10° to 60° (2Θ) with 0.5° scanning range and a scanning speed of 2°/min. In addition, atomic force microscope (AFM, Park AFM NX20) and scanning electron microscope (SEM, Zeiss VP 300) images were used for the surface analyses of the obtained perovskite and HTM layers. AFM analyses were performed using silicon nitride (Si_3N_4) tips smaller than 7 nm in "tapping-mode".
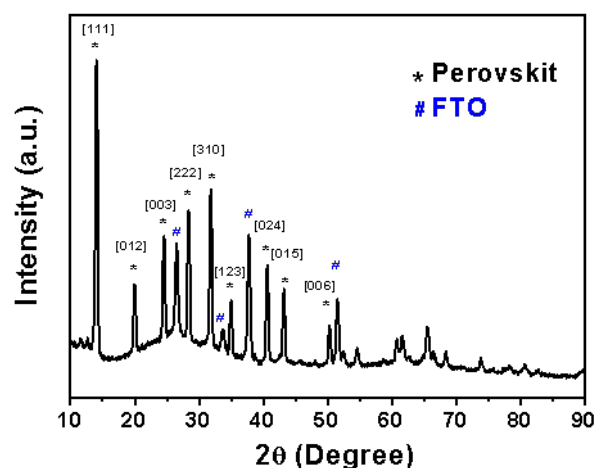
Figure 1. XRD pattern of triple cation perovskite coated on FTO glass.

Furthermore, SEM analyses were carried out at an accelerating voltage of 3 kV and magnification of 25kX and 100kX.

2.3.2 Photovoltaic (PV) Performance Analyses

The PV performances of prepared PSC devices were determined by extracting the current-voltage curves (scanning speed: 0.1 Vs^{-1}) under AM 1.5 standard radiation in an inert atmosphere, and the incident photon to current conversion efficiency (IPCE) analyses was taken under monochromatic light (scanning range: 1 nm).

3. Results and Discussion

The perovskite active layer was prepared as reported in previous studies [2]. The pattern of the XRD analysis performed for the structural analysis of the perovskite layer is shown in Figure 1. The characteristic XRD peaks of triple cation perovskite were observed at ~14º, 24º, 31º and 43º. These peaks belong to structures (111), (003), (123), and (015), respectively, and are in good agreement with the literature [27]. However, a PbI$_2$ peak around 12º was observed, albeit in a small amount. In addition, AFM and SEM analyses were performed to examine the morphological properties of the prepared perovskite layers (Figure 2-3).
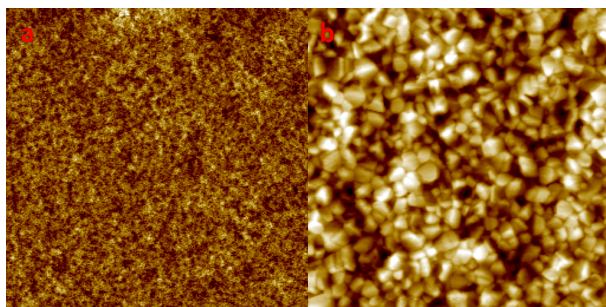
Figure 2. (a) 50μm and (b) 5μm AFM images of triple cation perovskite thin film.

In perovskite crystals, the grain boundaries of the crystal particles are act as trap states for charges [28]. Therefore, small particle sizes or wide intersection distances cause ascending of charge trap levels and descending in current density in device applications. It has been reported in many publications that annealing of perovskite thin films at 100 °C for 1 hour provides optimized crystal structure [29]. In both SEM and AFM images, it is observed that the size of the crystal domains is close to each other, indicating a homogeneous crystal growth on the compact TiO$_2$ layer. Furthermore, as can be seen from the 50μm*50μm AFM image in Figure 2(a), the distance between the deepest point and the highest point on the film is 100 nm, and this roughness is homogeneously distributed on the surface. A similar situation exists in the 25k X SEM image in Figure 3(a). The sizes of the crystal particles and the distances between the particles show a regular distribution throughout the thin film and support the AFM image. However, crystal defects marked with red rings are observed, especially in the 100.00KX SEM image in Figure 3(b). These defects would affect the charge transfer between the active layer and the HTM layer by increasing the trap states in the same way as grain boundaries. On the other hand, from the 2μm*2μm image obtained by the AFM technique, which allows us to obtain a three-dimensional (3D) image of the surface, it is seen that the crystals do not have a flat surface, unlike the two-dimensional (2D) SEM image. It has been determined that perovskite crystals are located on the film as mounds with sharp or pointed peaks. In contrast to the SEM image, the presence of smaller crystals was detected by the AFM image. Due to the determined morphology of the perovskite, the small molecular size of the HTM material and its amorphous state in the film phase increase the contact points at the perovskite/HTM interface and initiate charge transfer at the interface [28]. The absorption spectrum of the perovskite film is in the range of 300-750 nm (Figure 4.). In other words, it covers almost the entire visible region. In addition, the absorption band of P3HT in the solution (chlorobenzene) phase is in the range of 300-550nm (λ_{max}=453nm) and that of Spiro-O-MeTAD is in the range of 360-420nm (λ_{max}=389nm).
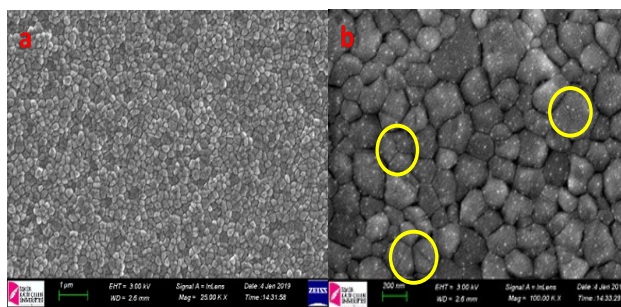
Figure 3. (a) 25kX and (b) 100kX SEM images of triple cation perovskite thin film.
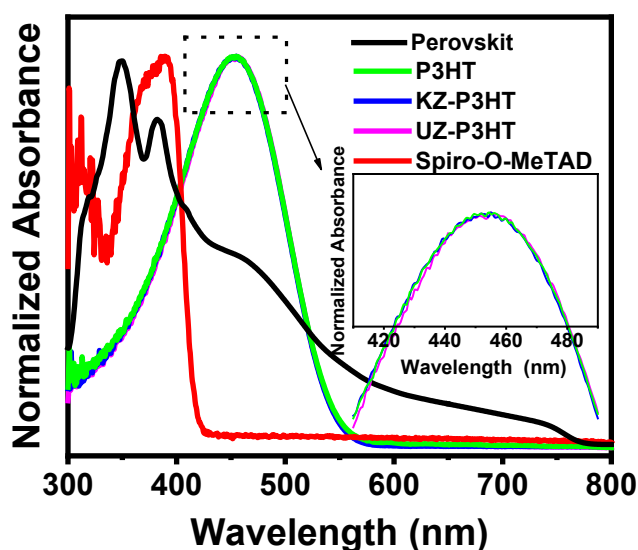
Figure 4. Absorption spectra of perovskit and HTM materials.
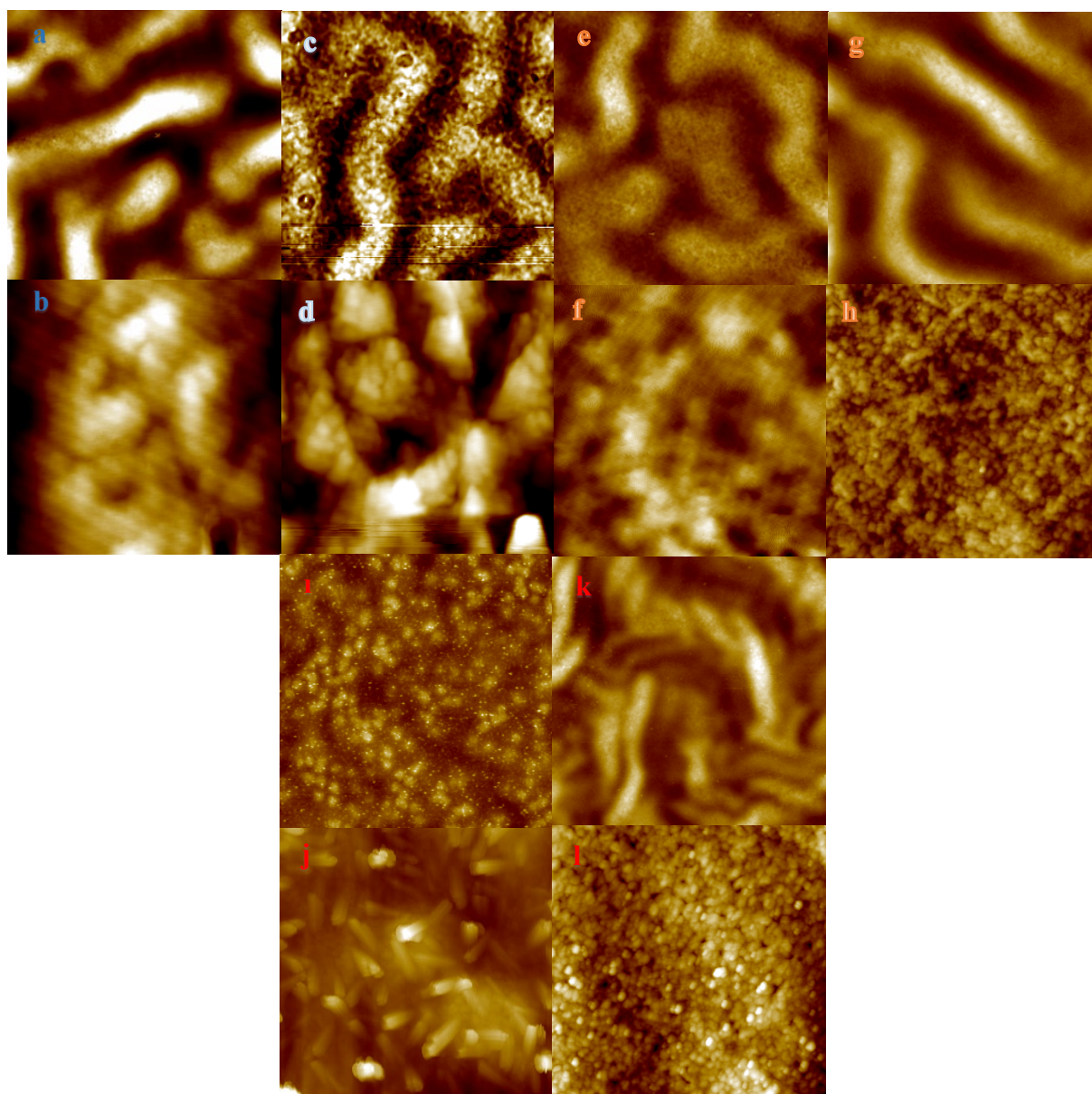
Figure 5. AFM images of different HTLs. Here (a) 50µm and (b) 5µm Spiro-O-MeTAD, (c) 50µm and (d) 5µm P3HT, (e) 50µm and (f) 5µm UZ- P3HT, (g) 50 µm and (h) 5 µm UZ-P3HT nanowire, (i) 50 µm and (j) 5 µm KZ-P3HT, (k) 50µm and (l) 5µm KZ-P3HT nanowire.

Separation of P3HT into low and high molecular weights did not cause differences in the maximum wavelengths (λ_{max}) in the absorption spectra. This is an expected situation. Because after the critical chain length is exceeded, the optical properties of semiconductor polymers do not show any change in the solution phase in the absence of any stereochemical differences (such as regioregular-regiorandom). This is because the resulting physical properties become ineffective as the chain length increases, as the intermolecular interactions in the solution phase are almost non-existent. However, in the solid phase, since the chain length change of the polymers leads to

changes in the morphology of the thin films, it also directly affects the charge transfer processes. Thin-film morphology directly influences charge transport and interfacial charge transfer processes [24].

The structural properties and stereochemistry of the molecules used in the HTM layer are also factors that directly affect the morphology of the film. For these reasons, film morphologies were investigated by AFM analysis in order to determine the physical changes that appeared by the changes in the polymer chain length. In Figure 5, AFM images of bare P3HT, long-chain P3HT (UZ-P3HT) and short-chain P3HT (KZ-P3HT) films coated on perovskite layer are presented together with

that of Spiro-O-MeTAD. As can be understood from the AFM images, it is observed that the HTMs are in an amorphous structure. However, it can be claimed that nanowires have a more regular morphology. After the P3HT polymer is dissolved in its solvent (chlorobenzene), a weak solvent (hexane) is added to it. The weak solvent interacts with the alkyl chains of P3HT after the addition, reducing the vibrational motion of the chains and allowing π-orbitals of neighbouring polymers to overlap with its own π-orbitals. After that, π-π stacking takes place along the entire chain and forms the nanowire structure [24].

Table 1 Morphology properties of HTM thin films.

HTL	RMS roughness (nm)	Avarage height (nm)	Areal Avarage roughness (nm)
Spiro-O-MeTAD	8.09	59.91	6.60
P3HT	10.62	79.77	8.50
KZ-P3HT	57.35	541.88	42.99
KZ-P3HT Nano wire	13.64	126.89	10.74
UZ-P3HT	72.60	222.20	64.20
UZ-P3HT Nano wire	9.47	74.08	7.62

Although nanowire formation causes a redshift in the absorption spectrum, its more dominant effect in device applications is due to the film morphology. According to the performance parameters in Table 2, the device with the highest efficiency is Spiro-O-MeTAD. However, no doping was applied to he P3HT layers and an efficiency of 5.99% was obtained. In the literature, it has been stated that relatively higher efficiency is obtained from the devices for polymeric HTMs when the polydispersity is low and the chain length is high [23]. However, contrary to the literature, in this study, KZ-P3HT with low molecular weight showed higher performance thanks to its morphological features. As seen in Figure 5, the AFM image of KZ-P3HT is distinctly different from other images with the nano-spots on it, while it is almost the same for all other films obtained with P3HT in 50μm images. In the 5μm images taken for further examination, it is observed that the KZ-P3HT chains form films in heaps, and also, due to the short-chain size, the ends of some chains are seen to protrude out of the stacks and form fringes. It is possible for this structure to improve the perovskite/HTM interface by penetrating into the crystal defects on the perovskite surface like the Spiro-O-MeTAD structure. Thus, the charge transfer increases and also the short-circuit currents obtained from the device containing the KZ-P3HT HTM increase (Table 2).
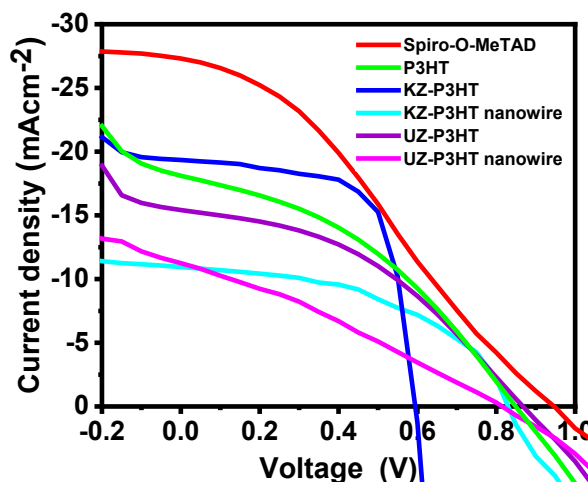
Figure 6. I-V curves of PSC devices with various HTM materials.

In order to examine the morphology of the films coated with nanowires of UZ-P3HT and KZ-P3HT polymers, 5μm and 50 μm AFM images were taken. It is observed that narrower peaks are formed as a result of the transformation of the UZ-P3HT structure into nanowires. Looking at the 5 μm images, it is seen that the islets on the surface of the UZ-P3HT film have turned into smaller and more prominent indentations and protrusions, while the RMS roughness has decreased (Table 1). It is thought that the increase in the short-circuit current and filling factor in the devices produced with UZ-P3HT nanowires is due to the mentioned changes in the nanowire morphology. While the nanowires forming the HTM layer increase the amount of contact at the perovskite-HTM interface, on the other hand, the charge transport within the HTM layer increases thanks to the nano-wire structure [24]. The same situation could not be observed in the transition of KZ-P3HT to the nanowire structure. As seen from the AFM images, because of KZ-P3HT's transition to the nanowire structure, the fringed structures on the film disappeared and the morphology became completely the same as the other P3HT structures. As a result, device efficiency has decreased to the level of device efficiency based on P3HT and UZ-P3HT.

PV performance tests were carried out under AM 1.5 G, with the devices created as specified in the device fabrication section. Before the PV performance analysis, the light intensity of the simulator was calibrated with a silicon solar cell with an area of 4 cm^2. The resulting J-V graphs are exhibited in Figure 6 and the performance parameters are summarized in Table 2. Among the devices prepared after annealing the perovskite active layer at 100 ºC, a power conversion efficiency of 8.69% was obtained with the standard Spiro-O-MeTAD, while a power conversion efficiency of 5.99% was obtained with the standard P3HT.

When the PV performances of UZ and KZ P3HT based devices are evaluated, it is noticed that KZ-P3HT exhibits higher power conversion efficiency (PCE) (7.74%) than P3HT. As indicated in the AFM results, in contrast to P3HT and UZ-P3HT, the fringed structure of KZ-P3HT in the film phase increases the contact points at the perovskite/HTM interface, thereby reducing trap levels.

Table 2. PV performances of PSC devices with various HTMs.

HTL	$J_{SC(MAX)}$ (mA cm^{-2})	V_{OC} (MAX) (mV)	FF (MAX)	PCE (MAX) (%)
Spiro-OMeTAD	27.51	950	0.33	8.69
P3HT	18.11	850	0.39	5.99
KZ-P3HT	19.35	650	0.66	7.74
KZ-P3HT Nanowire	10.94	820	0.62	5.81
UZ-P3HT	10.70	800	0.31	2.68
UZ-P3HT Nanowire	15.42	870	0.42	5.51

The relatively higher fill factor (FF) and short-circuit current (I_{SC}) observed in electrical measurements are proof of this result. On the other hand, the PCE of the device in which UZ-P3HT is used as HTM is far below P3HT. The main reasons for the 2.68% efficiency obtained from the KZ-P3HT are its low short-circuit current (I_{SC}) and fill factor (FF). This result shows that electron-hole pairs (exciton) formed in the perovskite layer are highly recombined (recombined) without dissociation at the perovskite/HTM interface. If we look at the PSC applications of nanowire structures of UZ and KZ P3HTs, it is seen that both structures present PCE values close to each other. As observed in the AFM images, both nanowire thin films have the same morphologies. In this case, due to the decrease in the contact points of the KZ-P3HT nanowire at the perovskite/HTM interface, a significant decrease in I_{SC} occurred.

4. Conclusion

As a result, the effects of chain length-dependent morphology changes of P3HT, which is used as an alternative to Spiro-O-MeTAD in PSC devices, on PCE were determined comparatively. The PCEs of Spiro-O-MeTAD and P3HT-based devices were 8.69% and 5.99%, respectively, while the PCEs of KZ-P3HT and UZ-P3HT-based devices were 7.74% and 2.68%, respectively. In particular, it is thought that the fringed structure of KZ-P3HT, determined by AFM images, increases the amount of contact by penetrating the boundaries between the crystal particles observed on the perovskite surface, thus improving the perovskite/HTM

interface. Thus, it is understood from the increase of I_{SC} in the J-V characteristic of the device that higher charge transfer is provided than the standard P3HT. In addition, the effects of P3HT nanowire structures on device performances were also revealed through morphology and interface properties. In devices prepared with nanowires of UZ-P3HT, PCE increased from 2.68% to 5.51%. This is thought to be due to the increased charge transfer on the HTM layer via more ordered aggregation of the P3HT chains. In particular, the increase in I_{SC} and FF values indicates an increase in charge transfer. Contrary to UZ-P3HT nanowires, the efficiency of devices containing KZ-P3HT nanowires decreased by 5.81%. In AFM images, it was observed that the fringed structure of KZ-P3HT disappeared after conversion to nanowire. For this reason, it was concluded that the interfacial interactions decreased and thus the efficiency decreased.

Acknowledgement

Author's Contributions

Oğuz Çiçek: Performed the experiments and result analyses, drafted the manuscript.
Burak Gültekin: Supervised and managed the study, drafted, and wrote the manuscript.

Ethics

There are no ethical issues after the publication of this manuscript.

References

[1]. "Best Research-Cell Efficiency Chart | Photovoltaic Research | NREL." https://www.nrel.gov/pv/cell-efficiency.html (accessed Dec.. 3, 2021).

[2]. M. Saliba *et al.*, 2016, "Cesium-containing triple cation perovskite solar cells: Improved stability, reproducibility and high efficiency," *Energy and Environmental Science*, 9(6), 1989–1997.

[3]. M. Liu, M. B. Johnston, and H. J. Snaith, 2013, "Efficient planar heterojunction perovskite solar cells by vapour deposition," *Nature*, 501(7467): 395–398.

[4]. O. Almora *et al.*, 2021, "Device Performance of Emerging Photovoltaic Materials (Version 1)," *Advanced Energy Materials*, 11(11).

[5]. S. S. Ashrafi *et al.*, 2020, "Characterization and Fabrication of Pb-Based Perovskites Solar Cells under Atmospheric Condition and Stability Enhancement," *Advances in Materials Physics and Chemistry*, 10(11): 282–296.

[6]. Q. Chen *et al.*, 2014, "Planar Heterojunction Perovskite Solar Cells via Vapor-Assisted Solution Process,", *Journal of the American*

Chemical Society, 136(2): 3–6.

[7]. G. E. Eperon, V. M. Burlakov, P. Docampo, A. Goriely, and H. J. Snaith, 2014, **"**Morphological Control for High Performance , Solution- Processed Planar Heterojunction Perovskite Solar Cells,", Advanced Functional Materials, 24 (1): 151–157.

[8]. S. Rutile *et al.*, 2013, **"**High Efficiency Solid-State Sensitized Solar Cell-Based on Submicrometer Rutile TiO 2 Nanorod and CH 3 NH 3 PbI 3 Perovskite Sensitizer", *Nano Letters,* 13(6): 2412-2417.

[9]. K. Wojciechowski, M. Saliba, T. Leijtens, A. Abate, and H. J. Snaith, 2014, "Environmental Science Sub-150 C processed meso-superstructured perovskite solar cells with enhanced efficiency", *Energy and Environmental Science*, 7(3), 1142–1147.

[10]. Q. An, P. Fassl, Y. J. Hofstetter, D. Becker-koch, and A. Bausch, 2017, "Nano Energy High performance planar perovskite solar cells by ZnO electron transport layer engineering", *Nano Energy*, 39(4)**:** 400–408.

[11]. T. Matsui, W. Tress, M. Saliba, A. Abate, M. Gra, and A. Hagfeldt, 2016, "Environmental Science cells by solution-processed tin oxide", *Energy & Environmental Science*, 9: 3128–3134.

[12]. Y. Wu *et al.*, 2016, "Perovskite solar cells with 18.21% efficiency and area over 1 cm2 fabricated by heterojunction engineering", *Nature Energy,* 1(11):1–7.

[13]. P. Yadav, D. Prochowicz, M. Saliba, P. P. Boix, S. M. Zakeeruddin, and M. Grätzel, 2017, "Interfacial kinetics of efficient perovskite solar cells,**"** *Crystals***,** 7(8)**:**1–9.

[14]. L. Miao, Z. Song, D. Zhu, L. Li, L. Gan, and M. Liu, 2020, "Recent advances in carbon-based supercapacitors," *Materials Advances*, 1(5):945–966.

[15]. T. Leijtens, K. Bush, R. Cheacharoen, R. Beal, A. Bowring, and M. D. McGehee, 2017, "Towards enabling stable lead halide perovskite solar cells," *J. Mater. Chem. A*, 5(23), 11483–11500.

[16]. M. Kim *et al.*, 2021, "Moisture resistance in perovskite solar cells attributed to a water-splitting layer," *Communications Materials 2021 2:1*, 2(1), 1–12.

[17]. G. Ren *et al.*, 2021, "Strategies of modifying spiro-OMeTAD materials for perovskite solar cells: a review," *Journal of Materials Chemistry A*, 9(8): 4589–4625.

[18]. J. Y. Seo *et al.*, 2021, "Dopant Engineering for Spiro-OMeTAD Hole-Transporting Materials towards Efficient Perovskite Solar Cells," *Advanced Functional Materials*, 31(45): 2102124.

[19]. X. Sun, X. Yu, and Z. Li, 2020, "Recent advances of dopant-free polymer hole-transporting materials for perovskite solar cells," *ACS Applied Energy Materials*, 3(11)**:** 10282–10302.

[20]. N. Yaghoobi Nia *et al.*, 2021, "Impact of P3HT Regioregularity and Molecular Weight on the Efficiency and Stability of Perovskite Solar Cells," *ACS Sustainable Chemistry and Engineering*, 9(14): 5061–5073.

[21]. Y. Zhang, M. Elawad, Z. Yu, X. Jiang, J. Lai, and L. Sun, 2016, "Enhanced performance of perovskite solar cells with P3HT hole-transporting materials via molecular p-type doping," *RSC Advances*, 6(110): 108888–108895.

[22]. E. H. Jung *et al.*, 2019, "Efficient, stable and scalable perovskite solar cells using poly(3-hexylthiophene)," *Nature 2019 567:7749*, 567(7749): 511–515.

[23]. N. Y. Nia, F. Matteocci, L. Cina, and A. Di Carlo, 2017, "High-Efficiency Perovskite Solar Cell Based on Poly(3-Hexylthiophene): Influence of Molecular Weight and Mesoscopic Scaffold Layer," *ChemSusChem*, 10(19): 3854–3860.

[24]. D. Kiymaz, A. Kiymaz, and C. Zafer, 2020, **"**Performance improvement of P3HT nanowire-based organic solar cells by interfacial morphology engineering,**"** *Nanotechnology***:** 32(10)**,** 105401.

[25]. N. Y. Nia, F. Matteocci, L. Cina, and A. Di, 2017, "High-Efficiency Perovskite Solar Cell Based on Poly (3-Hexylthiophene): Influence of Molecular Weight and Mesoscopic Scaffold Layer," *Aldo Di Carlo*, 10 (19) : 3854–3860.

[26]. M. Sapolsky and D. Boucher, 2018, "Poly (3-Hexylthiophene) Aggregation at Solvent – Solvent Interfaces,**"** *Journal of Polymer Science, Part B: Polymer Physics***,** 56 (13): 999–1011.

[27]. Y. Wang *et al.*, 2017, "Stitching triple cation perovskite by a mixed anti-solvent process for high performance perovskite solar cells," *Nano Energy*, 39(July): 616–625.

[28]. J. W. Lee, S. H. Bae, N. De Marco, Y. T. Hsieh, Z. Dai, and Y. Yang, 2018, "The role of grain boundaries in perovskite solar cells,**"** *Materials Today Energy***,** 7**:** 149–160.

[29]. L. Tian *et al.*, 2020, "Effects of Annealing Time on Triple Cation Perovskite Films and Their Solar Cells," *ACS Applied Materials and Interfaces*, 12(26): 29344–29356.

Voting Combinations Based Ensemble: A Hybrid Approach

Abdul Ahad Abro[1]* iD , Mir Sajjad Hussain Talpur[2] iD , Awais Khan Jumani[3] iD , Waqas Ahmed Siddique[3] iD ,
Erkan Yaşar[1] iD

[1]Department of Computer Engineering, Ege University, Izmir, Türkiye
[2]Information Technology Centre, Sindh Agriculture University, Pakistan
[3]Department of Computer Science, Ilma University, Pakistan
*abdulahadabro1@gmail.com
*0000-0002-3591-9231

Abstract

In the field of Artificial Intelligence (AI), Machine Learning (ML) is a well-known and actively researched concept that assists to strengthen the accomplishment of classification results. The primary goal of this study is to categories and analyze ML and Ensemble Learning (EL) techniques. Six algorithms Bagging, C4.5 (J48), Stacking, Support Vector Machine (SVM), Naive Bayes (NB), and Boosting as well as the five UCI Datasets of ML Repository are being used to support this notion. These algorithms show the robustness and effectiveness of numerous approaches. To improve the performance, a voting-based ensemble classifier has been developed in this research along with two base learners (namely, Random Forest and Rotation Forest). Whereas important parameters have been taken into account for analytical processes, including: F-measure values, recall, precision, Area under Curve (Auc), and accuracy values. As a result, the main goal of this research is to improve binary classification and values by enhancing ML and EL approaches. We illustrate the experimental results that demonstrate the superiority of our model approach over well-known competing strategies. Image recognition and ML challenges, such as binary classification, can be solved using this method.

Keywords: Artificial Intelligence, Data Mining, Machine Learning, Pattern Recognition.

1. Introduction

To discover; the relation and patterns in enormous datasets, sophisticated data analysis tools are being adopted and utilized for the extraction of data mining techniques [1]. Numerous theoretical and empirical research that demonstrate the benefits of the combination paradigm over separate classifier models have been published [2-5]. In recent years, ML has gained significant traction in a number of areas, including remote sensing, image categorization, and pattern identification.

These resources are interdisciplinary research fields including mathematical algorithms, statistical models, ML techniques, and intelligent information systems, etc [6].

A C4.5 decision is produced by the clear and easy-to-use algorithm J48 [7]. The classification process is modelled using a binary tree. It is a successor to the ID3 algorithm. Recursively choosing the test feature with the highest knowledge gain frequency as the test feature in [8] is an effective assessment model that eventually yields acceptable results.

One-dimensional convolutional neural network (1D-CNN), stacking-based ensemble deep learning model to carry out a multiclass classification on the five most prevalent kinds of cancer based on RNASeq data. The results of the single 1D-CNN, support vector machines with radial basis function, linear, and polynomial kernels, artificial neural networks, k-nearest neighbors, and bagging trees with the results of the novel suggested model with and without LASSO. The findings demonstrate that the suggested model, both with and without LASSO, outperforms competing classifiers. Additionally, the results demonstrate that under sampling improves performance compared to oversampling for the machine learning algorithms Support Vector Machine (SVM)-R, SVM-L, SVM-P, Artificial Neural Network (ANN), K-Nearest Neighbor (KNN), and bagging trees.[9].

Scientific classifications bagging and Neural Networks among the best representations available for the other models. As ML models are used to assess the risk of the most common deadly diseases with low occurrence, it produces considerable presentation. ML outperforms traditional regression for illness forecast modelling when the likelihood of disease occurrence is low. [10].

The conceivable outcome is aggregated by the NB classifier with the Bayes paradigm in decision rules. The learning framework for large-scale computational value and multi-domain platform classification [11].

Multiple continuous and categorical variables can be handled by the robust and adaptable SVM method. In addition, the overall results and comparisons are provided, highlighting the BER drops considerable non-linear explanation. The SVM multi-in-phase classifier's and quadrature components are largely reliant on the in-phase and quadrature components, which are comparably perfect when considering the impacts of intention and storage [12].

The choice of accessible base classifiers and combiner techniques are two of the primary obstacles in creating an ensemble [13]. The stack of ensemble (SoE) is an ensemble classifier that uses parallel architecture to merge three separate ensemble learners—Random Forest, Gradient Boosting Machine, and Extreme Gradient Boosting Machine in a consistent way. According to their Matthews correlation coefficients, accuracies, false positive rates, and area under ROC curve metrics that are satisfactory in terms of the analyzed parameters, classification algorithms performance importance is statistically examined.

There are several sections to the paper. Section 2 provides a brief description of the literature review. Section 3 contains the proposed approach used for carrying out various tests. Section 4 includes performance evaluation, experimental analysis, and detailed datasets. Finally, Section 5 recommends further work based on the findings and draws a conclusion.

2. Literature Review

Recently, research efforts focused on bagging, C4.5, stacking, SVM, boosting, and classification have increased [14]. In this study, we employ supervised learning's binary classification method. In classification, the goal class is anticipated properly and suitably for each situation involving data. The model is creating the training process, and a classification algorithm incorporates the standards of the analysts and the objectives [15]. Many classification algorithms use different methods to find associations. These relationships are models that can be applied to diverse datasets where the class is unknown [16]. The model was trained with the combined prediction model

utilizing a vote-based ensemble learning technique. It demonstrates that when the vote-based ensemble method is combined with an ANN, the results are more accurate than those produced by an ANN alone

When the C-C4.5 procedure's applications on noisy facts are compared to the C4.5 algorithm in C4.5 [17], it is found to be more reliable. The various locations have a big impact on how the C-C4.5 method is presented. The C-C4.5 trees with large standards yield the outcomes that are effective and accurate on average.

In [18] stacking strategy for creating ensembles of machine learning models is described. The cases for logistic regression and time series forecasting have been taken into consideration. The findings indicate the enhancement in the performance of prediction models in the scenarios under consideration by applying stacking techniques [19].

In [20], properties of bagging and NB are being investigated and a contrast is made between them. The hybrid bagging-NB prototyping approach, which strategically monitors the pattern of controlling the tradeoff between prototypical bias and prototypical variation, reduces the sum of inaccuracies. By enhancing fewer factors, the hybrid prototype offers an improvement that is authentic in terms of the training period.

The most well-known and distinctive data mining algorithms in are NB [21]. According to the empirical findings, the intended NB exhibits improved classification performance while preserving simplicity and flexibility.

In [22], presented the concepts of incorporating imprecise previous knowledge and sophisticated ML SVM-constructed procedures techniques. It utilizes the duality illustration in the framework of the minimax approach of decision making, which allows us to get straightforward extensions of SVMs, comprising supplementary limitations for optimization variables.

Boosting is a basic classification method that generates a single-level decision tree, as described. It has the capability to grip misplaced values and numeric features representing flexibility instead of the easiness. The Boosting procedure creates set of instruction and every characteristic in the training data, then captures the instruction with the least error rate.

3. Proposed Methodology

The pre-processing step of the data and the classification algorithms utilized in this study are described in the overview of the suggested technique provided in this part.

3.1. Proposed System

The proposed system is given in Figure. 1. It consists of numerous phases: datasets, base learners and comparative analysis of results. Besides, the generalization presentation of the system, 10-fold cross-validation is helpful intended for all classifier learners and datasets.

3.2. Data Pre-processing

The data from various ML datasets may have high range values. In this situation, specific features may have a considerable positive or negative impact on the classification accuracy of algorithms. Therefore, using the min-max normalization technique [23], data standards are restricted to the [0,1] range.

3.3. Classification of Algorithms

In this study, base learners, including bagging, C4.5, stacking, SVM, NB and boosting, are employed.

There are numerous phases of method related to datasets and classifiers focused on ML. In this work, six ML classifiers, along with five datasets, are experienced for binary classification.

Among all the methods, including NB, multilayer perceptron, C4.5 and random forest produces effective outcomes. This hybrid algorithm offers a classification accuracy of 75.625 percent. Then, the C4.5 method and random forest algorithm were integrated, yielding a classification accuracy of 76.4583%. Compared to individual classification algorithms, the hybrid classification algorithm is more accurate [24].

The most widely utilized fraud detection approaches are NB, SVM, and KNN. These methods can be used independently or in conjunction with one another to create classifiers utilizing ensemble or meta-learning methods. Ensemble learning techniques, however, stand out among the rest of the methods available not just for their ease of use but also for their extraordinary ability to predict outcomes in real-world situations [25]. Due to its independence from attribute values, the bagging classifier based on decision three performs well with this kind of data.

In [26], NB and random forest overlap the implementation, and both ML techniques outperform a number of algorithms. ML techniques such as bagging, NB, and random forest can identify persistence at the population level. Even though all methods would have resulted in the same results in reality, it is preferable to pick the most appropriate course of action for every situation.

In [27], a set of rules is suggested to improve the feature subclasses of models, and integrate the constraints of the SVM to use the sorting in a proper manner. The experimental outcomes depict that the procedure has a satisfactory consequence on the classification of adequate instant messaging evidence of the Internet of things big data and has a virtuous impact and applied application value.

Boosting classification algorithm produces for each analyst in the data population. In [28], a procedure for ML is a general evident unexpectedly useful on the ordinary datasets generally used for evaluating the results. It takes as input a set of incidents, each with various features and a category like other learning methods. The boosting algorithm selects the most revealing single feature and bases the idea on this feature alone. However, the result is not satisfactory with continuous-esteemed features and handling the hidden values.
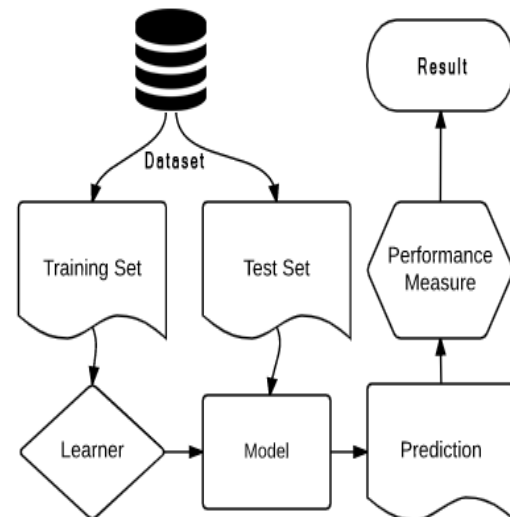
Figure 1. Proposed Layout.

4. Experiment and Analysis

In these subsections, we describe and present the experimental process, evaluation measures and experimental outcomes.

4.1 Experimental Process

The datasets utilized in the experiment extracted from the UCI ML Repository [29].

All studies rely on a total of 6 ML and EL classifiers thanks to the use of the WEKA (Waikato Environment for Knowledge Analysis) ML tools and the Java programming language. For all of WEKA's classifiers, we used the default parameter values [30].

A.A. Abro

To produce accurate findings, we use 10-fold cross-validation to all datasets. The initial dataset is subjected to the 10-fold cross-validation after being randomly divided into ten sets of equal size, one of which is utilized for test validation and the rest for testing. Ten times of the technique are done, and the averages of the results are calculated.

The attributes and the overall number of instances are considered when evaluating dataset properties. Usually, these datasets are utilized to address ML-related issues. Table 1 shows various numerical properties, instances, and class descriptions. The datasets were picked out of the UCI ML Repository based on the unique attributes that were being used for binary classification issues.

Table 1. Datasets detail.

Datasets	Instances	Attributes	Classes
Arrhythmia	452	279	2
Balance Scale	625	4	2
Car Evaluation	1728	6	4
Iris	150	4	3
Spambase	4601	8	6

The datasets used in this work have been considered suitable for classification, and various supervised ML techniques have been used. The performance measurements, however, are determined using confusion matrices to solve binary classification problems.

4.2 Assessment of Measures

This section describes the five performance evaluation measures of the proposed method, consisting of accuracy, Auc, precision, recall and F-measure.

Accuracy reflects how close an agreed number is to a measurement. It is specified further in Equation (1).

$$Acc = \left(\frac{TP+TN}{TP + FP+FN+TN}\right) \qquad (1)$$

In equation 1, TN, FN, FP and TP show the number of True Negatives, False Negatives, False Positives and True Positives. The Auc represents the area under the ROC Curve. It procedures the whole two-dimensional region under the entire ROC curve from (0,0) to (1,1).

Precision is a positive analytical value [31]. Precision defines how reliable measurements are, although they are farther from the accepted value. The equation of precision is shown in Equation (2).

$$Precision = \left(\frac{TP}{TP+FP}\right) \qquad (2)$$

The recall is the hit rate [32]. The recall is the reverse of precision; it calculates false negatives against true positives. The equation is illustrated in Equation (3).

$$Recall \quad \left(\frac{TP}{TP+FN}\right) \qquad (3)$$

F-measure can be defined as the weighted average [32] of precision and recall [33]. This rating considers both false positives and false negatives. The equation is illustrated in Equation (4).

$$F = 2 \, x \, \frac{Precision * Recall}{Precision+ Recall} \qquad (4)$$

These criteria are adjusted proportionally in the data by the reference class prevalence in the weighting operation.

Table 2. Results of ML methods for Arrhythmia dataset.

Methods	Acc (%)	Auc	Precision	Recall	F-Measure
J48	85.1705	0.875	0.845	0.852	0.845
Stacking	79.8718	0.722	0.798	0.799	0.798
Bagging	**85.6988**	0.911	0.851	0.857	0.852
NB	82.3779	0.902	0.846	0.824	0.831
SVM	85.4367	0.764	0.848	0.854	0.848
Boosting	79.6569	0.592	0.797	0.797	0.747

Table 3. Results of ML methods for Balance Scale dataset.

Methods	Acc (%)	Auc	Precision	Recall	F-Measure
J48	**75.5245**	0.584	0.752	0.755	0.713
Stacking	72.3776	0.628	0.699	0.724	0.697
Bagging	68.8811	0.646	0.668	0.689	0.675
NB	71.6783	0.701	0.704	0.717	0.708
SVM	69.5804	0.590	0.671	0.696	0.677
Boosting	65.7343	0.542	0.624	0.657	0.635

Table 4. Results of ML methods for car evaluation dataset.

Methods	Acc (%)	Auc	Precision	Recall	F-Measure
J48	92.3611	0.976	0.924	0.924	0.924
Stacking	93.5185	0.997	0.940	0.935	0.925
Bagging	93.1134	0.990	0.932	0.931	0.931
NB	85.5324	0.976	0.852	0.855	0.847
SVM	**93.7500**	0.953	0.939	0.938	0.938
Boosting	70.0231	0.500	0.700	0.700	0.824

Table 5. Results of ML methods for iris dataset.

Methods	Acc (%)	Auc	Precision	Recall	F-Measure
	Iris				
J48	96.0000	0.968	0.960	0.960	0.960
Stacking	95.3333	0.966	0.953	0.953	0.953
Bagging	**96.1000**	0.981	0.960	0.960	0.960
NB	96.0000	0.994	0.960	0.960	0.960
SVM	96.0000	0.978	0.962	0.960	0.960
Boosting	92.0000	0.940	0.920	0.920	0.920

Table 6. Results of ML methods for Spambase dataset.

Methods	Acc (%)	Auc	Precision	Recall	F-Measure
	Spambase				
J48	55.9299	0.733	0.549	0.559	0.553
Stacking	52.2911	0.685	0.524	0.523	0.522
Bagging	**58.6253**	0.825	0.585	0.586	0.577
NB	57.6146	0.816	0.585	0.576	0.566
SVM	57.0755	0.781	0.478	0.571	0.596
Boosting	53.2911	0.585	0.404	0.400	0.517

Table 7. Proposed Voting-Based Hybrid Apporach.

Datasets	Acc (%)	Impr. (%)	Auc	Precision	Recall	F-Measure
	Hybrid Approach Voting-Based Random and Rotation Forest					
Arrhythmia	**85.7222**	0.0234	0.902	0.840	*0.857	**0.856**
Balance Scale	**75.5247**	**0.0002**	0.651	**0.707**	0.731	0.691
Car Evaluation	**97.8009**	4.0509	**0.999**	**0.979**	**0.978**	**0.978**
Iris	*96.1000	0	**0.995**	0.947	0.947	0.947
Spambase	62.4663	3.841	**0.851**	**0.620**	**0.625**	**0.618**

- * Indicates the similar performance results concerning base learner.

- High Acc, Auc, Precision, Recall and F- measure is shown in Bold, while the greyed shows insufficient results.

- Impr. represents improvement according to best results of Tables 2-6.

4.3 Experimental Results

There are several algorithms for classification of which the most well-known and widely applicable dataset.

Tables 2-6 for all datasets present accuracy, Auc, precision, recall and F-measurement values of ML algorithms. In Table 2-6, high Acc, Auc, Precision, Recall and F-measure are shown in Bold, while the greyed shows insufficient results.

To sum up, Tables 2-6, has been designed in terms of different specifications according to the multiple datasets relating to the numerous approaches to ML. In Table 2, bagging has better outcomes, which provides 85.6988% Acc in comparison to others. Probably, in Table 3, J48 indicates 75.5245% Acc adequate consequences. Similarly, in Table 4, the SVM presents 93.7500% Acc effective results. Likewise, in Table 5, the bagging illustrates the 96.1000% Acc productive outcomes. However, in the end, bagging shows a 58.6253% Acc result in Table 6. Moreover, it is analyzed that bagging in Arrhythmia dataset Table 2, provides positive findings. Likely, J48 in the Balance Scale dataset concerning Table 3, indicates the progressive result.

Similarly, Table 4, SVM presents effective results in the car evaluation dataset. Likewise, in Table 5, the iris dataset bagging provides a more accurate outcome and It indicates adequate consequences in Table 6, Spambase dataset. Finally, high Acc, Auc, precision, recall and F-measure is shown in Bold, while the greyed shows insufficient results.

Table 7, demonstrates the comparison of all datasets results, with respect to our proposed voting-based hybrid approach meta-ensemble method. As it is clearly shown in Table 7, a meta-ensemble classifier, voting with two base learners (namely, Random Forest and Rotation Forest) provide highly accurate outcomes as compare to others.

5. Conclusıon and Future Work

The outcomes of supervised ML algorithms such as bagging, C4.5, Stacking, SVM, NB and boosting to classify numerous datasets. Algorithm effectiveness is further broken down into recall/sensitivity, accuracy, precision, and F-score categories. A retrospective study that analysed the different sizes of training and test sets can have a significant impact on the sensitivity and specificity of the same algorithm. This study suggests a hybrid voting-based technique. With this strategy, we may produce more beneficial and successful results by utilising the advantages of these algorithms. Other data mining approaches, such as clustering and association, can benefit from this research.

We intend to enhance our research on classification models in the future by using a hybrid framework of an intelligent ML system to a large number of real-world datasets.

Author's Contributions

Abdul Ahad ABRO: Drafted and wrote the manuscript, performed the experiment and result analysis.

Mir Sajjad Hussain TALPUR: As the project consultant, supervised the works and helped prepare the manuscript.

Awais Khan JUMANI: Assisted in analytical analysis on the structure, supervised the experiment's progress, result interpretation and helped in manuscript preparation.

Waqas Ahmed SİDDİQUE: Assisted in analytical analysis on the structure, supervised the experiment's progress, result interpretation and helped in manuscript preparation.

Erkan YAŞAR: Searched the literature and helped in manuscript preparation.

Ethics

There are no ethical issues after the publication of this manuscript.

References

[1]. Accorsi R, Manzini R, Pascarella P, Patella M, Sassi S. "Data Mining and Machine Learning for Condition-based Maintenance". *Procedia manufacturing*, 11,1153–1161, 2017.

[2]. Shao Y, Liu Y, Ye X, Zhang S. "A Machine Learning based global simulation data mining approach for efficient design changes". *Advances in Engineering Software,*124, 22–41, 2018.

[3]. Hüllermeier E. "Fuzzy sets in Machine Learning and data mining". *Applied Soft Computing,* 11(2). 1493–1505, 2011.

[4]. Kavakiotis I, Tsave O, Salifoglou A, Maglaveras N, Vlahavas I, Chouvarda I." Machine Learning and data mining methods in diabetes research". *Computational and structural biotechnology journal*, *15*, 104-116, 2017.

[5]. Shafiq M, Tian Z, Bashir AK, Jolfaei A, Yu X." Data mining and Machine Learning methods for sustainable smart cities traffic classification: a survey". *Sustainable Cities and Society*, *60*, 102177, 2020

[6]. Deepajothi S, Selvarajan S. "A comparative study of classification techniques on adult data set". *International Journal of Engineering Research & Technology (IJERT)*, *1,* 2012.

[7]. Bansal D, Chhikara R, Khanna K, Gupta P. "Comparative analysis of various Machine Learning algorithms for detecting dementia". *Procedia computer science*, *132*, 1497-1502, 2018.

[8]. Wang X, Zhou C, Xu X. "Application of C4. 5 decision tree for scholarship evaluations". *Procedia Computer Science*, *151*, 179-184,2019.

[9]. Mohammed M, Mwambi H, Mboya, IB, Elbashir MK, & Omolo B. "A stacking ensemble deep learning approach to cancer type classification based on TCGA data. *Scientific reports*", 11(1), 1-22, 2021.

[10]. Nusinovici S, Tham YC, Yan MYC, Ting DSW, Li J, Sabanayagam C, Cheng CY. "Logistic regression was as good as Machine Learning for predicting major chronic diseases" *Journal of clinical epidemiology*, *122*, 56-69, 2020.

[11]. Xu F, Pan Z, Xia R. "E-commerce product review sentiment classification based on a naïve Bayes continuous learning framework". *Information Processing & Management*, *57*(5), 102221,2020.

[12]. Wang C, Du J, Chen G, Wang H, Sun L, Xu K, He Z. "QAM classification methods by SVM Machine Learning for improved optical interconnection. " *Optics Communications*, *444*, 1-8,2019.

[**13].** Tama BA, & Lim S. "Ensemble learning for intrusion detection systems: A systematic mapping study and cross-benchmark evaluation", *Computer Science Review*, 39, 100357, 2021.

[14]. Abro AA, Yimer MA, Bhatti Z. "Identifying the Machine Learning Techniques for Classification of Target Datasets". *Sukkur IBA Journal of Computing and Mathematical Sciences*, *4*(1), 45-52,2020.

[15]. Abro AA, Taşcı E, Ugur A. "A Stacking-based Ensemble Learning Method for Outlier Detection". *Balkan Journal of Electrical and Computer Engineering*, *8*(2), 181-185,2020

[16]. Abro AA. "Vote-Based: Ensemble Approach". *Sakarya University Journal of Science*, *25*(3), 871-879, 2021.

[17]. Mantas CJ, Abellán J, Castellano JG. "Analysis of Credal-C4. 5 for classification in noisy domains. *Expert Systems with Applications". 61*, 314-326, 2016.

[18]. Pavlyshenko B. "Using stacking approaches for machine learning models", I*EEE Second International Conference on Data Stream Mining & Processing*, 255-258, 2018.

[19]. Sikora R. "A modified stacking ensemble machine learning algorithm using genetic algorithms", *In Handbook of research on organizational transformations through big data analytics*, 43-53, 2015.

[20]. Tan Y,Shenoy PP. "A bias-variance based heuristic for constructing a hybrid logistic regression-naïve Bayes model for classification" *International Journal of Approximate Reasoning*, 117, 15-28, 2020.

[21]. Chen S, Webb GI, Liu L, Ma X. "A novel selective naïve Bayes algorithm". *Knowledge-Based Systems*, *192*, 105361, 2020.

[22]. Utkin LV. "An imprecise extension of SVM-based Machine Learning models". *Neurocomputing*, *331*, 18-32, 2019.

[23]. Singh BK, Verma K, Thoke AS. "Investigations on impact of feature normalization techniques on classifier's performance in breast tumor classification". *International Journal of Computer Applications*, *116*(19), 2017.

[24]. Kumar AD, Selvam RP, & Palanisamy V. "Hybrid classification algorithms for predicting student performance", *International Conference on Artificial Intelligence and Smart Systems*, 1074-1079, 2021.

[25]. Zareapoor M, & Shamsolmoali P. "Application of credit card fraud detection: Based on bagging ensemble classifier", *Procedia computer science*, 48(2015), 679-685, 2015..

[26]. Van der Heide EMM, Veerkamp RF, Van Pelt ML, Kamphuis, C, Athanasiadis I, Ducro BJ. "Comparing regression, naive Bayes, and random forest methods in the prediction of individual survival to second lactation in Holstein cattle". *Journal of dairy science*, *102*(10), 9409-9421, 2019.

[27]. Chen Y. "Mining of instant messaging data in the Internet of Things based on support vector machine" *Computer Communications*, *154*, 278-287., 2020., 2020.

[28]. Nevill-Manning CG, Holmes G, Witten IH. "The development of Holte's 1R classifier" In *Proceedings 1995 Second New Zealand International Two-Stream Conference on Artificial Neural Networks and Expert Systems,* 239-242,1995.

[29]. Dua D, Graff C. "UCI Machine Learning Repository". http://archive.ics.uci.edu/ml (9.07.2021).

A.A. Abro

[30]. Engel TA, Charão AS, Kirsch-Pinheiro M, Steffenel LA. "Performance improvement of data mining in Weka through GPU acceleration". Procedia Computer Science, 32, 93-100,2014.

[31]. Abro, A. A., Siddique, W. A., Talpur, M. S. H., Jumani, A. K., & Yaşar, E. "A combined approach of base and meta learners for hybrid system". *Turkish Journal of Engineering*, 7(1), 25-32, 2023.

[32]. Abro, A. A., Khan, A. A., Talpur, M. S. H., & Kayijuka, I. "Machine Learning Classifiers: A Brief Primer". *University of Sindh Journal of Information and Communication Technology, 5(2), 63-68, 2021.*

[33]. Chandio, J. A., Talpur, M. S. H., Abro, A. A., Bux, H., Khokhar, N. U. A. A., Shah, A. A., & Saima, M. "Study Of Customers Perception About Shopping Trend Involving E-Commerce: A Comparative Study". *Turkish Online Journal of Qualitative Inquiry,* 12(8), 5415-5424, 2021.

Celal Bayar University Journal of Science

Attendance as a Service:
A Multi-Layered System Design in Attendance Applications for Covid-19

Alparslan Çay[1] , Doğan Kasas[1] , Müge Erel-Özçevik[1]*

[1]Manisa Celal Bayar Üniversitesi, Hasan Ferdi Turgutlu Teknoloji Fakültesi,
Yazılım Mühendisliği Bölümü, Turgutlu/Manisa, Türkiye
*muge.ozcevik@cbu.edu.tr
* Orcid: 0000-0003-3077-160X

Abstract

During COVID-19, there has been a requirement for a distributed architecture for contact-less and available smart applications that can be deployed in personal mobile devices. However, the single-layer architecture of the other similar applications in the literature has not met the user requirements according to the preliminary tests. Moreover, the conventional ones offer a high-cost architecture. To overcome these challenges, Software as a service (SaaS) has been preferred for the integration of distributed applications in the cloud market in a cost-efficient way. Therefore, we propose Attendance as a Service, i.e., a new multi-layered system which includes such technologies as QR code, face recognition, and fingerprint to meet the reliability and contact-less performance. In the performance evaluation, the proposed system operates with lower delay and higher scalability when compared to conventional ones. It has been observed that the multi-layered structure provides eight milliseconds of gain in delay compared to the traditional one and overcomes the students' inability to attend due to server density.

Keywords: Face Recognition Technology, Fingerprint Technology, Multi-Layered, Software as a Service, QR Technology

1. Introduction

Recently, the importance of smart applications that do not require physical contact in software-based services has tremendously increased by Covid-19 [1,2]. Significantly, some state and local governments have requested the suspension of biometric contact systems in attendance systems used in businesses [3]. To provide contactless execution in applications used with remote work, face recognition or fingerprint services and their distributed implementation on personal mobile devices have been considered [4,5].

There are three different methods in the cloud market for the integration of such applications: Infrastructure as a service (IaaS), Platform as a Service (PaaS), and Software as a Service (SaaS). These services minimize the physical risk and reduce operational and capital expenditures (OPEX/CAPEX) in a different manner. According to the literature, the market sizes of these services are given as $67 billion for SaaS, $34 billion for IaaS, and $11 billion for PaaS [6]. It clearly proves that SaaS is much more preferred than platform and infrastructure-based services because it provides a reliable service with a lower cost [7,9]. Accordingly, the

following research question is taken into account: "What kind of architecture should we build for current attendance systems to reduce human contact and provide a higher user experience with a lower cost?"

This paper proposes a novel system that can be easily adapted to wherever attendance is needed efficiently. Thanks to the network-based attendance system, users' participation is controlled in the fastest and contactless way possible by using QR codes and biometric recognition. By adding a network-based middleware, the proposed system overcomes the challenges of the conventional attendance systems that have a single-layer architecture. The literature survey and the problem definition are detailed in the following subsections.

1.1. The Literature Survey and Problem Definition

The attendance systems that have recently been used are exemplified in Figure 1. The usage areas of attendance are for student, employee, cafeteria, and membership systems. The attendance process taken in the classes is a factor that increases the participation rate and performance of the students.
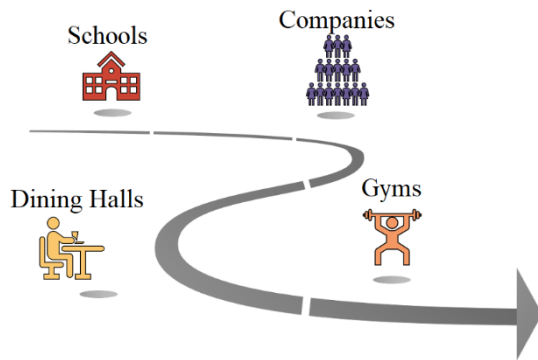
M. Erel-Özçevik

Figure 1. Attendance Systems.

Employee attendance systems are the process of tracking and storing users' coming to work and leaving time. Moreover, in the cafeteria systems, it is possible to track the employees who eat lunch in the cafeteria. On the other hand, membership attendance systems enable determining whether members of the club are in the membership areas such as gyms and fitness centers. The main purpose of all types is the same: managing attendance [10].

However, the conventional design of such attendance systems cannot meet end-user requirements because the single-layer architectural design cannot handle features such as the contactless process in today's Covid-19 [11]. Using automatic tracking systems rather than manual systems is safer and more efficient [12]. In a conventional system, the attendance paper is distributed among the students while they are taking attendance, which causes high contact between users. In other cases, the attendance can be taken by reading all the students' names aloud by the lecturers, resulting in huge time consumption. It is also prone to errors [13]. There are QR codes, RFID, wireless communication, fingerprint, iris, and face recognition based architectures in the literature [14].

In the QR code-based attendance system, a QR code that the lecturer projects on the screen is recorded by students' mobile devices. However, this solution ignores the location and authentication of the student. It cannot control whether or not the student attends the lecture in the class. Therefore, this reduces the reliability of the system. There are also other studies in the literature that try to enhance the reliability of such attendance systems. However, they require high expenditure for additional equipment used to increase the system's reliability.

For that reason, conventional QR-based attendance systems block users from participating in the attendance at a high number of incoming attendance requests to the system for a specific time [15,17]. The participation test results of the QR code-based attendance system designed with a single-layer architecture for 10,000 end-users are displayed in Figure 2.
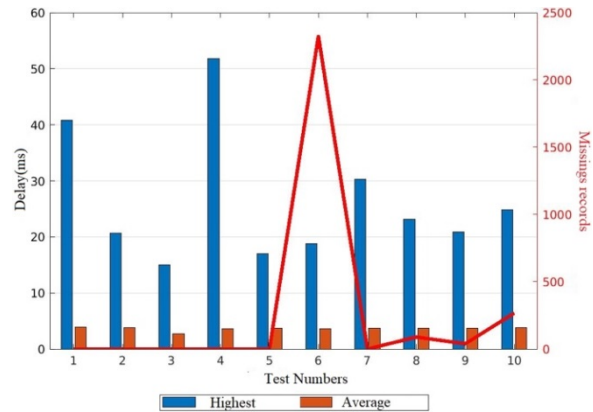
Figure 2. Preliminary Test for Conventional Attendance System.

On the y-axis on the left, the delay in milliseconds is indicated with a bar graph. The y-axis on the right indicates the number of those who could not participate in the attendance (the number of blocked) with a line graph. In light of this, the highest delay is observed at a level of 50 milliseconds, which is rather high above the acceptable level due to the excessive load in single-layered architecture. According to the new generation 5G requirements, it is requested that the delay level of software as a service should not be higher than four milliseconds [18]. Therefore, it is clear that the response time is not acceptable in the conventional single-layered systems, and some of the end-users can be blocked by the system, which reduces the reliability.

1.2. Contributions of Proposed System

In light of the aforementioned studies, a more efficient and reliable architectural design is required. This can only be handled by multi-layered architectural design compared to the conventional single-layer design [19,20]. Therefore, we propose a new Attendance as a Service, a multi-layered system including such technologies as QR code, face recognition, and fingerprint. The whole contributions are listed as follows:

- A novel middleware to reduce the cloud-centric server load,
- Integration of this system with a low cost by a software as a service,
- Minimizing human contact by using personal mobile devices for QR codes, face recognition systems, and fingerprint technology.

The remainder of the paper is organized as follows: In Section II, the analysis of the Attendance-as-a-Service architecture is given by comparing the conventional and proposed system architectures. The implementation details of the proposed system and its cost analysis are given in Section III. The proposed architecture in terms of delay, contactless and scalability metrics has been evaluated in Section IV.

2. Attendance as a Service and System Analysis
2.1. The comparison of conventional and proposed attendance systems

The conventional and proposed attendance systems are compared in terms of layering (Figure 3). Here, the conventional system is a QR code-based attendance system with a single-layered approach. The lecturer starts attendance at the attendance server layer, and by QR code read from the end-user's mobile devices, the attendance data is recorded in the cloud database. On the other hand, the proposed attendance architecture, thanks to added middleware and its multi-layered architecture, increases the reliability that checks that both the student and the lecturer are in the same local network (in the same class).
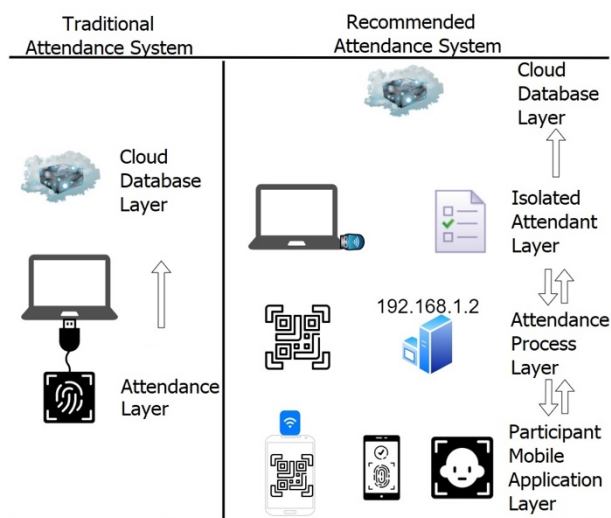
Figure 3. The comparison of conventional and proposed system architectures.

This implementation is performed at a minimal cost. Here, the attendance server layer and the lecturer's computer are used as the middleware, and it is used to open a local network. Students' attendance data first stored on the attendance server layer, i.e., not on a centralized cloud server. Afterwards, the saved attendance data is synchronized with the central server. Thanks to the added middleware, AaaS can be executed and synchronized with the enhanced system's reliability.

2.2. System Analysis

The system analysis of the proposed AaaS is detailed in the following subsections:

2.2.1. Strengths of the proposed AaaS

One of the strengths of the proposed AaaS is biometric data security. It is served to the end-user at the highest level because personal data is saved on the device of the relevant user. According to the Personal Data Protection Law, it is a law that biometric recognition systems should save personal data only on a personal device. In the light of this decision, the proposed architecture complies with this law. On the other hand, it offers a flexible architecture and can be adapted to specific services. For example, if attendance is desired to be implemented as a shift system, the architecture can be easily integrated accordingly. Moreover, taking attendance is based on asynchronous communication; there is no queue when executed. Therefore, the user experience is good.

On the other hand, there are three different packages according to the different customer types: simple, QR, and advanced package. In a simple package, the attendance network includes a mobile application that enables attendance by clicking the attend button, provided that it is connected to the attendance network using the newly added middleware. In the QR package, attendance is tracked by scanning the QR code as an addition to the simple package. Attendance is ensured by using QR codes and biometric control in the advanced package.

Furthermore, the suggested system is more resilient than existing systems. In current systems, systems such as fingerprint, face recognition, and RFID are inoperable in the event of a power outage; however, in the suggested multi-layer design, attendance can be performed asynchronously until the battery on portable computers is depleted. Cloud-based systems cannot function in traditional systems due to server and internet difficulties; however, attendance data can be temporarily saved in middleware in the suggested design, so attendance can still be received.

2.2.2. Weak aspects of proposed AaaS

To isolate the complexity of the middleware from the user, the proposed system acts as a relay against incoming requests. Therefore, any attendance data is portable in the middleware computer. The proposed multi-layer architectures may not be desirable where high security is required. However, in this case, the strength of security can be maximized with encryption algorithms such as SHA-2. Apart from these, a familiarization process is required to adapt to the new generation of technology. It is assumed that mobile users who are especially behind in digitalization can use QR scanning and/or fingerprint scanning on their mobile phones. The system's user interface is kept very simple to increase the user experience and speed up the process.

2.2.3. Possible opportunities with proposed AaaS

There is a new requirement for contactless work by COVID-19. We believe that the newly proposed system will enable mobile devices to be capable of more biometric recognition. Moreover, the significance of

M. Erel-Özçevik

personal data will increase even more. Thanks to these systems that enable personal and contactless work, digital devices will become more widespread, and incentives for this transformation will increase.

2.2.4. Risk analysis of proposed AaaS

There are also many risks because of the programming background. It may occur that the programming languages in which the proposed system is deployed will not be supported in the future. In order to minimize this risk, the system uses a new generation of MongoDB database that provides high-performance data logging. It is also built on a modular structure with Single Page Application (SPA) support. It is compatible with Angular, a JavaScript-based framework. Back-end services are also written with Node.js. The mobile app is built with React Native. All such technologies are quite valid in todays' deployments. On the other hand, there may be another threat, such as the cost of existing biometric devices. However, it is unlikely to not use a mobile application due to physical device based challenges.

3. The implementation of AaaS and the cost analysis
3.1. The implementation of AaaS

The implementation details of the proposed architecture are displayed in Figure 5. It has three layers. The attendant uses layers 1 and 2; whereas, layer 3 manages the communication with the attendance of personal mobile devices.

3.1.1. The Work Flow of AaaS

Firstly, the attendant opens the desktop application, which is newly called QRFace Attendance. The application routes it to the login screen located in Layer 1. After the login is successful, it is routed to Layer 2.1 by transferring the attendant data. The interface opens the attendance network with a button and selects the group to be attended (for example, courses for universities, departments for workplaces, etc.). It starts the timing period for taking attendance. When attendance is initiated, a middleware called Layer 2.2 is automatically built. The attendant projects the QR code and the remaining time on a screen that the participants can see. Attendance requests are taken and routed through Layer 2.2. Incoming requests are temporarily recorded on the attendant's computer, and Layer 2.2 is terminated. When attendance is finished, the attendant confirms the attendance list via Layer 2.1. The process is completed by transmitting data to Layer 1.

Meanwhile, the participant who uses the QRFace mobile app should first connect to the network created by the attendant.
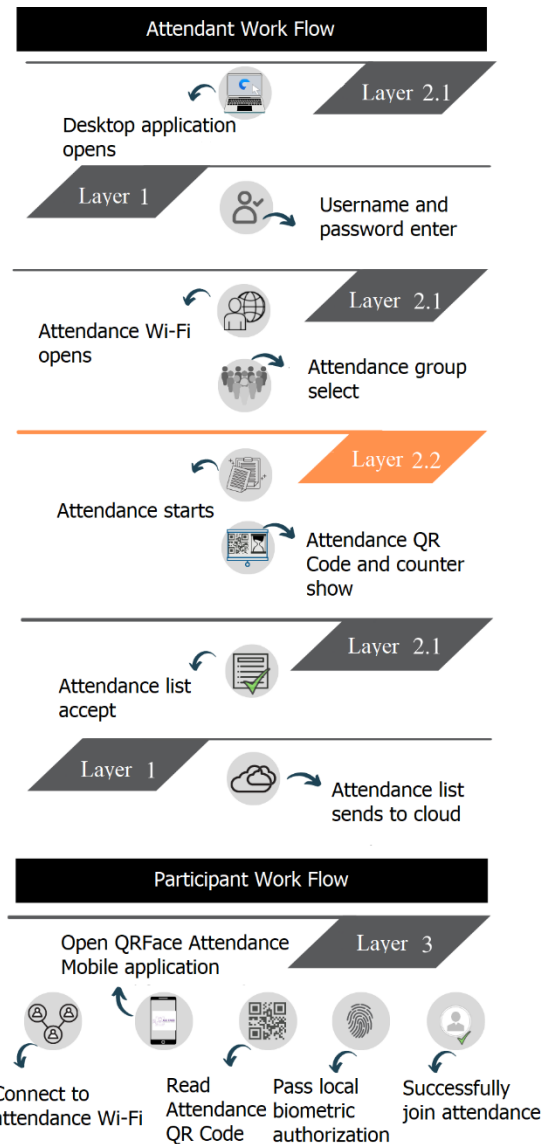
Figure 4. The Work Flows for Attendant and Participant.

The QR code on the screen is read by this mobile app. It is a 2D barcode technology that has common usage in applications. It improves the user experience by easily overcoming the difficulties faced in daily life. As an example in [21], the QR code screen is clearly represented to the end-user so they can easily read it with the mobile device. In [22], the willingness of Romanian people to use QR codes for based shopping is investigated, and the results indicate that the applicability of QR codes and enabling quick access to information about products improves the shopping experience of the respondents. The QR code minimizes the user interaction to transfer any data to the applications which gives altenative to manual entry [23].
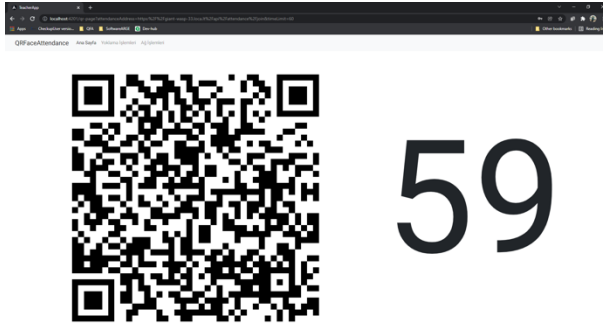
Figure 5. An example for QR code implementation in Layer 2.
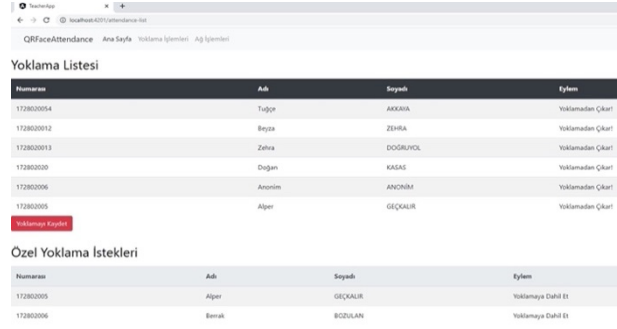
Figure 6. An example for Attendance List in Layer 2.
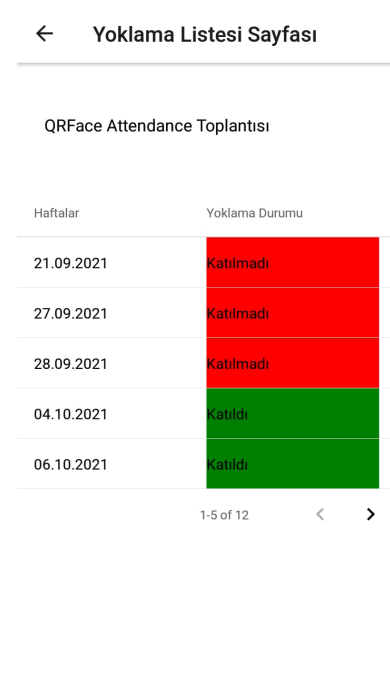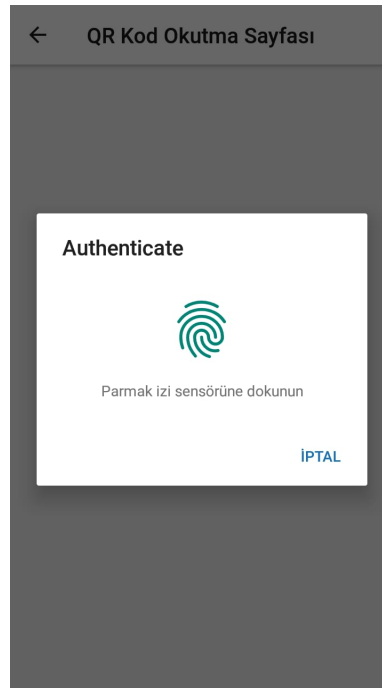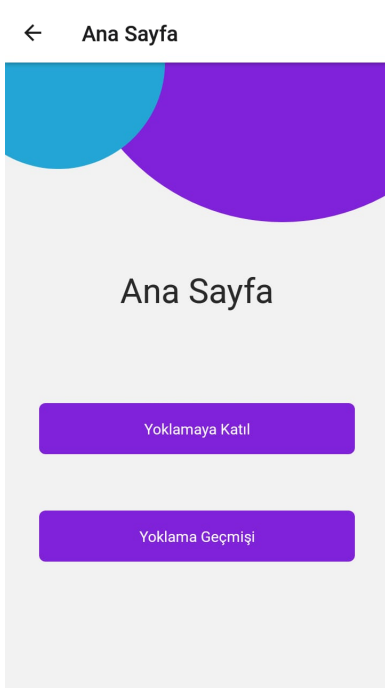
Figure 7. Main page in Layer 3.   **Figure 8.** FingerPrint check-in Layer 3.   **Figure 9.** Attendance Status in Layer 3.

Furthermore, a mobile application is analyzed in terms of user experience that use a QR code- based payment system in [24]. It is believed that such designs make users more comfortable in COVID-19 pandemics because there is no need for any touch to the screen. According to analyze which has many respondents from Sarawak and Malaysia, the fast loading time and QR code based payment are prioritized according to their important factors. Therefore, we use QR code in our application to accelerate taking attandence. According to user experience literature of QR code technology, we designed this screen by using a QR code that is placed centrally and implemented as plug-in service [25].

After the QR code screen, the user recognition should be performed. If the device supports face recognition or fingerprints for biometric checks, they are used. For example, the fingerprint screen is designed uniquely for

all mobile applications to meet user requirements as also mentioned in [26]. If the device does not support biometric recognition, it performs biometric control with the alternative face recognition system, which is available in the mobile application. This is currently used in such systems to check the personality with a quick response time [27]. The AdaBoost algorithm is used to enhance the performance of face detection [28]. According to the studies [29,30], the fingerprint is not suitable while compared to face recognition in terms of possible treats and hygiene. Therefore, we design our face recognition module which is implemented to mobile application as plug-in service in the light of these literatures. When the check is successful, the data is transmitted to Layer 2.2. Figures 5-6 illustrate the examples the proposed designs of Layer2 for web platform; whereas, the examples of Layer3 for mobile platform are given in Figures 7-8-9.

M. Erel-Özçevik
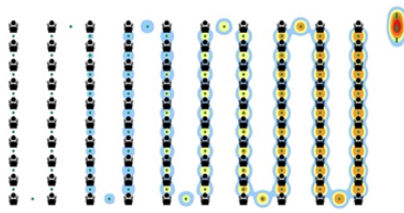
Figure 10. Contacts in Conventional System.
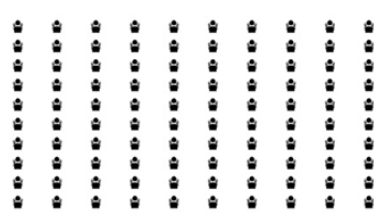
Figure 11. Contacts in RFID based Systems.
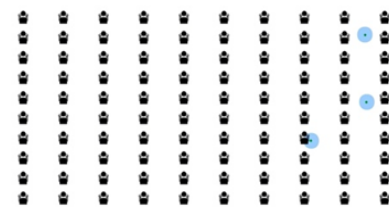
Figure 12. Contacts in Proposed System.

3.1.2. Technology Stack of AaaS

There is MongoDB with NoSQL in the technology stack, which performs high-performance data logging and flexible data modeling for the database. It has a modular structure with Single Page Application (SPA) in Angular, which divides the application into parts and enables it to be reusable, and it is easy and fast to develop projects with third-party frameworks. It also uses Node.js, which is compatible with JavaScript and enables new updates. Mobile applications use a cross-platform language named React Native that enables fast testability, a high user experience, and compatibility with the JavaScript back-end. The whole technology stack for the proposed AaaS is listed as below:

- In the first layer, MongoDB, Angular for the web interface, and a Node.js server for Create, Read, Update, Delete, operations on cloud databases are implemented.
- The second layer has two sublayers, as layer 2.1 layer and layer 2.2 (middleware). Layer 2.1 runs on "localhost" and includes Angular, which provides the interface for the participant, There is also a Node.js server that enables network operations, attendance listing, or sending data. The middleware is executed by the local IP address of the attendance network (For example, 192.168.1.2), and it contains the Node.js server that receives the incoming attendance requests.
- In the third layer, if the participant's device does not support biometric recognition, an alternative React Native application with face recognition is also available.

3.2. The Cost Analysis of AaaS

Table 1. Cost comparison of Cloud Database for a system that serves 100.000 participants.

Service	Conventional Attendance System	Proposed Attendance System
Cloud Database	$749/month	$57/month (-92%)

The cost analyses of the conventional system and the proposed multi-layered system are given in Table 1.

Here, the cost of the MongoDB database dated 15.03.2021 is given for both cases. In the conventional system, the workload is executed on the cloud because of the lack of middleware. There is a bottleneck which results in an ability to participate in attendance. To overcome this challenge, more costly database services are needed. On the other hand, the proposed multi-layered architecture greatly reduces the cost and handles the inability to participate in the attendance without any extra expenditure. It is indicated in the performance evaluation that it overcomes the case of not being able to participate in the poll by minimizing the incoming load to the cloud database. Therefore, the database cost for multi-layered architecture is 92% lower than the conventional one for the same user experience.

4. The performance evaluation of AaaS

Table 2. Testbed Environment for Performance Evaluation.

Network Adapter	RAM	CPU	Disk Speed (Read/Write)
Internal, External	8GB	Intel (R) Core (TM) i5 7300HQ 2.5Ghz	2000MB/s-1500MB/s
Local	12GB	Intel (R) Core (TM) i7 7700HQ 2.81Ghz	500MB/s-500MB/s

The performance of the proposed system is evaluated in 10 runs of real tests where the details are given in Table 2. Here, there are three network definitions such as "internal", "external", and "local". These shows in which real environment the performance tests are performed. The internal network adapter is the existing network adapter in the computer. The external network adapter is the network adapter used with USB. If it is local, it is treated as the local computer's IP address, also known as "localhost".

4.1.1. The Physical Contact HeatMaps

In Figures 10-11-12, the physical contacts resulting from the conventional or proposed attendance system are given in heatmaps. Here, the red color indicates the

M. Erel-Özçevik

points where there is high physical contact between participants, while the blue color indicates the contact is low, which is suitable for COVID-19 spread. The contact status of conventional methods when taking attendance of between 100 participants is given in Figures 10 and 11. The proposed AaaS is given in Figure 12. In the first one, there is a high level of contact and attendance queue formation is observed due to the attendance queue and the location of the participants. Due to the location of the RFID and biometric recognition devices, the physical contact and attendance queues are observed according to the proximity between the participants at a high level. However, in the proposed system, the physical proximity between the participants is very low, as it can be understood that only blue colors are seen on the heat map. Compared to biometric and conventional attendance systems, this proposed one has both less contact and physical proximity between participants and fewer attendance queues.

4.1.2. Delay Analysis

Table 3. Delay gain of Proposed Attendance System while comparing the conventional one.

The Number of Participants	Average Delay	Observed Maximum Delay
25	6.122 msecs	8.428 msecs
50	5.065 msecs	3.338 msecs
100	2.857 msecs	4.071 msecs

As in Table 3, it is indicated that the gain in user experience for the proposed multi-layered architecture compared to the conventional one. It has been observed that the average delay is reduced to 8 milliseconds by the use of middleware. The factors affecting delay are the computer's hardware features, the network adapter and the number of participants.

As indicated in Figures 13 and 14, the average delay results for the conventional and the proposed architectures are given according to the increasing number of participants. It has been observed that while the average delay is in the order of 8 milliseconds in the conventional one, it is decreased to the level of 2 milliseconds in the proposed architecture thanks to the multilayered architecture. In both graphs, the average values decrease as the number of participants increases. This is because of a queue to participate in attendance. The narrowing of the confidence interval means that the high delay is less than the other ones as the number of participants increases. When the highest delay values of the conventional architecture are examined, it is clear that the confidence interval is wider in the 54-person tests and the highest delay is more minor in the 108-

person tests. When the outputs are analyzed, it is clear that the system is working at optimum performance between 54 and 108 people, which caused a delay between 27 and 54 people because they are not used to the attendance system.

According to the adapter type used in the proposed architecture, internal values are slower than external and external values are slower than local ones. Despite the increase in the number of participants, the average delay values obtained are very close due to the isolation of the workload to the middleware and the complexity to the end-user.
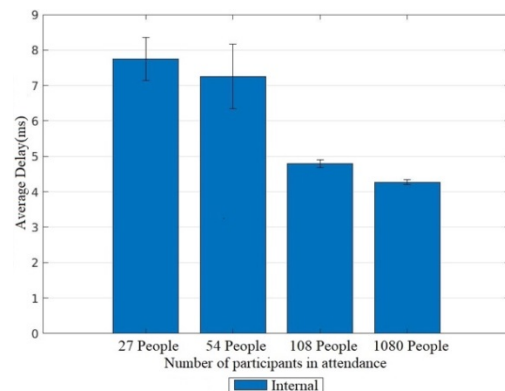

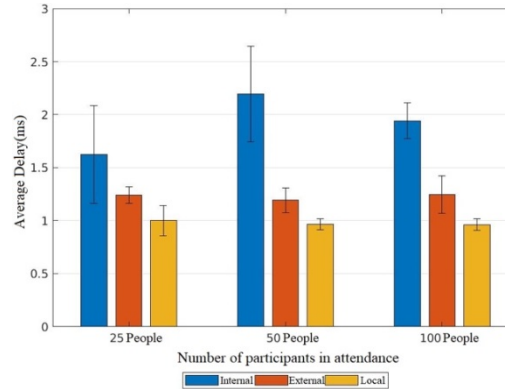**Figure 13.** The Average Delay for Conventional System.

Figure 14. The Average Delay for Proposed System.
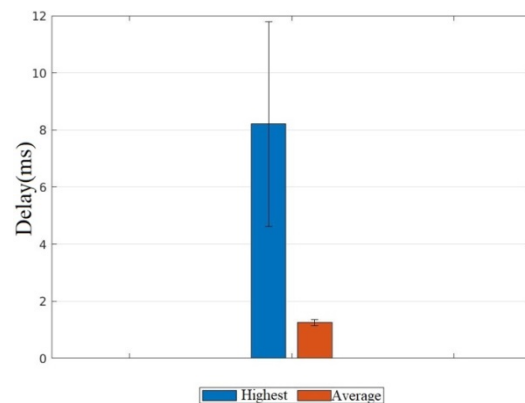
Figure 15. The Scalability of Proposed AaaS.

4.1.3. Scalability Analysis

The scalability of the AaaS architecture proposed in Figure 15 has been examined by simulating the attendance of 100,000 participants. Delay values are obtained by sending 1000 attendance requests to the database, where each contains the data of 100 participants. In this evaluation, the attendance of 100,000 participants was successfully saved in the database. On the other hand, the delay values obtained are at the level of 2 milliseconds for each 1000 participants saving, while it reaches the order of 8 milliseconds at the most. Despite this high user participation, the user delay can be kept at an acceptable level. On the other hand, the proposed system reaches the delay value (8 milliseconds) that the conventional method can provide at a low user level. Namely, the proposed system can be scalable up to 100,000 participants.

5. Conclusion and Future Work

Due to the contactless requirement of COVID-19 on smart applications, we propose an Attendance as a Service (AaaS) system with its multi-layered architectural design. The proposed system is easily integrated into the contactless working conditions brought about by COVID-19 compared to conventional single-layer attendance systems. Here, a distributed multi-layer architecture is executed on personalized mobile devices. It is implemented by software integration as a service in the cloud market, and the security level is increased by the use of technologies such as QR codes, face recognition, and fingerprints.

These biometric systems in attendance are highly used but not implemented as plug-in services in the conventional ones. The distributed implementation of the personnel check system on the attendance application keeps privacy without any data on central servers. There are also other studies in the literature that try to enhance the reliability of such attendance systems. However, they require high expenditure for additional equipment used to increase the reliability of the system. By using QR codes and mobile device-based checks (face recognition and fingerprints) on personal devices, there is no extra expenditure to build such a proposed system. Namely, it is easily implemented with low OPEX and CAPEX. According to the performance evaluation, the proposed AaaS serves end-users with a lower delay and a high scalability level compared to the conventional attendance systems commonly used today. In the future, the proposed multi-layered design can be easily applied to other research and application-based areas that require low operational costs while also providing higher security. For example, blockchain-based systems can easily be integrated with this proposed multi-layered architecture without any need for centralized authority. Therefore, the data privacy and integrity in an application can also be handled at the same time.

Acknowledgement

Author's Contributions

Alparslan Çay: Conceptualization, methodology, preliminary analysis, front-end and back-end implementation, mobile application, writing-original draft.

Doğan Kasas: Conceptualization, face recognition algorithm, mobile application, back-end implementation, writing-original draft.

Müge Erel-Özçevik: Conceptualization, methodology, validation, preliminary analysis, performance evaluation, writing-original draft, consultancy.

Ethics

There are no ethical issues after the publication of this manuscript.

References

[1]. European Centre for Disease Prevention and Control. Mobile applications in support of contact tracing for COVID-19 – A guidance for EU/EEA Member States. June 2020. Stockholm: ECDC; 2020.

[2]. Islam, M et.al.2020. A Review on the Mobile Applications Developed for COVID-19: An Exploratory Analysis. in *IEEE Access,*. 8: 145601- 145610. doi: 10.1109/ACCESS.2020.3015102.

[3]. Roy, P et.al. An Automated and Scalable Tool for Fingerprint based Biometric Attendance Management System. 2021 International Conference on Electronics, Communications and Information Technology (ICECIT), 2021, pp. 1-4, doi: 10.1109/ICECIT54077.2021.9641418.

[4]. Yan N. et.al. DP-Face: Privacy-Preserving Face Recognition Using Siamese Network. 20th International Symposium on Distributed Computing and Applications for Business Engineering and Science (DCABES), 2021, pp. 92-95, doi: 10.1109/DCABES52998.2021.00030.

[5]. Sharma, T et.al. 2021. Enabling User-centered Privacy Controls for Mobile Applications: COVID-19 Perspective. *ACM Transaction. Internet Technology.* 21, 1, Article 26 (February 2021), 24 pages. https://doi.org/10.1145/3434777

[6]. Linthicum, D. S. 2017. Paas death watch?. in Cloud Tidbits Column. *IEEE Cloud Computing.*

[7]. Patricia, J. M. A, Morreale, A. 2015. Design and deployment. *in Software Defined Networking.* Boca Raton, FL, USA: CRC Press.

[8]. Guan, W, Wen, Wang, X, Lu, Z, Shen, Y. 2018. A service-oriented deployment policy of end-to-end network slicing based on complex network theory. *IEEE Access*, 6: 19691–19701.

[9]. Jonatha, A, et.al. 2017. The Economics of the Cloud. *ACM Transactions on Modeling and Performance Evaluation of Computing Systems*, 2 (4): 23 pages.

[10]. Personel Attendance Control Systems: Face recognition systems. https://www.perkotek.com/en/main/. Perkotek. (accessed at 08.2021).

[11]. Lucy, S et.al. 2021. COVID-19 Contact Tracing and Privacy: A Longitudinal Study of Public Opinion. *Digital Threats: Research and Practice.*

[12]. Arpan, R et. al. 2015. Secure the Cloud: From the Perspective of a Service-Oriented Organization. *ACM Computing Surveys* 47 (3): 30 pages.

[13]. Tanrıverdi, M. 2017. Yüz Bulma ve Tanıma Tabanlı otomatik Sınıf Yoklama Yönetim Sistemi, *Ankara Üniversitesi Fen Bilimleri Enstitüsü*, Ankara..

[14]. Omlet Yoklama Yönetim Sistemi, Omlet bilişim ve egitim teknolojileri. https://omlet.com.tr/yazilim/omlet-yoklama-yonetim-sistemi.html (accessed at 10.2021)

[15]. Bayılmış, C, Özdemir, M. Bluetooth Düşük Enerji Teknolojisine Sahip İşaretçi ve Akıllı Telefon Temelli Öğrenci Yoklama Sistemi. *Bilişim Teknolojileri Dergisi*, 9(3), 249, 2016.

[16]. Garrone, E, Cakır, A, Kaygısız, H. Kablosuz Öğrenci Yoklama Kontrol Sistemi. in 6th International Advanced Technologies Symposium (IATS'11), 33-35. 2011.

[17]. Patel, A., Joseph, A., Survase, S., Nair, R., Smart Student Attendance System Using QR Code. 2nd International Conference on Advances in Science & Technology (ICAST) by K J Somaiya Institute of Engineering & Information Technology, Mumbai, India, 2019.

[18]. Recommendations for NGMN KPIs and Requirements for 5G, NGMN Alliance, Tech. Rep. P1 WS3 BBTS, June 2016.

[19]. Claus, P, Pooyan, J, Olaf, Z. 2018. Architectural Principles for Cloud Software. *ACM Transactions on Internet Technology*. 18 (2): 23 pages.

[20]. Yasser, D. Al-Otaibi. 2021. A Shared Two-way Cybersecurity Model for Enhancing Cloud Service Sharing for Distributed User Applications. *ACM Transactions on Internet Technology*. 22 (2).

[21]. Wara, A. A, Dugga, S. 2014. Enhancing User Experience using Mobile QR-Code Application.

[22]. Albastroiu, I, Felea, M. 2015. Enhancing the shopping experience through QR codes: the perspective of the Romanian users. *The AMFITEATRU ECONOMIC journal* 17 : 553-553.

[23]. Huseynov E. Improving user experience with TOTP hardware tokens by implementing QR codes and HID keyboard emulation. 2020 IEEE 14th International Conference on Application of Information and Communication Technologies (AICT), pp. 1-5, 2020. doi: 10.1109/AICT50176.2020.9368574.

[24]. Ubam E., Hipiny I. Ujir H. User Interface/User Experience (UI/UX) Analysis & Design of Mobile Banking App for Senior Citizens: A Case Study in Sarawak, Malaysia. 2021 International Conference on Electrical Engineering and Informatics (ICEEI), 2021, pp. 1-6, doi: 10.1109/ICEEI52609.2021.9611136.

[25]. Xuan W. et. al. Research on the Optimal Threshold of QR Code Recognition Based on Maximum Likelihood Criterion. 2018 4th Annual International Conference on Network and Information Systems for Computers (ICNISC). pp. 107-111, (2018). doi: 10.1109/ICNISC.2018.00029.

[26]. Guo J. Lu Y. Xie Q. Guo Q. Performance Evaluation of Fingerprint Recognition Modules on Mobile Device Based on Rule of Three. 2019 International Conference on Computer, Information and Telecommunication Systems (CITS), pp. 1-4, (2019). doi: 10.1109/CITS.2019.8862069.

[27]. Antanius G., Trivedi R. Kwasnick R. Platform qualification methodology: Face recognition. 2015 IEEE International Reliability Physics Symposium. pp. 3C.3.1-3C.3.4, (2015). doi: 10.1109/IRPS.2015.7112709.

[28]. Xiang L. Jie S. A Context-Aware Middleware for User Experience Improvement in Mobile Payment. 2012 Fourth International Conference on Multimedia Information Networking and Security, pp. 370-373, (2012). doi: 10.1109/MINES.2012.15.

[29]. Ozdemir D., Uğur M.E. 2021. A model proposal on the determination of student attendance in distance education with face recognition technology. Turk. Online J. Dist. Educ. 22(1), 19–32.

[30]. Uğur M. E, Ozdemir D. Taşlıbeyaz E. 2017. Uzaktan Eğitimde Yüz Tanıma ve Göz İzleme Teknolojileri ile Derse Katılım Durumunun Belirlenmesi. International Computer & Instructional Technologies Symposium (ICITS), Sayfalar 962-96.

Celal Bayar University Journal of Science

On Parafree Leibniz Algebras

Nil Mansuroğlu[1]*

[1] Department of Mathematics, Kırşehir Ahi Evran University Bağbaşı Yerleşkesi, 40100-Merkez, Kırşehir, Türkiye
*nil.mansuroglu@ahievran.edu.tr
*Orcid: 0000-0002-6400-2115

Abstract

The parafree Leibniz algebras are a special class of Leibniz algebras which have many properties with a free Leibniz algebra. In this note, we introduce the structure of parafree Leibniz algebras. We survey the important results in parafree Leibniz algebras which are analogs of corresponding results in parafree Lie algebras. We first investigate some properties of subalgebras and quotient algebras of parafree Leibniz algebras. Then, we describe the direct sum of parafree Leibniz algebras. We show that the direct sum of two parafree Leibniz algebras is a Leibniz algebra. Furthermore, we prove that the direct sum of two parafree Leibniz algebras is again parafree.

Keywords: Parafree Leibniz algebra, subalgebras, quotient algebras, direct sum

1. Introduction

Let F be a field with characteristic zero. A Leibniz algebra L over a field F is a non-associative algebra with multiplication $[\,,\,]: L \times L \to L$ satisfying the Leibniz identity. Firstly, Leibniz algebras were introduced by Loday in the early 90's as a generalization of Lie algebras. The free Leibniz algebra was described by Loday [9,10] and Pirashvili [10]. H. Baur [4] defined a non-free parafree Lie algebra. Further, N. Ekici and Z. Velioğlu have worked on some important results of parafree Lie algebras [6,7] and Z. Velioğlu has investigated the subalgebras and quotient algebras of parafree Lie algebras [11]. In this paper following [2] we focus on parafree Leibniz algebras and state all important known results for such algebras. We turn our attention to the structure of subalgebras of parafree Leibniz algebras. Our aim is to investigate some properties of subalgebras and quotient algebras of parafree Leibniz algebras.

Moreover, we prove that the direct sum of two parafree Leibniz algebras is a Leibniz algebra and also this direct sum is again parafree.

2. Notations and Definitions

In this section we recall some basic definitions and some basic results which we need for our aims (see [1,3,5]). We use standard notation.

Throughout this note, F denotes a field with characteristic zero. The algebra L is called a (left) Leibniz algebra if it satisfies the Leibniz identity

$$[[x, y], z] = [x, [y, z]] - [y, [x, z]] \qquad \textbf{(2.1)}$$

for all $x, y, z \in L$. Throughout of this paper, we prefer to work with left Leibniz algebra. Define the series of ideals

$$L^1 \supseteq L^2 \supseteq \dots \supseteq L^k \supseteq \dots$$

where $L^1 = L$, $L^2 = [L, L], \dots, L^{k+1} = [L^k, L]$ for $k \geq 1$. This series is called the lower central sequence of L. The Leibniz algebra L is called a nilpotent Leibniz algebra if there exists a positive integer $k \geq 1$ such that $L^k = \{0\}$. We say that two Leibniz algebras L_1 and L_2 have the same lower central sequence if $L_1/L_1^n \cong L_2/L_2^n$.

Let X be a set and $A(X)$ be the free non-associative algebra on X over F, I be the two-sided ideal of $A(X)$ generated by the elements

$$[[x, y], z] - [x, [y, z]] + [y, [x, z]]$$

for all $x, y, z \in A(X)$. Then the algebra $L(X) = A(X)/I$ is a free Leibniz algebra.

Now we give some definitions on Leibniz algebras analogs to those of Lie algebras.

Definition 2.1. A Leibniz algebra is called Hopfian if it satisfies the following equivalent conditions
 (i) it is isomorphic to any of its proper quotients,
 (ii) every surjective endomorphism of it is an automorphism.

Definition 2.2. Any Leibniz algebra L is said to be residually nilpotent if $\bigcap_{n=1}^{\infty} L^n = \{0\}$.

Definition 2.3. Let $L(X)$ be the free Leibniz algebra freely generated by X. A Leibniz algebra P is said to be parafree over a set X if

 (i) P is residually nilpotent,

 (ii) for every $n \geq 1$, $P/P^n = L(X)/L(X)^n$, i.e. P has the same lower central sequence as $L(X)$.

The cardinality of X is called the rank of P.

3. Subalgebras and Quotient algebras of Parafree Leibniz algebras

In this section we give the proofs of our main results on subalgebras and quotient algebras of parafree Leibniz algebras. In [11], the main theorem states that a subalgebra of a parafree Lie algebra is parafree. Unfortunately, this case for parafree Leibniz algebras is not true. Since every subalgebra of free Leibniz algebra is not free, a subalgebra of a parafree Leibniz algebra need not to be parafree. By the following theorem, we show that every free subalgebra of a parafree Leibniz algebra is parafree.

Theorem 3.1. A free subalgebra of a parafree Leibniz algebra is parafree.

Proof. Let P be a parafree Leibniz algebra with the same lower central sequence as a free Leibniz algebra $L(X)$. The canonical mapping $\varphi: P \to L(X)$ induces the isomorphisms
$$\varphi_n: P/P^n \to L(X)/L(X)^n,$$
for $n \geq 2$. We take a free subalgebra of P, say H. We have $H \cap P^n = H^n$, then $\bigcap_{i=1}^{\infty} H^i \subset \bigcap_{i=1}^{\infty} P^i$. Since P is parafree, then P is residually nilpotent, that is,
$$\bigcap_{i=1}^{\infty} P^i = \{0\}.$$

Hence, we obtain $\bigcap_{i=1}^{\infty} H^i = \{0\}$. This means that H is residually nilpotent. Since H is free Leibniz subalgebra, H has the same lower central sequence as a free Leibniz algebra. Thus the free subalgebra H is parafree.

Now we have the following theorem for parafree Leibniz algebras with an easy proof using the corresponding parafree Lie algebra result which is given in [11].

Theorem 3.2. A quotient of a parafree Leibniz algebra is parafree.

Proof. Let P be a parafree Leibniz algebra and I be an ideal of P. Firstly we need to show that the quotient algebra P/I is residually nilpotent.

Suppose that $x \in \bigcap_{n=1}^{\infty} (P/I)^n$. Therefore, for all n,

$x \in (P/I)^n = (P^n + I)/I$. We have $x = y + I$, where $y \in P^n + I$. Clearly, $y \in \bigcap_{n=1}^{\infty} (P^n + I)$. By the residually nilpotence of P, P/I is residually nilpotent. It remains to prove that P / I has the same lower central sequence as a free Leibniz algebra.

We consider $(P / I)/(P / I)^n$. We have $(P^n + I)/I \cong P^n/I$. Therefore, we get

$$\left.(P/I)\middle/(P/I)^n\right. \cong (P/I)/((P^n + I)/I)$$

$$\cong (P/I)/(P^n/I) \cong P/P^n.$$

This demostrates that $(P / I) / (P/I)^n$ has the same lower central sequence as a free Leibniz algebra. Therefore,
$$(P/I)/(P/I)^n \cong L(X)/(L(X))^n.$$

Namely, P/I is parafree.

Lemma 3.3. Let P be a parafree Leibniz algebra with the finite rank and I be an ideal of P. If P and P/I have the same rank, then $I = \{0\}$.

Proof. We suppose that P and P/I have the same rank. For every positive integer n,
$$P/I \cong (P/I)/(P/I)^n \cong (P/I)/((P^n + I)/I)$$
$$\cong P/(P^n + I).$$

By the Theorem 3.2, P/I is residually nilpotent. Then by [8], P/I is Hopfian. Moreover,
$$P/(P^n + I) \subseteq P/P^n$$
and
$$P/P^n \cong P/(P^n + I).$$

Since P/I is Hopfian, a contradiction. Hence for all n, $I \subseteq P^n$, then $I = \{0\}$.

4. Direct sums of Leibniz algebras

Let $L_1, L_2, \ldots, L_n$ be Leibniz algebras. We define the direct sum $L = L_1 \oplus L_2 \oplus \ldots \oplus L_n$ as the vector space direct sum of the L_i with the Leibniz product $[\sum_{i=1}^{n} x_i, \sum_{i=1}^{n} y_i] = \sum_{i=1}^{n} [x_i, y_i]$, where $[x_i, y_i] \in L_i \cap L_j = \{0\}$ for $i \neq j, x_i \in L_i, x_j \in L_j$.

Lemma 4.1. Let L_1, L_2 be Leibniz algebras. The direct sum $L = L_1 \oplus L_2$ is Leibniz algebra with the product $[x_1 + x_2, y_1 + y_2] = [x_1, y_1] + [x_2, y_2]$ for $x_1, y_1 \in L_1$, $x_2, y_2 \in L_2$.

Proof. By (2.1), for $x = x_1 + x_2$, $y = y_1 + y_2$, $z = z_1 + z_2 \in L_1 \oplus L_2$ where $x_1, y_1, z_1 \in L_1$ and $x_2, y_2, z_2 \in L_2$, we have

$$[[x, y], z] = [[x_1 + x_2, y_1 + y_2], z_1 + z_2]$$
$$= [[x_1, y_1] + [x_2, y_2], z_1 + z_2]$$
$$= [[x_1, y_1], z_1 + z_2] + [[x_2, y_2], z_1 + z_2]$$
$$= [[x_1, y_1], z_1] + [[x_2, y_2], z_2]$$
$$[x, [y, z]] = [x_1 + x_2, [y_1 + y_2, z_1 + z_2]]$$
$$= [x_1 + x_2, [y_1 + z_1] + [y_2 + z_2]]$$
$$= [x_1, [y_1, z_1]] + [x_2, [y_2, z_2]]$$
$$[y, [x, z]] = [y_1 + y_2, [x_1 + x_2, z_1 + z_2]]$$
$$= [y_1 + y_2, [x_1, z_1] + [x_2, z_2]]$$
$$= [y_1, [x_1, z_1]] + [y_2, [x_2, z_2]].$$

It is clear to see that

$$[[x, y], z] = [x, [y, z]] - [y, [x, z]].$$

Therefore, $L = L_1 \oplus L_2$ is a Leibniz algebra.

Theorem 4.2. Let F_1 and F_2 be free Leibniz algebras. Then $F_1 \oplus F_2$ is again free.

Proof. By Lemma 4.1, $F_1 \oplus F_2$ is Leibniz algebra. Let X, Y be freely generating sets of F_1 and F_2 respectively. Then $X \cup Y$ freely generates $F_1 \oplus F_2$. Hence $F_1 \oplus F_2$ is a free Leibniz algebra freely generated by $X \cup Y$.

The following theorem for parafree Leibniz algebras is proved by using the corresponding parafree Lie algebra result which is given in [12].

Theorem 4.3. Let P_1 and P_2 be parafree Leibniz algebras and $P = P_1 \oplus P_2$. Then P is parafree.

Proof. First, we need to prove that P is residually nilpotent and P has the same lower central sequence as a free Leibniz algebra. Now, we need to show that

$$P^n = (P_1 \oplus P_2)^n = P_1^n \oplus P_2^n.$$

By induction on n, for $n = 1$ we have

$$P^1 = (P_1 \oplus P_2)^1 = P_1^1 \oplus P_2^1.$$

We suppose that for all $k < n$, $P^k = P_1^k \oplus P_2^k$. Then, we have

$$P^n = [P^{n-1}, P] = [P_1^{n-1} \oplus P_2^{n-1}, P_1 \oplus P_2].$$

Therefore,

$$P^n = [P_1^{n-1} + P_2^{n-1}, P_1 + P_2]$$
$$= [P_1^{n-1}, P_1] + [P_2^{n-1}, P_2]$$
$$= P_1^n + P_2^n$$

and

$$P_1^n \cap P_2^n = \{0\}.$$

Thus, we obtain $P^n = P_1^n \oplus P_2^n$. In order to prove residually nilpotency of P, we compute

$$\bigcap_{n=1}^{\infty} P^n = \bigcap_{n=1}^{\infty} (P_1^n \oplus P_2^n).$$

By using the definition of direct sum, we have

$$\bigcap_{n=1}^{\infty} (P_1^n \oplus P_2^n) = \bigcap_{n=1}^{\infty} P_1^n \oplus \bigcap_{n=1}^{\infty} P_2^n.$$

Since P_1 and P_2 are parafree, then we have

$$\bigcap_{n=1}^{\infty} P_1^n = \{0\} \text{ and } \bigcap_{n=1}^{\infty} P_2^n = \{0\}.$$

Therefore, $\bigcap_{n=1}^{\infty} P^n = \{0\}$, namely P is residually nilpotent. Now we show that P has the same lower central sequence as a free Leibniz algebra. Since P_1 and P_2 are parafree Leibniz algebras, then there exist free Leibniz algebra F_1 and F_2 such that

$$P_i / P_i^n \cong F_i / F_i^n,$$

$i = 1,2$; $n \geq 1$. Hence

$$P/P^n = (P_1 \oplus P_2)/(P_1 \oplus P_2)^n \cong P_1 / P_1^n \oplus P_2 / P_2^n$$
$$\cong F_1 / F_1^n \oplus F_2 / F_2^n$$
$$\cong (F_1 \oplus F_2) / (F_1 \oplus F_2)^n.$$

Since $F_1 \oplus F_2$ is free, P is parafree.

Author's Contributions

Nil Mansuroğlu: Drafted and wrote the manuscript, performed the experiment and result analysis.

Ethics

There are no ethical issues after the publication of this manuscript.

References

[1]. Bahturin, Y. Identity relations in Lie algebras, VNU Science Press, Utrecht, 1987.

[2]. Baur, H. 1980. A note on parafree Lie algebras, *Commun. in Alg.;* 8(10): 953-960.

[3]. Baur, H. 1978. Parafreie Lie algebren and homologie, *Diss. Eth Nr.;* 6126: 60 pp.

[4]. Bloh, A.M. 1965. A generalization of the concept of Lie algebra, *Dokl. Akad. Nauk SSSR;* 165: 471-473.

[5]. A.M. Bloh, A.M. 1971. A certain generalization of the concept of Lie algebra, Algebra and Number Theory, *Moskow. Gos. Ped. Inst. U`cen;* 375: 9-20.

[6]. Ekici, N, Velioğlu, Z. 2014. Unions of Parafree Lie algebras, *Algebra;* Article ID 385397.

[7]. Ekici, N, Velioğlu, Z. 2015. Direct Limit of Parafree Lie algebras, *Journal of Lie Theory;* 25(2): 477-484.

[8]. Evans, T. 1969. Finitely presented loops, lattices, etc. are Hopfian, *J. London Math. Soc.;* 44: 551-552.

[9]. Loday, J.L. 1993. Une version non commutative des algebres de Lie, *les algebres de Leibniz. Enseign Math.;* 39: 269-293.

[10]. Loday, J.L., Pirashvili, T. 1993. Universal enveloping algebras of Leibniz algebras and (co)homology, *Math. Ann.;* 269(1): 139-158.

[11]. Velioğlu, Z. 2013. Subalgebras and Quotient algebras of Parafree Lie algebras, *I. Journal Pure and Applied Maths.;* 83(3): 507-514.

[12]. Velioğlu, Z. 2013. Direct Sum and Free Factors of Parafree Lie Algebras, *I. Journal Pure and Applied Maths.;* 83(4): 601-606.

Celal Bayar University Journal of Science

Preparation A Cross-Linked Copolymer By Using Unsaturated Poly (2-Butene Maleate) Polyester and Methyl Methacrylate

Fehmi Saltan[1*] (iD)

[1] Department of Chemistry, Faculty of Science, Çankırı Karatekin University, Uluyazı, 18100, Çankırı, Türkiye
*fehmisaltan@hotmail.com
* Orcid: 0000-0002-9347-6416

Abstract

In this study, synthesis of unsaturated Poly(2-Butene Maleate) polyester by condensation polymerization and preparation of cross-linked graft copolymer with methyl methacrylate are presented. For this purpose, unsaturated polyesters were synthesized in four different time periods (12h, 24h, 36h, 48h) in the presence of hydroquinone using 1,4-Butanediol-2-ene and maleic anhydride. Then, the obtained unsaturated polyester was purified on the alumina column and used to obtain cross-linked copolymer with methyl methacrylate. Here in, methyl methacrylate acts as both co-monomer and cross-linking agent.

In the preparation of Poly(2-Butene Maleate), the optimization study of the molecular weight and yield ratios with the time parameter was carried out. In the results obtained, it was observed that the maximum molecular weight was reached after almost 36 hours (Mn=3400). It was observed that time did not have much effect on the yield. Structural characterizations of the obtained products were supported by FT-IR and NMR analyzes. In thermal analysis, it was observed that the thermal stability of Cross-linked graft copolymer is higher than unsaturated polyester but lower than pure Poly(methyl methacrylate). Elementals analyze was used to determine the quantity of C, H and O elements within synthesized polymers. According to obtained results, the percentage of H atom in the structure increased as expected by obtaining cross-linked copolymer using methyl methacrylate

Keywords: Cross-linked, Graft, Methyl methacrylate, Unsaturated polyester

1. Introduction

Unsaturated polyester resins are an important part of thermoset polymers and the third largest class of thermoset molding resins. They are commonly used due to their easy processability, low cost, availability in a variety of grades and good corrosion resistance [1-4]. They are generally produced by the condensation of a diol with anhydrides. The obtained condensation products form very durable structures and coatings when cross-linked with vinyl monomers such as methyl methacrylate, styrene [5-7]. The mechanical and chemical properties of the cross-linked resin depend on the types and amounts of anhydrides and diols used. Many commercial unsaturated polyester resins are derived from phthalic and maleic anhydride as the saturated and unsaturated component in the polymer and 1,2-propylene glycol as the diol [8,9]. Many other glycols and anhydrides or acids can be used to alter the character of unsaturated polyesters. E.g., terephthalic acid and isophthalic acid are chosen to obtain much

better chemical and thermal resistance, whereas long-chain aliphatic acids, such as succinic acid or adipic acid, enhance the flexibility but reduce the thermal and chemical resistance [10,11].

On the other hand, despite the many advantages of unsaturated polyesters, when the disadvantages are considered, it has been seen that product improvement has been made in different ways. One of these ways is the cross-linking technique, as in this study. Because in this way, the low modulus, that is, stiffness, disadvantage of polyester can be eliminated, aging resistance can be increased, and the deformation time can be extended [12-14].

There are some studies in literature on cross-linked structures based on unsaturated polyesters as well as blends of commercial unsaturated polyesters with ready polymers. It is generally focused on the morphology, miscibility, and thermal properties in these studies [6, 15].

Studies in the literature have focused on similar techniques. Ready-made polyesters are generally cross-linked by the curing method. New types of products and product preparation methodology have not been given much attention in this regard. In this study, a new cross-linked unsaturated polyester was produced. Unlike previous studies, this product was obtained without using an auxiliary cross-linking agent and curing process.

2. Materials and Methods
2.1. Materials

2-butene-1,4-diol (97%, cis-isomer, Merck), Maleic Anhydride (for synthesis, Sigma-Aldrich), Hydroquinone (Reagent plus, ≥99%, Merck), Methylmethacrylate (99%, stabilized, Sigma-Aldrich),

Benzoyl Peroxide (with %25 H_2O, for synthesis, Sigma-Aldrich), Chloroform (anhydrous, ≥99%, Merck)

2.2. Experimental
2.2.1. General Procedure

A stepwise polymerization method was used for the synthesis of polyester. At this stage, hydroquinone was used to protect the double bonds in the monomers.

An inert atmosphere was created by removing O_2 by applying vacuum to the reaction medium and passing argon gas. In the experiments carried out with maleic anhydride, to prevent the esterification reaction, which is an equilibrium reaction, from proceeding in favor of the reactants, the removal of the released water was provided by using the Dean-Stark adapter.
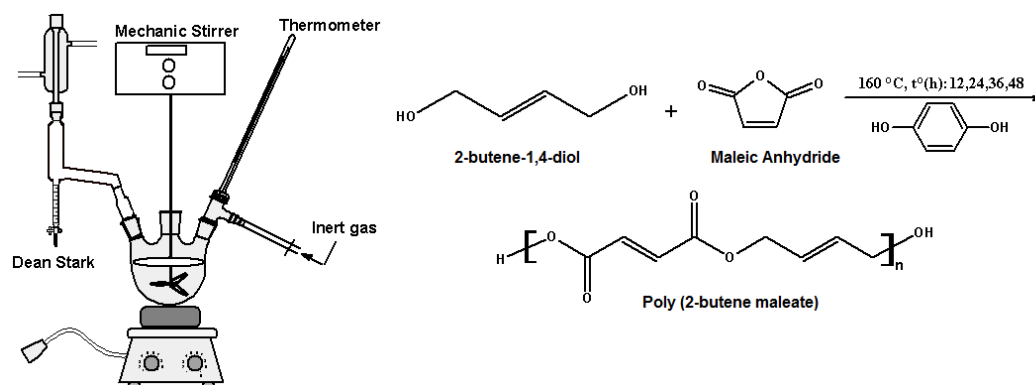
Figure 1. Synthesis of Poly (2-butene maleate) and reaction setup

2.2.2. Synthesis of Poly(2-Butene Maleate)

9.806 g maleic anhydride (0.1mol), 1.01 g hydroquinone (0.01 mol) and 9.30 ml 2-butene-1,4-diol (0.1 mol) were placed in a four-necked flask. Dean-Stark adapter and condenser were connected to one neck of the balloon and mechanical mixer was connected to the other neck. At the same time, argon gas was passed through the environment to ensure a continuous inert environment, while the temperature was monitored at 160 °C. The reaction was carried out under the conditions determined as four separate trials of 12, 24, 36 and 48 hours. The representation of the reaction setup is as in Figure 1.

2.2.3. Crosslinked Copolymer Synthesis

Hydroquinone was removed by passing the obtained Poly(2-Butene Maleate) through a column formed with unsaturated polyester alumina. One gram of the purified polyester was taken and cross-linked with equivalent moles of methyl methacrylate in the presence of chloroform. As the initiator, 3% of the total mole of benzoyl peroxide was used. Polymerization continued for 24 hours at a temperature of 75 °C. The synthesis of the cross-linked unsaturated copolymer is summarized in the Figure 2.
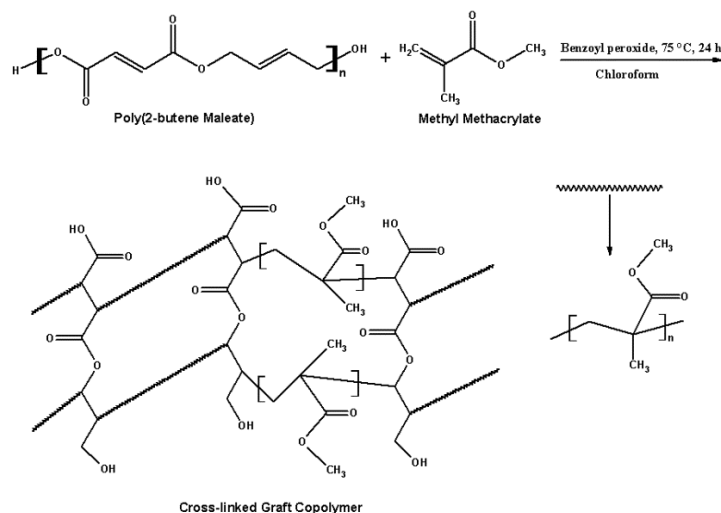
Figure 2. Synthesis of Cross-linked Copolymer

3. Results and Discussion

In this study, structural characterization was performed with FT-IR (Fourier Transform Infrared Spectroscopy, Perkin Elmer FT-IR Spectrum One-B spectrometer) and NMR (Nuclear Magnetic Resonance, ^{1}H-NMR spectra were recorded on Varian AS-400 spectrometers in CDCl$_3$ with Si(CH$_3$)$_4$ as internal standard). Molecular weight optimization of poly(2-butene Maleate) unsaturated polyester against time was performed. Molecular weight was determined by end group analysis. Thermal analysis of cross-linked graft copolymer obtained using poly (2-butene maleate) and methyl methacrylate was performed with TG (Thermogravimetry, performed on Perkin-Elmer Diamond TA/TGA with a heating rate of 10 ^{o}C/min under nitrogen flow). It was supported the work with elemental analyzes was successful. Elemental analysis was performed by Perkin Elmer 2400 CHNS Organic Elemental Analyzer 100V

Determination of Molecular Weight

To perform the time molecular weight optimization of the synthesized unsaturated polyester, the experiment was carried out in 4 different periods, 12, 24, 36 and 48 hours. The molecular weights obtained in these time periods were determined as 1200 (12h), 2200 (24h), 2800 (36h), 2805 (48h). Calculation of molecular weight was carried out by end group analysis.

Figure 3 shows the molecular weight plot of the synthesized Poly (2-butene maleate) polyester versus time. Experimental results of end group analysis are given in Table 1. The formulation used in Equation 1 is given.
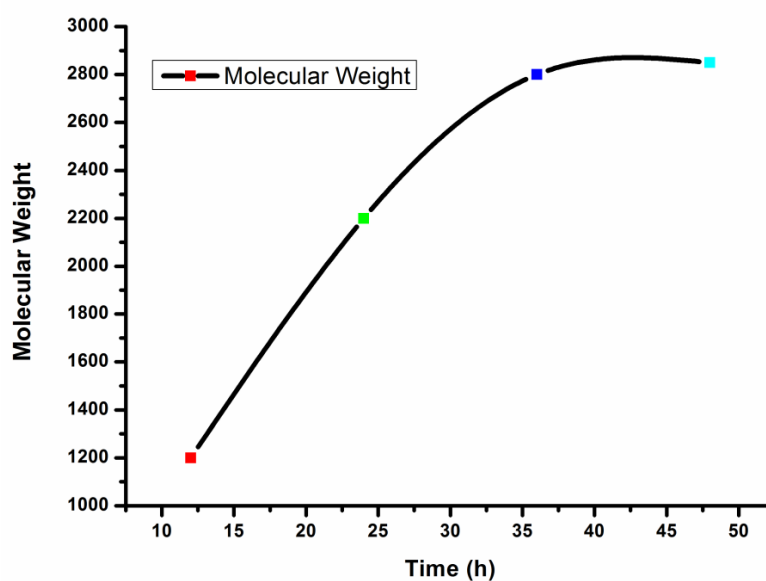
Figure 3. The molecular weight plot of the synthesized Poly (2-butene maleate) versus time

In the end-group analysis method, the number of chemical groups at the ends of the polymer chains is determined by an appropriate analysis method. In general, chains of cascading polymers have certain end groups suitable for analysis. For this reason, the method is mostly used to find the molar mass of cascading polymers such as polyamide, polyester, which have end groups such as $-H_2N$, -COOH. In the end-group analysis method, polymer samples were taken as 0.15 grams in all tests. According to the results obtained, the molecular weights of the polymers increased with enhancing time. According to the optimization, the maximum molecular weight was reached after 36 hours.

Moles of acid group in polymer = moles of spent base
Number of moles of acid group in the polymer = $0.025 \times 5.0 \times 10^{-3} = 125 \times 10^{-6}$ (experiment 1 sample calculation)

$$M_n = \frac{Amount\ of\ polymer\ sample\ used}{Number\ of\ moles\ of\ functional\ groups\ in\ the\ polymer} = \frac{0{,}15\ g}{125 \times 10^{-6} mol} = 1200\ g/mol \qquad (1)$$

Table 1. Experimental results of end group analysis

Experiment		End Group Analysis Results		Molecular Weight (g/mol)
No	Hours	Molarity of Titrant Used NaoH, (N)	Amount of Titrant Consumed (cm³)	
1	12	0,025	5	1200
2	24	0,025	2,72	2200
3	36	0,025	≈2,14	2800
4	48	0,025	2,14	2805

FT-IR

Figure 4 shows the FT-IR spectra of monomers and polymers. According to this figure, asymmetric –C-O-C- stress at 1230-1236 cm^{-1}, symmetrical –C-O-C- strain at 1028-1036 cm^{-1}, CH_2 release at 1327-1340 cm^{-1}, =C-H- stretch at 3084 cm^{-1}, at 1644 cm^{-1} the -C=C- stretch was determined. In the spectrum of the final product, the cross-linked graft copolymer, it was observed that the peak of the double bond disappeared, as expected, and the carbonyl peak was very prominent at 1750 cm^{-1}.
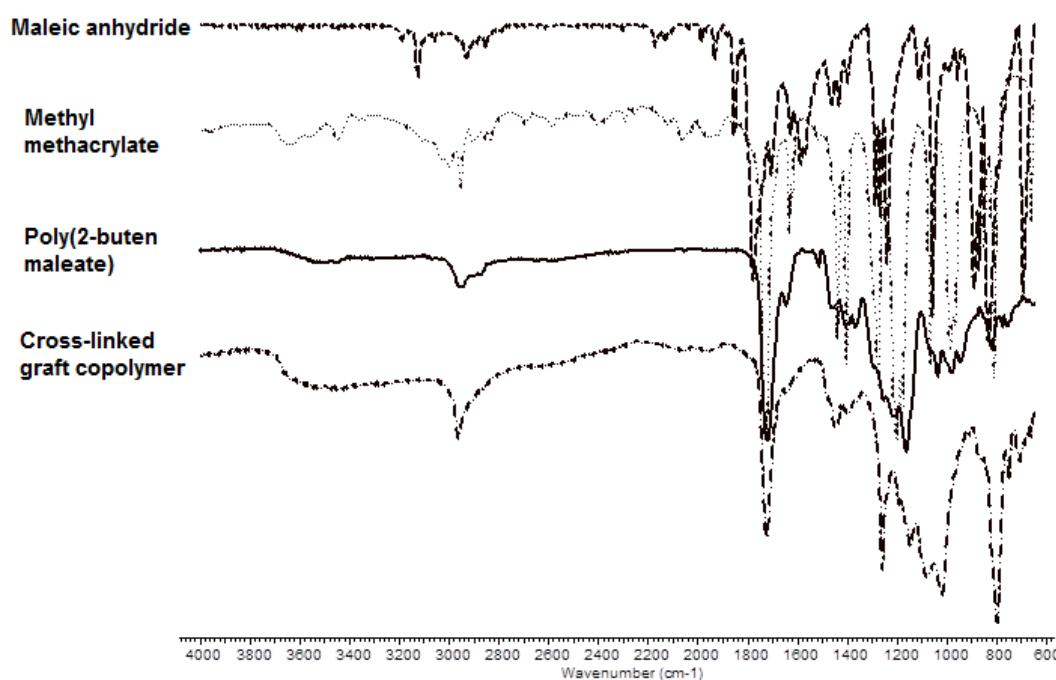
Figure 4. FT-IR spectra of monomers and synthesized polymers

^{1}H-NMR

The NMR spectrum of Poly(2-Butene Maleate) is shown in Figure 5. The positions of the protons are marked on the figure. The hydrogen atoms in the -CH_2=CH_2- structure between two carbonyl groups are approximately 6.8 ppm. The chemical shift value of the methylene group attached to oxygen, -O-CH_2-, is around 4.2 ppm. The chemical shift value of the -CH_2- group on the aliphatic chain was seen at 1.8 ppm. The result obtained supports the successful synthesis of poly(2-butene maleate).

TG

Thermal characterization of cross-linked graft copolymer was performed by thermogravimetry. Figure 6 shows the obtained thermogram. In this figure, the blue line represents pure PMMA, while the red line represents cross-linked graft copolymer. When we look at the thermal results of the products obtained under similar conditions to compare the results correctly, Poly(methyl methacrylate) (PMMA) showed one degradation step as seen in the literature [16,17]. It is seen that the decomposition, which started at about 320 ^{o}C, completely ended around 470 ^{o}C. PMMA decomposed sharply at 400 ^{o}C. This main degradation can be due to the cleavage of the backbone of the polymer. It is seen that the thermal stability of the obtained PMMA is higher than many similar ones in the literature. When the thermal degradation of the cross-linked copolymer is examined, it is clearly seen that there are significant differences compared to pure PMMA. According to figure 6 cross-linked copolymer has three main transition regions: the first one of these transitions is because of evaporation of CO_2 and water that occurs in the range of 80-180 °C. It has been observed that the second transition is between 230-430 ^{o}C. The cleavage of the backbone may be the cause of the degradation in this region. The third and final decomposition stage was determined to be between 450-580 ^{o}C. Although the thermal stability of the obtained cross-linked polyester is lower than PMMA, its thermal resistance is significantly better. In PMMA, decomposition completely ends at 470 ^{o}C, while in cross-linked polymer this value increased up to 600 °C.
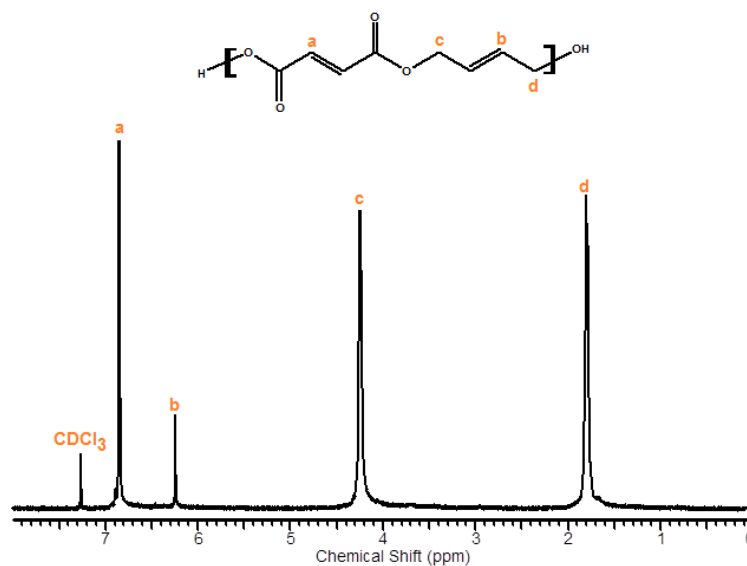
Figure 5. The ^{1}H-NMR spectrum of Poly(2-Butene Maleate)
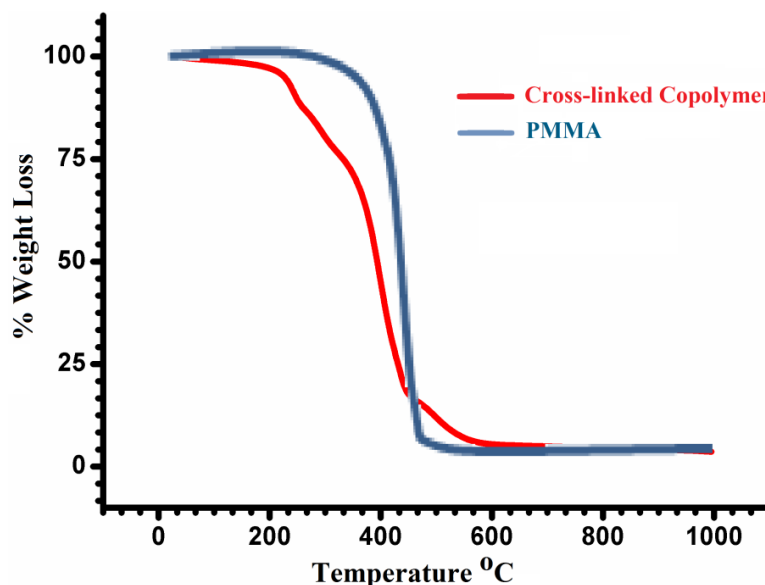
Figure 6. TG Curves of the PMMA and Cross-linked Copolymer

Elemental Analysis

Also, elemental analyzes of unsaturated polyester and cross-linked copolymer were carried out to determine the quantity of C, H and O elements within synthesized polymers. The data obtained are shown in Table 2. The highest molecular weight (2800 g/mol) Poly (2-butene maleate) was used in the analysis. An example of a cross-linked copolymer is the product obtained from this high molar mass polyester. The results of the C and H elements obtained from the analysis are in line with the theoretical expected results. The theoretically expected percentages (%) of C, H, and O in poly (2-butene maleate) are 57, 4, and 39, respectively. It was observed that the percentage of H atom in the structure increased as expected by obtaining cross-linked copolymer using methyl methacrylate.

Tablo 2. Elemental Analysis of the Cross-linked Copolymer and Poly (2-butene maleate)

Sample	Segment	Unit	Calculated			Found		
			C	H	O	C	H	O*
Poly (2-butene maleate)	$-(C_8O_4H_8)-$	%	57	4	39	56	5	39
Cross-linked Copolymer	$-(C_5H_8O_2)-/-(C_8O_4H_8)-/-(C_5H_8O_2)$	%				58	8	34

*Computed by difference

4. Conclusion

In this study, it was aimed to obtain a cross-linked copolymer by cross-linking methyl methacrylate with Poly (2-butene maleate) polyester obtained by condensation polymerization. Considering the thermal analysis of the cross-linked product, it was observed that although its thermal stability was not as high as Poly (methyl methacrylate), its thermal resistance was higher. In addition to being new in the literature, it is noteworthy that this product was obtained with very accessible, inexpensive materials and an easy method. Also, it was supported by FT-IR, NMR, and elemental analysis methods that the targeted materials were successfully obtained. It is thought that with further studies, the mechanical and thermal properties of the material will be improved, and it will allow the production of fire resistant materials.

Author's Contributions

Fehmi Saltan: Drafted and wrote the manuscript, performed the experiment and result analysis.

Ethics

There are no ethical issues after the publication of this manuscript.

References

[1]. Wang, XL, An, WL, Tian, F, Yang, Y, Zhao, X, Xu, PP, Wang, YZ. 2020. High-Efficiency Hydrolysis of Thermosetting Polyester Resins into Porous Functional Materials Using Low-Boiling Aqueous Solvents. *ACS Sustainable Chemistry & Engineering*; 8(42): 16010–16019.

[2]. Ikladious, N, Shukry, N, El-Kalyoubi, S, Asaad, J, Mansour, S, Tawfik, S, Abou-Zeid, R. 2017. Eco-friendly composites based on peanut shell powder / unsaturated polyester resin. *Proceedings of the Institution of Mechanical Engineers, Part L: Journal of Materials: Design and Applications;* 233(5): 955-964.

[3]. Zhang, H, Zhang, G, Han, F, Zhang, Z, Lv, W. 2018. A lab study to develop a bridge deck pavement using bisphenol A unsaturated polyester resin modified asphalt mixture. *Construction and Building Materials;* 159: 83–98.

[4]. Rajaee, P, Ashenai Ghasemi, F, Fasihi, M, Saberian, M. 2019. Effect of styrene-butadiene rubber and fumed silica nano-filler on the microstructure and mechanical properties of glass fiber reinforced unsaturated polyester resin. *Composites Part B: Engineering;* 173: 106803.

[5]. Dave, PN, Khosla, E. Fundamentals, Design, Fabrication, and Applications. Blends, Interpenetrating Polymer Networks, and Gels of Unsaturated Polyester Resin Polymers With Other Polymers, Unsaturated Polyester Resins, Chapter 6, 2019, pp 153–172.

[6]. Abral, H, Fajrul, R, Mahardika, M, Handayani, D, Sugiarti, E, Muslimin, AN, Rosanti, SD. 2019. Improving impact, tensile and thermal properties of thermoset unsaturated polyester via mixing with thermoset vinyl ester and methyl methacrylate. *Polymer Testing*; 81: 106193.

[7]. Sassmann, PB, Weichold, O. 2021. Synergistic effects in cross-linked blends of ion-conducting PEO-/PPO-based unsaturated polyesters. Ionics; 27(9): 3857–3867.

[8]. Sassmann, PB, Weichold, O. 2019. Preparation and characterisation of ion-conductive unsaturated polyester resins for the on-site production of resistivity sensors. *Ionics*; 25: 3971-3978.

[9]. Kakati, N, Assanvo, EF, Kalita, D. 2019. Synthesis and Performance Evaluation of Unsaturated Polyester Blends of Resins and Its Application on Non-woven/Fabric Jute Fibers Reinforced Composites. *Journal of Polymes and Environment*; 27: 2540–2548.

[10]. Bhagia, S, Bornani, K, Ozcan, S, Ragauskas, AJ. 2021. Terephthalic Acid Copolyesters Containing Tetramethylcyclobutanediol for High-Performance Plastics. *ChemistryOpen*; 10(8): 830–841.

[11]. Jeemol, PA, Mathew, S, Nair, CPR. 2021. Itaconimide telechelics of polyethers, synthesis, and their impact on mechanical properties of unsaturated polyester resins. *Polymers for Advanced Technologies*; 32(4): 1727–1741.

[12]. Wang, D, Chen, S, Zhao, J, Zhang, Z. 2020. Synthesis and characterization of self-healing cross-linked non-isocyanate polyurethanes based on Diels-Alder reaction with unsaturated polyester. *Materials Today Communications*; 23: 101138.

[13]. Chen, T, Liu, W. 2019. Highly Unsaturated Microcrystalline Cellulose and its Crosslinked Soybean Oil-based Thermoset Composites. *ACS Sustainable Chemistry & Engineering;* 7(1): 1796-1805.

[14]. Dai, J, Ma, S, Teng, N, Dai, X, Shen, X, Wang, S, Liu, X, Zhu, J. 2017. 2,5-Furandicarboxylic Acid- and Itaconic Acid-Derived Fully Biobased Unsaturated Polyesters and Their Cross-Linked Networks. *Industrial & Engineering Chemistry Research*; 56(10): 2650–2657.

[15]. Ahmadi, Sh. 2020. Phenol Novalac Epoxy-modified unsaturated polyester hybrid networks by Silica Nanoparticles/ and Cross linking with Silane Compounds. *Advances in Applied Nano-Bio Technologies*; 1(2): 28-32.

[16]. Hato, MJ, Ray, SS, Luyt, AS. 2010. The Thermal and Rheological Properties of POSS-Containing Poly(methyl methacrylate) Nanocomposites. *Advanced Science Letter*; 3: 1-7.

[17]. Gornicka, B, Sieradzka, K. 2009. Barrier properties of impregnating varnishes with nanosilica. Journal of Physics: Conference Series; 146: 012016.

Celal Bayar University Journal of Science

Sexual Size Dimorphism and Pattern Polymorphism of the *Bufotes sitibundus* (Syn. *Bufotes variabilis*) Pallas, 1771 in Azerbaijan

Gulbaniz Gasimova[1,2*] iD

[1]Institute Zoology of Azerbaijan National Academy of Sciences, AZ1073, passage 1128, block 504, Baku, Azerbaijan
[2]Khazar University, Life Sciences department, AZ1096, 41 Mehseti Street, Baku, Azerbaijan
* gqasimova@mail.ru
* Orcid No: 0000-0003-4916-0112

Abstract

The paper contains data on sexual size dimorphism of *Bufotes sitibundus* Pallas, 1771 with samples from the "Greater Caucasus", "Lankaran" and "Absheron" territories of Azerbaijan. The 139 adult specimens (62♂ and 77♀) from 3 populations were collected. They were released after morphometric measurements and pattern morphs analysis. Reliability of differences was estimated using Independent Sample t-test. Statistical analysis of morphological features showed that there are differences in different features between males and females in different populations. In each of the populations studied, the femur (FmL) and tibia (TbL) were longer in males than in females. Investigation of the pattern polymorphism in 126 specimens has shown that dorsal pattern with spots separated by short distance between them is dominant in 2 studied populations ("Absheron" and "Lankaran"). There were not found any differences between males and females according to pattern characteristics.

Keywords: Amphibia, Azerbaijan, *Bufotes sitibundus*, pattern polymorphism, sexual size, dimorphism.

1. Introduction

The vital activity of animal organisms mainly reflects the characteristics of their growth and development, life expectancy, the sexual maturity, reproduction and the degree of endurance. These characteristics are to some extent hereditary and form the basis of natural selection. However, abiotic factors such as temperature, quantity and quality of food, and humidity affect the life of each individual to varying degrees, which causes variability among populations. In addition to these factors, the duration of the period of activity can also affect body size. For example, it has been found that the growth rate in individuals of the same age with a long annual period of activity is higher than in individuals with a low period of activity. Therefore, changing environmental factors can affect body size, which is a genetic feature. Ectotherms, such as amphibians and reptiles are more sensitive to such factors. Changes that an organism undergoes under the influence of environmental factors are studied at the level of individuals, populations and species [1,2].

The taxonomy of the genus *Bufo* has changed several times in recent years. First, Frost et al. (2006) merged the former "*Bufo*" *viridis* group with a new genus, described as *Pseudepidalea*, and proposed to divide *Bufo* into several genera [3]. Then Dubois and Boer (2010) showed that *Pseudepidalea* is a junior synonym for *Bufotes* (Rafinesque, 1815) [4]. They also recommended 3 different subgenus of the same genus *Bufo* (*Bufo*, *Bufotes*, *Epidalea*); therefore, *Pseudepidalea variabilis* was changed to *Bufo* (*Bufotes*) *variabilis* (Pallas, 1769) [5].

A molecular study showed that green toads of Asia Minor, the Middle East, and northern Eurasia form a separate clade [6]. Since the range of this clade includes the type locality, they referred to these populations as *B. variabilis* (Pallas, 1769) [7]. Recently, Dufresnes et al. (2019) stated that the Middle Eastern green toads might instead be considered *Bufotes sitibundus* (Pallas, 1771), which is the oldest name for this species [8].

Therefore, we use *B. sitibundus* as the scientific name in this study. *B. sitibundus* spreads from Greece eastwards through Türkiye to Syria, Jordan, and Lebanon.

It is also reported from Iraq, Iran and is distributed through the Caucasus and Russia to Kazakhstan [9].
In Azerbaijan territory *B. sitibundus* was first registered by Menetrie near the city of Baku in 1830 [10]. In our republic the species is distributed in all regions having favourable biotops including territories at the altitudes up to 2100 m a.s.l., Guba dstrict, Khinalig village. The aim of this study was a comparative study of morphometric measurements, sexual size dimorphism and pattern polymorphism of specimens taken from 3 populations of the widely distributed *B. sitibundus.*

2. Materials and Methods

Material collection covered the years of 2006-2016 in seasons when the amphibians are active. Totally 139 specimen of *B. sitibundus* were analyzed. From them 82 specimen (40♂ and 42♀) were from the "Greater Caucasus" (northern Azerbaijan) population; 31 specimens (7♂ and 24♀) from the "Absheron" (Absheron Peninsula, eastern Azerbaijan) population; 26 specimens (15♂ and 11♀) from the "Lankaran" (south-eastern Azerbaijan) population (Table 1). The coordinates of the areas where the amphibians were found were recorded using the Garmin eTrex GPS device. ArcGIS 10.3 the electronic mapping software have been used for preparing the map based on the collected materials (Figure1).

Table 1. Coordinates, sample sizes and altitude for each population.

Populations	N	Locality	Coordinates		Altitude (m)	Capture date
			N	E		
"Greater Caucasus"	82	Qakh	41.375556	46.801111	249	20.04.2011
		Qakh/Ilisu	41.460556	47.048333	1372	15.05.2013
		Oghuz/Deymedere	40.943056	47.559722	392	03.05.2012
		Zagatala SNR	41.750278	46.500556	893	04.06.2006
		Zagatala/Qebizdere	41.703889	46.593333	543	07.06.2006
		İsmayilli/Buynuz	40.917778	48.060833	757	11.08.2006
		Balakan/Katex	41.687222	46.527222	1089	21.07.2010
		Balakan/Mazymchay	41.794444	46.323611	438	05.05.2012
		Quba Khinalig	41.181667	48.118889	2063	07.05.2016
		Quba Khinalig	41.176944	48.127222	2131	07.05.2016
"Absheron"	31	Gobustan Boyukdash	40.112222	49.375833	171	18.04.2010
		Gobustan Gizil Gaya	40.113889	49.377222	171	11.05.2011
		Baku/Nardaran	40.573611	49.988056	11	05.04.2012
		Baku/8th kilometer	40.41	49.938056	46	25.06.2014
		Baku/Saray	40.532222	49.710278	35	17.05.2007
		Baku/Incirlik	40.527222	49.846111	65	12.04.2007
		Baku/Zykh	40.345278	49.977778	-21	19.05.2008
		Baku/Ahmedly	40.384167	49.959722	88	24.03.2009
"Lankaran"	26	Lerik, Cangamiran	38.7575	48.4375	1126	18.04.2010
		Lankaran, Ashagy Nuvadi	38.710833	48.8575	-15	12.04.2006
		Astara, Mashkhan	38.5475	48.815833	69	23.05.2008
		Astara, Chayoba	38.633056	48.806111	-4	14.04.2006

The specimens were collected using a handmade butterfly net and by hand in streams, brooks and cultivation waterways. Snout-urostyle (SUL), femur length (FmL), tibia length (TbL), first toe length (T1L), inner metatarsal tubercle length (IMTL) of collected specimens were measured and the ratios SUL/TbL, FmL/TbL, TbL/IMTL, T1L/IMTL were computed. The morphometric measurements were taken with the calipers in each adult specimen to the nearest 0.1 mm in the standardized manner. After morphometric measuring specimens were released to nature.Data obtained were processed in the STATISTICA StatSoft 10 program. To test significance of sexually dimorphic characters, Independent Sample t-test at the significance

level of 0.01 were employed. Color photographs were made and the pattern characteristics of the live specimens only were taken.

The pattern polymorphism in populations of amphibian species was identified based on variations in the pattern of the dorsal and ventral sides of the body [11, 12]. For the *B. sitibundus* in Azerbaijan 7 pattern morphs were established: a-with small spots with shorter distance between them, b-with large spots with shorter distance between them, c-with small spots with greater distance between them, d-with large spots with greater distance between them (Figure 2), e-dense ventral spots, f-sparse ventral spots, g-without ventral patterns.
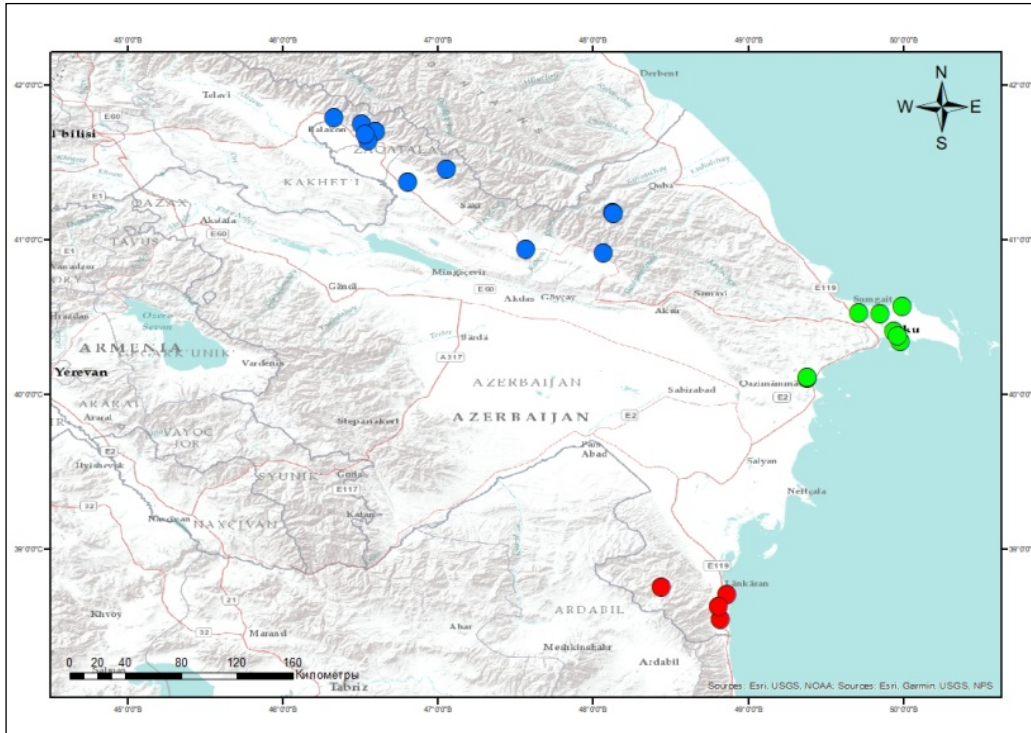
Figure 1. Map showing the study area in Azerbaijan (green circle - "Absheron", blue circle - "Greater Caucasus" and red circle - "Lankaran").
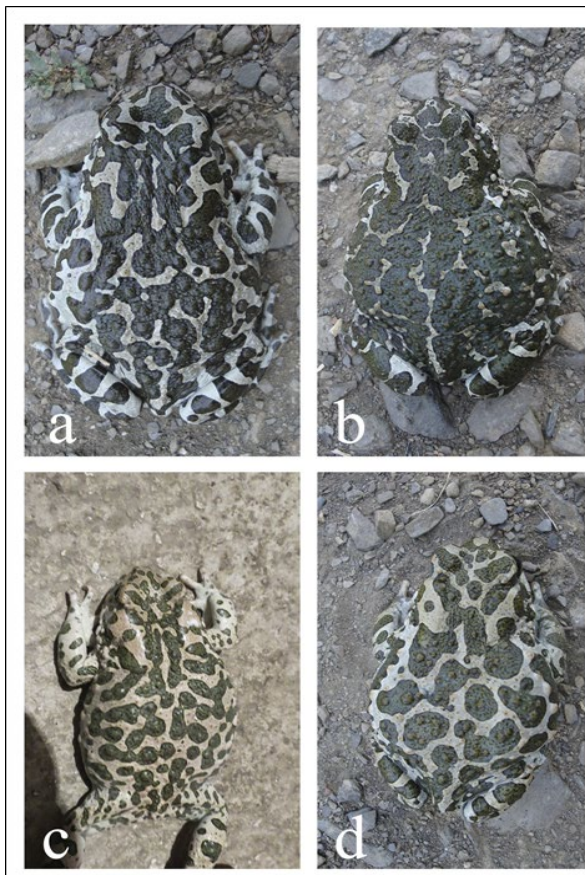
Figure 2. Four types of dorsal pattern as observed in the specimens of *B. sitibundus* Pallas, 1771 from the Azerbaijan: a-with small spots with shorter distance between them, b-with large spots with shorter distance between them, c-with small spots with greater distance between them, d-with large spots with greater distance between them.

2. Results and Discussion

Anuran amphibians grow throughout life [13]. Therefore, it is recommended that individuals compared in size be from the same age group. Taking this condition into account, the study compared only adults of the species *B. sitibundus* taken from 3 populations of Azerbaijan. Statistical analysis of the size and proportions of the body of individuals from the populations of the Greater Caucasus, Absheron, and Lankaran is shown in Table 2.

From the morphometric analysis of samples taken from all three populations, it can be seen that specimens of the Greater Caucasus population are larger in size (T1L), and specimens of the Absheron population in some sizes and ratios (FmL, IMTL, TbL / IMTL) than individuals of the Lankaran population. In terms of body length (SUL), specimens from the Greater Caucasus population differ slightly from those from the other two populations.

Table 2. Comparison of morphometric characteristics of *B. sitibundus* from "Absheron", "Lankaran" and "Greater Caucasus" populations.

Character	Greater Caucasus (n=82♀♂)		Lankaran (n=26♀♂)		Absheron (n=31♀♂)	
	M±SD	Range	M±SD	Range	M±SD	Range
SUL	68.43±13.01	33.50-91.10	70.74±49.90	43.40-80.80	70.15±9.43	46.40-87.50
FmL	27.58±5.76	1.90-39.50	28.70±14.15	17.80-33.90	27.54±3.43	18.00-35.20
TbL	25.47±5.12	11.10-38.10	26.81±11.34	16.90-31.60	24.56±3.29	16.60-29.80
T1L	5.95±1.64	3.40-11.20	5.57±5.90	3.40-11.40	6.18±1.89	3.50-11.70
IMTL	3.85±0.78	2.10-6.50	4.85±1.67	2.20-7.40	3.88±0.77	2.60-5.20
SUL/TbL	2.71±0.23	1.88-3.37	2.66±0.05	2.22-2.98	2.87±0.35	2.39-4.43
FmL/TbL	1.09±0.14	0.09-1.45	1.07±0.00	0.87-1.17	1.13±0.13	1.01-1.73
TbL/IMTL	6.66±1.27	4.00-12.07	5.78±1.10	3.81-7.68	6.51±1.18	3.61-8.62
T1L/IMTL	1.59±0.49	0.97-3.37	1.23±0.35	0.57-2.40	1.59±0.35	0.81-2.54

The sizes of males and females were compared separately for each population (Table 3). Results of Independent Sample t-test (2-tailed) presented in Table 3 detect significant sexual size dimorphism (p≤0.01) in some morphometric parameters (FmL and TbL) of the females and males of *B. sitibundus* taken from the "Absheron", "Lankaran" and "Greater Caucasus" populations. There are also differences in some ratios (SUL/TbL and TbL/IMTL) of specimens taken from the "Greater Caucasus" population and "Lankaran". However the results of inner metatarsal tubercle length (IMTL) measures were different in "Absheron" and "Lankaran" populations. The snout-urostyle length (SUL) measures of specimens taken from "Greater Caucasus" and "Absheron" population differed from "Lankaran" populations. Comparison of morphometric characters in each population has shown that males are larger than females.

Table 3. Comparison of morphometric characters (mm) in males and females of *B. sitibundus*. n: number; M:arithmetic mean; SE: standard error of mean; significant at level*p≤0.05, **p≤0.01, ***p≤0.001. Morphometric abbreviations: SUL (snout–urostylelength), FmL (femur length), TbL (tibia length), T1L (first toe length), IMTL (inner metatarsal tubercle length), SUL/TbL; FmL/TbL; TbL/IMTL; T1L/IMTL.

	SEX		SUL	FmL	TbL	T1L	IMTL	SUL/TbL	FmL/TbL	TbL/IMTL	T1L/IMTL
"Greater Caucasus"	♂	M	71.63	29.61	27.51	5.70	3.88	2.65	1.09	7.14	1,49
	(n=40)	SE	0.74	0.39	0.52	0.26	0.10	0.03	0.01	0.19	0,08
	♀	M	65.38	25.65	23.54	6.20	3.82	2.76	1.09	6.20	1,68
	(n=42)	SE	2.65	1.11	0.90	0.25	0.14	0.04	0.03	0.18	0,07
	p		0,021 *	0.002 **	0.001 ***	0.139	0.612	0.034 *	0.923	0.002 **	0.052
"Absheron"	♂	M	76.13	30.21	27.61	7.30	4.57	2.75	1.09	6.06	1,59
	(n=7)	SE	3.34	1.05	0.62	0.87	0.13	0.08	0.02	0.13	0,17
	♀	M	68.41	26.76	23.67	5.85	3.68	2.91	1.14	6.64	1,60
	(n=24)	SE	1.85	0.66	0.64	0.34	0.15	0.08	0.03	0.27	0,07
	p		0,040 *	0.046 *	0.007 **	0.183	0.045 *	0.289	0.377	0.947	0.865
"Lankaran"	♂ (n=15)	M	71.91	29.81	27.97	6.38	5.18	2.58	1.07	5.57	1,32
		SE	1.12	0.67	0.60	0.75	0.28	0.06	0.02	0.25	0,18
	♀ (n=11)	M	69.14	27.19	25.24	4.45	4.40	2.75	1.07	6.07	1,12
		SE	2.92	1.40	1.20	0.21	0.45	0.07	0.01	0.34	0,12
	p		0,385	0.046 *	0.034 *	0.159	0.021 *	0.002 **	0.738	0.030 *	0.831

The dorsal part of *B. sitibundus* is light olive-gray, surrounded by a narrow black border with large and small dark green spots. Specimens of this species have different patterns, and it is difficult to find two identical individuals in the number, location and color of spots.

The study of 126 specimens of *B. sitibundus* has revealed 4 dorsal (a-with small spots with shorter distance between them, b-with large spots with shorter distance between them, c-with small spots with greater distance between them, d-with large spots with greater distance between them), and 3 ventral (with dense spots, with sparse spots, without patterns) pattern forms.

Pattern consisted of small spots with shorter distance between them accounted for 28.57%in the "Greater Caucasus" population, 30% in the "Absheron" population, and 84%in the "Lankaran" population; pattern consisted of large spots with shorter distance between them accounted for 22.22% in the "Greater Caucasus" population, 50% in the "Absheron" and 4% in the "Lankaran" population; pattern consisted of small spots with greater distance between them accounted for 12.69 % in the "Greater Caucasus" population, 13.33% in "Absheron" population, 0% in the "Lankaran" population; pattern consisted of large spots with greater distance between them 36.50% in the "Greater Caucasus" population, 6.67% in the "Absheron" population and 12% in "Lankaran" population. Pattern with small spots with shorter distance between them

predominated in two populations ("Absheron" and "Lankaran"). The dense ventral spots of individual from "Greater Caucasus" population are observed. We have not recorded specimens without ventral patterns in "Lankaran" population (Table 4). According to the theory of evolution, sexual selection is a special form of natural selection that has led to sexual dimorphism.

Sexual dimorphism consists of phenotypic differences between males and females of the same species. Kuo et al. [14] point to morphological differences between males and females in shape and size, while Selander [15] points to differences in behavior [14, 15]. Sexual dimorphism in terms of body size is a common feature in the animal kingdom (*Regnum Animale*), differing in size and direction in different classes [16,17].

The reasons for sexual size dimorphism in all animals are explained by 3 accepted hypotheses: 1) Large body size in males has an influence on superiority in the process of sexual selection. During the breeding season, males with larger body sizes are more likely to mate, competing with other males [18]; 2) The large body size of females has a positive effect on their reproductive performance during reproduction [19]; 3) The large body size of individuals of both sexes has an effect on intraspecific competition from an ecological point of view [20, 21].

Table 4. Occurrence of pattern morphs in populations of *B. sitibundus* in the studied biotopes in Azerbaijan. (*- 6 specimens without patterns in Greater Caucasus populations).

Morph		Populations					
		"Greater Caucasus"		"Absheron"		"Lankaran"	
		n=69* (♂♀)	%	n=30 (♂♀)	%	n=25 (♂♀)	%
Dorsal	A	18	28.57	9	30	21	84
	B	14	22.22	15	50	1	4
	C	8	12.69	4	13.33	-	-
	D	23	36.50	2	6.67	3	12
Ventral	e	37	53.62	13	43.33	17	68
	F	25	36.23	10	33.33	8	32
	G	7	10.14	7	23.33	-	-

In 90% of anuran amphibians, females are larger than males [22]. However it is known that in some species of frogs, males are larger than females. The morphometric analysis of the *B. sitibundus* species was carried out to resolve the issue of the size of the sexes of this species in the territory of Azerbaijan. Statistical analysis of morphological characters by sex showed that males and females of different populations differ in different characters. However, as can be seen from Table 3, in each of the three studied populations, the length of the femur and tibia in males was greater than that of

females. It is known that in the amplexus position during reproduction, the male squeezes the female's abdomen with his hind limbs and helps her to lay eggs. In this regard, we believe that the length of the femur and tibia in males plays an important role during mating.

The sexual size dimorphism that we observe in *B. sitibundus*, that is, the fact that males are larger than females in some morphological characteristics, can be caused by several reasons. One of these reasons can be

G. Gasimova

explained by the first of the above considerations. However, more research is needed to determine other causes of sexual size dimorphism.

It is believed that the degree of polymorphism of a species is directly proportional to the diversity of its habitat. Thus, the degree of polymorphism is high in species living in different landscapes and having a wide range.

According to the results of the analysis of to the shape of the waist and abdomen of the specimens of the genus *B. sitibundus* from 3 populations, it can be said that individuals of the "Greater Caucasus" population show a higher degree of polymorphism than individuals of other populations. The reason for this is the capture of individuals of the "Greater Caucasus" population from different landscapes. Such differences in the degree of polymorphism of individuals within a population can also be associated with intraspecific variability and genetic factors. Therefore, more research is needed in this direction.

Acknowledgement

The author is grateful to F.R.Ganiyev for his help in field research.

Author's Contributions

Gulbaniz Gasimova: Literature research, data collection, field survey and measurement, article writing.

Ethics

There are no ethical issues after the publication of this manuscript.

References

[1]. Altunışık, A, Özdemir, 2015. Life history traits in *Bufotes variabilis* (Pallas, 1769) from 2 different altitudes in Turkey. *Turkish Journal of Zoology*, 39(1), 153-159.

[2]. Altunışık, A, Gül, S, Özdemir, N, 2021. Impact of various ecological parameters on the life-history characteristics of *Bufotes viridis sitibundus* from Turkey. *The Anatomical Record*, 304:1745 - 1758.

[3]. Frost, D, Grant, T, Faivovich, J, Bain, R, Haas, A, Haddad, CFB, De Sa, RO, Channing, A, Wilkinson, M, Donnellan, SC, Raxworthy, C, Campbell, J, Blotto, B, Moler, P, Drewes, R, Nussbaum, R, Lynch, J, Green D, Wheeler W, 2006. The amphibian tree of life, *Bull. Am. Mus. Nat. Hist*; 297, 1- 370.

[4]. Dubois, A, Bour, R, 2010. The nomenclatural status of the nomina of amphibians and reptiles created by Garsault (1764), with a parsimonious solution to an old nomenclatural problem regarding the genus Bufo (Amphibia, Anura), comments on the taxonomy of this genus, and comments on some nomina created by Laurenti (1768), *Zootaxa;* 2447, 1-52.

[5]. Ozdemir, N, Gul, S, Poyarkov, NA, Kutrup, B, Tosunoglu, M, Doglio, S, 2014. Molecular systematics and phylogeography of *Bufotes variabilis* (syn.*Pseudepidalea variabilis*) (Pallas, 1769) in Turkey, *Turkish Journal of Zoology*; 38: 412-420.

[6]. Stock, M, Moritz, C, Hickerson, M, Frynta, D, Dujsebayeva, T, Eremchenko, V, Macey, JR, Papenfuss, TJ, Wake, DB, 2006. Evolution of mitochondrial relationships and biogeography of Palearctic green toads (Bufo viridis subgroup) with insights in their genomic plasticity, *Molecular Phylogentics and Evolution;* 41: 663- 689.

[7]. Stök, M, Günther, R, Bohme, W, 2001a. Progress towards a taxonomic revision of the Asian Bufo viridis group: Current status of nominal taxa and unsolved problems (Amphibia Anura: Bufonidae), *Zool Abh Staatl Mus Tierkunde Dresden*; vol. 51, pp. 253-319.

[8]. Dufresnes, C, Mazepa, GO, Jablonski, D, Oliveira, RC, Wenseleers, T, Shabanov, DA, Markus, A, Ernsth, R, Kochi, C, Ramírez-Chavesj, HE, Mulder, KP, Simonovo, E, Tiutenko, A, Kryvokhyzhar, D, Wennekes, PL, Zinenko, OI, Korshunov, OV, Al-Johany, AM, Peregontsev, EA, Masroor, R, Betto-Colliard, C, Denoël, M, Borkin, LJ, Skorinov, DV, Pasynkova, RA, Mazanaeva, LF, Rosanov, JM, Dubey, S, Litvinchuk, S, 2019. Fifteen shades of green: The evolution of Bufotes toads revisited, *Mol. Phyl. Evol.*; vol.141, pp. 1-5.

[9]. Fakharzadeh, F, Mahboubeh, SH, 2021. Overview of taxonomy and prediction potential distribution of *Bufotes sitibundus* (Anura: Bufonidae) using environmental factors, *Journal of Wildlife and Biodiversity*; 5 (1).

[10]. Alekperov, AM, Amphibians and Reptiles of Azerbaijan [in Russian]. Science Press, Baku, Azerbaijan, 1978; pp 264.

[11]. Zhelev, ZH, Arnaudov, AT, Boyadzhiev, P, 2014. Colour polymorphism, sex ratio and age structure in the populations of *Pelophylax ridibundus* and *Pseudepidalea viridis* (Amphibia: Anura) from anthropogenically polluted biotopes in southern Bulgaria and their usage as bioindicators, *Trakia Journal of Sciences*; 1: 1-12.

[12]. Peskova, TY, 2003. Intrapopulation polymorphism of green toad color. In: Bakiyev, A.G. (ed.), *Current Problems of Herpetology and Toxicology*. IEVB publishing: Tolyatti [in Russian], pp. 90-91.

[13]. Brem, A, Animal life, [in Russian]. Moscow, OLMA-press, Red proletarian, 2004; pp. 1192.

[14]. Kuo, C-Y, Lin, Y-T, Lin, Y-S, 2009. Sexual size and shape dimorphism in an agamid lizard, Japalura swinhonis (Squamata: Lacertilia: Agamidae), *Zoological Studies*; 48(3):351-361.

[15]. Selander, RK, Sexual selection and dimorphism in birds In: *Sexual Selection and the Descent of Man*, (Campbell, B. ed.), Aldine, Chicago, 1972, pp. 180 - 230.

[16]. Fairbairn, DJ, 1997. Allometry for sexual size dimorphism: Pattern and process in the coevolution of body size in males and females, *Annual Review of Ecology and Systematics*; 28:659-687.

[17]. Fathinia, B, Rastegar-Pouyani, N, Darvishnia, H, Mohamadi, H, Faizi, H, 2012. Sexual size dimorphism in *Rana* (*Pelophylax*) *ridibunda ridibunda* Pallas, 1771 from a population in Darre-Shahr Township, Ilam Province, western Iran. *Amphibian and Reptile Conservation,* 5(1): 92-97.

[18]. Wiklund, C, Karlsson, B, 1988. Sexual size dimorphism in relation to fecundity in some Swedish satyrid butterflies, *American Naturalist;* 131(1):132-138.

[19]. Dubois, A, Bour, R, 2010. The nomenclatural status of the nomina of amphibians and reptiles created by Garsault (1764), with a parsimonious solution to an old nomenclatural problem regarding the genus Bufo (Amphibia, Anura), comments on the taxonomy of this

genus, and comments on some nomina created by Laurenti (1768), *Zootaxa*; 2447, 1-52.

[20]. Butler, MA, Schoener, TW, Losos, JB, 2000. The relationship between sexual size dimorphism and habitat use in greater Antiliean Anolis lizards, *Evolution*; 54(1):259-272.

[21]. Bolnick, DI, Dobelli, M, 2003. Sexual dimorphism and sympatric speciation: Two sides of the same ecological coin, *Evolution*; 57(11): 2433-2449.

[22]. Shine, R, 1979. Sexual selection and sexual dimorphism in the Amphibia, *Copeia*; 2: 297-306.

Celal Bayar University Journal of Science

Seed Geometric Morphometrics of Neottioid Orchids

Şenay Süngü Şeker[1*] (iD)

Department of Biology, Faculty of Sciences and Arts, Ondokuz Mayıs University, Samsun, Türkiye
*senay.sungu@omu.edu.tr
*Orcid: 0000-0003-4993-988X

Abstract

Cephalanthera, *Limodorum* and *Neottia*, which are known as primitive orchids, are rhizomatous orchids and commonly distributed in Turkey. This study aims to investigate orchid seed variation between some representatives of Neottieae, *Cephalanthera rubra*, *Limodorum abortivum*, *Neottia nidus-avis*, and *Neottia ovata*, naturally distributed in Turkey by using geometric morphometric analyses based on 2-dimensional landmarks. For this purpose, a total of 95 specimens were evaluated and photographed using scanning electron microscopy. Using software, 12 homologous landmarks were obtained to reflect the main aspects of the seed shape. Species were compared with various statistical methods by calculating the data obtained from shape and size variables with the Procrustes method. The difference in both size and shape were significant between the species. Shape differences were most prominent in the chalazal and micropylar regions of the seed as well as the whole seed width. Discriminant analysis and cross-validation scores were a highly powerful to distinguish the species with scores ranging from 60% to 88%. Regression analyses also revealed allometric effect of the size on seed shape with a similar trend across species. Based on current results, geometric morphometric analysis is encouraging in the research of structural variation within plant parts. The present study is also significant in terms of the widespread use of such studies in the field of botany, especially in the context of systematic or functional morphology.

1. Introduction

Orchidaceae family have so many species distributed in a broad area with various vegetation types [1, 2] and has also a great species diversity in Turkey [3,4]. Tribe Neottieae (subfamily Epidendroideae) is often referred to as primitive orchids. Tribe Neottieae was firstly described by Lindley [5]. After that, different classifications have been proposed by many researchers [6-10]. Today Neottieae is more limited involved in only six genera recognized (*Aphyllorchis* Blume, *Cephalanthera* Rich., *Epipactis* Zinn, *Limodorum* Boehm., *Neottia* Guett., *Palmorchis* Barb. Rodr.) of which four are represented by various taxa in Turkey.

Orchid seeds are typically dispersed by the wind because they are extremely small, so-called dust seeds. The first detailed studies on orchid seeds were published as a review by Rasmussen [12] and Arditti and Ghani [13]. Although they are so small, have an undifferentiated embryo, and have not to contain endosperm, observations of orchid seed morphology

using electron microscopy revealed detailed information on the seeds. Many studies such as descriptive morphology, and morphometry performed on the orchid seeds emphasized the distinguishing values of a few characters [14-18]. Especially, these studies revealed that the properties such as cell shape and number in the testa, and cell size in the medial or chalazal region, and periclinal wall pattern are systematically valuable.

On the other hand, in recent years there has been a growing attention in the usage of modern geometric morphometric (GMM) [19]. Beyond classical qualitative or quantitative definitions, GMM allows the researcher to quantify size and shape by analyzing relative landmark positions and point sets used for frames and surfaces [20]. Thus taxonomists and systematists tended to use geometric morphometry in their field. But, these analyses, which have mostly focused on insects, mammals, and fishes as not yet been greatly carried on plant [21]. Recently, GMM studies on the leaf shape comparison between different populations or taxon have got priority in the literature [19, 22].

Unfortunately, such studies are very rare in Orchids. Firstly, Chemisquy et al. [23] studied the orchid seed shape applying the geometric morphometric approach and they stated that seed size, referred to centroid size, was a changeable features and illustrative at a phylogenetic level.

The current research aimed to analyse the seed morphology of a few representatives of Neottieae using scanning electron microscopy and geometric morphometrics. The aim was also to identify whether the geometric clue of seed shape or size differences is conserved among genera in the tribe and reflects the phylogenetic relationship of this group.

2. Materials and Methods
2.1. Seed acquisition

Mature seed samples of four different taxa classified in the genus *Cephalanthera*, *Neottia,* and *Limodorum* were gathered from various localities (Table 1). Species identification was completed using Flora of Turkey and Türkiye Bitkileri Listesi [3,4] and current plant names checked from the Plantlist database [24]. At least two different individuals from each locality were evaluated and different locality samples were examined together to eliminate intraspecific variation. The mature capsules were selected at random from different positions on the inflorescence of each individual and about five mature, undamaged capsules were dissected for each taxon and dried for about one month. The seeds of the collected specimens were put in the sterile tubes and stored in our laboratory collection with the specimen number (Table 1).

Table 1. List of studied species, localities, voucher specimens

Taxon	Specimen number	Collection location	Collection date
Cephalanthera rubra (L.) Rich.	CepRubSss32	Turkey, Samsun Kurupelit, 209m.	July, 2017
Cephalanthera rubra	CepRubBss69	Turkey, Bolu, Abant, 839m.	August, 2015
Limodorum abortivum (L.) Sw.	LimAboSss64	Turkey, Samsun Kurupelit, 198m.	May, 2012
Neottia nidus-avis (L.) Rich.	NeoNidAviBss73	Turkey, Bolu, Abant, 1028m.	June, 2021
Neottia nidus-avis	NeoNidAviSmka29	Turkey, Samsun, Kurupelit, 209m.	May, 2014
Neottia ovata (L.) Bluff & Fingerh.	NeoOvaSmka39	Turkey, Samsun, Çarşamba, 18m.	June, 2015

2.2. Scanning electron microscopy

For electron microscopy, a small amount of sample was covered with 12.5–15 mm gold-palladium (scanning electron microscope (SEM) coating system, SC7620) on the stubs and was observed on the voltage of 5–15 kV in JEOL JMS-7001F SEM [25]. The seed shapes on about 30 photographs for each taxon were evaluated through SEM observation.

2.3. Geometric morphometric analysis

Thin-plate spline (TPS) series programs were used to prepare datasets using software tpsUtil version 1.74 [26,27]. All seed images were sequentially scaled and landmarked using tpsDig v. 2.16 [28]. The homologous landmarks set determined in this research (Figure 2) was chosen to explain the major aspects of the seed shape in taxa. These landmarks represent the clearest frame of the seed to aid with descriptions of shape changes: chalazal region (landmarks 1-3, 11-12), medial region (landmarks 4-5, 9-10), and micropyle (landmarks 6-8) on the lateral view of the seed (Figure 1).

The coordinates data sorted in txt file format were imported into the MorphoJ program [29] for analysis. To study shape, a Generalized Procrustes Analysis (GPA) was performed on the landmark configurations to extract shape data by removing information about size and orientation from each specimen [30, 31]. In this way, the coordinates representing the seed morphology were subdivided into shape and size variables. [32]. The Procrustes shape coordinates of each seed were superimposed to make a common profile [33].
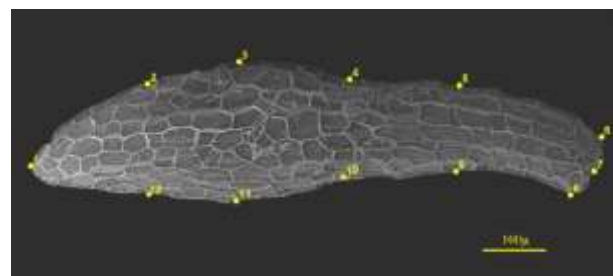

Figure 2. Landmark configuration on the seed

2.4. Data analysis

For detecting differences in size among the species, the Kruskal-Wallis test was performed with centroid size. After being tested with Kruskal-Wallis, a Pairwise Dunn's test was conducted to determine which species made a significant difference. For shape analysis, principal component analysis (PCA) was carried out to Procrustes shape coordinates to determine the shape changes in the seed. After the dimension reduction of the data of the 12 landmarks, the combined variables that effected mainly to the variation in seed morphology were determined. Cross-validated discriminant function analysis was also subjected to statistically examine the success of seed shape variation for taxonomic assignment. Moreover, a multivariate regression analysis was used to estimate any allometric effect. The analyse was performed among species and within each species distinctly using a permutation test with 10,000 rounds. Output transformation grid and wireframe graph were obtained to analyze the direction of the shape compression or enlargement. All analyses were carried out by using the PAST version 4.03 [34] and MorphoJ version 1.07 packages [35].

3. Results and Discussion
3.1. Size variation

It was obtained chi-squared value = 61.46, df = 3, and p-value < 0.001 from Kruskal-Wallis test. The analysis result showed that the difference among seeds of the species is statistically significant. These differences can also be related to shape differences among the species due to allometric effects (see below). Pairwise Dunn's test showed that *C. rubra* gave a significant difference between *L. abortivum* (p < 0.01), and *N. nidus-avis* (p = 0.01). Other than that, *L. abortivum* gave significant difference between *N. nidus-avis* (p < 0.01), and *N. ovata* (p < 0.01). The difference between *N. nidus-avis* and *N. ovata* was a significant (p<0.05), but there were no significant differences between *C. rubra* and *N. ovata* (p = 0.295). Moreover, boxplot graphics showed that *L. abortivum* was the largest in centroid size, (Figure 2). Based on traditional morphometry, seed width and lengths were found to be the same in *C. rubra* and *N. ovata* and *L. abortivum* have the largest seed [36]. These result show that geometric morphometry yields results with the same trend as traditional morphometry. The present study was therefore compatible with the results of that previous study in terms of size.

Many studies conducted on orchid seed morphometry have demonstrated that orchid seeds vary enormously in size from 150 mm to 6000 mm [37]. This diversity may be related to seed distribution as well as reflecting the phylogenetic relationship. Chemisquy et al., (2009) analyzed the seed morphology of some taxa of the tribe Chloraeae performing tools of geometric morphometrics and they emphasized that seed size, namely centroid

size, was a variable feature and illuminating at a phylogenetic level [23]. On the other hand, Nakanishi (2022) found that the dispersibility values calculated by proportioning the seed length by embryo length indicate the anemochorous potential and the seed size and dispersibility of terrestrial orchids are between epiphytes and saprophytes. [38]. These results indicate that, at least in the species subject to the present study, seed size may be related to seed distribution and indirectly reproductive success rather than reflecting the phylogenetic relationship between the genera. For this reason, in these species with different seed sizes, it may be interesting to evaluate the seed distribution about size in future studies.
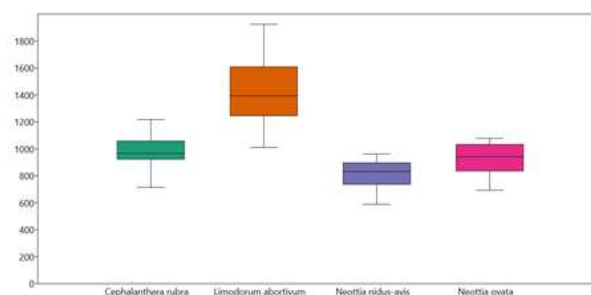
Figure 2. Boxplot graphics show the variation of centroid size for seed between the four species.

3.2. Shape variation

PCA was carried out on the Procrustes shape coordinates of seed morphology of the species and revealed that the first six principal components used for the shape analyses explained 83.7% of overall shape variation of the seed among the species. Figure 3 displays the scatter plot graphic of the PC1 and PC2 scores accounted for 56.4% of the total seed shape variables (PC1 accounted for 34.8%, and PC2 accounted for 21.6%). Based on the graphic, specimens of *C. rubra* and *L. abortivum* created different groups, whereas those of the other species were scattered between these two species. Along with the positive extremes of both PC1 and PC2 axes, the transformation grid and wireframe graphs were visualized. Based on this, the seed was curved at the medial region and, the chalazal pole was narrowed towards the positive value of the PC1 axis. There was also clear variation along the PC2 axis separating the specimens of *C. rubra* and *L. abortivum*. The chalazal region tip was gradually shortened and the medial region increasingly became narrower in the positive PC2 direction.

Discriminant analysis (Figure 4) revealed that the seed shape of *C. rubra* displayed a small overlap with that of *L. abortivum* and *N. ovata* and a large overlap with that of *N. nidus-avis*. Likewise, the seed shape of *L. abortivum* showed relatively greater overlap with *Neottia* sp. In these pairs of taxa, *L. abortivum* and *N. ovata* were more accurately classified based on seed
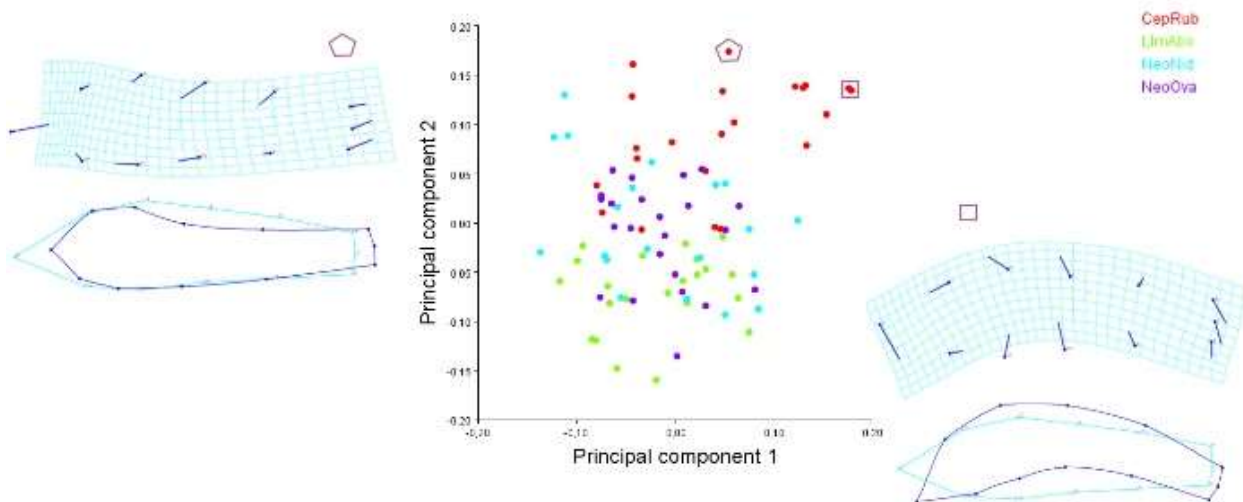
Figure 3. PCA scatter plot graphics (on the middle) show the shape variations in the studied species; shapes on the right and left sides visualize the positive extremes of PC axes using transformation grids and wireframe graphs and square/polygon symbols are used to show the positions of visualized shapes in the PCA scatterplot.
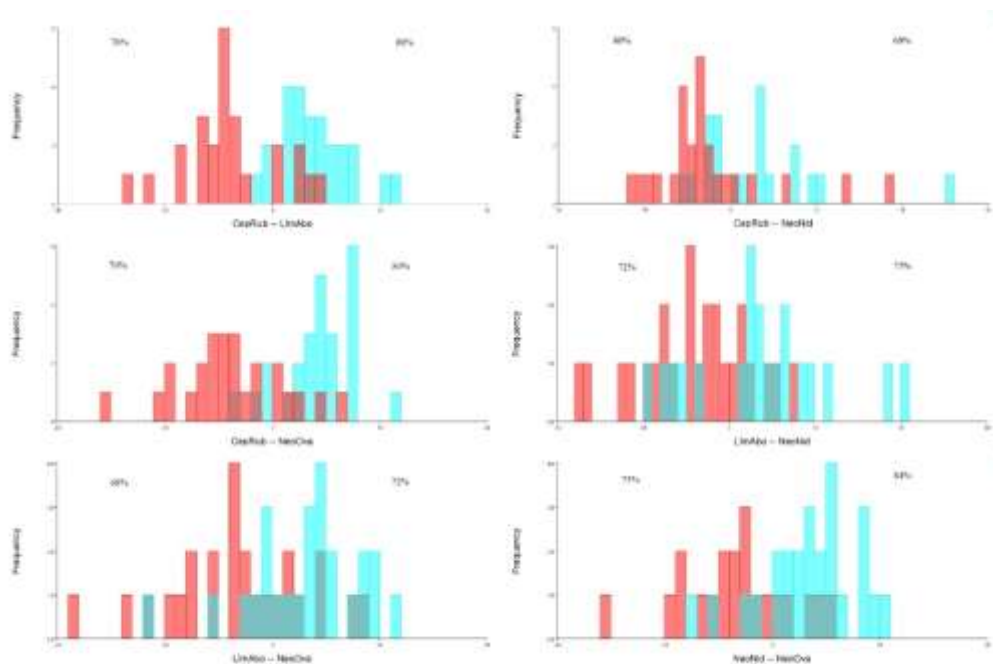
Figure 4. The cross-validation results of discriminant analysis using the seed shapes of *C. rubra, L. abortivum, N. nidus-avis,* and *N. ovata*. The red and blue color represent specimens of species with abbreviations at the bottom of each graph, respectively.

shape than the others (Figure 4). Of 95 admixed individuals, ca. 60–88% were correctly classified as true species using seed shape. Qualitative micromorphological characters of seeds were analyzed in many studies. These characters appear very useful at the supraspecific level in the subtribe Orchidinae [39,40]. However, in these studies, the seed shape was evaluated as a whole and defined qualitatively as clavate, fusiform, filiform, etc. On the other hand, a geometric morphometric study allows us to examine the shape changes in the chalazal or micropylar regions separately and to prevent the errors arising from the researcher's observation by digitizing the shape data.

In their geometric morphometric study on the tribe Chloraeeae, Chemisquy et al. (2009) showed that seed shape resulted in a continuum among the taxa studied, and in only a few cases could genera or groups of species be discriminated on the basis [23]. But the

present study was not compatible with the results of that Chemisquy et al. (2009) in terms of shape. The result revealed that Procrustes shape were different among the studied species in present research. In addition, Magrini et al. (2010) 's findings with her outline study on *Limodorum* support the current study [41]. They aimed to verify the taxonomic value of *Limodorum* seeds, particularly of the shape of two close species (*L. abortivum* and *L. trabutianum*) growing sympatrically. The outline analysis confirmed a low intraspecific variability of seed shape, but show a very high interspecific variability, thus geometric morphometry

allowed us to distinguish between these two species even during the fruiting phase, simply using seed shape as a diagnostic character. In addition, the last study [42] explained the relationship between closely related parent species and their hybrids belonging to the *Orchis* Tourn. ex L. genus with a geometric morphometric approach with labellum morphology. This situation is inspiring for the evaluation of species with systematic problems, such as orchids, whose systematic category often changes, using geometric morphometric approaches.
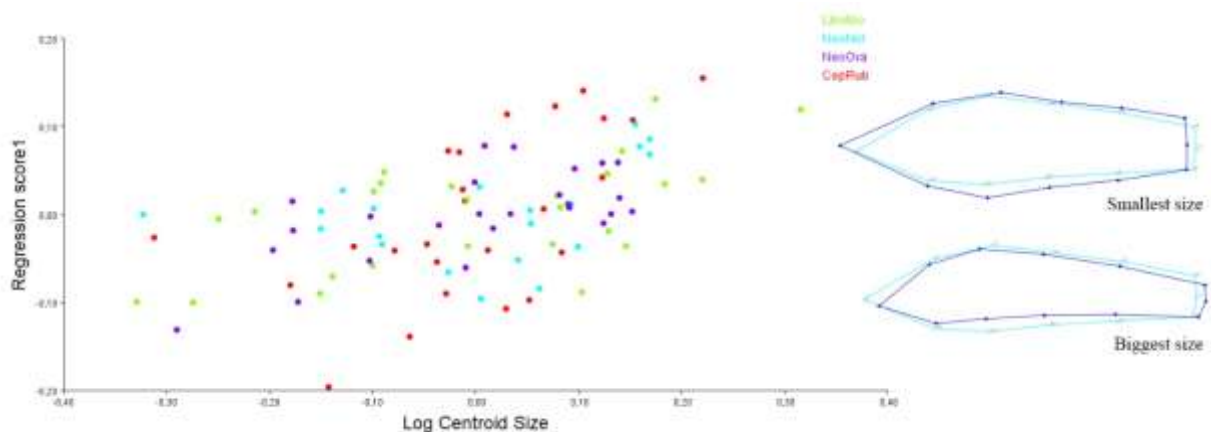
Figure 5. The Scatterplot of regression scores vs centroid size; shapes at the opposite extremes of the range of allometric variations are visualized using a seed wireframe.

3.3. Allometric effect

Before proceeding with full regression analysis, the significance of allometry within groups was evaluated by splitting species into separate samples and, then applying multivariate regressions of the shape onto size one group if at least one of the groups is statistically significant. Regressions of the shape onto size one species were marginally significant ($P < 0.01 – P = 0.01$, 12.7 – 20.7 % of variance explained) for all species. For the seed, multivariate regression of the Procrustes coordinates on log centroid size for the four species showed a highly significant result ($p < 0.001$), with allometry explaining 28.5% of total shape variation. This test as well as the large overlap between species in the scatterplot (Figure 5) suggested that the effect of size on shape was similar in the four species: bigger seeds tend to be shorter in the chalazal region, but be longer at the micropyle and all the seed tend to be narrower. On the contrary, as can be also seen from the wireframe graphs, at the negative extreme of the centroid size, the seed became shorter at the micropyle but became longer at the chalazal region and all the seeds tend to be wider (Figure 5).

Because orchid seeds are very small, they are called dust seeds and are dispersed by the wind. The anemochorous potential of the seed is estimated based on the ratio of seed length to embryo length [43]. As the

seed size increases, the shrinkage of the seed means that the spherical embryo also gets smaller. The ratio of seed size to embryo length increases, thus it is logical that this allometric effect may be a positive adaptation to the reproductive biology of the species by improving the buoyancy of the seed for wind dispersal.

4. Conclusion

Geometric morphometric analysis is a powerful procedure that determines and display the shape differences effectively. Orchid seeds are commonly used in taxonomic analyses in many other groups at diverse taxonomic levels. However, orchidologists avoid using the method for this purpose in their studies as much as zoologists have done. Using free software and a dataset from SEM observation of orchid seeds, a detailed but simple analysis computing size and shape variables using Procrustes methods was performed. The present result is impressive that Procrustes-based methods for the analysis of landmarks were extremely effective in determining the differences in shape and size and in revealing very small-scale variations. For this reason, botanists need to illuminate functional morphology as well as taxonomy.

Acknowledgment

The author would like to thank Dr. Sadık Demirtaş for technical assistance, and Prof. Gülcan Şenel and Dr. Mustafa Kemal Akbulut for providing some seed materials.

Author's Contributions

Şenay Süngü Şeker: Collected the seed, performed the experiment and geometric morphometric analysis, interpreted the results, wrote the manuscript.

Ethics

There are no ethical issues after the publication of this manuscript.

References

[1]. Delforge, P. Orchids of Europe, North Africa and the Middle East; A&C Black: London, England, 2006.

[2]. The Plant List. 2022. Retrieved from http://www.theplantlist.org/ (accessed at 23.03.2022).

[3]. Davis, PH. Flora of Turkey and Aegean Islands (Vol. 8).; Edinburgh University Press: Edinburgh, Scotland, 1982.

[4]. Güner, A, Aslan, S, Ekim, T, Vural, M, Babaç, MT. 2012. Türkiye Bitkileri Listesi. Damarlı Bitkiler, Istanbul: Nezahat Gökyigit Botanik Bahçesi ve Flora Araştırmaları Dernegi Yayını; İstanbul, Turkey, 2012.

[5]. Lindley, J. The genera and species of orchidaceous plants; Ridgways: London, UK, 1830-1840.

[6]. Schlechter, R. 1926. Das System der Orchidaceen. *Notizblatt des Botanischen Gartens und Museums zu Berlin-Dahlem;* 9: 563–591.

[7]. Rasmussen, F. 1982. The gynostemium of the Neottioid orchids. - *Opera Botanica*; 65: 1-96.

[8]. Pfitzer, E. 1887. Zur organophyletischen Natur des Orchideen labellums. *Botanische Jahrbücher fur Systematik, Pflanzengeschichte und Pflanzengeographie;* 84: 175-214.

[9]. Dressler, R. The orchids, Natural history and classification; Harvard Univ. Press: Cambridge, USA, 1981.

[10]. Brieger, FG, Maatsch, R, Senghas, K. Tribus Neottieae. In Schlechter, R., (ed.): Die Orchideen, Paul Parey, Berlin, 1974, pp. 287 - 294.

[11]. Bentham, G. 1881. Notes on Orchideae. *The Journal of the Linnean Society*; 18: 281-360.

[12]. Rasmussen, HN. Terrestrial orchids: From seed to mycotrophic plant; Cambridge University Press: New York, 1995.

[13]. Arditti, J, Ghani, AKA. 2000. Tansley review no. 110. Numerical and physical properties of orchid seeds and their biological implications. *New Phytologist*; 145(3): 367-421.

[14]. Chase, MW, Pippen, J. 1990. Seed morphology and phylogeny in subtribe Catasetinae (Orchidaceae). *Lindleyana*; 5: 126-133.

[15]. Kurzweil, H. 1993. Seed morphology in Southern African Orchidoideae (Orchidaceae). *Plant Systematics and Evolution*; 185: 229-247.

[16]. Molvray, M, Kores, PJ. 1995. Character analysis of the seed coat in Spiranthoideae and Orchidoideae, with special reference to the Diurideae (Orchidaceae). *American Journal of Botany*; 82: 1443-1454.

[17]. Aybeke, M. 2007. Pollen and seed morphology of some *Ophrys* L.(Orchidaceae) taxa. *Journal of Plant Biology*; 50: 387-395.

[18]. Gamarra, R, Ortúˉnez, E, Cela, PG, Guadaˉno, V. 2012. *Anacamptis* versus *Orchis* (Orchidaceae): Seed micromorphology and its taxonomic significance. *Plant Systematics and Evolution*; 298: 597-607.

[19]. Viscosi, V, Cardini, A. 2011. Leaf morphology, taxonomy and geometric morphometrics: a simplified protocol for beginners. *PloS one*; 6(10): e25630.

[20]. Jensen, RJ. 2003. The conundrum of morphometrics. *Taxon*; 52: 663-671.

[21]. Demirtaş, S, Gündüz, İ, Herman, JS. 2022. Discrimination of the sister hedgehog species *Erinaceus concolor* and *E. roumanicus* (Erinaceomorpha: Mammalia): A Geometric morphometric approach. *Turkish Journal of Zoology*; 46(2): 238-235.

[22]. Yang, K, Wu, J, Li, X, Pang, X, Yuan, Y, Qi, G, Yang, M. 2022. Intraspecific leaf morphological variation in *Quercus dentata* Thunb.: a comparison of traditional and geometric morphometric methods, a pilot study. *Journal of Forestry Research*; 1-14.

[23]. Chemisquy, MA, Prevosti, FJ, Morrone, O. 2009. Seed morphology in the tribe Chloraeeae (Orchidaceae): combining traditional and geometric morphometrics. *Botanical Journal of the Linnean Society*; 160(2): 171-183.

[24]. The Plant List 2022. Aavailable from http://www.theplantlist.org/.

[25]. Akbulut, MK, Şenel, G. 2016. The seeds micromorphology and morphometry of certain *Dactylorhiza* (Orchidaceae) species distributed in Turkey. *Rendiconti Lincei*; 27(4): 679-686.

[26]. Rohlf, FJ. 2015. The TPS series of software. *Hystrix*; 26: 9-12.

[27]. Rohlf, FJ. tpsUtil, version 1.46. Department of Ecology and Evolution State University of New York; Stony Brook, NY, USA, 2010a.

[28]. Rohlf, FJ. tpsDig, version 2.16; Department of Ecology and Evolution, State University of New York at Stony Brook: Stony Brook, NY, USA, 2010b.

[29]. Klingenberg, CP. 2011. MorphoJ: an integrated software package for geometric morphometrics. *Molecular Ecology Resources*; 11: 353-357.

[30]. Rohlf, FJ, Slice DE 1990. Extensions of the Procrustes method for the optimal superimposition of landmarks. *Systematic Zoology*; 39: 40-59.

[31]. Dryden, IL, Mardia, KV. Statistical shape analysis: with applications in R, vol. 995; John Wiley: Chichester, UK, 2016.

[32]. Sanflippo, PG, Cardini, A, Hewitt, AW, Crowston, JG, Mackey, DA, 2009. Optic disc morphology: rethinking shape. *Progress in Retinal and Eye Research*; 28(4): 227-248.

[33]. Klingenberg, CP, Barluenga, M, Meyer, A. 2002. Shape analysis of symmetric structures: quantifying variation among individuals and asymmetry. *Evolution*; 56(10): 1909-1920.

[34]. Hammer, Ø, Harper, DAT, Ryan, PD. 2001. PAST: Paleontological Statistics Software Package for Education and Data Analysis. *Palaeontologia Electronica*; 4(1): 1-9.

[35]. Klingenberg, CP. 2011. MorphoJ: an integrated software package for geometric morphometrics. *Molecular Ecology Resources*; 11: 353-357.

[36]. Süngü Şeker, Ş, Akbulut, MK, Şenel, G. 2021. Seed morphometry and ultrastructure studies on some Turkish orchids (Orchidaceae). *Microscopy Research and Technique*; 84(10): 2409-2420.

[37]. Molvray, M, Kores, P. 1995. Character analysis of the seed coat in Spiranthoideae and Orchidoideae, with special reference to the Diurideae (Orchidaceae). *American Journal of Botany*; 82: 1443-1454.

[38]. Nakanishi, H. 2022. Seed Morphology and Dispersibility of Orchids in Warm Temperate Japan. *Acta Phytotaxonomica et Geobotanica*; 73(1): 19-33.

[39]. Gamarra, R. Ortúñez, E, Galán Cela, P, Guadaño, V. 2012. *Anacamptis* versus *Orchis* (Orchidaceae): seed micromorphology and its taxonomic significance. *Plant systematics and evolution*; 298(3): 597-607.

[40]. Süngü Şeker, Ş, Şenel, G. 2017. Comparative seed micromorphology and morphometry of some orchid species (Orchidaceae) belong to the related *Anacamptis*, *Orchis* and *Neotinea* genera. *Biologia*; 72(1): 14-23.

[41]. Magrini, S, Buono, S, Gransinigh, E, Rempicci, M, Onofri, S, Scoppola, A. Outline analysis for identifying *Limodorum* species from seeds. In: Nimis, PL, Vignes Lebbe, R, (eds.) Tools for identifying biodiversity. Edizioni Università di Trieste (EUT), Trieste, 2010, pp. 249–250**.**

[42]. Bersweden, L, Viruel, J, Schatz, B, Harland, J, Gargiulo, R, Cowan, RS, ... Fay, MF. 2021. Microsatellites and petal morphology reveal new patterns of admixture in *Orchis* hybrid zones. *American journal of botany*; 108(8): 1388-1404.

[43]. Arditti, J, Michaud, J, Healey, P. 1980. Morphometry of orchid seeds. II. Native Californian and related species of Calypso, *Cephalanthera*, *Corallorhiza* and *Epipactis*. *American Journal of Botany*; 67: 347-360.

Celal Bayar University Journal of Science

Glycoprofiling of Oligosaccharides of Regular and Lactose-Free Milk by Mass Spectrometry

Umut Şahar[1]*

[1] Department of Biology, Molecular Biology Section, Faculty of Science, Ege University, 35040 Bornova/Izmir, Türkiye
*umut.sahar@ege.edu.tr
*Orcid: 0000-0002-2200-6986

Abstract

Oligosaccharides from regular milk and lactose-free milk were analyzed by Electrospray Ionization interface coupled with Ion Trap Mass Spectrometry (IT-MS). The negative mode mass spectrometry of sugar compositions was obtained either by direct infusion and mass spectrometry with Liquid Chromatography (LC). Hexose (Hex) and the other oligomeric sugar components were observed in both regular and lactose-free milk. While lactose derivatives (deprotonated lactose dimer, chloride adducts, chloride dimer) in regular milk have seen to be dominated, monosaccharide derivatives (Hex-H_2O, Hex, Hex-Cl) in the lactose-free milk were observed as abundant which was lytic product of lactose. Phosphate/sulfate ester substitution on lactose and sialyllactose in both regular and lactose-free milk samples were observed with similar intensity thus it has been understood that these important milk components are not digested during lactose removing process.

Keywords: Milk, Lactose-free, LC-MS, Oligosaccharides, Sialic acid

1. Introduction

Milk and milk products are valuable food sources because of their high content of essential fatty acids, vitamins, minerals, amino acids, and carbohydrates [1, 2]. Lactose is not present in the milk of some mammals however, it is the main sugar that gives to the energy value of bovine milk [3, 4]. Most mammals show high lactase (β-galactosidase) activity in the infancy period of their lives if milk is their sole food source [3] on the other hand digestion problem of lactose known as lactose intolerance is a common problem in adult human [5] therefore a variety in lactose-free and low-lactose milk or dairy products would be favorable the people who are lactose-intolerant [6]. Industrial production processes and lactose separation from milk by specific methods has been patented [7] and lactose hydrolysis methods and technology have been well reviewed in the literature [8, 9].

Bovine milk glycans are bioactive materials and have vital biological roles comprising the inhibiting of pathogen binding to the gut system and as supplies for beneficial bacteria [10].

Some of studies showing that oligosaccharides may have positive effects on diseases such as diarrhea, necrotizing enterocolitis and allergies related to microbiota [11, 12]. Additionally, it has been attributed that sialylated glycomacropeptide could improve memory and learning in piglets [13]. 3′-sialyllactose (3′-SL) and 6′-sialyllactose (6′-SL) have been shown to possess prebiotic properties that able to reduce stressor-induced alterations and anxiety-like behavior on mice [14]. Considerably glycomics results of milk oligosaccharides of human, bovine, and porcine have been reported which offer opportunities to compare their structural properties [15–17] and it is important to examine the profile and quantity of animal milk oligosaccharides to discover sources of bioactive analogous to human milk glycans [18].

Mass spectrometry has been used extensively both independently and coupled with LC for the investigation and structural characterization of milk oligosaccharides [19–24]. Since the gas phase basicities of some glycans and chloride are close to each other, it has been reported that the chloride adduct ion signal will be higher [25, 26] therefore negative mode analysis would be performed for both neutral and acidic oligosaccharides.

There are numerous of analytical methods used to milk oligosaccharides analysis and in this study it was aimed to characterize the differences or similarities of oligosaccharide in regular and lactose-free milk by mass spectrometry. To the best of my knowledge, there have been no reported applications of MSn and LC-MS/MS for the characterization of regular and lactose-free bovine milk oligosaccharides. It was also aimed to identify sialyllactose and the other sulfate/phosphate substituted lactose in lactose-free milk.

2. Materials and Methods
2.1. Chemicals and Reagents

The organic solvents used in this study were HPLC grade. Acetonitrile was LiChrosolv from Merck (Merck, Darmstadt) and ethanol was from Sigma-Aldrich (USA). The ultrapure water for the mobile phase was obtained using a Sartorius Arium water purification systems (Germany).

2.2. Isolation of Milk Oligosaccharides

Regular and lactose-free milk samples were obtained from local markets. Samples were centrifuged in refrigerated centrifuge at 4 °C for 30 minutes. Following centrifugation upper lipid layer was discarded. The proteins in the remaining sample were then precipitated by adding ethanol in same volume. After precipitation, samples were centrifuged at 4 °C for 30 min again. The supernatant which was containing the oligosaccharides were filtered and then analyzed by mass spectrometry.

2.3. Capillary LC and Ion Trap MS System Parameters

Bruker HCT Ultra ion trap mass spectrometry (Bremen, Germany) was used to perform analyses in negative mode. Data acquisition, processing and the system controls, such as ion transmission voltages, nebulizing gas (Nitrogen) pressure (15.0 psi), dry gas flow (5.0 l/min), and the temperature of dry gas (300 °C) were operated by expert tune mode of Esquire Control software 6.1. Collision and fragmentation of ions operated by Helium in MS analyzer. Multiple-reaction monitoring (MRM) system was used to obtain fragment ion spectra. Total spectral data were collected between m/z 100 and 1500, and scanning were performed in ultrascan mode (26,000 m/z per second). Data Analysis version 3.4 was used for the data processing.

Milk extract was continuously infused at 160 μL/h flow rate using syringe pump to the ESI source. Pseudomolecular ions of monosaccharides and oligosaccharides were both scanned in negative MS and MS/MS mode.

Chromatographic analyses were performed on an Agilent 1200 Series Capillary HPLC system. Separation of sialyllactoses were performed by using ODS column (Zorbax C18 150 × 0.5 mm 5μm). Elution was performed using acetonitrile and water as mobile phase. Chromatographic elution was carried out in gradient mode. Fast reconditioning valve of autosampler was positioned to the direct at the beginning of elution. Sample injection volume was set at 0.1 μl and flow rate of binary pumps were adjusted to 20 μl/min.

3. Results and Discussion

Mass spectrometry has been using as a powerful technique for both structural characterization and quantification of glycans. Mass spectrum for monosaccharides and oligosaccharides mixture from regular milk and lactose-free milk were analyzed by electrospray ionization IT-MS and shown in Figure 1. The samples were obtained from the markets. Milk extracts were scanned by accurate mass and tandem MS options. Some ions in the negative mode corresponded to anionic adducts e.g. $(M+Cl)^-$ and others were $(M-H)^-$ type molecular ions.

3.1. Negative Mode Mass Spectrometry for Oligosaccharides

The negative mode mass spectra profiles in this study provide a crude analysis of sugar compositions of regular and lactose-free milk. Both spectra (Figure 1) were obtained by direct infusion of the solutions of oligosaccharides.extracts.

There are three common disaccharides in nature which were named as sucrose, lactose, and maltose. More than 20 disaccharides which have same molecular weight (m/z 341 in negative mode) have been studied by mass spectrometry [26]. Lactose is a disaccharide (Hex2) also and it is abundant in bovine milk. Although some unknown disaccharides reported in milk [22] pseudomolecular ion m/z 341 was accepted as lactose in this study and m/z 377 likely the chloride adducts of this ion.

The whole mass spectrum profile of regular milk was found to be similar to those discussed and reported previously [27]. In regular milk spectrum that shown in formation of m/z 341. Chloride adducts of lactose at m/z 377 also have intense signal. The other ion m/z 719 correspond to dimer formation of m/z 341 with chloride adducts. Pseudomolecular ions in Figure 1A, m/z 161 was the probable $[M - H]^-$ forms of anhydrohexose (Hex-H_2O), and the other ions 179, 341 and 503 were Hex, Hex2 and Hex3 respectively, as also detected by ESI-MS and comparison with the described data in the literature [28, 29].
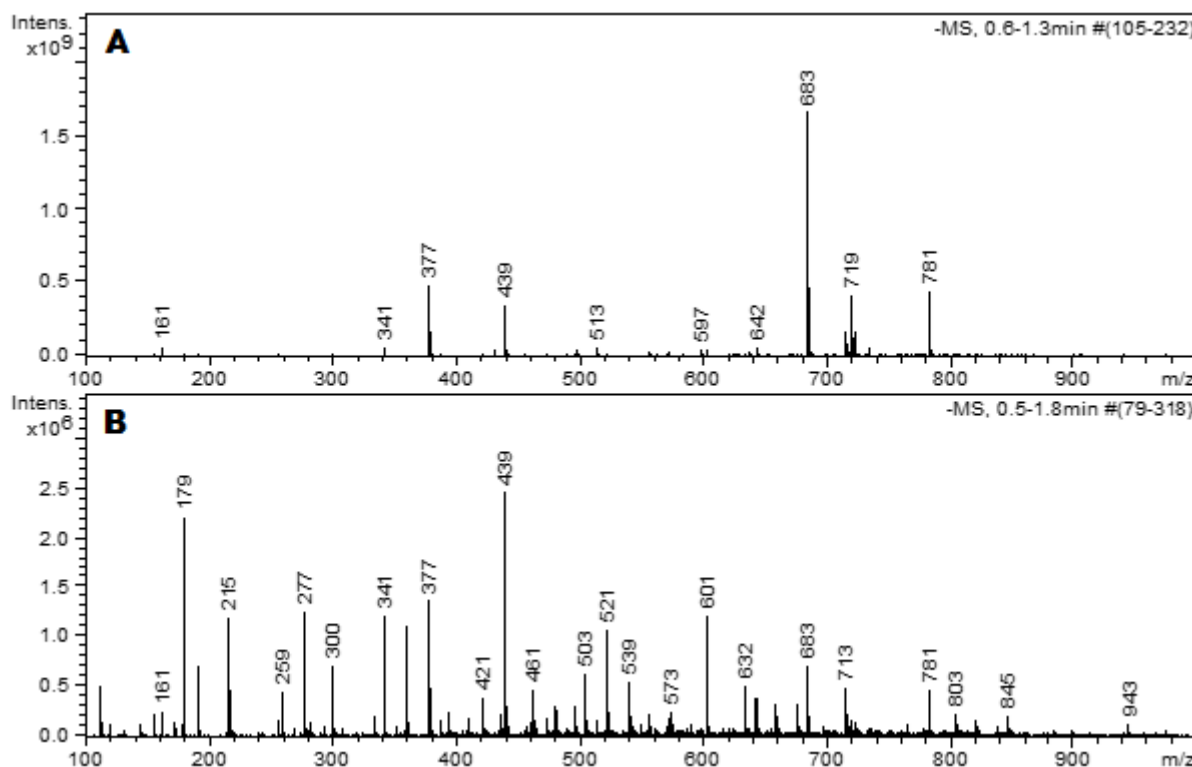
Figure 1. Mass spectrometry results of underivatized oligosaccharides from the milk samples in negative mode by direct infusion. A; Regular Milk, B; Lactose-free Milk.

Anions of m/z 539 was likely the chloride adducts (with isotope of the ^{35}Cl) Hex3 as previously suggested [29] and these ions were observed also in lactose-free milk in Figure 1B.

In the lactose-free milk spectrum (Figure 1B) one of the prominent ion was present corresponding to the composition monosaccharides (Hex) (m/z 179). It was probably the result of the enzymatic digestion reaction of lactose. As similar to the lactose-free milk, greater concentration of galactose and glucose was reported in skimmed milk [22]. m/z 215 reflects the chloride adducts of Hex also that was shown in Figure 1B. Hex (m/z 179) abundance in the regular milk spectrum was lower than the m/z 341 and m/z 377 signal in the Figure 1A. When it was compared to the lactose-free milk the Hex abundance is relatively smaller in regular milk. It was speculated that, m/z 179 was reflects the glucose and galactose which was the digestive product of lactose in lactose-free milk spectrum (Figure 1A).

In the previous studies about glycan ingredients of regular and lactose-free milk, lactose concentration was found to be around 5% (w/v) in regular milk samples and around 0.01% (w/v) in lactose-free labeled milk samples from markets [34-36]. In another study, glucose was found to be 0.05 g/L in regular milk and 19.55 g/L in lactose-free milk [38] which has correlation about results from our study that shown in Figure 1.

3.2. Structural Analysis of Oligosaccharides by Tandem MS

In the literature, m/z 421 in bovine milk was indicated as a phosphorylated dihexose and/or a sulfated dihexose [23, 30]. The fragmentation process of m/z 421 most likely indicate the presence of phosphate/sulfate ester substitution on lactose which was shown in Figure 2 also as reported in literature [24, 27, 29]. A fragment ion at m/z 259 was detected for m/z 439 and 601, which could be evidence of phosphate/sulfate ester substitution in both regular and lactose-free milk (Figure 2). To the best of our knowledge, information on the phosphated/sulfated lactose in milk is rather limited in literature, but important roles on mucous defense mechanism was reported by Ideo et al [42]. Hex3, Hex2HexNAc, 3'-SL and 6'-SL were determined in lactose-free milk that were separated using CarboPac™ PA300-4 μm column [37]. Likewise, we identified phosphate/sulfate ester substituted lactose as additionally.

In this study, more attention has been paid to the analysis of sialic acid-containing glycans especially sialyllactose because it was aimed to observe whether the enzyme used in the production of lactose-free milk digests sialyllactose structure. Sialyllactose has been known an important glycan for microbiota [18]. Mass spectrometry of sialylated oligosaccharides have been

Figure 2. MS/MS analysis of a milk samples. The mass spectrum shows phosphate/sulfate ester substitued oligosaccharide structures and its mass/charge ratio (m/z): A; fragmentation spectrum of m/z 421, B; fragmentation spectrum of m/z 439, C; fragmentation spectrum of m/z 601. Fragment ion at m/z 259 shows phosphate/sulfate ester substitution on oligosaccharides.

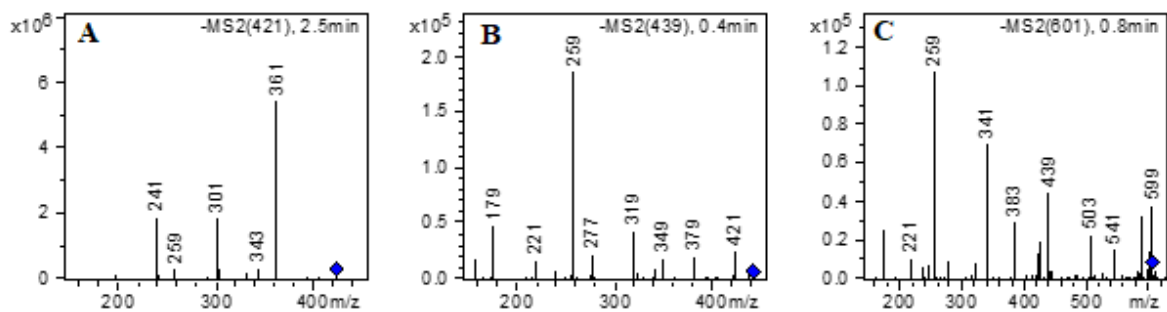widely studied in the previous studies [15, 19, 31]. Sialic acid modification usually occurs on lactose or lactosamine, which results as sialylgalactose, sialyllactose, and sialyllactosamine. The negative mode ESI spectra provide useful information (Figure 3) about sialic acid attached glycans because of the anionic nature of this molecule. Although conventional mass spectrometry is known to yield less information about anomericity and monosaccharide stereoisomers [41], some of fragment ions (Figure 3) in ion trap mass spectrometry that was used in our study provide useful information on linkage positions. Chromatographic separation of glycoforms could be performed by using specific columns and isomeric separation could be done either by state-of-art mass spectrometers. In this study 3'-SL and 6'-SL were not separated on C18 reverse phase column but the results were accepted as satisfactory to claim that 3'-SL and 6'-SL were not digested during lactose removing process.

In the negative mode, m/z 632 corresponds to sialyllactose with the composition 2Hex+1NeuAc. Since these isomers contain the negatively charged sialic acid, it was studied in negative mode by singly deprotonated ions. The IT−MS^2 spectrum of sialyllactoses were shown in Figure 3. In the spectrum the precursor ion [M-H]$^-$ at m/z 632 and the fragment ion at m/z 290 were observed clearly. It was reported that glycoform of the the sialyllactose (α2-3 or α2-6 linkage) have different fragmentation patterns and m/z 306 and m/z 470 look like to be diagnostic ions of the existence of an α2-6-linked sialyllactose (6'-SL), m/z 468 and m/z 408 presence of an α2-3-linked sialyllactose (3'-SL).

3'-SL and 6'-SL are acidic oligosaccharides and they are found in almost all mammalian milk, 3'-SL was reported to be the most abundant bovine milk oligosaccharide [24, 31–33]. Although, 3'-SL and 6'-SL were not separated chromatographically, the Figure 3 shows that 6'-SL is probably abundant form in both regular and lactose-free milk samples because m/z 470 was the prominent ion in the both samples. Low abundance was reported about the Neu5Gc and Fucose-containing oligosaccharides in bovine milk [10] and with this relation these oligosaccharides were not detected in this study.

Milk-based products are applied to several types of nutrients therefore, characterization of the milk samples is very important for the health and food industry. Bovine milk oligosaccharides shows similarity to those found in human milk and characterizing the structures of these sugars is very important for their biological profit [37,39]. In a recent study, more hexosylation (hexose-derived glycation) of amino acids on protein has been detected in lactose-free milk samples [40], with regard to these reults, characterization of glycan components of normal and lactose-free milk may contribute to the glycoproteomic studies.

4. Conclusion

The results obtained in this work provide an insight into the oligosaccharide composition from regular milk and lactose-free milk. From deprotonated and anionic adducts of monosaccharides to larger oligosaccharides were observed and characterized by MS and MS/MS system in this study. Moreover, this study suggests that although lactose intensity in mass spectrum is lower in the lactose-free milk, sialyllactose concentration appears to be closer in both samples and sialyllactoses were not digested in lactose removal process. While lactose adducts were found to be abundant in regular milk, intense hexose adducts were observed in lactose free milk. These findings help to evaluate sugar composition of regular milk and lactose-free milk samples.

Sialoglycans have known to be essential ingredients in human milk and infant formula for infant neural development, construction of microbiota, and defense against pathogenic bacteria. Our results show that both regular and lactose-free bovine milk oligosaccharides could be added to the infant formula, but we must take into account that lactose-free milk contains more glucose which means more "sweet".
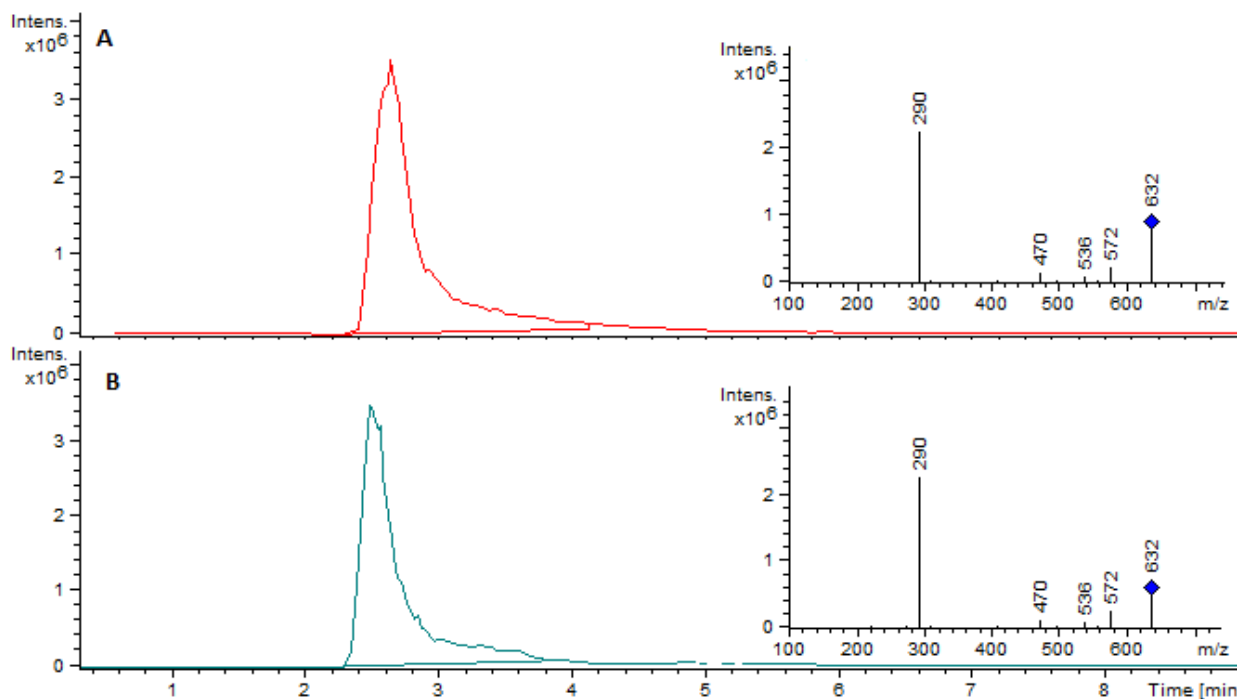
Figure 3. Extracted-ion chromatogram of ion m/z 632. Sialyllactose oligosaccharide (3SL or 6SL) isomers were not separated on the analytical column. A; Sialyllactose in regular milk, B; Sialyllactose in lactose-free milk.

Author's Contributions

Umut Şahar: Drafted and wrote the manuscript, performed the experiment and result analysis.

Ethics

There are no ethical issues after the publication of this manuscript.

References

[1]. Costa, A, Lopez-Villalobos, N, Sneddon, NW, Shalloo, L, Franzoi, M, De Marchi, M, Penasa, M. 2019. Invited review: Milk Lactose-Current Status and Future Challenges in Dairy Cattle. *Journal of Dairy Science*; 102: 5883–5898.

[2]. Barłowska, J, Szwajkowska, M, Litwińczuk, Z, Król, J. 2011. Nutritional Value and Technological Suitability of Milk from Various Animal Species Used for Dairy Production. *Comprehensive Reviews in Food Science and Food Safety*; 10: 291–302.

[3]. Adam, AC, Rubio-Texeira, M, Polaina, J. 2004. Lactose: The milk sugar from a biotechnological perspective. *Critical Reviews in Food Science and Nutrition*; 44: 553–557.

[4]. Urashima, T, Saito, T, Nakamura, T, Messer, M. 2001. Oligosaccharides of milk and colostrum in non-human mammals. *Glycoconjugate Journal*; 185: 357–371.

[5]. Swagerty, DL, Walling, AD, Klein, RM. 2002. Lactose Intolerance. *American Academy of Family Physicians*; 65: 1855–1861.

[6]. Sharp, E, D'Cunha, NM, Ranadheera, CS, Vasiljevic, T, Panagiotakos, DB, Naumovski, N. 2021. Effects of lactose-free and low-lactose dairy on symptoms of gastrointestinal health: A systematic review. *International Dairy Journal*; 114: 104936.

[7]. Harju, M, Patent. 1989. Process for the specific separation of lactose from milk. *US Patent* 4820348A.

[8]. Harju, M, Kallioinen, H, Tossavainen, O. 2012. Lactose hydrolysis and other conversions in dairy products: Technological aspects. *International Dairy Journal*; 22(2): 104-109.

[9]. Dekker, PJT, Koenders, D, Bruins, MJ. 2019 .Lactose-Free Dairy Products: Market Developments, Production, Nutrition and Health Benefits. *Nutrients*; 11(3): 551.

[10]. Tao, N, DePeters, EJ, Freeman, S, German, JB, Grimm, R, Lebrilla, CB. 2008. Bovine milk glycome. *Journal of Dairy Science*. 91(10): 3768–3778.

[11]. Açar, Y, Yassibaş, E. 2021. Anne Sütü Oligosakkaritleri ve Sağlık Üzerine Etkileri. *Gazi Sağlık Bilimleri Dergisi*. 6: 22–33.

[12]. Bode, L. 2015. The functional biology of human milk oligosaccharides. *Early Human Development*. 91: 619–22.

[13]. Wang, B, Yu, B, Karim, M, Hu, H, Sun, Y, McGreevy, P, Petocz, P, Held, S, Brand-Miller, J. 2007. Dietary sialic acid supplementation improves learning and memory in piglets. *American Journal of Clinical Nutrition*. 85(2): 561–569.

[14]. Tarr, AJ, Galley, JD, Fisher, SE, Chichlowski, M, Berg, BM, Bailey, MT. 2015. The prebiotics 3′Sialyllactose and 6′Sialyllactose diminish stressor-induced anxiety-like behavior and colonic microbiota alterations: Evidence for effects on the gut–brain axis. *Brain, Behavior, and Immunity*. 50: 166–177.

[15]. Mudd, AT, Salcedo, J, Alexander, LS, Johnson, SK, Getty, CM, Chichlowski, M, Berg, BM, Barile, D, Dilger, RN. 2016. Porcine Milk Oligosaccharides and Sialic Acid Concentrations Vary Throughout Lactation. *Frontiers in Nutrition*. 3: 39.

[16]. Tao, N, DePeters, EJ, German, JB, Grimm, R, Lebrilla, CB. 2009. Variations in bovine milk oligosaccharides during early and middle lactation stages analyzed by high-performance liquid chromatography-chip/mass spectrometry. *Journal of Dairy Science.* 92(7): 2991–3001.

[17]. Ninonuevo, MR, Park, Y, Yin, H, Zhang, J, Ward, RE, Clowers, BH, German, JB, Freeman, SL, Killeen, K, Grimm, R, Lebrilla, CB. 2006. A strategy for annotating the human milk glycome. *Journal of Agricultural and Food Chemistry.* 54(20): 7471–7480.

[18]. Kirmiz, N, Robinson, RC, Shah, IM, Barile, D, Mills, DA. 2018. Milk Glycans and Their Interaction with the Infant-Gut Microbiota. *Annual Review of Food Science and Technology.* 9: 429-450.

[19]. Kelly, V, Davis, S, Berry, S, Melis, J, Spelman, R, Snell, R, Lehnert, K, Palmer, D. 2013. Rapid, quantitative analysis of 3′- and 6′-sialyllactose in milk by flow-injection analysis–mass spectrometry: Screening of milks for naturally elevated sialyllactose concentration. *Journal of Dairy Science.* 96: 7684–7691.

[20]. Remoroza, CA, Mak, TD, Lorna, M, De Leoz, A, Mirokhin, YA, Stein, SE. 2018. Creating a Mass Spectral Reference Library for Oligosaccharides in Human Milk. *Analytical Chemistry.* 90(15): 8977-8988.

[21]. Mathon, C, Barding, GA, Larive, CK. 2017. Separation of ten phosphorylated mono-and disaccharides using HILIC and ion-pairing interactions. *Analytica Chimica Acta.* 972: 102–110.

[22]. Panseri, S, Pavlovic, R, Castrica, M, Nobile, M, Di Cesare, F, Chiesa, LM. 2021. Determination of carbohydrates in lactose-free dairy products to support food labelling. *Foods.* 10(6): 1219.

[23]. Ilves, A, Harzia, H, Ling, K, Ots, M, Soomets, U, Kilk, K. 2012. Alterations in milk and blood metabolomes during the first months of lactation in dairy cows. *Journal of Dairy Science.* 95(10): 5788–5797.

[24]. Li, J, Jiang, M, Zhou, JR, Ding, J, Guo, Z, Li, M, Ding, F, Chai, W, Yan, J, Liang, X. 2021. Characterization of rat and mouse acidic milk oligosaccharides based on hydrophilic interaction chromatography coupled with electrospray tandem mass spectrometry. *Carbohydrate Polymers.* 259: 117734.

[25]. Cai, Y, Cole, RB. 2002. Stabilization of anionic adducts in negative ion electrospray mass spectrometry. *Analytical Chemistry.* 74(5): 985–991.

[26]. Guan, B, Cole, RB. 2008. MALDI Linear-Field Reflectron TOF Post-Source Decay Analysis of Underivatized Oligosaccharides: Determination of Glycosidic Linkages and Anomeric Configurations Using Anion Attachment. *Journal of the American Society for Mass Spectrometry.* 19(8): 1119–1131.

[27]. Madson, MA. Mass Spectrometry: Techniques for Structural Characterization of Glycans, 1st edn. Elsevier Press: USA, 2016, pp 1-17.

[28]. Araújo, AS, Da Rocha, LL, Tomazela, DM, Sawaya, ACHF, Almeida, RR, Catharino, RR, Eberlin, MN. 2005. Electrospray ionization mass spectrometry fingerprinting of beer. *Analyst.* 130(6): 884–889.

[29]. Moriwaki, H, Hagiwara, A, Takasaki, M, Izumi, F, Watanabe, A, Shimizu, R, Kuribayashi, N, Totani, Y, Suzuki, Y. 2010. Electrospray ionization-mass spectrometric measurement of sake, a traditional japanese alcohol beverage, for characterization. *Analytical Sciences.* 26(3): 379-382.

[30]. Petzold, CJ, Leavell, MD, Leary, JA. 2004. Screening and Identification of Acidic Carbohydrates in Bovine Colostrum by Using Ion/Molecule Reactions and Fourier Transform Ion Cyclotron Resonance Mass Spectrometry: Specificity toward Phosphorylated Complexes. *Analytical Chemistry.* 76(1): 203–210.

[31]. Fong, B, Ma, K, McJarrow, P. 2011. Quantification of bovine milk oligosaccharides using liquid chromatography-selected reaction monitoring-mass spectrometry. *Journal of Agricultural and Food Chemistry.* 59(18): 9788–9795.

[32]. Wheeler, SF, Harvey, DJ. 2000. Negative ion mass spectrometry of sialylated carbohydrates: Discrimination of N-acetylneuraminic acid linkages by MALDI-TOF and ESI-TOF mass spectrometry. *Analytical Chemistry.* 72(20): 5027–5039.

[33]. Chai, W, Piskarev, VE, Mulloy, B, Liu, V, Evans, PG, Osborn, HMI, Lawson, AM. 2006. Analysis of chain and blood group type and branching pattern of sialylated oligosaccharides by negative ion electrospray tandem mass spectrometry. *Analytical Chemistry.* 78(5): 1581–1592.

[34]. Chiavelli, LUR, Galuch, MB, Senes, CER, Maia LC, Lopes TAM, Rufato KB, Santos OO, Visentainer JV. 2022. Validation of UHPLC-MS/MS Method and Measurement Uncertainty Evaluation for Lactose Quantification in Lactose-Free and Regular UHT Milk. *Food Anal. Methods.* 15(5): 1418–1431.

[35]. Trani, A, Gambacorta, G, Loizzo, P, Cassone, A, Fasciano, C, Zambrini, AV, and Faccia, M. 2017. Comparison of HPLC-RI, LC/MS-MS and enzymatic assays for the analysis of residual lactose in lactose-free milk. *Food Chemistry.* 233: 385–390.

[36]. Garballo-Rubio, A, Soto-Chinchilla, J, Moreno, A, and Zafra-Gómez, A. 2018. Determination of residual lactose in lactose-free cow milk by hydrophilic interaction liquid chromatography (HILIC) coupled to tandem mass spectrometry. *Journal of Food Composition and Analysis.* 66: 39–45.

[37]. Rumachik, N, Tian, T, Hou, Y, Saini, C, Cheng, J, Pohl, C, and Liu, Y. 2021. Towards a more complete glycome: Advances in ion chromatography-mass spectrometry (IC-MS) for improved separation and analysis of carbohydrates. *Journal of Chromatography B: Analytical Technologies in the Biomedical and Life Sciences.* 1175.

[38]. Jariyasopit, N, Khamsaeng, S, Panya, A, Vinaisuratern, P, Metem, P, Asawalertpanich, W, Visessanguan, W, Sirivatanauksorn, V, and Khoomrung, S. 2021. Quantitative analysis of nutrient metabolite compositions of retail cow's milk and milk alternatives in Thailand using GC-MS. *Journal of Food Composition and Analysis.* 97: 103785.

[39]. Dantas, A, Verruck, S, Machado Canella, MH, Maran, BM, Murakami, FS, de Avila Junior, LB, de Campos, CEM, Hernandez, E, and Prudencio, ES. 2021. Current knowledge about physical properties of innovative probiotic spray-dried powders produced with lactose-free milk and prebiotics. *LWT.* 151: 112175

[40]. Milkovska-Stamenova, S., and Hoffmann, R. (2016). Hexose-derived glycation sites in processed bovine milk. *Journal of Proteomics.* 134, 102–111

[41]. Weng, WC, Liao, HE, Huang, SP, Tsai, ST, Hsu, HC, Liew, CY, Gannedi, V, Hung, SC, Ni CK. 2022. Unusual free oligosaccharides in human bovine and caprine milk. *Sci Rep.* 12(1):10790.

[42]. Ideo, H, Seko, A, Ohkura, T, Matta, KL, and Yamashita, K. 2002. High-affinity binding of recombinant human galectin-4 to SO3-→3Galβ1-→3GalNAc. *Glycobiology.* 12: 199–208.

Celal Bayar University Journal of Science

Investigating the Effect of Shading on the Capacity Factor of Floating Photovoltaic Systems

Ali Murat Ateş[1*] iD, Osman Salih Yılmaz[2] iD, Fatih Gülgen[3] iD

[1*]Manisa Celal Bayar University, Faculy of Education 45900 Demirci, Manisa, Türkiye
[2]Manisa Celal Bayar University, Demirci Vocational School 45900 Demirci, Manisa, Türkiye
[3] Yıldız Technical University, Faculty of Civil Engineering, 34220 Esenler, İstanbul, Türkiye
* murat.ates@cbu.edu.tr
* Orcid: 0000-0002-2815-1404

Abstract

This study proposes a method to identify the most efficient regions for energy production before installing FPV on any water reservoir. Remote sensing (RS) was used to determine the 20-year area and shoreline changes of the Demirköprü Dam reservoir. The reservoir's annual and monthly total global horizontal irradiance (GHI) values were calculated based on 20 years of observations using a geographic information system (GIS) solar analysis tool. The regional theoretical capacity factor (RTCF) proposed in this study was modelled using total annual GHI values. The water surface was divided into four regions using RTCFs. 94.97%, 4.92%, 0.08% and 0.02% of the total water surface area were classified as RTCF21, RTCF20, RTCF19 and RTCF18, respectively. The annual electrical energy potentials per unit for each RTCF were calculated. The novel method developed in this study for determining the optimum location of FPV SPPs to be installed on water surfaces reveals the importance of evaluating land topography and considering annual shading patterns.

Keywords: Floating photovoltaic, geographical information system, regional theoretical capacity factor, remote sensing, solar analysis

1. Introduction

Photovoltaic (PV) solar power plants (SPPs) that convert solar energy into electrical energy are widely used in many countries. PV systems started to be used intensively in rural areas where electricity grid problems were experienced at first. However, recently, it has been frequently used to reduce economic costs and carbon emissions by supporting the electricity needed with solar energy. Even though their efficiency has increased with the new techniques developed recently, PV modules still work with around 20% efficiency. This shows that large areas are needed to install solar power plants.

Recent studies and practical applications show that solar panels are often installed on marginal agricultural lands, building facades, roofs, lakes, dams, canals, and offshore areas. Soil is an indispensable resource for humanity. Even if it has lost its ability to be cultivated, it can be used as settlement, forestation, or pasture.

Land occupation by PV SPPs causes land prices to rise sharply, especially in high-density urban residential areas. This adds additional costs to PV systems. On the other hand, installing PV modules on building roofs or façades may not always give the desired result due to the shading of surrounding buildings or objects such as trees. Using broad water surfaces to install PV systems has emerged as a new concept when all these factors are considered together.

FPV technology was first commissioned in Aichi, Japan, in 2007, with a capacity of 20 MW to facilitate research on solar power generation on water surfaces [1]. Rapidly increasing FPV SPPs worldwide have applications in countries such as China, India, the Republic of Korea, and Brazil [2]. One of the reasons for the rapid spread of FPV SPPs is the cooling effect of evaporating water. A decrease in module temperature can increase system efficiency and the amount of energy produced [3]. [4] observed that the front temperature of the FPV modules is 2–4% lower and the back

temperature is 5–11% lower compared to similar On Ground PV modules. Since FPV systems create shade on the water surface, the evaporation rate of the water is lowered by approximately 25–70% [5]. In addition to these advantages, FPV plants installed on freshwater surfaces also increase water quality by reducing algae growth and preventing eutrophication [6]. Due to all these advantages, the installed capacity of FPV in the world is growing exponentially every year.

Dam reservoirs, one of the surfaces where FPV systems can be installed, are a reliable water source for various applications. Water reservoirs generally have optimal conditions for FPV installation, such as constant water inlet and outlet, optimum temperature, and water availability for cleaning the modules [7]. In addition, the intermittent operation of the equivalent FPV system to meet the energy demand reduces the pressure on the power turbines in the hydroelectric power plant by removing some or all of the electricity generation load [1]. FPV systems are seen as an alternative that addresses increasing energy demand and contributes to the generation capacity of the existing hydroelectric power plants where they are installed without requiring additional land costs [8], [9].

The installation of FPVs should be planned considering the water dynamics of the region. Remote sensing (RS) offers the opportunity to rapidly and cost-effectively identify changes in reservoir size resulting from seasonal influences, agricultural irrigation, and power generation processes [10]. It is possible to determine the shoreline of a large dam reservoir's surface using medium-resolution images from free satellites such as Landsat and Sentinel [11]. The cloud-based Google Earth Engine (GEE) platform has been highly preferred recently. Google developed GEE to map human settlements in large areas, analyze past changes, and constantly update current estimates [12]. GEE can provide easy and simultaneous access to all archives of Landsat and Sentinel images. GEE, through its application program interface (API), allows development with JavaScript and Python coding languages and the ability to access and apply petabyte-scale data [13].

Regardless of the PV systems' surface installed, the most crucial parameter is the amount of total radiation falling on the module surface. Therefore, it is essential to evaluate solar sources by analyzing and predicting the spatiotemporal distribution of solar radiation [14]. In this planning, the slope of the modules, reflections, and shadows from the environment are the criteria to be considered separately. GIS, which includes spatial analysis and query methods, offers various tools such as Hillshade and Solar analysis for calculating shading. The solar radiation value can be calculated for a specific geographic location in certain periods using solar analysis tools that consider the shading effect [15].

Topographic factors such as height differences and slope changes that make up the land surface shapes in the region are the main factors used in calculating the shading effect and the amount of total solar radiation on the surface.

Many studies in the literature consider shading in the installation of PV SPPs in rural areas and on rooftop surfaces using GIS and RS techniques together. Some studies have focused on the three-dimensional modelling of roofs for appropriate placement of PV modules [16]–[18]. Several studies employed three-dimensional models using light detection and ranging (LIDAR) data, and the shading effect and other factors were evaluated together [19], [20]. In addition, digital surface models (DSMs) have been used to calculate the shading effects caused by the topography of the land [21], [22]. Some studies aimed to determine appropriate locations for PV SPP installation using GIS [23]–[25]. However, few studies have investigated the effects of shading on water surfaces for FPV system installation. [26] performed shading analysis using a fish-eye lens camera and a digital elevation model (DEM) in a mining lake in Korea. [27] suggested using RS and GIS techniques to increase the efficiency of FPV projects. [28] considered the shading effect of artificial elements around a lake in India on a 2 MW FPV system installed on the water surface. Determining the boundaries of the water surface on which an FPV-SPP will be installed to pinpoint the region with the highest efficiency is crucial for researchers and investors.

Revealing temporal changes to energy demands is critical to determining the renewable energy supply cost and calculating the capacity factor [29]. The capacity factor is an important indicator used in determining PV system performance. The capacity factor is the ratio of energy generated by a system over a given time to the energy generated by operating at nominal power for 24 hours a day [30]. In recent years, the trend toward electricity generation from wind and solar energy increased due to the developing technology and increasing capacity factors [31]. Capacity factors in coal, geothermal, hydroelectric, oil, natural gas, wind, and solar power plants used for electrical energy generation are 73%, 58%, 56%, 54%, 44%, 33%, and 20%, respectively [32]. This clearly shows how installing solar power plants, which produce at the lowest capacity factor than other systems, in proper areas can benefit the system's profitability.

This study proposes a novel method for projecting the energy to be obtained from FPV panels installed on the surface of a dam's reservoir. The developed method reveals the potential benefits of using RS and GIS technologies in solar resource assessment. The 20-year images of satellites are processed to determine the reservoir's shorelines properly. The GIS solar analysis tool offers the energy potential over the water surface.

The effect of shading on the capacity factor is assessed by calculating annual and monthly total irradiance per m^2 on the horizontal surface of the regions classified within the shorelines. The developed method results show that topographic factors around the planned area that cause shading effects must be considered before installing FPVs on water surfaces.

2. Study Area

The Köprübaşı district of Manisa Province, Turkey, where the Demirköprü Dam is located, is a rural area where people make their living from agriculture and animal husbandry.

The Demirköprü Dam was built between 1954 and 1960 for electricity generation, flood control, and agricultural irrigation (Figure 1). The Dam's volume, which is the earth-fill type, is approximately 4,300,000 m^3. The average water level volume is 1,320 hm^3. The reservoir surface area is about 3,000 ha depending on electricity generation, irrigation, and seasonal variables. The hydroelectric power plant, which has an installed power capacity of 69 MW, generates 193 GWh of electrical energy per year. It also provides irrigation services to an area of 99,220 ha.
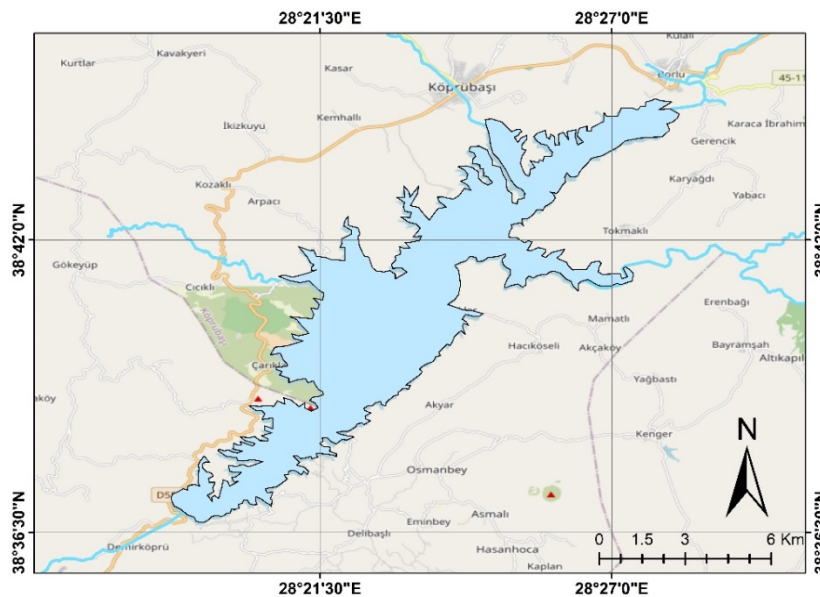
Figure 1. Location of the study area.

3. Method
3.1 Image Processing Method

Various algorithms and indices are used for image processing. Two basic approaches to classifying satellite images are supervised and unsupervised classification techniques. Classification approaches can be listed as pixel-based classification, sub-pixel classification, area-based classification, and object-based classification. Water surfaces can be differentiated from other details using pixel-based supervised classification algorithms and various extraction indices. The random forest (RF) algorithm and the normalized difference water index (NDWI) are examples of the algorithms and indices used herein. [33] applied maximum likelihood classification (MLC) and RF algorithms using Sentinel-2 (MSI) satellite images of the Demirköprü Dam in Turkey. Each algorithm used was tested separately on Sentinel-2 (MSI) images with visible (VIS) + infra-red band (NIR), normalized difference water index (NDWI), and modified normalized difference water index (MNDWI). The obtained images were compared

with producer's accuracy (PA), user's accuracy (UA), overall accuracy (OA), and Kappa statistics testing. As a result of comparisons based on classification accuracies, it was concluded that the RF algorithm performs better than the MLC algorithm for the Demirköprü Dam's reservoir.

In recent years, RF has been widely used in many fields such as medicine, economy and geography. [34] proposed RF, which changes the way a classification or regression tree is constructed. It has been proven to outperform many algorithms such as Support vector machine, k-nearest neighbours, and maximum likelihood classification, which make predictions by creating forests from RF decision trees [35]–[37].

[38] derived the Demirköprü Dam shoreline using the RF algorithm and NDWI water extraction indices (Eq. 3.1) on the GEE platform.

$$NDWI = (\rho_{Green} - \rho_{NIR})/(\rho_{Green} + \rho_{NIR}) \qquad \textbf{(3.1)}$$

A. M. Ateş

3.2 Insolation Map Creation Method

Topography is an essential factor in determining the amount of solar energy falling on any surface on Earth. Solar radiation is affected by topographic factors such as elevation, aspect, slope, and shading. The spatial analyst tool provided by ArcGIS enables analysis of the total amount of radiation that falls on any surface on Earth over a given period. The ability to calculate the amount of radiation falling on the Dam's water surface provides excellent convenience in calculating the annual energy production and capacity factor of the FPV plant to be installed thereon. In this study, ArcGIS solar radiation tool was preferred to calculate the amount of solar radiation. The data obtained from the digital elevation model (DEM) of the 30-meter spatial resolution shuttle radar topography mission (SRTM) was used as the elevation model.

Although there are standard parameters in the solar Analysis tool, it is necessary to make some changes in the parameters depending on the atmospheric conditions. This tool's parameters were calibrated in this study considering the radiation data provided by PVGIS software, Era-5 and Merra-2 satellites according to the region's location. Topographic and radiation parameters are shown in Table 1.

Table 1. Solar radiation parameters used in this study.

Topographic parameters	
Z factor	1
Calculation directions	DEM
Calculation direction	16
Radiation parameters	
Zenith divisions	8
Azimuth divisions	8
Diffuse model type	Standard overcast sky
Diffuse Proportion	0.5
Transmittivity	0.5

3.3 Regional Theoretical Capacity Factor Calculation Method

The capacity factor is calculated using equation 3.2 as the ratio of the energy generated by the system in one year to the total energy generated if operating at full capacity, according to IEC 61724 [39].

$$CF = \frac{E_G}{24 * 365 * P_R} \qquad (3.2)$$

where CF is the capacity factor, E_G is the annual energy generated by the system, and P_R is the rated output power of the system.

The output power of a PV module depends on the incident solar radiation on its surface and the PV cell temperature. PV modules operate at rated power under standard test conditions (STC: 1000 W/m^2 irradiance, 25°C ambient temperature, and 1.5 air mass). The module output power shows a positive correlation with the total solar radiation falling on its surface and a negative correlation with the cell temperature. PV module output power depending on cell temperature and solar radiation is calculated as shown in equation 3.3 [40].

$$P_{PV} = P_R \left(\frac{I_t}{I_{STC}}\right)[1 - \alpha_T(T_{Cell} - T_{STC})] \qquad (3.3)$$

where P_{PV} is module output power, P_R is rated power of the module, I_t is instantaneous total (direct + diffuse + reflected) solar radiation on the module surface, α_T is PV module temperature coefficient of power, and T_c is cell temperature. Since the α_T value in the equation usually has a too low value of 0.04%/°C, it can be ignored in practice; in this case, the temperature-independent output power of the module is calculated using equation 3.4.

$$P_{PV} = P_R \left(\frac{I_t}{I_{STC}}\right) \qquad (3.4)$$

Because the total amount of hourly radiation in an area of 1 m^2 at any location on Earth is shown as GHI (Wh/m^2), the total amount of annual radiation (GHI_a) falling in this area is calculated with equation 3.5.

$$GHI_a = \sum_{day=1}^{365} \sum_{hour=1}^{24} GHI_{(day,hour)} \qquad (3.5)$$

The annual electrical energy generated by a horizontally positioned module is calculated with equation 3.6.

$$E_G = P_R \left(\frac{GHI_a}{I_{STC}}\right) \qquad (3.6)$$

Accordingly, it can be said that the amount of energy generated by a horizontally positioned PV module in any region is directly related to the GHI in that region. Based on this, the capacity factor of the PV system can be calculated with the local GHI. When equation 3.6 and equation 1 are summed together, equation 3.7 is obtained.

$$CF = \frac{E_G}{24 * 365 * P_R} = \frac{P_R\left(\frac{GHI_a}{I_{STC}}\right)}{8760 * P_R} \qquad (3.7)$$

When the necessary simplifications are made in the equation, it is seen that the capacity factor of the PV-SPP to be installed in a horizontal position in a region is directly related to the GHI in that region.

In this case, to express the highest possible capacity factor of an SPP to be installed in a horizontal position in an area, the concept of regional theoretical capacity factor (RTCF) can be used; the RTCF of a region can be calculated with the equation 3.8.

$$RTCF = \frac{GHI_a}{8760 * I_{STC}} \qquad (3.8)$$

Using the annual total GHI values calculated with the ArcGIS solar analysis tool, the RTCF value of each pixel was calculated. The RTCF map of the water surface was created by reclassifying the calculated RTCF values to correspond to integer numbers. The area of each region on the reclassified map and the

average amount of the annual total GHI were calculated with ArcGIS software.

3.4 Floating Photovoltaic System Design

Although many methods are used as flotation elements in floating photovoltaic systems, the most accepted materials in the literature are high-density polyethylene (HDPE) materials [27]. In this study, the PV modules were horizontally placed on flotation elements made of HDPE material with an interlocking structure. Between strings of 2 × 20 modules, one-meter pathways were left for module cleaning, assembly of string inverters, maintenance, and easy intervention in case of malfunction. Each SPP consisting of 40 PV modules and a 12 kWp string inverter, covers an area of 91.84 m^2 (Figure 2).
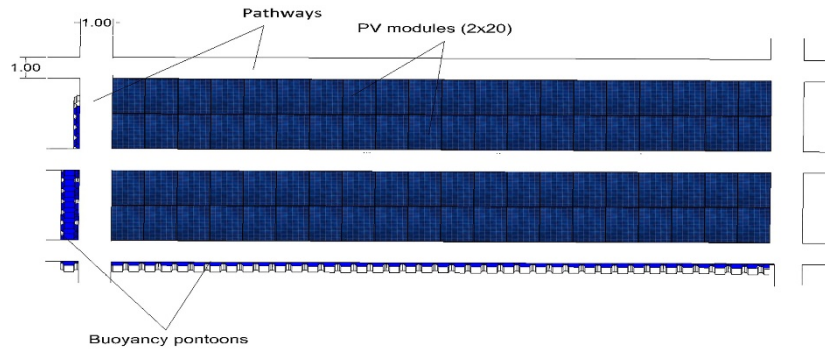
Figure 2. Designed FPV system.

The efficiency of the monocrystalline Axitec AC300M / 156-60S 300 W PV module used in the system is 18.44%, the temperature coefficient of Pmax is 0.42%/°C, and the module dimensions are 1640 × 992 mm. The maximum efficiency of the Huawei SUN 2000-12 KTL 12 kWp 3-phase string inverter is 98.5%, and the maximum number of power point trackers is 2.

3.5 Calculation of Annual Generated Electrical Energy

Total area and average annual total irradiance values in the region within the boundaries of each RTCF generated as a result of reclassification were calculated. The electrical energy potential generated from each RTCF region is calculated using equation 3.9 [41].

$$EGP_{RTCF} = A_{RTCF} . R_{GHI} . AF . \eta_{PV} \qquad (3.9)$$

where EGP_{RTCF} (GWh) is the energy potential that can be generated from an RTCF zone, A_{RTCF} (m^2) is the total area of the zone, R_{GHI} (GWh/m^2) is the average annual total GHI value per square meter in each region, AF (%) is the area factor, and η_{PV} (%) is the efficiency of the PV system. The AF in the formula is calculated by the ratio of total module surface area (A_{PV}) on the designed platform to the platform area (A_P) (Eq 3.10).

$$AF = \frac{A_{PV}}{A_P} \qquad (3.10)$$

The efficiency of the PV GES system is calculated by multiplying the efficiency of all components in the system (Eq 3.11).

$$\eta_{sys} = \eta_m . \eta_{cable} . \eta_{inv} . \eta_T . (1 - Losses) \qquad (3.11)$$

η_m = module efficiency (18.44% from manufacturer's datasheet)
η_{cable} = cable and junction box efficiencies (99.4%) [42]
η_{inv} = average inverter efficiency (98%)
η_T = transformer efficiency (97%) [42]
$Losses$ = total losses (7% temperature, low irradiance, and others)

4. Results
4.1 Satellite classification

The lowest water surface area reported of the Demirköprü Dam's reservoir was 1,562.45 ha by [38] (Figure 3).

A. M. Ateş
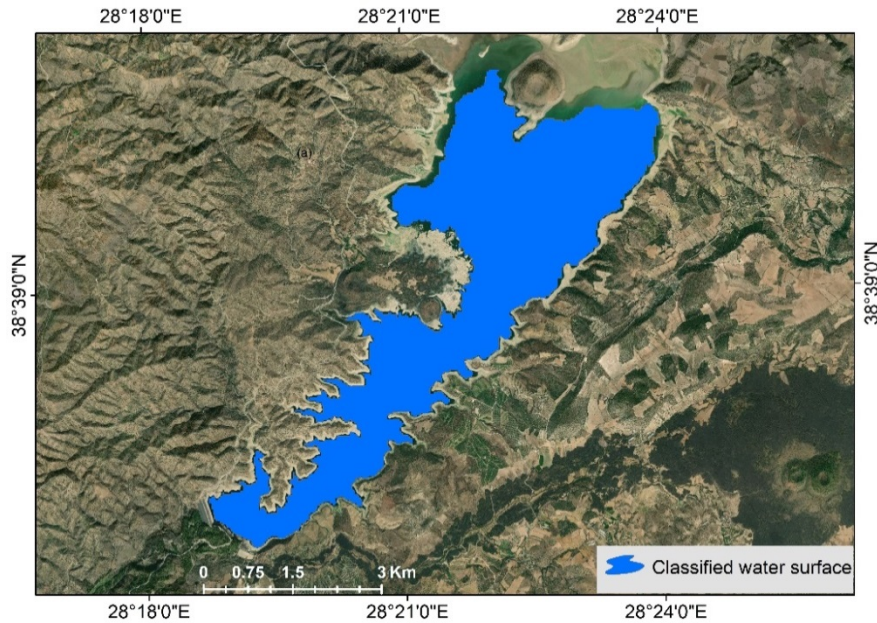
Figure 3. Lowest water surface.

The 10 m spatial resolution Sentinel satellite image dated 02.09.2018, the day when the water surface area was the lowest, was classified with RS and the islands detected on the water surface were marked with a red ellipse (Figure 4). The total area of the islands, consisting of sharp rocks, was calculated as 0.91 ha. The islands emerge in August and September when the water level is low and disappear in February and March when the water level rises. Since the FPV SPP systems to be installed in this area would be damaged by receding water levels, the design must take these rocky islands into account.
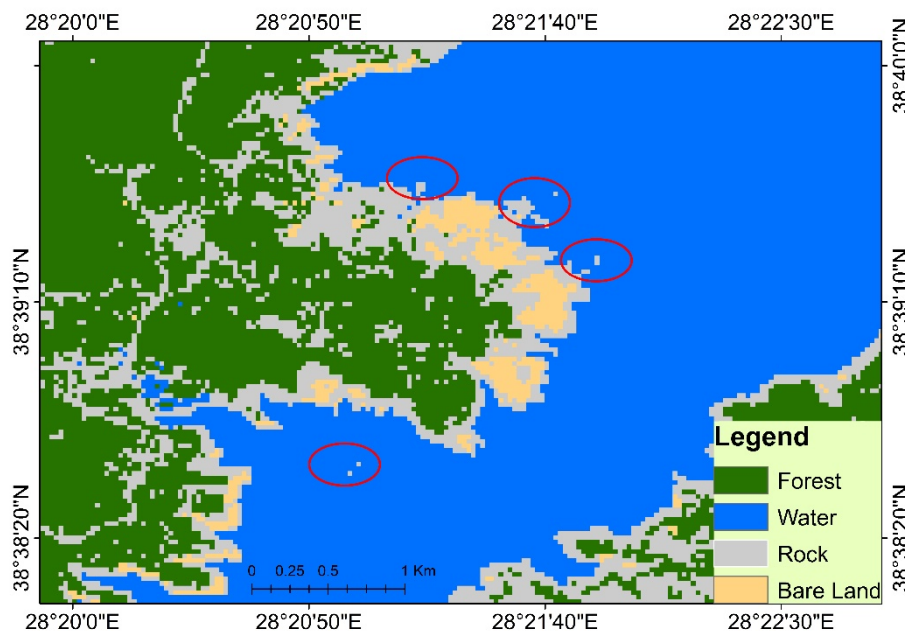
Figure 4. Islands composed of rock.

4.2 Regional Theoretical Capacity Factors

The total annual GHI for 2020 was calculated for each pixel in the area of the lowest water level in the Demirköprü Dam reservoir. The lowest and highest total annual GHIs calculated on the water surface were 1,553.96 kWh/m^2 and 1,875.25 kWh/m^2, respectively. In these GHI intervals, RTCF values were found to vary between 18% and 21%, and a class was created for each percentage. The minimum, maximum, and average values of total annual GHI for each RTCF class are shown in Table 2.

314

A. M. Ateş

Table 2. RTCF classes and minimum, maximum, and average values of total annual GHI.

Zone	RTCF21	RTCF20	RTCF19	RTCF18
RTCF (%)	21	20	19	18
GHI Range (kWh/m²-year)	1795.80 1875.25	1708.74 1795.79	1633.15 1705.68	1553.96 1606.82
Average of Regional Annual Total GHI (kWh/m²-year)	1798.36	1790.85	1678.54	1576.19
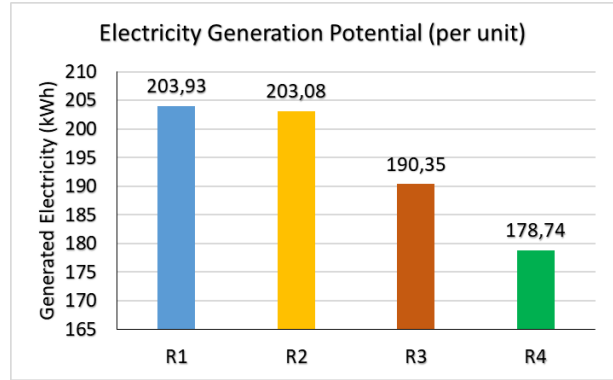
Figure 5. The potential electrical energy generated from an area of 1m² in each region.
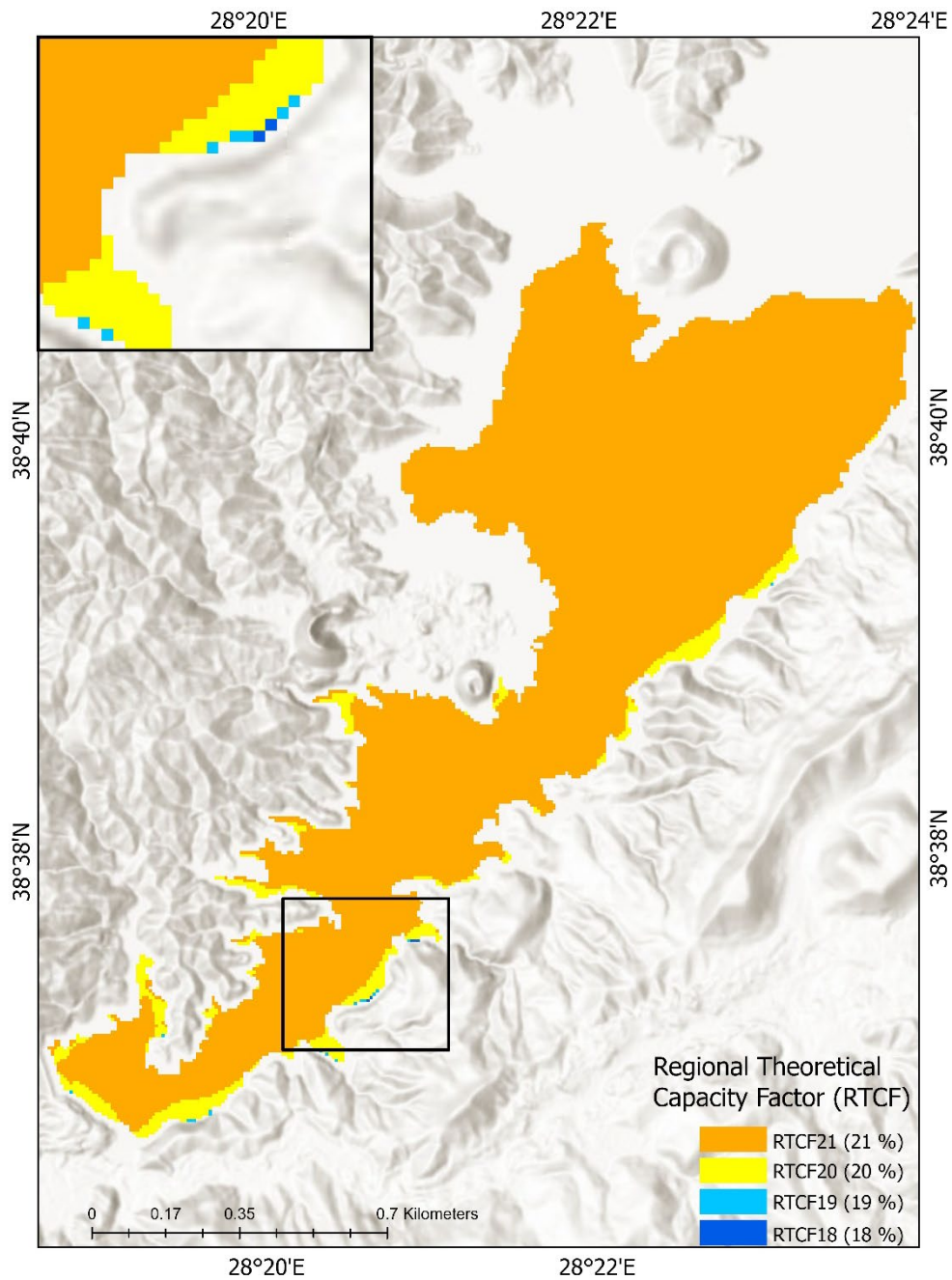
Figure 6. RTCF map.

The Table 2 shows that the average regional total annual GHI values of RTCF21 and RTCF20 are very similar, but RTCF19 and RTCF18 are lower by about 220 kWh/m^2 than RTCF21.

The total efficiency (η_{sys}) of the FPV system to be installed on the reservoir's surface was calculated as 16.20% using equation 11, and the area factor (AF) value of the designed floating platform was 0.7 using equation 10. Under these conditions, the potential annual electricity generation of 1 m^2 unit surface in each region was calculated and is shown in Figure 5.

According to the graph, while the potential of generating electricity from solar energy on the unit surface is above 200 kWh/year in RTCF21 and RTCF20 regions, it is 190 kWh/year in RTCF19 and 178 kWh/year in RTCF18. According to these values, RTCF21 and RTCF20 were more efficient for FPV installation than in the other regions.

The regional theoretical capacity factor map obtained using the four RTCF regions detected on the water surface is given in Figure 6.

As noted in Figure 4, a massive part of the water surface is classified as having an RTCF value of 21%. In areas close to the reservoir's shoreline, the RTCF value decreases to 20%. RTCF values of 19% and 18% were observed in a small area in the southern parts of the reservoir. The surface areas of each region were calculated with ArcGIS software. The small islands with an area of 0.91 ha determined in Figure 4 were subtracted from the total size of RTCF21. The total area of each region was multiplied by the region's potential electricity generation, and each region's real electricity generation potential was calculated and shown in Table 3.

Table 3. Area of regions.

Zone	Area (ha)	EGP (GWh)
RTCF21	1,482.95	3,024.24
RTCF20	76.9	156.17
RTCF19	1.3	2.47
RTCF18	0.38	0.68
Total	1,561.53	3,183.57

Monthly minimum, maximum, and average distributions of total annual GHI values calculated for each region are given in Table 4.

In January, when total radiation was lowest, the regional average monthly GHI values in RTCF21, RTCF20, RTCF19, and RTCF18 regions were calculated as 57.29 kWh/m^2, 56.80 kWh/m^2, 46.77 kWh/m^2, and 40.41 kWh/m^2, respectively. In July, at the highest radiation,

Table 4. Regional averages of monthly total GHI (kWh/m^2)

GHI		Regions			
		RTCF 21	RTCF 20	RTCF 19	RTCF 18
Jan.	Min	57.03	40.58	36.14	35.91
	Max	65.46	57.70	51.32	45.01
	Avg.	57.29	56.80	46.77	40.41
Feb.	Min	95.46	87.79	81.27	75.98
	Max	104.87	95.82	90.99	80.29
	Avg.	95.70	95.13	85.75	77.59
Mar.	Min	152.47	142.97	135.02	129.16
	Max	162.64	152.55	148.77	133.41
	Avg.	152.77	152.04	141.21	130.75
Apr.	Min	170.02	162.09	154.94	149.60
	Max	177.10	170.11	167.06	152.77
	Avg.	170.26	169.66	160.42	150.79
May	Min	203.36	201.65	194.90	190.62
	Max	210.74	207.81	204.22	192.43
	Avg.	207.94	207.39	199.70	191.33
Jun.	Min	206.43	208.75	202.40	199.28
	Max	214.83	213.60	209.96	200.16
	Avg.	213.73	213.21	206.87	199.75
Jul.	Min	239.06	241.09	233.71	229.62
	Max	249.23	247.21	241.96	231.02
	Avg.	247.43	246.70	238.71	230.22
Aug.	Min	213.78	207.91	200.39	194.61
	Max	221.62	216.08	211.38	197.43
	Avg.	216.30	215.54	205.76	195.67
Sep.	Min	161.82	152.63	144.87	139.04
	Max	171.07	161.86	158.12	143.11
	Avg.	162.07	161.36	150.87	140.57
Oct.	Min	113.28	104.63	97.27	91.60
	Max	123.63	113.54	109.23	96.16
	Avg.	113.53	112.88	102.67	93.32
Nov.	Min	88.58	76.13	69.82	68.18
	Max	96.74	88.91	82.03	75.11
	Avg.	88.92	88.30	78.23	71.63
Dec.	Min	71.87	50.77	50.14	50.27
	Max	79.33	72.46	66.47	59.91
	Avg.	72.42	71.83	61.58	54.15

these values were 247.43 kWh/m^2, 246.70 kWh/m^2, 238.71 kWh/m^2, and 230.22 kWh/m^2, respectively. This situation is related to the climatic conditions in the area. The lowest monthly total GHI value in RTCF21 was 71.87 kWh/m^2 in December, when the sun's altitude

angle (α) was the lowest, while it was 50.27 kWh/m^2 in RTCF18. In June, when the α angle was highest, the lowest monthly total GHI values in RTCF21 and RTCF18 regions were 206.43 kWh/m^2 and 199.28 kWh/m^2, respectively. It was observed that the difference between RTCF21 and RTCF18 in December was 21.60 kWh/m^2 and 7.14 kWh/m^2 in June. The monthly total GHI loss in the RTCF18 region due to shading was calculated as 30% in December and 4% in June. The effect of topography and α angle on the shading on the water surface, and thus on total GHI, is higher in the winter due to the lower α angle and lower in summer due to the higher α angle.

5. Conclusion

This study proposes a new method considering the importance of land topography and shading to determine the optimum location of FPV SPPs installed on water surfaces. The shading effect of the land topography on the water surface was carried out with the solar analysis tool using the DEM data of the land. As a result of the research, the annual and monthly total GHI values of each pixel in the satellite images were calculated. It has been observed that the RTCF values of the areas on the water surface vary between 18% and 21%.

Demirköprü Dam was chosen as the pilot area in this study. It is seen that the shoreline of the study area is shallow, and there are no high hills around it. Therefore, it was observed that the capacity factor decreased only in a tiny place with ridges on the south side. Total monthly GHI analysis was performed with the ArcGIS solar analysis tool to reveal the effect of the land topography and the sun's elevation angle (α) on shading and total annual GHI. The difference between the lowest GHI values of the RTCF21 and RTCF18 regions indicates that the monthly total GHI loss due to shading in the RTCF18 region was 30% in December and 4% in June.

In this study area, where the coastline is shallow, the shading effect of the topography is clearly visible. In addition, it is understood that the shading effect will be much more significant in the topography, where the terrain is wavy. The necessity of investigating the shading effect on water surfaces as well as in terrestrial systems has been demonstrated by this study. In this study, the horizontal variation of the water surface is considered, but it is recommended to investigate the effect of the vertical variation of the water on the shading.

Acknowledgement

Author's Contributions

Ali Murat Ateş: Drafted and wrote the energy analysis part and determined the simulation parameters. Assisted in the result interpretation and helped in manuscript preparation.
Osman Salih Yilmaz: Drafted and wrote the RS and GIS parts. He did the simulation. Assisted in the result interpretation and helped in manuscript preparation.
Fatih Gulgen: Planned and managed the RS and GIS parts. Assisted in the result interpretation and helped in manuscript preparation.

Ethics

There are no ethical issues after the publication of this manuscript.

References

[1]. R. Nagananthini and R. Nagavinothini, "Investigation on floating photovoltaic covering system in rural Indian reservoir to minimize evaporation loss," *Int. J. Sustain. Energy*, vol. 40, no. 8, pp. 781–805, Sep. 2021, doi: 10.1080/14786451.2020.1870975.

[2]. M. Tina, F. Bontempo Scavo, L. Merlo, and F. Bizzarri, "Analysis of water environment on the performances of floating photovoltaic plants," *Renew. Energy*, vol. 175, pp. 281–295, 2021, doi: 10.1016/j.renene.2021.04.082.

[3]. G. Mamatha and P. S. Kulkarni, "Assessment of floating solar photovoltaic potential in India's existing hydropower reservoirs," *Energy Sustain. Dev.*, vol. 69, pp. 64–76, Aug. 2022, doi: 10.1016/j.esd.2022.05.011.

[4]. H. Nisar, A. Kashif Janjua, H. Hafeez, S. Shakir, N. Shahzad, and A. Waqas, "Thermal and electrical performance of solar floating PV system compared to on-ground PV system-an experimental investigation," *Sol. Energy*, vol. 241, no. March, pp. 231–247, Jul. 2022, doi: 10.1016/j.solener.2022.05.062.

[5]. A. El Hammoumi, A. Chalh, A. Allouhi, S. Motahhir, A. El Ghzizal, and A. Derouich, "Design and construction of a test bench to investigate the potential of floating PV systems," *J. Clean. Prod.*, vol. 278, p. 123917, 2021, doi: 10.1016/j.jclepro.2020.123917.

[6]. R. Claus and M. López, "Key issues in the design of floating photovoltaic structures for the marine environment," *Renew. Sustain. Energy Rev.*, vol. 164, no. March, p. 112502, Aug. 2022, doi: 10.1016/j.rser.2022.112502.

[7]. H. Rauf, M. S. Gull, and N. Arshad, "Integrating Floating Solar PV with Hydroelectric Power Plant: Analysis of Ghazi Barotha Reservoir in Pakistan," *Energy Procedia*, vol. 158, pp. 816–821, Feb. 2019, doi: 10.1016/j.egypro.2019.01.214.

[8]. I. S. Rodrigues, G. L. B. Ramalho, and P. H. A. Medeiros, "Potential of floating photovoltaic plant in a tropical reservoir in Brazil," *J. Environ. Plan. Manag.*, vol. 63, no. 13, pp. 2334–2356, 2020, doi: 10.1080/09640568.2020.1719824.

[9]. S. Sulaeman, E. Brown, R. Quispe-Abad, and N. Müller, "Floating PV system as an alternative pathway to the amazon dam underproduction," *Renew. Sustain. Energy Rev.*, vol. 135, no. July 2020, p. 110082, Jan. 2021, doi: 10.1016/j.rser.2020.110082.

[10]. M. Arekhi, C. Goksel, F. Balik Sanli, and G. Senel, "Comparative Evaluation of the Spectral and Spatial Consistency of Sentinel-2 and Landsat-8 OLI Data for Igneada Longos Forest," *ISPRS Int. J. Geo-Information*, vol. 8, no. 2, p. 56, 2019, doi: 10.3390/ijgi8020056.

[11]. X. Yang, S. Zhao, X. Qin, N. Zhao, and L. Liang, "Mapping of urban surface water bodies from sentinel-2 MSI imagery at 10 m resolution via NDWI-based image sharpening," *Remote Sens.*, vol. 9, no. 6, pp. 1–19, 2017, doi: 10.3390/rs9060596.

[12]. N. N. Patel *et al.*, "Multitemporal settlement and population mapping from Landsat using Google Earth Engine," *Int. J. Appl. Earth Obs. Geoinf.*, vol. 35, no. PB, pp. 199–208, Mar. 2015, doi: 10.1016/j.jag.2014.09.005.

[13]. R. Goldblatt, W. You, G. Hanson, and A. Khandelwal, "Detecting the Boundaries of Urban Areas in India: A Dataset for Pixel-Based Image Classification in Google Earth Engine," *Remote Sens.*, vol. 8, no. 8, p. 634, Aug. 2016, doi: 10.3390/rs8080634.

[14]. Y. Choi, "Solar Power System Planning and Design," *Appl. Sci.*, vol. 10, no. 1, p. 367, Jan. 2020, doi: 10.3390/app10010367.

[15]. Y. Charabi and A. Gastli, "GIS assessment of large CSP plant in Duqum, Oman," *Renew. Sustain. Energy Rev.*, vol. 14, no. 2, pp. 835–841, 2010.

[16]. H. Jiang *et al.*, "Geospatial assessment of rooftop solar photovoltaic potential using multi-source remote sensing data," *Energy AI*, vol. 10, no. July, p. 100185, Nov. 2022, doi: 10.1016/j.egyai.2022.100185.

[17]. S. Lin *et al.*, "Accurate Recognition of Building Rooftops and Assessment of Long-Term Carbon Emission Reduction from Rooftop Solar Photovoltaic Systems Fusing GF-2 and Multi-Source Data," *Remote Sens.*, vol. 14, no. 3144, Jun. 2022, doi: 10.3390/rs14133144.

[18]. B. Chen, Y. Che, J. Wang, H. Li, L. Yu, and D. Wang, "An estimation framework of regional rooftop photovoltaic potential based on satellite remote sensing images," *Glob. Energy Interconnect.*, vol. 5, no. 3, pp. 281–292, Jun. 2022, doi: 10.1016/j.gloei.2022.06.006.

[19]. X. Huang, K. Hayashi, T. Matsumoto, L. Tao, Y. Huang, and Y. Tomino, "Estimation of Rooftop Solar Power Potential by Comparing Solar Radiation Data and Remote Sensing Data—A Case Study in Aichi, Japan," *Remote Sens.*, vol. 14, no. 1742, Apr. 2022, doi: 10.3390/rs14071742.

[20]. V. Stack and L. L. Narine, "Sustainability at Auburn University: Assessing Rooftop Solar Energy Potential for Electricity Generation with Remote Sensing and GIS in a Southern US Campus," *Sustainability*, vol. 14, no. 626, Jan. 2022, doi: 10.3390/su14020626.

[21]. L. Romero Rodríguez, E. Duminil, J. Sánchez Ramos, and U. Eicker, "Assessment of the photovoltaic potential at urban level based on 3D city models: A case study and new methodological approach," *Sol. Energy*, vol. 146, pp. 264–275, 2017, doi: 10.1016/j.solener.2017.02.043.

[22]. M. Aslani and S. Seipel, "Automatic identification of utilizable rooftop areas in digital surface models for photovoltaics potential assessment," *Appl. Energy*, vol. 306, no. 118033, Jan. 2022, doi: 10.1016/j.apenergy.2021.118033.

[23]. Villacreses, J. Martínez-Gómez, D. Jijón, and M. Cordovez, "Geolocation of photovoltaic farms using Geographic Information Systems (GIS) with Multiple-criteria decision-making (MCDM) methods: Case of the Ecuadorian energy regulation," *Energy Reports*, vol. 8, pp. 3526–3548, Nov. 2022, doi: 10.1016/j.egyr.2022.02.152.

[24]. B. Elboshy, M. Alwetaishi, R. M. H. Aly, and A. S. Zalhaf, "A suitability mapping for the PV solar farms in Egypt based on GIS-AHP to optimize multi-criteria feasibility," *Ain Shams Eng. J.*, vol. 13,

no. 101618, May 2022, doi: 10.1016/j.asej.2021.10.013.

[25]. S. Zambrano-Asanza, J. Quiros-Tortos, and J. F. Franco, "Optimal site selection for photovoltaic power plants using a GIS-based multi-criteria decision making and spatial overlay with electric load," *Renew. Sustain. Energy Rev.*, vol. 143, no. 110853, Jun. 2021, doi: 10.1016/j.rser.2021.110853.

[26]. J. Song and Y. Choi, "Analysis of the Potential for Use of Floating Photovoltaic Systems on Mine Pit Lakes: Case Study at the Ssangyong Open-Pit Limestone Mine in Korea," *Energies*, vol. 9, no. 2, p. 102, Feb. 2016, doi: 10.3390/en9020102.

[27]. A. Sahu, N. Yadav, and K. Sudhakar, "Floating photovoltaic power plant: A review," *Renew. Sustain. Energy Rev.*, vol. 66, pp. 815–824, 2016, doi: 10.1016/j.rser.2016.08.051.

[28]. M. Abid, Z. Abid, J. Sagin, R. Murtaza, D. Sarbassov, and M. Shabbir, "Prospects of floating photovoltaic technology and its implementation in Central and South Asian Countries," *Int. J. Environ. Sci. Technol.*, vol. 16, no. 3, pp. 1755–1762, Mar. 2019, doi: 10.1007/s13762-018-2080-5.

[29]. N. Mattsson, V. Verendel, F. Hedenus, and L. Reichenberg, "An autopilot for energy models – Automatic generation of renewable supply curves, hourly capacity factors and hourly synthetic electricity demand for arbitrary world regions," *Energy Strateg. Rev.*, vol. 33, p. 100606, Jan. 2021, doi: 10.1016/j.esr.2020.100606.

[30]. A. Goswami and P. K. Sadhu, "Degradation analysis and the impacts on feasibility study of floating solar photovoltaic systems," *Sustain. Energy, Grids Networks*, vol. 26, p. 100425, 2021, doi: 10.1016/j.segan.2020.100425.

[31]. P. A. Adedeji, S. A. Akinlabi, N. Madushele, and O. O. Olatunji, "Neuro-fuzzy resource forecast in site suitability assessment for wind and solar energy: A mini review," *J. Clean. Prod.*, vol. 269, p. 122104, 2020, doi: 10.1016/j.jclepro.2020.122104.

[32]. P. A. Trotter, R. Maconachie, and M. C. McManus, "Solar energy's potential to mitigate political risks: The case of an optimized Africa-wide network," *Energy Policy*, vol. 117, no. March, pp. 108–126, 2018, doi: 10.1016/j.enpol.2018.02.013.

[33]. O. S. Yılmaz, F. Gülgen, F. Balık Şanlı, and A. M. Ateş, "Demirköprü Barajının Su Yüzey Sınırlarının Belirlenmesinde Sentinel –2 (MSI) Görüntüleri Kullanılarak Farklı Algoritmalar ve Su Endeksleri Performanslarının Araştrılması," in *Hezarfen International Science, Mathematics, and Engineering Sciences Congress*, 2019, pp. 293–305.

[34]. L. Breiman, "Random Forests," *Mach. Learn.*, vol. 45, pp. 5–32, 2001, doi: 10.1023/A:1010933404324.

[35]. Y. Jin, X. Liu, Y. Chen, and X. Liang, "Land-cover mapping using Random Forest classification and incorporating NDVI time-series and texture: a case study of central Shandong," *Int. J. Remote Sens.*, vol. 39, no. 23, pp. 8703–8723, Dec. 2018, doi: 10.1080/01431161.2018.1490976.

[36]. Y. He, C. Wang, F. Chen, H. Jia, D. Liang, and A. Yang, "Feature comparison and optimization for 30-M winter wheat mapping based on Landsat-8 and Sentinel-2 data using random forest algorithm," *Remote Sens.*, vol. 11, no. 5, 2019, doi: 10.3390/rs11050535.

[37]. T. Noi Phan, V. Kuch, and L. W. Lehnert, "Land cover classification using google earth engine and random forest classifier-the role of image composition," *Remote Sens.*, vol. 12, no. 15, 2020, doi: 10.3390/RS12152411.

[38]. A. M. Ates, O. S. Yilmaz, and F. Gülgen, "Using remote sensing to calculate fl oating photovoltaic technical potential of a dam' s surface," *Sustain. Energy Technol. Assessments*, vol. 41, no. July, p.

100799, 2020, doi: 10.1016/j.seta.2020.100799.

[39]. M. Mwanza and K. Ulgen, *GIS-Based Assessment of Solar Energy Harvesting Sites and Electricity Generation Potential in Zambia*. 2021.

[40]. A. M. Ates and H. Singh, "Rooftop solar Photovoltaic (PV) plant – One year measured performance and simulations," *J. King Saud Univ. - Sci.*, vol. 33, no. 3, p. 101361, 2021, doi: 10.1016/j.jksus.2021.101361.

[41]. A. Gerbo, K. V. Suryabhagavan, and T. Kumar Raghuvanshi, "GIS-based approach for modeling grid-connected solar power potential sites: a case study of East Shewa Zone, Ethiopia," *Geol. Ecol. Landscapes*, vol. 00, no. 00, pp. 1–15, 2020, doi: 10.1080/24749508.2020.1809059.

[42]. E. Ghiani, F. Pilo, and S. Cossu, "Evaluation of photovoltaic installations performances in Sardinia," *Energy Convers. Manag.*, vol. 76, pp. 1134–1142, Dec. 2013, doi: 10.1016/j.enconman.2013.09.012.

Celal Bayar University Journal of Science

Production of AA2024-Matrix B_4C-SiC- and B_4C-Y_2O_3-Particle-Reinforced Composites by Powder Metallurgy and Investigation of Their Mechanical Properties

Halit Doğan[1*] iD, Yılmaz Mutlu[2] iD

[1] Manisa Celal Bayar University, Faculty of Engineering, Department of Mechanical Engineering, 45140 Manisa, Türkiye
[2] Manisa Celal Bayar University, Institute of Natural and Applied Sciences, Department of Mechanical Engineering, 45140 Manisa, Türkiye
*halit.dogan@cbu.edu.tr
*Orcid: 0000-0001-9263-8068

Abstract

In this study, it was aimed to produce Al-matrix composite materials with B_4C-SiC and B_4C-Y_2O_3 particle reinforcement using the Powder Metallurgy (PM) method. In the composites in which the reinforcement materials were used at different particle sizes and ratios, AA2024 powders were selected as the matrix material. The powders were homogeneously mixed and compacted at room temperature under a pressure of 525 MPa. The raw specimens were sintered by keeping them at different temperatures for 45 minutes. The composite materials were subjected to wear tests, and their hardness and density values were investigated. In the study, the effects of reinforcement materials added to the matrix at different particle sizes and ratios on wear resistance, hardness, and density at different sintering temperatures were examined. As a result of the mechanical tests that were performed, wear values decreased along with B_4C reinforcement ratios that increased in parallel with density values. The highest hardness value was observed as 71.73 HB in the composite specimen with a B_4C reinforcement ratio of 20% at the sintering temperature of 595°C.

1.Introduction

Advanced materials have become prevalent worldwide as a consequence of advancements in science and technology, to meet the need for specialized products. The reason for this is that a single material usually cannot meet the requirements of all engineering fields. Therefore, researchers have shown great effort to use composite materials with unique properties. As a result of this, there has been an increase in the production and application fields of metal matrix composites in recent years [1]. In previous years, metal-matrix composites (MMCs) received worldwide attention with their excellent properties combining the best properties of metal matrices and reinforcements [2]. The physical and mechanical properties of MMCs can be improved by adding reinforcement material particles into the matrix. As the matrix material, light metals such as Ti, Al, and Mg that provide support for the reinforcement material are used in general. Among MMCs, the production of aluminum-matrix composites (AMCs) is becoming more prominent each day and finding various usage areas in the industry [3]. Aluminum is an excellent matrix material for developing wear-resistant AMCs [2]. Aluminum alloys are the most convenient alloys following iron alloys [4]. It is well-known that the performance of AMCs is highly dependent on the reinforcements that are added [2]. AMCs use an aluminum alloy as the matrix material and mostly include ceramics like SiC [5-8], B_4C [6,7,9], Si_3N_4 [7], Al_2O_3 [5,6,8], BN [7], Zr [8], and TiC [7] as the reinforcement material. The properties of AMCs can be changed based on their elemental and volumetric ratios [3]. AMCs reinforced with hard ceramic particles are the most promising materials for various automotive and aviation applications with their low density and high wear resistance [5,7], and they are

used in many fields in the industry, especially in critical applications such as brake calipers, gears, engine blocks, pump components, and valve components [10,11]. Several Al alloys (e.g., 2xxx, 5xxx, 6xxx, 7xxx) are industrially utilized [12]. As a reinforcement material for AMCs, B_4C has attracted special attention [13]. Boron carbide (B_4C) and silicon carbide (SiC) particles, which are the most preferred reinforcement materials for AMCs, strengthen the matrix structure and provide good wear resistance and high thermal stability [12]. B_4C, which is called "black diamond", has a low density (2.52 g/cm^3), high hardness (29.1 GPa), high modulus of elasticity (470 GPa), and high melting point (2540°C) [14]. Because SiC has high hardness values, high resistance to rupture, a high modulus of elasticity, low density, and a low thermal expansion coefficient, its use as a reinforcement material is common [12]. Y_2O_3 ceramics have critical properties such as high thermal and crystallographic stability, and they are used in various applications including protective coatings, microwave radars, solid-state lasers, superconductors, and catalytic converters [27]. In the literature, there are different methods of production including squeeze casting, stir casting, liquid metal infiltration, mechanical alloying, and powder metallurgy for MMCs [15]. The powder metallurgy [PM] method is a production method where mixed metal powders are shaped by compaction into a mold that has been prepared based on the shape and dimensions of the part to be produced and then sintered [6]. PM allows manufacturing processes that result in parts close to those with precisely shaped parts produced out of Al-based materials and MMCs with certain mechanical, thermal, and functional properties [16]. In this study, by ceramic particle reinforcement, Al-B_4C, Al-B_4C-SiC, and Al-B_4C-Y_2O_3 composites with an aluminum alloy matrix were produced, and the effects of the reinforcement materials on the mechanical and microstructure properties of the composites were examined.

2. Materials and Methods

In this study, where reinforcement materials were used at different ratios and particle sizes, AA2024 aluminum alloy powder was used as the matrix component, and B_4C, SiC, and Y_2O_3 powders were used as the reinforcement components at different ratios and particle sizes. Aluminum alloy at a particle size of 100 μm was used as the matrix, while the reinforcement materials included boron carbide (B 4 C) at ratios of 7, 10, 15, and 20% and particle sizes of 10 and 22-59 μm, 20% B_4C + silicon carbide (SiC) at ratios of 3-10% and a particle size of 10 μm, and 20% B_4C + yttrium oxide (Y_2O_3) at ratios of 3-10% and a particle size

of 10 μm. The chemical composition of the AA2024 alloy that was used as the matrix material is shown in Table 1.

2.1 Specimen Preparation

The powders were weighed using a RADWAG PS 1000/C/2 brand precision scale with a sensitivity of 0.001 g and homogeneously mixed at different weight ratios. Composite materials were produced by applying a pressure of 525 MPa onto a mold prepared with the dimensions of 10x10x55 mm using a 100-ton uniaxial hydraulic press branded Hidrokar. Polyethylene glycol (1% wt.) was added to the powder mixtures as a binder. The specimens were sintered at 550, 575, and 595°C for 45 minutes using a Protherm brand furnace.

2.2 Hardness Test

The hardness measurements were made with specimens that were brought to the dimensions of 10x10x10 mm using an EMCO-TEST DuraVision Brinell hardness tester device (Load: 15.625 kg, Ball Diameter: 2.5 mm, Time: 10 s). The effects of B_4C at a particle size of 10 μm that was added to the AA2024 matrix on hardness are shown in Figure 1. It was seen that at all sintering temperatures, as the ratio of the B_4C reinforcement increased, hardness values also increased. This was an expected result because of the higher harness value of the B_4C that was added to the matrix compared to the matrix material. The highest hardness value was found as 71.73 HB in the composite specimen produced using 20% B_4C and sintered at 595°C. Similarly, in the study conducted by Karakoc H. et al. using Al6061 as the matrix material and B_4C and SiC powders as the reinforcement materials, it was found that the composite materials including reinforcements were harder than the unreinforced Al6061 alloy, where the unreinforced alloy had a mean hardness of 50 HB, and the 12% B_4C composite had a mean hardness of 76 HB [12]. Likewise, in their hardness tests on SiC- and B_4C-reinforced Al7071-matrix composite materials they produced with the PM method, Pul M. and Baydaroğlu V. observed that as the reinforcement particle ratio in the structure increased, hardness values also increased [6]. Hasırcı H. and Gül F. also produced AMCs with B_4C reinforcement and examined their mechanical properties. They found higher hardness values in the composite material produced with B_4C reinforcement addition to the Al [17]. Additionally, Ergul E, Kurt H. İ., Cıvı C. and Eyıcı G. mixed 50% MgO and 50% carbon nanotubes (CNT) by weight with the die casting method, added these reinforcement materials to the Al2024 matrix material at ratios of 0.2, 0.5, 1, and 2% by weight,

produced MgO/CNT-reinforced Al2024 composite materials, and investigated hardness results. They observed that the hardness values of the specimens increased by reinforcement addition [18]. Şenel M. C., Gürbüz M. and Koç E. produced composite materials with the PM method by adding Si_3N_4 reinforcement to the aluminum matrix at ratios varying in the range of 0-12% and examined the effects of the reinforcement ratio on the mechanical properties of the composites. According to the results of their experiments, while the hardness value of the pure aluminum was approximately 28 HV, hardness could be increased to 58 HV by adding 9% Si_3N_4 by weight [19].

Table 1. Chemical composition of the AA2024 matrix material (%). [20]

Matrix Material Chemical Properties								
AA2024	Fe	Si	Cu	Mn	Mg	Zn	Ti	Cr
	0.50	0.50	3.80-4.90	0.30-0.90	1.20-1.80	0.25	0.15	0.10

Figure 1. Changes in the hardness values of AA2024 + 10 μm B_4C depending on temperatures and reinforcement ratios.

Figure 2 shows the effects of the B_4C+SiC added into the AA2024 matrix on hardness. Accordingly, in all specimens sintered at different temperatures, as the ratio of SiC increased, hardness values also increased. The reason for this result was the fact that the hardness values of the B_4C and SiC reinforcement materials were higher than that of the matrix material. The highest hardness value was found as 91.82 HB in the specimen that was produced by adding 20% B_4C + 10% SiC and sintered at 595°C. Likewise, Gündoğan K. and Özsarı A. R. B. investigated the mechanical properties of composite materials produced with an AA2024 or AA6061 matrix and reinforced with B_4C and SiC particles using the pressure infiltration technique. As the pressure values of the composite materials increased, the authors observed an increase in their hardness and strength values. After they compared the reinforcement components, they concluded that the composites with the B_4C reinforcement had better mechanical properties than those with the SiC reinforcement [21].
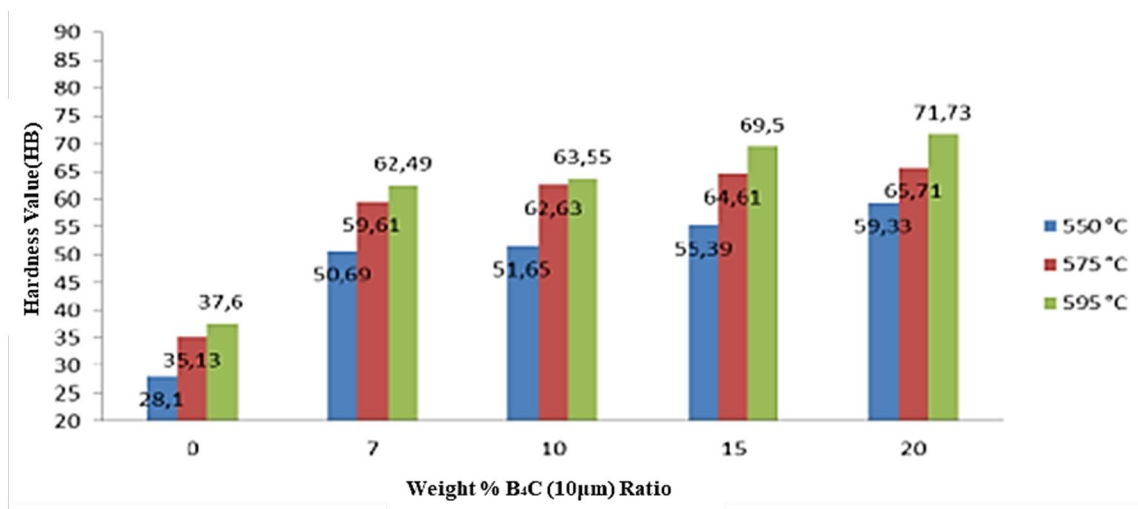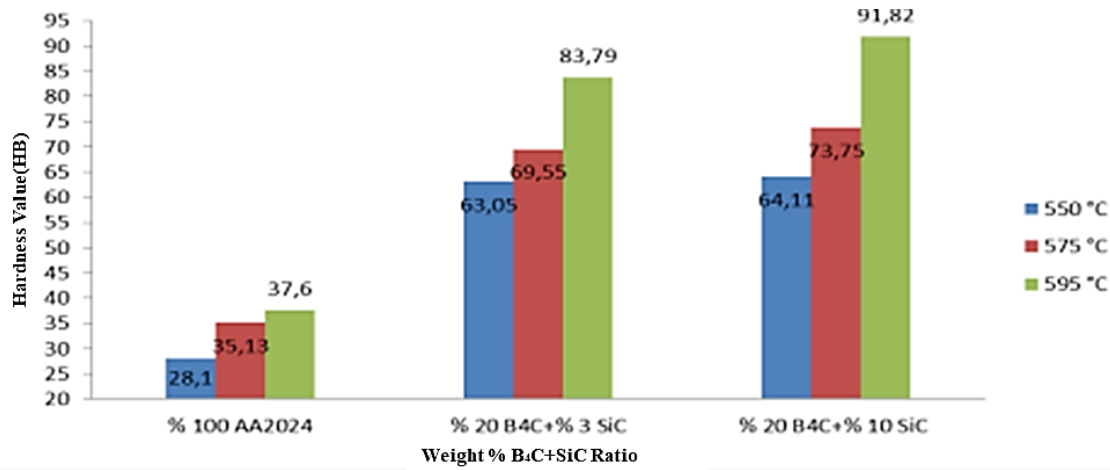
H. Doğan

Figure 2. Changes in the hardness values of AA2024+B_4C+SiC depending on temperatures and reinforcement ratios.

Figure 3 shows the effects of B_4C+Y_2O_3 added into the AA2024 matrix on hardness. It is seen that as the ratio of Y_2O_3 increased, hardness values also increased. The reason for this result was the fact that the hardness values of the B_4C and Y_2O_3 reinforcement materials were higher than that of the matrix material. The highest hardness value among the AA2024-matrix B_4C+Y_2O_3-reinforced composite materials was found as 85.33 HB in the specimen that was produced by adding 20% B_4C + 10% Y_2O_3 and sintered at 595 °C.

Figure 3. Changes in the hardness values of AA2024+B_4C+ Y_2O_3 depending on temperatures and reinforcement ratios.

In the composites that were produced, in general, hardness values were observed to increase along with increased reinforcement ratios and sintering temperatures.

2.3 Density

The density measurements of the composite materials were made using a RADWAG AS 220/C/2 brand density measurement device based on the Archimedes principle. Figure 4 presents the effects of B_4C at a particle size of 10 μm that was added into the AA2024 matrix on density and porosity. Accordingly, in all specimens sintered at

different temperatures, as the ratio of B_4C reinforcement increased, density decreased, and porosity increased. The density values of the examined specimens were compatible with those reported in the literature, and as the B_4C reinforcement ratio increased, density decreased. The main reason for this was the increased porosity that was observed and the fact that B_4C is a material that has a low density.

Similarly, in the Al2024-matrix B_4C- and TiB_2-reinforced composite materials produced by Pul M., as the ratio of reinforcement increased, the ratio of pores between TiB_2 and B_4C particles and the

aluminum powder increased, and thus, density values decreased [22]. Topcu İ., Dikici M. and İpek C. also investigated the density and wear resistance of aluminum-matrix B_4C-reinforced composite materials. The lowest density value was observed in the Al/B_4C composite with the highest B_4C ratio by weight (15%). It was seen that the density values of the specimens decreased along with increased B_4C ratios, but the values of the specimens with the same B_4C reinforcement ratios increased along with increased sintering temperatures [23].

Figure 4. Changes in the density values of AA2024 + 10 μm B_4C depending on temperatures and reinforcement ratios.

The effects of B_4C+SiC added into the AA2024 matrix on density are shown in Table 2. Accordingly, as the ratio of SiC that was added increased, the ratio of porosity also increased. The effects of B_4C and Y_2O_3 added into the AA2024 matrix on density are shown in Table 3. Accordingly, in all specimens sintered at different temperatures, as the ratio of Y_2O_3 that was added increased, both density and porosity increased.

Table 2. Changes in the density values of AA2024 + B_4C+SiC depending on temperatures and reinforcement ratios.

AA2024+(B4C+SiC)									
Sequence No	% AA2024	% B₄C	% SiC	AA2024 particle size (μm)	B₄C particle size (μm)	SiC particle size (μm)	Sintering temperature (°C)	Theoretical density value (g/cm³)	Experimental density value (g/cm³)	Pore ratio (%)
1	77	20	3	100-150	22-59	10	550 575 595	2,754	2,470 2,479 2,495	10,31 9,98 9,40
2	70	20	10	100-150	22-59	10	550 575 595	2,783	2,475 2,483 2,499	11,06 10,77 10,20

Table 3. Changes in the density values of AA2024 + B$_4$C+Y$_2$O$_3$ depending on temperatures and reinforcement ratios.

AA2024+(B4C+Y$_2$O$_3$)										
Sequence No	% AA2024	% B$_4$C	% Y$_2$O$_3$	AA2024 particle size (µm)	B$_4$C particle size (µm)	Y$_2$O$_3$ particle size (µm)	Sintering temperature (°C)	Theoretical density value (g/cm^3)	Experimental density value (g/cm^3)	Pore Ratio (%)
1	77	20	3	100-150	22-59	10	550	2,808	2,501	10,93
							575		2,519	10,29
							595		2,523	10,14
2	70	20	10	100-150	22-59	10	550	2,963	2,609	11,94
							575		2,619	11,60
							595		2,635	11,06

2.4 Wear Test

The wear tests were carried out with the Tribometer pin-on-disk wear testing device shown in Figure 5 under a 2N load for 15 minutes (3.516 mm track diameter, 20000 mm sliding distance, and 2000 cm/s linear velocity). Like the density test results, as the ratio of B$_4$C reinforcement increased, wear values decreased. As seen in Figure 6, in all specimens sintered at different temperatures, wear values decreased along with increasing reinforcement ratios. These results were similar to the results of other studies conducted with composite materials. Hasırcı H. and Gül F. produced Al-matrix B$_4$C-reinforced composite materials and investigated their wear behaviors. They reported that the hardness of the composite increased due to the B$_4$C reinforcement particles added into the matrix, the pure Al material had the lowest hardness values, and in general, wear amounts decreased in the composites in comparison to the pure Al material as the ratio of reinforcement increased [17]. Likewise, Karakoç H. observed lower wear amounts based on weight loss as a result of B$_4$C and Si$_3$N$_4$ reinforcement addition [24]. In another study by Karakoç H., Al7075/B$_4$C and Al7075/B$_4$C/Si$_3$N$_4$ composite materials were produced using the powder metallurgy method, and their wear behaviors were analyzed. The researcher determined a decrease depending on increased ratios of B$_4$C and Si$_3$N$_4$ by weight and found the lowest weight loss value in the Al7075/15%B$_4$C/2%Si$_3$N$_4$ material [24]. Furthermore, Arık H. studied the effects of SiC as a reinforcement component on the wear properties of aluminum-matrix composite materials. The author used PM as the production method for Al-SiC composite materials and the pin-on-disk method in the wear test. It was observed that the weight loss value decreased by 48.4% to 79.6% when SiC was added at 10% by weight to the matrix [25]. Aksöz S. and Bostan B. produced 10/20% B$_4$C-reinforced AA2014-matrix composite materials using the casting method and sintering at 600°C for 2 hours after casting and examined the effects of reinforcement ratios on wear behaviors. They found lower wear-related weight loss as a result of adding increased ratios of B$_4$C reinforcement and sintering. The lowest weight loss was observed in the composite material containing 20% B$_4$C that was sintered at 600°C for 2 hours [26].

Figure 5. Wear tests of the composite specimens (a: Weighing before the test; b: Wear test; c: Weighing after the test).

	0% (10 μm B4C)	7% (10 μm B4C)	10% (10 μm B4C)	15% (10 μm B4C)	20% (10 μm B4C)
555 °C	77,889	57,803	50,745	43,665	41,325
580 °C	73,855	56,980	48,687	42,889	37,741
595 °C	71,905	55,451	47,876	41,201	36,891

Figure 6. Changes in the weight loss values of AA2024 + 10 μm B_4C depending on temperatures and reinforcement ratios.

Figure 7. Changes in the weight loss values of AA2024+(B$_4$C+SiC) and AA2024+(B$_4$C+Y$_2$O$_3$) depending on temperatures and reinforcement ratios.

Figure 7 presents the changes in the weight loss values of AA2024+(B$_4$C+SiC) and AA2024+(B$_4$C+Y$_2$O$_3$) along with increased sintering temperatures. It is seen that with the increase in the sintering temperature, wear values decreased, and the AA2024+(B$_4$C+SiC) composite had higher wear resistance values in comparison to the AA2024+(B$_4$C+Y$_2$O$_3$) composite.

2.5 SEM

The microstructures of the specimens were examined using a JEOL JSM-6060 brand SEM device.

Figure 8. SEM image of 85%AA2024+15%B$_4$C (10 μm) sintered at 575°C (x1000).
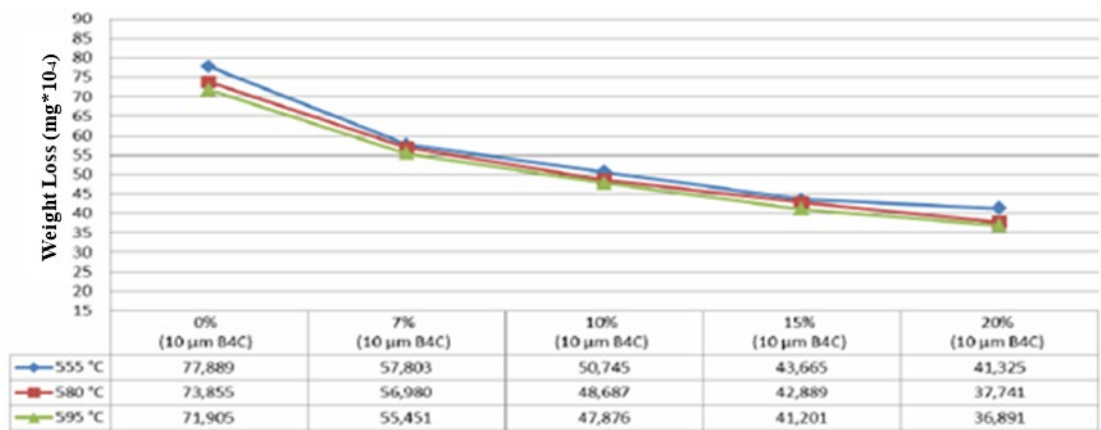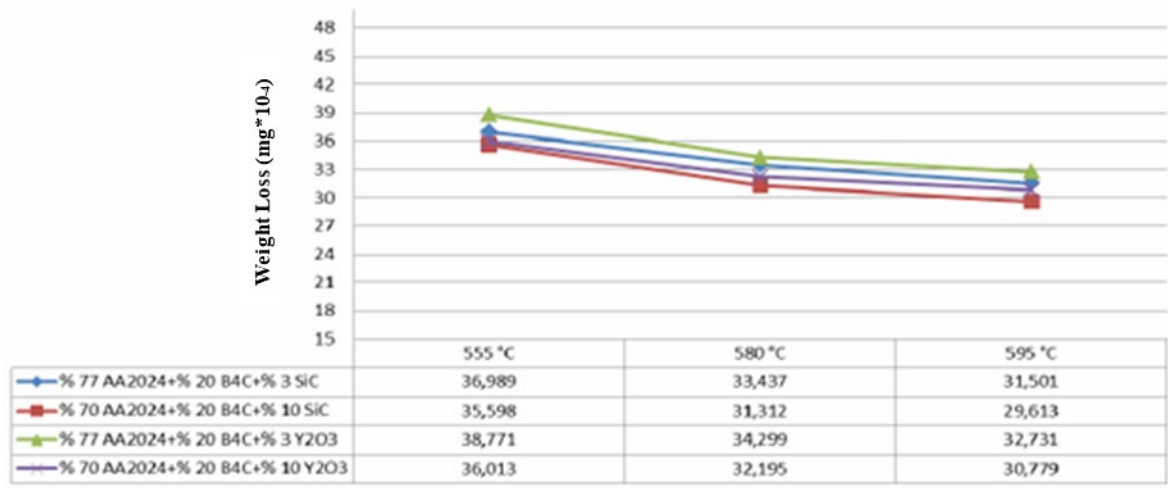

Figure 9. SEM image of 77%AA2024+20%B$_4$C (22-49 μm) +3%SiC sintered at 575°C (x500).

It was observed in the microstructure of the 77%AA2024+20% B$_4$C (22-59 μm) +3% SiC composite shown in Figure 9 that the distributions of B$_4$C and SiC were generally homogeneous but occasionally non-homogeneous, and the structure was non-porous in general.

As seen in Figures 8 and 9, although both materials were sintered at the same temperature, the 77%AA2024+20% B$_4$C (22-59 μm) +3%SiC composite had a lower porosity value because a more compacted structure was obtained with the addition of SiC (10 μm).

Figure 10. SEM image of 70%AA2024+20%B$_4$C (22-59 µm) +10%Y$_2$O$_3$ sintered at 575°C (x1000).

Figure 10 shows the microstructure of the composite that had lower porosity due to the more compacted structure that was obtained with the addition of 10 µm Y$_2$O$_3$.

3. Results

The conclusions made based on the results of the experiments that were conducted in this study are given below.

1- As the reinforcement particle ratio by weight increased, the hardness values of the composites increased, and in comparison to the unreinforced AA2024 matrix material, the hardness values of the composites were approximately 2.5 times higher.
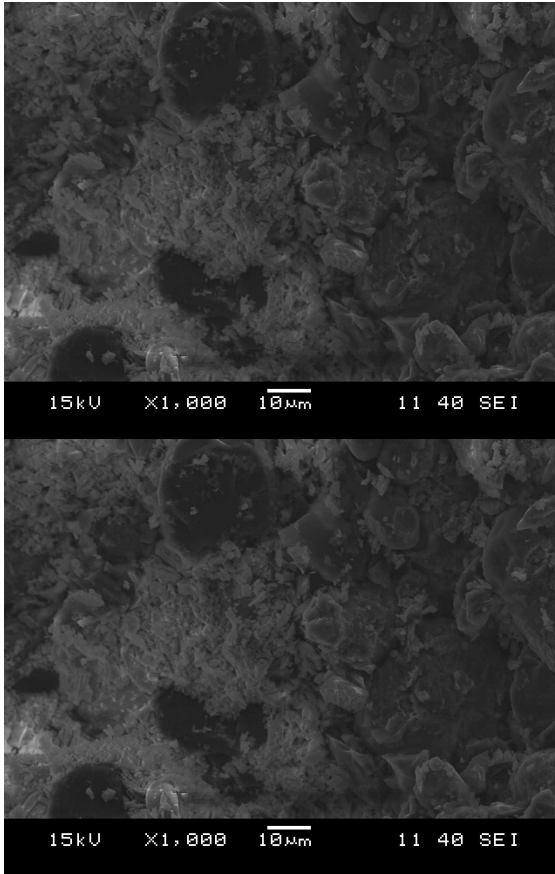2- The density values of the 10 µm B$_4$C-reinforced composites decreased along with increasing reinforcement ratios.
3- With the increase in the reinforcement particle ratio by weight, there was a decrease in the wear-related weight loss values of the composites.
4- The SEM examinations (Figures 9 and 10) showed lower porosity values depending on the addition of SiC (10 µm) and Y$_2$O$_3$ (10 µm) due to the more compacted structure that was obtained.

Author Contributions

Halit Doğan: He planned, designed and performed the analysis.
Yılmaz Mutlu: He designed the study, made the statistical analyzes and wrote the article.

Ethics

There are no ethical issues after the publication of this manuscript**.**

References

[1]. Herzallah H., Elsayd A., Shash A., Adly M.,; Effect of carbon nanotubes (CNTs) and silicon carbide (SiC) on mechanical properties of pure Al manufactured by powder metallurgy, j m a t e r r e s t e c h n o l . 2 0 2 0;9(2):1948–1954. https://doi.org/10.1016/j.jmrt.2019.12.027

[2]. Zhang J., Liu Q., Yang S., Chen Z., Liu Q., Jiang Z.,; Microstructural evolution of hybrid aluminum matrix composites reinforced with SiC nanoparticles and graphene/graphite prepared by powder metallurgy, Progress in Natural Science: Materials International 30 (2020) 192–199. https://doi.org/10.1016/j.pnsc.2020.01.024

[3]. Sharma A. K., Bhandari R., Pinca-Bretotean C.,; A systematic overview on fabrication aspects and methods of aluminum metal matrix composites, Materials Today: Proceedings 45 (2021) 4133–4138. https://doi.org/10.1016/j.matpr.2020.11.899

[4]. Fuse K., Badheka V., Patel V., Andersson J.,; Dual sided composite formation in Al 6061/B4C using novel bobbin tool friction stir processing, j o u r n a l of m a t e r i a l s r e s e a r c h and technology 2 0 2 1 ; 1 3 : 1 7 0 9 e1 7 2 1. https://doi.org/10.1016/j.jmrt.2021.05.079

[5]. Devadiga U., Fernandes P.,; Taguchi analysis for sliding wear characteristics of carbon nanotube-flyash reinforced aluminium nanocomposites, Heliyon 7 (2021) e06170. https://doi.org/10.1016/j.heliyon.2021.e06170

[6]. Pul M. ve Baydaroğlu V., B4C/SiC katkılı alüminyum esaslı kompozitlerin mekanik özelliklerin incelenmesi ve balistik performanslarının modellenmesi, Politeknik Dergisi, 23(2): 383-392, (2020). https://doi.org/10.2339/politeknik.525011

[7]. Şenel M. C.,; Toz Metalürjisi Yöntemiyle Üretilen Saf Al ve Al-B4C, Al-Al2O3 Kompozitlerin Mekanik ve Mikroyapı Özelliklerinin Karşılaştırılması, GÜFBED/GUSTIJ (2020) 10 (3): 783-795. https://doi.org/10.17714/gumusfenbil.689359

[8] . Yang J., Chung D.D.L.,; Wear of bauxite-particle reinforced aluminum alloys", Composite Materials Research Laboratory,

Furnas Hall, State University of New York, Buffalo, NY 14260(U.S.A.), Wear, 135: 53-65 (1989). https://doi.org/10.1016/0043-1648(89)90095-1

[9]. Abenojar J.; Velasco F.; Martinez M.A.; Optimization of Processing Parameters for The Al + 10% B4C System Obtained by Mechanical Alloying, Journal of Materials Processing Technology 184(2007) 441–446. https://doi.org/10.1016/j.jmatprotec.2006.11.122

[10]. Saessı M., Alızadeh A., Abdollahı A.,; Wear behavior and dry sliding tribological properties of ultra-fine grained Al5083 alloy and boron carbide-reinforced Al5083-based composite at room and elevated temperatures, Trans. Nonferrous Met. Soc. China 31(2021) 74−91. https://doi.org/10.1016/S1003-6326(20)65479-6

[11]. Lakshmikanthan A., Prabhu T.R., Babu U. S., Koppad P. G., Gupta M., Krishna M., Bontha S.,; The effect of heat treatment on the mechanical and tribological properties of dual size SiC reinforced A357 matrix composites, j m a t e r r e s t e c h n o l . 2 0 2 0;9(3):6434–6452. https://doi.org/10.1016/j.jmrt.2020.04.027

[12]. Karakoc H., Ovalı İ, Dündar S., Çıtak R.,; Wear and mechanical properties of Al6061/SiC/B4C hybrid composites produced with powder metallurgy, j m a t e r r e s t e c h n o l . 2 0 1 9;8(6):5348–5361. https://doi.org/10.1016/j.jmrt.2019.09.002

[13]. Aherwar A., Patnaik A., Pruncu C. I.,; Effect of B4C and waste porcelain ceramic particulate reinforcements on mechanical and tribological characteristics of high strength AA7075 based hybrid composite, j m a t e r r e s t e c h n o l . 2 0 2 0;9(5):9882–9894. https://doi.org/10.1016/j.jmrt.2020.07.003

[14]. Boussebha H., Bakan S., Kurt A. O.,; Dynamic / thermochemical method: A novel approach in the synthesis of B4C powder, Open Ceramics 6 (2021) 100133. https://doi.org/10.1016/j.oceram.2021.100133

[15]. Abd-Elwahed M.S., Sadoun A.M., Elmahdy M.,; Electroless-plating of Ag nanoparticles on Al2O3 for enhanced mechanical and wear properties of Cu–Al2O3 nanocomposites, j m a t e r r e s t e c h n o l . 2 0 2 0;9(6):13749–13758. https://doi.org/10.1016/j.jmrt.2020.09.077

[16]. Balog M., Orovcik L., Nagy S., Krizik P., Nosko M., Oslanec P., Zifcak P.,; To what extent does friction-stir welding deteriorate the properties of powder metallurgy Al?, j m a t e r r e s t e c h n o l . 2 0 2 0;9(3):6733–6744. https://doi.org/10.1016/j.jmrt.2020.04.087

[17]. Hasan H., Ferhat G.,; B4C / Al Kompozitlerin Takviye Hacim Oranına Bağlı Olarak Abrasif Aşınma Davranışlarının İncelenmesi, SDU International Technologic Science, 2(1): 15-21, (2010). https://dergipark.org.tr/tr/pub/utbd/issue/25991/273754

[18]. Ergul E., Kurt H.I., Civi C., Eyici G., Wear Characteristics of Carbon Nanotube Reinforced Al2024 Composites, El-Cezerî Fen ve Mühendislik Dergisi 2020, 7(3); 1008-1016. https://doi.org/10.31202/ecjse.716287

[19]. Şenel M. C., Gürbüz M., Koç E.,; Toz Metalürjisi Metoduyla Üretilen Al-Si3N4 Metal Matrisli Kompozitlerin Mekanik Özelliklerinin İncelenmesi, Mühendis ve Makina Dergisi, cilt 59, sayı 693, s. 33-46, 2018. https://dergipark.org.tr/tr/pub/muhendismakina/issue/48384/612874

[20]. Şık A., Ertürk İ. ve Önder M., AA2024 Alüminyum Alaşımının Sürtünme Karıştırma Kaynağında Farklı Parametrelerin Mekanik Özelliklere Etkisinin İncelenmesi, Pamukkale Üniversitesi Mühendislik Bilimleri Dergisi Cilt 16, Sayı 2, 2010, Sayfa 139-147. https://dergipark.org.tr/en/pub/pajes/issue/20508/218316?publisher=pamukkale

[21]. Gündoğan K., Özsarı A.R.B.,; Basınçlı İnfiltrasyon Yöntemiyle Üretilen AA2024 ve AA6061 Matrisli, B4C ve SiC Takviyeli Kompozit Malzemelerin Mikroyapı, Mekanik ve Isıl İletkenlik Özelliklerine Basıncın Etkisi, UMAGD, (2019) 11(2), 657-669. https://doi.org/10.29137/umagd.540610

[22]. Pul M.,; Toz Metalurjisi Yöntemiyle Üretilen B4C+TiB2 Takviyeli Al 2024 Esaslı Kompozitlerde Takviye Miktarının Mekanik Özelliklere Etkisi, UMAGD, (2019) 11(1), 87-99. https://doi.org/10.29137/umagd.407488

[23]. Topcu İ., Dikici M., İpek C.; Seramik Takviyeli Alüminyum Esaslı Metal Matrik Kompozitlerin Aşınma Özelliklerinin İncelenmesi, Published in 6th International Symposium on Innovative Technologies in Engineering and Science 09-11 November 2018 (ISITES2018 Alanya – Antalya - Turkey). https://doi.org/10.33793/acperpro.01.01.91

[24]. Karakoç H., Toz metal Al7075/B4C/Si3N4 kompozit malzemelerin üretimi ve aşınma özelliklerinin incelenmesi, Politeknik Dergisi, 23(4): 1141-1151, (2020). https://doi.org/10.2339/politeknik.585813

[25]. Arık H.,; Investigation of Wear Properties of Al-SiC Composite Materials Produced by Powder Metallurgy Method, GU J Sci, Part C, 7(3): 741-754 (2019). https://doi.org/10.29109/gujsc.587637

[26]. Aksöz S., Bostan B.; AA2014/B4C MMK yapının döküm ve döküm sonrası sinterleme işlemleri ile üretiminin aşınma davranışlarına etkileri, BORON 3 (2), 132 - 137, 2018. https://doi.org/10.30728/boron.373140

Celal Bayar University Journal of Science

Statistical Analysis of Noise-induced Brain Electrical Activity of Employees in the Underground Mining Sector in the Soma Basin

Ayla Tekin[1] , Mustafa Oğuz Nalbant[1*] , Mustafa Orhan[1] , Fırat Tekin[1] , Fatih Suvaydan[1] , Kemal Berki[1] , Aslı Aydın Savran[2] ,Sami Gümüş[2]

[1] Manisa Celal Bayar University, Soma Vocational School
[2] Soma Medigün Hospital
* mustafa.nalbant@cbu.edu.tr
* Orcid: 0000-0002-9311-2241

Abstract

In the mining sector, which requires a lot of attention, excessive noise pollution is encountered during the works due to the use of mining machines, and this is observed as one of the most important factors causing various problems for the personnel working in underground mining. The present study investigated the neurological effects of instantaneous noise exposure and exposure to noise on workers' health in the underground mining sector using electroencephalography (EEG) device. Firstly, the noises that underground workers are exposed to in different working areas were determined. One hundred people working or working in the mining industry were included in the study. Brain electrical activities of these people were measured at periodic intervals under the noise that occurred in the underground mine. Their relationship with occupational noise exposure was analyzed statistically. As a result of these measurements, the values collected in noise-free and noisy environments were compared.

Keywords: Noise Effect, Underground Mining, Occupational Health, Statistical Analysis, EEG.

1. Introduction

Today, rapidly developing technology includes many positive developments that will make life easier. However, these developments also have aspects that negatively affect human health. One such negative problem is noise. Noise is an important problem in all workplaces and is one of the effective parameters in the occurrence of occupational accidents [1]. The most important effect of noise on human health is on the hearing system [2]. In addition to negatively impacting hearing loss and verbal communication, noise can also lead to distress, cardiovascular disease, sleep disturbance, and even cognitive performance. Many studies have confirmed a direct relationship between increased noise levels and decreased cognitive performance [3-6]. As noted in the study of Rostam Golmohammadi et al., noise caused people to react more quickly due to higher stress levels compared to silence, and the noise was found to be a distraction for cognitive performance in occupational settings [7]. Distraction on employees is quite common. However, the issue of distraction

at worksites has not yet been adequately explored. Since distraction occurs due to reasons such as noise, moving vehicles, body discomfort, fatigue, depression, a wearable physiological device has been proposed to monitor the distraction of employees. It has been conducted a research to improve hazard identification performance by analyzing people's physical and physiological responses through wearable sensors. The basic logic in this research is that employees show unusual or abnormal reactions when faced with a danger [8-9]. Physical responses (eg walking and stepping) have been studied using wearable sensors and the relationship between the presence of hazards and changes in physical responses has been demonstrated [10-12]. Similarly, physiological responses (eg, eye movement, brain activity) derived from wearable sensors have also been investigated to elicit and identify hazards in the environment [13-14]. Electroencephalogram (EEG) is a diagnostic imaging technique used to obtain information about brain activities by detecting voltage changes created by neurons on the scalp cortical surface, and new technologies have made it

possible to obtain EEG data without any problems [15]. Because the brain activity is directly linked to people's cognitive processes [16], some studies have also analyzed patterns of brain electrical activity measured using EEG to predict cognitive states such as stress, attention, mental workload, and alertness [17-19]. A different study suggested using EEG to detect a person's mind wandering. The findings showed that EEG data from several electrodes could predict the intensity of mind wandering and contributed to the development of neurofeedback studies [20]. Jeon and Cai [21] investigated the feasibility of identifying construction hazards by developing an EEG classifier based on wearable experiments that can classify EEG signals associated with perceived hazards in a virtual reality (VR) environment. At the work of You Bo et al; investigated the effects of underground mining conditions (high temperature, high humidity, noise, etc.) on human health and safety. They used a memory test before and after exercise to examine the effects of mining conditions on the brain nerve activity of workers. However, to analyze the effect of temperature and humidity on workers' body blood pressure (including systolic pressure, diastolic pressure, and mean pressure), heart rate, respiratory rate, body temperature, body weight, typing speed, and memory level, a bedside monitor, and EEG device have been used. As a result of the study, it has been quantitatively and accurately analyzed that high temperature and high humidity in the mine have a detrimental effect on body physiology and labor productivity and that occupational health standards should be taken as a reference [22]. Önder, and Önder [23] in their study, they made statistical noise analysis in three main mining areas including lavavar, open pit and underground mine.

In summary, noise exposure is dangerous for occupational health, harms the perception of risk, and increases the psychophysiological burden. Since the noise of the machines in the mining industry is harmful, the focus of the present research is to evaluate the noise levels and analyze the physiological responses of the machines with a wearable EEG that can classify the EEG signals in the noise environment in which they operate.

2. Materials and Methods

In this study, an Electroencephalography (EEG) device was used to measure and analyze the electrical activities in the brain during exposure to noise of people who work or will work in the underground mining sector. Measurements were made on 100 people. Selected 100 people work in the mining company with 5500 personnel. Factors such as the fact that the people are male and

working in the underground area were taken into consideration during the selection.

2.1. Location of Measurements

Measurements were made in the underground mine training pit, where chain conveyor, belt conveyor, water discharge systems, and ventilation systems, which are constant source of noise in underground mining enterprises, are located. The underground training colliery where measurements were made is shown in Figure 1.

Figure 1. Underground Training Colliery where the study was carried out.

The noise levels of each noise source were measured with a calibrated PCE-430 brand noise measuring device as listed in Table 1 and the noise intensity was observed to vary between 84 -94 dBA.

Table 1. Noise Intensities of Underground Training Machines.

Noise Source	Noise Intensity (dB)
Chain Conveyor	94
Belt Conveyor	86
Water Disposal System	84
Ventilation	88

2.2. Participants

One hundred male volunteers who work and will work in mining enterprises in Soma, which has the highest quality lignite reserves in Turkey, were studied. In the light of the information obtained as a

result of the survey conducted with the workers, the characteristics of the workers were formed as in Table 2. In addition, all volunteer employees were subjected to audiometric tests with the AMPLIVOX 240 brand audiometer device and audiometric tests were applied to all-volunteer employees. As seen in Figure 2, workers whose hearing limit is below the sound produced by noise sources were not included in the experiment.

Table 2. Characteristics of the Worker Population.

Worker (N:100)			
Old (year)			
Mean ± SD	Min-Max	23,95 ± 5,26	19 - 49
Weight (kg)			
Mean ± SD	Min-Max	76,46 ± 16,85	55 - 115
Height (cm)			
Mean ± SD	Min-Max	176,68 ± 5,80	166 - 186

All volunteers accepted the use of personal data in academic studies and accepted that these data are sensitive data and they were informed that the results obtained are handled collectively with methods and purposes in accordance with scientific principles. Also, before the experiment, all participants were fully informed about the general experimental procedure and signed a consent form.

Figure 2. Comparison of noise intensity per frequency of noise sources and minimum hearing thresholds per frequency of participants.

2.3. Equipment and Measurements

A wearable physiological device has been proposed to monitor employee distractions. Instead of transmitting events between a single neuron, EEG records the total activity of thousands or millions of neurons as oscillatory activity [24]. EEG signals are mostly between 0.5-4 Hz Delta (δ), 4-8 Hz signals Theta (θ), 8-16 Hz signals Alpha (α), 16-32 Hz signals Beta (β), 32 Hz and The signals above are divided into five frequency bands as Gamma (γ). The band gaps of the EEG signals cause different success rates depending on the classification target. Thanks to the research in this field, the band gaps in which emotional states are active and the brain activities that are generally active can be grouped [25].

Figure 3. Electroencephalography Device

M. O. Nalbant

With the Contec KT88-3200 brand electroencephalography device shown in Figure 3, the brain electrical activities of the individuals were recorded separately before and after the operation of the machines that are the source of noise in the underground training colliery.

In the study, in order to examine the effect of noise on mine workers, measurements were taken from 100 people (males) who are working or will work in mining companies in the Soma basin, with the algorithm drawn in Figure 4.

Figure 4. The procedure of each experimental personnel.

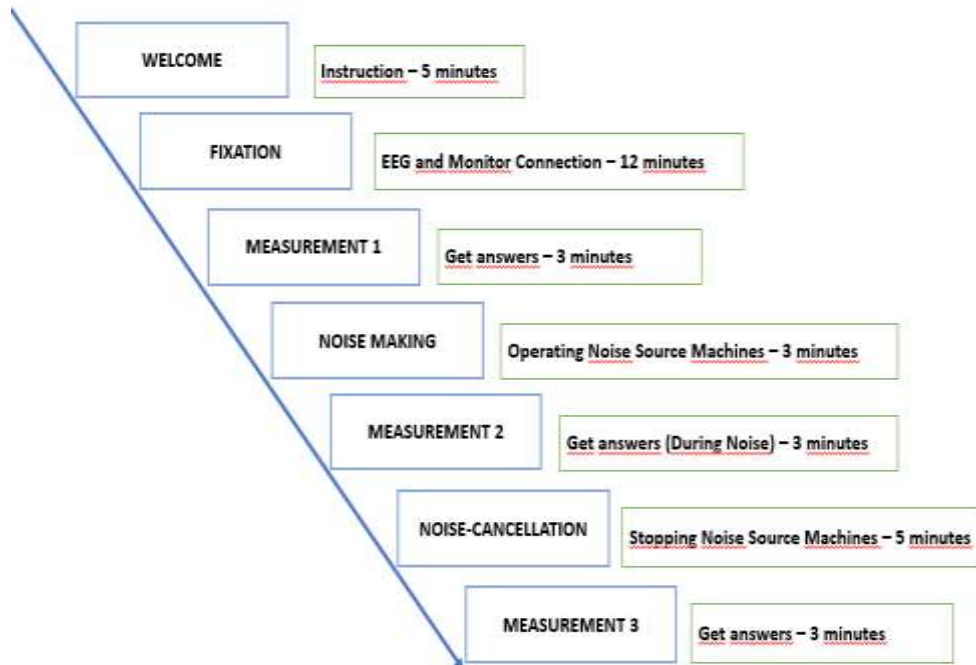In order to examine the electrical activities of the brain in the measurement area prepared in the Underground Training Colliery, 16 EEG electrodes were connected to the places included in the box in the diagram given in Figure 4. In the first place, the signals of the person were recorded under the conditions when the systems called the 1st state were turned off. Then the person was exposed to the noise of the machines for a while. After the noise, the person was measured after the noise as the 2nd situation, and the data were recorded. After these measurements, the person rested for 5 minutes outside the Underground Training Colliery.

The rested person was taken back to the Underground Training Colliery to take the final measurements. The person was connected to the bedside monitor and EEG in the sitting position and the last measurements were taken. The following values were recorded in three cases.

- **1.Case:** In a noise-free environment, SYS, DIA, MEAN, HR, PR, SPO2, RR, and body temperature values were obtained with a bedside monitor, and Brain Electrical Activity Mapping with EEG.
- **2.Case:** SYS, DIA, MEAN, HR, PR, SPO2, RR, and body temperature values were recorded in a noisy environment.

- **3.Case**: After the noise, SYS, DIA, MEAN, HR, PR, SPO2, RR, and body temperature values were recorded and Brain Electrical Activity Mapping was performed with EEG.

2.4. Monitoring the Electrical Activities of the Brain with Electroencephalography Device

In this study, the positions of the measurement and reference electrodes on the skull were predetermined. Figure 5 shows this arrangement. For signal recording, 18 channels of 32-channel Electroencephalography (EEG) device, 2 of which are references, were used. EEG data were recorded by placing electrodes on the scalp. The electrodes are placed symmetrically to the brain regions. Before the measurement was taken, the electrodes were checked for wear. Then the electrodes were washed and disinfected with alcohol. Here, "Nasion" defines the front part of the head and "Inion" defines the back part. In the 10-20 system, odd-numbered electrodes identify the left side of the brain, and even-numbered electrodes identify the right side of the brain. The letters in front of the numbers are the abbreviations of the names of the relevant regions of the brain. (Fp = frontopolar; F = frontal; C = central; P = parietal; O = occipital; T = temporal). The brain regions where they are located

and their electrode nomenclature are as follows; on the frontal lobe (Fp1, Fp2), (F3, F4, Fz, F7, F8), on the temporal lobe (T7, C3, C4, T8), on the occipital lobe (O1, O2), on the parietal lobe (P7, P3, P4, P8) and on the central region (C3, C4). Electrical activity was recorded by reference to the ear reference electrodes (A1 and A2). 500 Hz as the sampling frequency for each channel. value is used.
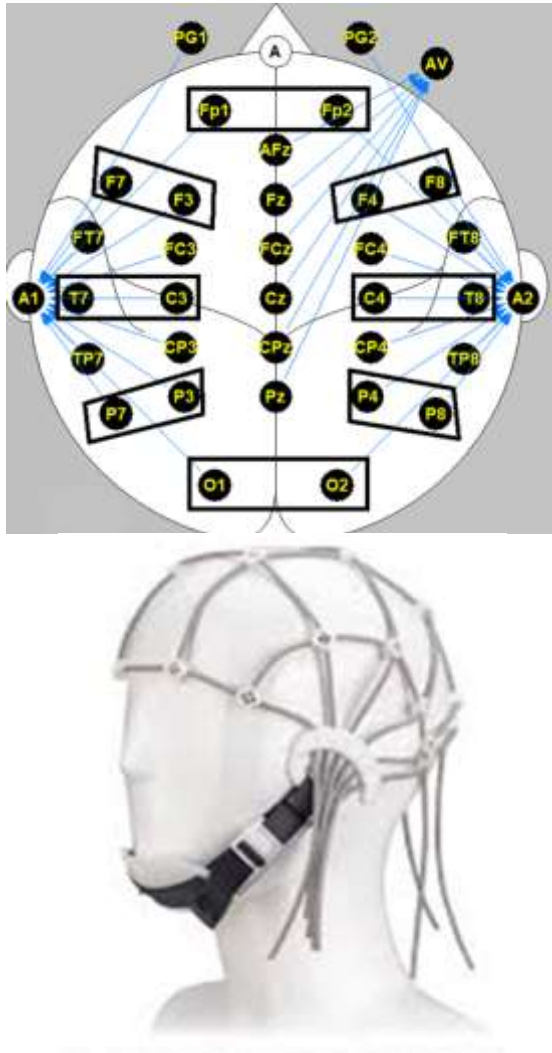

Figure 5. Electroencephalography Electrode Layout Diagram.

2.5. Statistical Analysis

The data obtained from the research were analyzed as dependent data in the SPSS statistical analysis program. Statistical analysis of the data, arithmetic mean and standard deviation (SD) were calculated according to the nature of each variable. Whether the data violated the assumption of normal distribution was checked using Kolmogorov-Smirnov's Lilliefors Significance Correction and Shapiro-Wilks Test. As a result of the controls, the tests of the workers and the scores they got from the attitude scale were compared using the Parametric T-Test for Related Samples, and the Nonparametric T Test for Unrelated Samples and the Wilcoxon Test. While analyzing the data, the significance level (p) was taken as 0.05.

3. Findings

In the present study, the effects of noise generated in underground mining on worker health were examined. During the study, the brain electrical activities of 100 people who work or will work in the mining sector were recorded for two different situations, and the data obtained in a noise-free environment and a noisy environment were compared, and the risk levels of noise and its effects on people were statistically analyzed.

3.1. Electroencephalography Results

At the measurement area prepared in the Underground Training , 16 EEG electrodes were connected to examine the brain's electrical activities to 100 volunteers who passed the audiometry test. In the first place, the signals of the people were recorded in the conditions when the systems called the 1st case were turned off. Afterward, people were exposed to the noise of machines for a while. After being exposed to noise, people rested outside the underground training for 5 minutes. The rested people were taken back to the underground training to take the final measurements, and in the 3rd case after the noise measurements were made and the data were recorded. EEG results of individuals were obtained as Numerical BEAM average values in microVolts for all frequency bands.

Statistical significance analyzes were performed using EEG signals recorded before and after noise. The results were created separately for the delta (0-4Hz), and theta (4-8Hz) bands of the EEG for each person. 16 electrode placements of each participant were examined. Case 1 and Case 3 values were compared for the Delta (δ) and Theta (θ) frequency bands with the highest electrical activity, and statistical analyzes of the remaining 61 individuals were made after the artifacts were filtered out.

When the values before noise (Case 1) and after (Case 3) were compared, no significant difference was observed in the values obtained from the Delta frequency bands (p>0.05, Table 3).

Similar to the delta band results, when the values before and after the noise were compared, there was no or very small change in the values obtained from the Theta frequency bands, and no significant difference was detected (p>0.05, Table 4).

Table 3. Table of Comparison of Delta Frequency Band Values of Volunteers in Before and After Noise Environments.

				Statistical Test[a]				
	Fp1_δ3	**Fp2_δ3**	**F7_δ3**	**F3_δ3**	**F4_δ3**	**F8_δ3**	**T7_δ3**	**C3_δ3**
	Fp1_δ1	**Fp2_δ1**	**F7_δ1**	**F3_δ1**	**F4_δ1**	**F8_δ1**	**T7_δ1**	**C3_δ1**
Z	-,798[b]	-,766[c]	-,383[c]	-,767[c]	-,600[b]	-,331[b]	-,366[b]	-,798[b]
Sig.	,425	,444	,701	,443	,548	,740	,715	,425
	C4_δ3	**T8_δ3**	**P7_δ3**	**P3_δ3**	**P4_δ3**	**P8_δ3**	**O1_δ3**	**O2_δ3**
	C4_δ1	**T8_δ1**	**P7_δ1**	**P3_δ1**	**P4_δ1**	**P8_δ1**	**O1_δ1**	**O2_δ1**
Z	-,250[c]	-,029[c]	-,891[b]	-,030[c]	-,430[b]	-,710[c]	-,941[b]	-,812[b]
Sig.	,802	,977	,373	,976	,667	,477	,347	,417

a: Wilcoxon Signed Ranks Test, b: According to positive ranks, c: According to negative ranks

Table 4. Table of Comparison of Volunteers' Theta Frequency Band Values in Before and After Noise Environments.

				Statistical Test[a]				
	Fp1_θ3	**Fp2_θ3**	**F7_θ3**	**F3_θ3**	**F4_θ3**	**F8_θ3**	**T7_θ3**	**C3_θ3**
	Fp1_θ1	**Fp2_θ1**	**F7_θ1**	**F3_θ1**	**F4_θ1**	**F8_θ1**	**T7_θ1**	**C3_θ1**
Z	-,662[b]	-,906[c]	-,807[c]	-1,20[c]	-,676[b]	-,751[c]	-,115[b]	-,792[c]
Sig.	,508	,365	,420	,227	,499	,453	,908	,428
	C4_θ3	**T8_θ3**	**P7_θ3**	**P3_θ3**	**P4_θ3**	**P8_θ3**	**O1_θ3**	**O2_θ3**
	C4_θ1	**T8_θ1**	**P7_θ1**	**P3_θ1**	**P4_θ1**	**P8_θ1**	**O1_θ1**	**O2_θ1**
Z	-1,07[c]	-1,38[b]	-,360[c]	-,284[c]	-,478[b]	-,086[b]	-,164[b]	-,254[c]
Sig.	,281	,167	,718	,776	,633	,931	,870	,799

a: Wilcoxon Signed Ranks Test, b: According to positive ranks, c: According to negative ranks

4. Discussion

The aim of this study is to determine the instantaneous noise exposure of workers exposed to noise in the mining sector and its effects on the body during noise exposure.

As a result of these measurements, the effects of the noise on the workers were observed by statistically comparing the values collected at the moment and after the noise exposure for the workers or volunteers who will work in underground mining.

When the neurological effects of the study were examined, the data obtained before and after the noise exposure in 6 frequency bands of 16 electrodes connected to the volunteers were analyzed and no significant difference was observed. Jinjing Ke et al. [26], in their study on the distraction of construction workers exposed to noise, concluded that although the noise group had a lower level of attention than the control group, there was no statistically significant difference. They concluded that this situation may be due to individual factors such as age, gender and noise sensitivity of the participants. In line with this view, they stated that the participants cared about

their performance during the experiment, they were willing to work harder, and they consciously controlled their attention levels to complete the task. In this study, which was conducted on underground mine workers or those who will work, it was concluded that the results did not differ significantly, due to similar individual effects.

5. Result and Suggestions

In this study, the effects of the noise that the workers who work or will work in the underground mining sector are exposed to in the working areas have been observed experimentally and the important results and suggestions to reduce these effects are as follows:

1. Noise measurements were made in 4 sections of the underground mining training colliery within the Soma Vocational School of Manisa Celal Bayar University, which are a constant source of the noise. In the ambient noise measurements made, 94 dB(A) values were obtained in the section with the chain conveyor, 86 dB(A) in the section with the belt conveyor, 84 dB(A) in the section with the water discharge system, and 88 dB(A) in the section with the ventilation system. The daily noise exposure values were determined in the section where the chain conveyor was the most.

2. Persons who work or will work in the underground training colliery were subjected to an audiometry test in a sound-insulated room and it was examined whether they could hear the noise intensity and frequency range revealed by the devices. Due to the fact that 4 out of 104 people could not hear the operating noise frequency threshold of the mentioned machines, they were not taken to the next measurements, and 100 people whose hearing ability was within the desired tolerances were taken to the Underground Training Colliery. Measurements were made for both ears at frequencies of 125, 250, 500, 750, 1,000, 1500, 2,000, 3,000, 4,000, 6,000, and 8,000 Hz. For the determination of hearing loss, 500, 1,000, 2,000, and 4,000 Hz frequency combination and 25 dB average hearing threshold value recommended in ISO-1999 and TS-2607: ISO 1999 standards were taken into consideration in the evaluation of the test results.

3. In the measurement area prepared in the Underground Training Colliery, 16 EEG electrodes were connected to examine the brain's electrical activities to 100 volunteers who passed the audiometry test. In the first place, the signals of the people were recorded under the conditions when the systems called the 1st case were closed. Afterward, people were exposed to the noise of

machines for a while. After being exposed to noise, people rested outside the underground training for 5 minutes. The rested people were taken back to the underground training to take the final measurements, and in the 3rd case after the noise measurements were made and the data were recorded.

• In the present work, EEG measurements were recorded using 16 electrodes placed (C3, C4, F3, F4, F7, F8, FP1, FP2, O1, O2, P3, P4, P7, P8, T7, T8) on the scalp using the Contec KT88-3200 brand electroencephalography device.

• After the EEG measurements were made, artifact evaluations of the measurements were made and measurements containing too many artifacts were eliminated. After this elimination, 61 data remained.

• In the EEG measurements of the participants, the digital BEAM data obtained before and after the noise exposure in 6 frequency bands (Delta, Theta, Alpha 1, Alpha 2, Beta 1, and Beta 2) of 16 electrodes were analyzed. The frequency bands for digital BEAM are Delta 1– 4 Hz, Theta 4 – 8 Hz, Alpha1 8-12 Hz, Alpha2 12 – 16 Hz, Beta1 16-24 Hz, and Beta2 24-32 Hz. When the before (Case 1) and after (Case 3) values were compared in the SPSS program analysis platform, no statistically significant difference was found as seen in Tables 2 and 3 (P>0.05). The main reasons for not finding a difference may be:

• Young workers participating in the experiment. Jinjing Ke et al. [26] emphasized in his study that this is likely.
• Awareness of the participants that they will be exposed to noise at the time of measurement.

As a result, in underground mines, noise-related physiological effects can be seen in workers who are exposed to noise, especially if they do not use personal protective equipment. For this reason, it is recommended that those who will work in unit areas with high ambient noise levels use personal protective equipment to reduce the noise level they are exposed to. In addition, it is recommended to provide training and inspections aimed at raising awareness among employees about the harmful effects of ambient noise on hearing and other physiological systems and reducing noise levels.

Employers are advised to evaluate risk factors by managing their employees' health examinations and health education, monitoring for significant hearing loss by having audiometry measurements at regular intervals and controlling noise measurements.

It is thought that the results of this study will be a guide for the people who work or will work in the mining sector and the sector representatives. The application of these findings is not only limited to

the mining sector but is important for any environment that requires constant attention in a noisy environment.

In the next study, the cardiovascular effects of noise will be discussed. It is also planned to take into account the age, weight, height and working time of the participants. In order to enrich the results of the study, it is planned to compare the measurements with a reference group.

Author contributions

All authors listed have significantly contributed to the development and the writing of this article.
Ayla TEKİN: Supervised the experimental work and the manuscript process.
Mustafa Oğuz NALBANT: Did literature review and prepared the manuscript
Mustafa ORHAN: Compiled study data.
Fırat TEKİN: Compiled study data.
Fatih SUVAYDAN: Compiled study data.
Kemal BERKİ: Compiled study data.
Sami GUMUS: Were involved in the analysis, interpretation of the data.
Aslı Aydın SAVRAN: Were involved in the analysis, interpretation of the data.

Acknowledgments

Ethics

There are no ethical issues after the publication of this manuscript.

References

[1]. Akbay, D, Altındağ, R, Şengün, N. 2019. Geleneksel Yöntemle Açılan Karayolu Tünellerinde Çalışanların Gürültü Maruziyetlerinin Değerlendirilmesi. *Politeknik Dergisi*. DOI: 10.2339/politeknik.495339.

[2]. Ikuharu M, Kazuhisa M, Shintaro T. 1997. Noise-Induced Hearing Loss in Working Environment and its Background, *Journal of Occupational Health*. 39(1), 5-17. DOI: https://doi.org/10.1539/joh.39.5.

[3]. Nassiri, P, Monazam, M, DehaghiFouladi, B, Abadi, LIG, Zakerian, A. 2013. The effect of noise on human performance: a clinical trial, *International Journal of Occupational and Environmental Health,* 4, pp. 87-95.

[4]. Monteiro, R, Tomé, D, Neves, P, Silva, D, Rodrigues, MA. 2018. Interactive effect of occupational noise on attention and short-term memory: a pilot study, *Noise Health*, 20, pp. 190-198.

[5]. Tekin, A. 2020. Noise Exposure Estimation of Surface-Mine- Heavy Equipment Operators Using Artificial Neural Networks . *Celal Bayar University Journal of Science* , 16 (4) , 429-436. Retrieved from https://dergipark.org.tr/tr/pub/cbayarfbe/issue/58992/773051.

[6]. Sensogut C. 2007. Occupational Noise in Mines and Its Control – A Case Study, *Polish Journal of Environmental Studies*. 16(6):939-942.

[7]. Golmohammadi, R, Darvishi, E, Faradmal, J, Poorolajal, J, Aliabadi, M. 2020. Attention and short-term memory during occupational noise exposure considering task difficulty, *Applied Acoust*ics, 158 107065, https://doi.org/10.1016/j.apacoust.2019.107065.

[7]. Schmidt-Daffy, M. 2012. Velocity versus safety: impact of goal conflict and task difficulty on drivers' behaviour, feelings of anxiety, and electrodermal responses, *Transportation Research Part F: Traffic Psychology and Behaviour,* 15 319–332, https://doi.org/10.1016/j. trf.2012.02.004.

[9]. Ahn, CR, Lee, S, Sun, C, Jebelli, H, Yang, K, Choi, B. 2019. Wearable sensing technology applications in construction safety and health, *Journal of Construction Engineering and Management,* 145, 03119007, https://doi.org/10.1061/(asce)co.1943-7862.0001708.

[10]. Yang, K, Ahn, C.R. 2019. Inferring workplace safety hazards from the spatial patterns of workers' wearable data, *Advanced Engineering Informatics,* 41,100924, https://doi.org/ 10.1016/j.aei.2019.100924.

[11]. Kim, H, Ahn, CR, Yang, K. 2017. Identifying safety hazards using collective bodily responses of workers, *Journal of Construction Engineering and Management,* 143, 04016090, https://doi. org/10.1061/(ASCE)CO.1943-7862.0001220.

[12]. Kim, H, Ahn, CR, Yang, K. 2019. Validating ambulatory gait assessment technique for hazard sensing in construction environments, *Automation in Construction,* 98, 302–309, https://doi.org/10.1016/j.autcon.2018.09.017.

[13]. Jeon, J, Cai, H, Yu, D, Xu, X. 2020. Identification of Safety Hazards Using Wearable EEG, Construction Research Congress, 2020, *American Society of Civil Engineers,* Reston, VA, pp. 185–194, https://doi.org/10.1061/9780784482872.021.

[14]. Choi, B, Jebelli, H, Lee, S. 2019. Feasibility analysis of electrodermal activity (EDA) acquired from wearable sensors to assess construction workers' perceived risk, *Safety Science,* 115, 110–120, https://doi.org/10.1016/j.ssci.2019.01.022.

[15]. Olbrich, S, Mulert, C, Karch, S, Trenner, M, Leicht, G, Pogarell, O, Hegerl, U. 2009. EEGvigilance and BOLD effect during simultaneous EEG/fMRI measurement, *NeuroImage* 45, 319–332, https://doi.org/10.1016/j.neuroimage.2008.11. 014.

[16]. Zhai, J, Chen, X, Ma, J, Yang, Q, Liu, Y. 2016. The vigilance-avoidance model of avoidant recognition: an ERP study under threat priming, *Psychiatry Research,* 246, 379–386, https://doi.org/10.1016/j.psychres.2016.10.014.

[17]. Eoh, HJ, Chung, MK, Kim, SH. 2005. Electroencephalographic study of drowsiness in simulated driving with sleep deprivation, *International Journal of Industrial Ergonomics,* 35, 307–320, https://doi.org/10.1016/j.ergon.2004.09.006.

[18]. Aryal, A, Ghahramani, A, Becerik-Gerber, B. 2017. Monitoring fatigue in construction workers using physiological measurements, *Automation in Construction,* 82, 154–165, https://doi.org/10.1016/j.autcon.2017.03.003.

[19]. Ikenishi, T, Kamada, T, Nagai, M. 2013. Analysis of longitudinal driving behaviors during car following situation by

the driver's EEG using PARAFAC, *IFAC Proc,* Vol. 46, 415–422, https://doi.org/10.3182/20130811-5-US-2037.00023.

[20]. Kawashima, I, Kumano, H. 2017. Prediction of mind-wandering with electroencephalogram and non-linear regression modeling, *Frontiers in Human Neuroscience,* 11, pp. 1-10, https://doi.org/10.3389/fnhum.2017.00365.

[21]. Jeon, J, Cai, H. 2021. Classification of construction hazard-related perceptions using: Wearable electroencephalogram and virtual reality. *Automation in Construction, 132*, 103975.

[22]. Bo, Y, Chao, W, Ji, L, Huimin, L. 2014. Physiological responses of people in working faces of deep underground mines. *International Journal of Mining Science and Technology.* 24(5), 683-688, https://doi.org/10.1016/j.ijmst.2014.03.024.

[24]. Önder, S, Önder, M. 2018. Statistical Investigation of the Noise Levels in Coal Mining Industry. Eskişehir Osmangazi Üniversitesi Mühendislik ve Mimarlık Fakültesi Dergisi. 26(1), 30-35.

[24]. Bashashati, A, Fatourechi, M, Ward, RK, Birch, GE. 2007. A survey of signal processing algorithms in brain-computer interfaces based on electrical brain signals, *Journal of Neural Engineering,* 4, R32–R57, https://doi.org/10.1088/1741-2560/4/2/R03.

[25]. Zauner, A, Fellinger, R, Gross, J, Hanslmayr, S, Shapiro, K, Gruber, W, Müller, S, Klimesch, W. 2021. Alpha entrainment is responsible for the attentional blink phenomenon, *NeuroImage* 63 674–686, https://doi.org/10.1016/j. neuroimage.2012.06.075.

[26]. Ke, J, et al. 2021. Monitoring distraction of construction workers caused by noise using a wearable Electroencephalography (EEG) device. *Automation in Construction,* 125, 103598.

Celal Bayar University Journal of Science

Production of AA2024-Matrix B$_4$C-SiC- and B$_4$C-Y$_2$O$_3$-Particle-Reinforced Composites by Powder Metallurgy and Investigation of Their Mechanical Properties

Halit Doğan[1*] iD, Yılmaz Mutlu[2] iD

[1] Manisa Celal Bayar University, Faculty of Engineering, Department of Mechanical Engineering, 45140 Manisa, Türkiye
[2] Manisa Celal Bayar University, Institute of Natural and Applied Sciences, Department of Mechanical Engineering, 45140 Manisa, Türkiye
*halit.dogan@cbu.edu.tr
*Orcid: 0000-0001-9263-8068

Abstract

In this study, it was aimed to produce Al-matrix composite materials with B$_4$C-SiC and B$_4$C-Y$_2$O$_3$ particle reinforcement using the Powder Metallurgy (PM) method. In the composites in which the reinforcement materials were used at different particle sizes and ratios, AA2024 powders were selected as the matrix material. The powders were homogeneously mixed and compacted at room temperature under a pressure of 525 MPa. The raw specimens were sintered by keeping them at different temperatures for 45 minutes. The composite materials were subjected to wear tests, and their hardness and density values were investigated. In the study, the effects of reinforcement materials added to the matrix at different particle sizes and ratios on wear resistance, hardness, and density at different sintering temperatures were examined. As a result of the mechanical tests that were performed, wear values decreased along with B$_4$C reinforcement ratios that increased in parallel with density values. The highest hardness value was observed as 71.73 HB in the composite specimen with a B$_4$C reinforcement ratio of 20% at the sintering temperature of 595°C.

Keywords: Composite Material, Particle Size and Ratio, Powder Metallurgy, Sintering, Wear.

1.Introduction

Advanced materials have become prevalent worldwide as a consequence of advancements in science and technology, to meet the need for specialized products. The reason for this is that a single material usually cannot meet the requirements of all engineering fields. Therefore, researchers have shown great effort to use composite materials with unique properties. As a result of this, there has been an increase in the production and application fields of metal matrix composites in recent years [1]. In previous years, metal-matrix composites (MMCs) received worldwide attention with their excellent properties combining the best properties of metal matrices and reinforcements [2]. The physical and mechanical properties of MMCs can be improved by adding reinforcement material particles into the matrix. As the matrix material, light metals such as Ti, Al, and Mg that provide support for the reinforcement material are used in general. Among MMCs, the production of aluminum-matrix composites (AMCs) is becoming more prominent each day and finding various usage areas in the industry [3]. Aluminum is an excellent matrix material for developing wear-resistant AMCs [2]. Aluminum alloys are the most convenient alloys following iron alloys [4]. It is well-known that the performance of AMCs is highly dependent on the reinforcements that are added [2]. AMCs use an aluminum alloy as the matrix material and mostly include ceramics like SiC [5-8], B$_4$C [6,7,9], Si$_3$N$_4$ [7], Al$_2$O$_3$ [5,6,8], BN [7], Zr [8], and TiC [7] as the reinforcement material. The properties of AMCs can be changed based on their elemental and volumetric ratios [3]. AMCs reinforced with hard ceramic particles are the most promising materials for various automotive and aviation applications with their low density and high wear resistance [5,7], and they are

used in many fields in the industry, especially in critical applications such as brake calipers, gears, engine blocks, pump components, and valve components [10,11]. Several Al alloys (e.g., 2xxx, 5xxx, 6xxx, 7xxx) are industrially utilized [12]. As a reinforcement material for AMCs, B_4C has attracted special attention [13]. Boron carbide (B_4C) and silicon carbide (SiC) particles, which are the most preferred reinforcement materials for AMCs, strengthen the matrix structure and provide good wear resistance and high thermal stability [12]. B_4C, which is called "black diamond", has a low density (2.52 g/cm^3), high hardness (29.1 GPa), high modulus of elasticity (470 GPa), and high melting point (2540°C) [14]. Because SiC has high hardness values, high resistance to rupture, a high modulus of elasticity, low density, and a low thermal expansion coefficient, its use as a reinforcement material is common [12]. Y_2O_3 ceramics have critical properties such as high thermal and crystallographic stability, and they are used in various applications including protective coatings, microwave radars, solid-state lasers, superconductors, and catalytic converters [27]. In the literature, there are different methods of production including squeeze casting, stir casting, liquid metal infiltration, mechanical alloying, and powder metallurgy for MMCs [15]. The powder metallurgy [PM] method is a production method where mixed metal powders are shaped by compaction into a mold that has been prepared based on the shape and dimensions of the part to be produced and then sintered [6]. PM allows manufacturing processes that result in parts close to those with precisely shaped parts produced out of Al-based materials and MMCs with certain mechanical, thermal, and functional properties [16]. In this study, by ceramic particle reinforcement, Al-B_4C, Al-B_4C-SiC, and Al-B_4C-Y_2O_3 composites with an aluminum alloy matrix were produced, and the effects of the reinforcement materials on the mechanical and microstructure properties of the composites were examined.

2. Materials and Methods

In this study, where reinforcement materials were used at different ratios and particle sizes, AA2024 aluminum alloy powder was used as the matrix component, and B_4C, SiC, and Y_2O_3 powders were used as the reinforcement components at different ratios and particle sizes. Aluminum alloy at a particle size of 100 μm was used as the matrix, while the reinforcement materials included boron carbide (B 4 C) at ratios of 7, 10, 15, and 20% and particle sizes of 10 and 22-59 μm, 20% B_4C + silicon carbide (SiC) at ratios of 3-10% and a particle size of 10 μm, and 20% B_4C + yttrium oxide (Y_2O_3) at ratios of 3-10% and a particle size

of 10 μm. The chemical composition of the AA2024 alloy that was used as the matrix material is shown in Table 1.

2.1 Specimen Preparation

The powders were weighed using a RADWAG PS 1000/C/2 brand precision scale with a sensitivity of 0.001 g and homogeneously mixed at different weight ratios. Composite materials were produced by applying a pressure of 525 MPa onto a mold prepared with the dimensions of 10x10x55 mm using a 100-ton uniaxial hydraulic press branded Hidrokar. Polyethylene glycol (1% wt.) was added to the powder mixtures as a binder. The specimens were sintered at 550, 575, and 595°C for 45 minutes using a Protherm brand furnace.

2.2 Hardness Test

The hardness measurements were made with specimens that were brought to the dimensions of 10x10x10 mm using an EMCO-TEST DuraVision Brinell hardness tester device (Load: 15.625 kg, Ball Diameter: 2.5 mm, Time: 10 s). The effects of B_4C at a particle size of 10 μm that was added to the AA2024 matrix on hardness are shown in Figure 1. It was seen that at all sintering temperatures, as the ratio of the B_4C reinforcement increased, hardness values also increased. This was an expected result because of the higher harness value of the B_4C that was added to the matrix compared to the matrix material. The highest hardness value was found as 71.73 HB in the composite specimen produced using 20% B_4C and sintered at 595°C. Similarly, in the study conducted by Karakoc H. et al. using Al6061 as the matrix material and B_4C and SiC powders as the reinforcement materials, it was found that the composite materials including reinforcements were harder than the unreinforced Al6061 alloy, where the unreinforced alloy had a mean hardness of 50 HB, and the 12% B_4C composite had a mean hardness of 76 HB [12]. Likewise, in their hardness tests on SiC- and B_4C-reinforced Al7071-matrix composite materials they produced with the PM method, Pul M. and Baydaroğlu V. observed that as the reinforcement particle ratio in the structure increased, hardness values also increased [6]. Hasırcı H. and Gül F. also produced AMCs with B_4C reinforcement and examined their mechanical properties. They found higher hardness values in the composite material produced with B_4C reinforcement addition to the Al [17]. Additionally, Ergul E, Kurt H. İ., Cıvı C. and Eyıcı G. mixed 50% MgO and 50% carbon nanotubes (CNT) by weight with the die casting method, added these reinforcement materials to the Al2024 matrix material at ratios of 0.2, 0.5, 1, and 2% by weight,

produced MgO/CNT-reinforced Al2024 composite materials, and investigated hardness results. They observed that the hardness values of the specimens increased by reinforcement addition [18]. Şenel M. C., Gürbüz M. and Koç E. produced composite materials with the PM method by adding Si_3N_4 reinforcement to the aluminum matrix at ratios varying in the range of 0-12% and examined the effects of the reinforcement ratio on the mechanical properties of the composites. According to the results of their experiments, while the hardness value of the pure aluminum was approximately 28 HV, hardness could be increased to 58 HV by adding 9% Si_3N_4 by weight [19].

Table 1. Chemical composition of the AA2024 matrix material (%). [20]

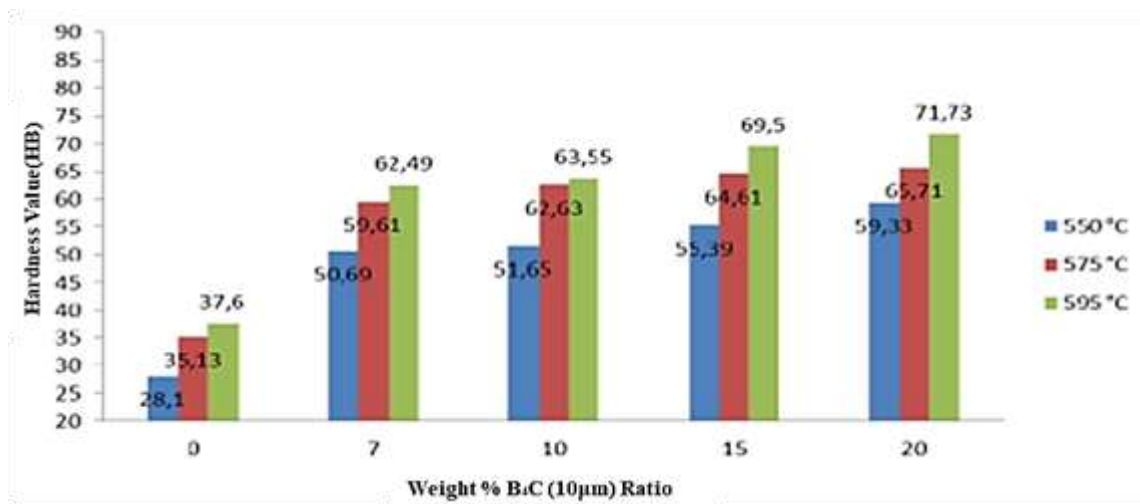| Matrix Material	Chemical Properties							
AA2024	Fe	Si	Cu	Mn	Mg	Zn	Ti	Cr
	0.50	0.50	3.80-4.90	0.30-0.90	1.20-1.80	0.25	0.15	0.10

Figure 1. Changes in the hardness values of AA2024 + 10 μm B_4C depending on temperatures and reinforcement ratios.

Figure 2 shows the effects of the B_4C+SiC added into the AA2024 matrix on hardness. Accordingly, in all specimens sintered at different temperatures, as the ratio of SiC increased, hardness values also increased. The reason for this result was the fact that the hardness values of the B_4C and SiC reinforcement materials were higher than that of the matrix material. The highest hardness value was found as 91.82 HB in the specimen that was produced by adding 20% B_4C + 10% SiC and sintered at 595°C. Likewise, Gündoğan K. and Özsarı A. R. B. investigated the mechanical properties of composite materials produced with an AA2024 or AA6061 matrix and reinforced with B_4C and SiC particles using the pressure infiltration technique. As the pressure values of the composite materials increased, the authors observed an increase in their hardness and strength values. After they compared the reinforcement components, they concluded that the composites with the B_4C reinforcement had better mechanical properties than those with the SiC reinforcement [21].
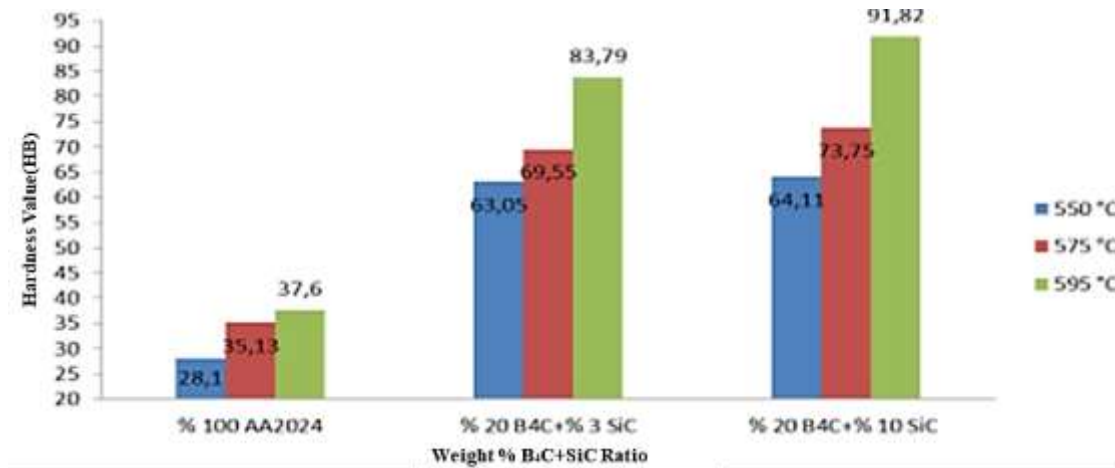
Figure 2. Changes in the hardness values of AA2024+B$_4$C+SiC depending on temperatures and reinforcement ratios.

Figure 3 shows the effects of B$_4$C+Y$_2$O$_3$ added into the AA2024 matrix on hardness. It is seen that as the ratio of Y$_2$O$_3$ increased, hardness values also increased. The reason for this result was the fact that the hardness values of the B$_4$C and Y$_2$O$_3$ reinforcement materials were higher than that of the matrix material. The highest hardness value among the AA2024-matrix B$_4$C+Y$_2$O$_3$-reinforced composite materials was found as 85.33 HB in the specimen that was produced by adding 20% B$_4$C + 10% Y$_2$O$_3$ and sintered at 595 °C.
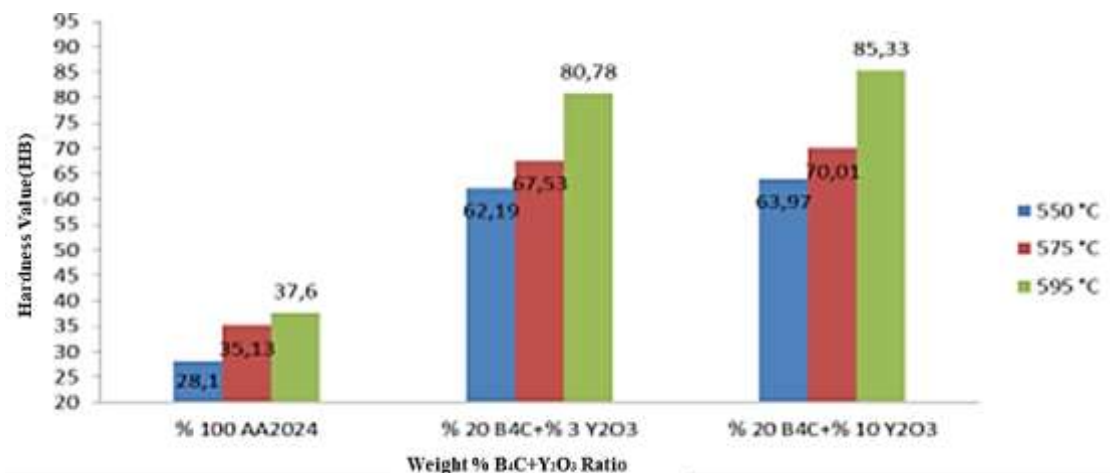

Figure 3. Changes in the hardness values of AA2024+B$_4$C+ Y$_2$O$_3$ depending on temperatures and reinforcement ratios.

In the composites that were produced, in general, hardness values were observed to increase along with increased reinforcement ratios and sintering temperatures.

2.3 Density

The density measurements of the composite materials were made using a RADWAG AS 220/C/2 brand density measurement device based on the Archimedes principle. Figure 4 presents the effects of B$_4$C at a particle size of 10 μm that was added into the AA2024 matrix on density and porosity. Accordingly, in all specimens sintered at

different temperatures, as the ratio of B$_4$C reinforcement increased, density decreased, and porosity increased. The density values of the examined specimens were compatible with those reported in the literature, and as the B$_4$C reinforcement ratio increased, density decreased. The main reason for this was the increased porosity that was observed and the fact that B$_4$C is a material that has a low density.

Similarly, in the Al2024-matrix B$_4$C- and TiB$_2$-reinforced composite materials produced by Pul M., as the ratio of reinforcement increased, the ratio of pores between TiB$_2$ and B$_4$C particles and the

aluminum powder increased, and thus, density values decreased [22]. Topcu İ., Dikici M. and İpek C. also investigated the density and wear resistance of aluminum-matrix B_4C-reinforced composite materials. The lowest density value was observed in the Al/B_4C composite with the highest B_4C ratio by weight (15%). It was seen that the density values of the specimens decreased along with increased B_4C ratios, but the values of the specimens with the same B_4C reinforcement ratios increased along with increased sintering temperatures [23].
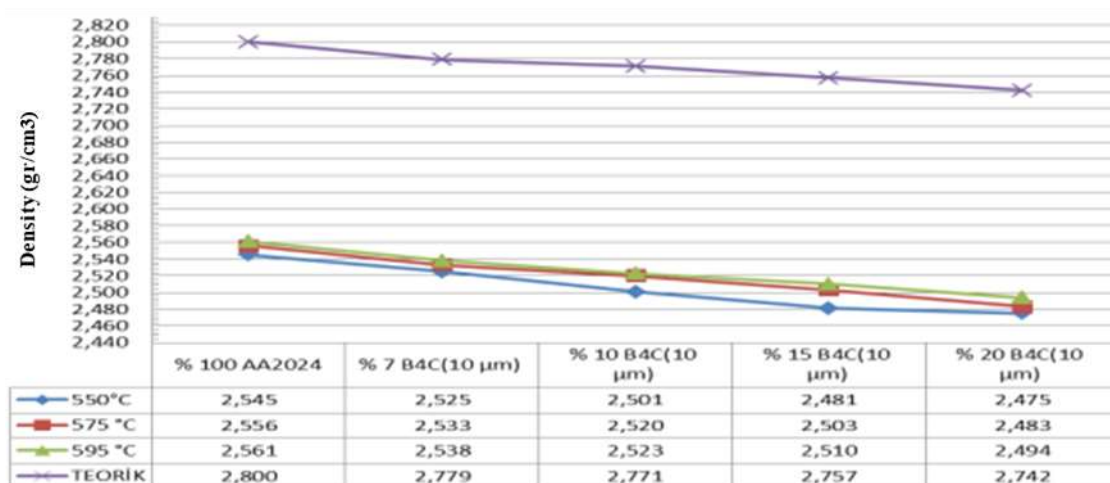

Figure 4. Changes in the density values of AA2024 + 10 μm B_4C depending on temperatures and reinforcement ratios.

The effects of B_4C+SiC added into the AA2024 matrix on density are shown in Table 2. Accordingly, as the ratio of SiC that was added increased, the ratio of porosity also increased. The effects of B_4C and Y_2O_3 added into the AA2024 matrix on density are shown in Table 3. Accordingly, in all specimens sintered at different temperatures, as the ratio of Y_2O_3 that was added increased, both density and porosity increased.

Table 2. Changes in the density values of AA2024 + B_4C+SiC depending on temperatures and reinforcement ratios.

AA2024+(B4C+SiC)									
Sequence No	**% AA2024**	**% B4C**	**% SiC**	**AA2024 particle size (μm)**	**B4C particle size (μm)**	**SiC particle size (μm)**	**Sintering temperature (°C)**	**Theoretical density value (g/cm³)**	**Experimental density value (g/cm³)**	**Pore ratio (%)**
1	77	20	3	100-150	22-59	10	550	2,754	2,470	10,31
							575		2,479	9,98
							595		2,495	9,40
2	70	20	10	100-150	22-59	10	550	2,783	2,475	11,06
							575		2,483	10,77
							595		2,499	10,20

Table 3. Changes in the density values of AA2024 + $B_4C+Y_2O_3$ depending on temperatures and reinforcement ratios.

				AA2024+(B4C+Y$_2$O$_3$)						
Sequence No	% AA2024	% B$_4$C	% Y$_2$O$_3$	AA2024 particle size (μm)	B$_4$C particle size (μm)	Y$_2$O$_3$ particle size (μm)	Sintering temperature (^{o}C)	Theoretical density value (g/cm^3)	Experimental density value (g/cm^3)	Pore Ratio (%)
1	77	20	3	100-150	22-59	10	550 575 595	2,808	2,501 2,519 2,523	10,93 10,29 10,14
2	70	20	10	100-150	22-59	10	550 575 595	2,963	2,609 2,619 2,635	11,94 11,60 11,06

2.4 Wear Test

The wear tests were carried out with the Tribometer pin-on-disk wear testing device shown in Figure 5 under a 2N load for 15 minutes (3.516 mm track diameter, 20000 mm sliding distance, and 2000 cm/s linear velocity). Like the density test results, as the ratio of B_4C reinforcement increased, wear values decreased. As seen in Figure 6, in all specimens sintered at different temperatures, wear values decreased along with increasing reinforcement ratios. These results were similar to the results of other studies conducted with composite materials. Hasırcı H. and Gül F. produced Al-matrix B_4C-reinforced composite materials and investigated their wear behaviors. They reported that the hardness of the composite increased due to the B_4C reinforcement particles added into the matrix, the pure Al material had the lowest hardness values, and in general, wear amounts decreased in the composites in comparison to the pure Al material as the ratio of reinforcement increased [17]. Likewise, Karakoç H. observed lower wear amounts based on weight loss as a result of B_4C and Si_3N_4 reinforcement addition [24]. In another study by Karakoç H., Al7075/B_4C and Al7075/B_4C/Si_3N_4 composite materials were produced using the powder metallurgy method, and their wear behaviors were analyzed. The researcher determined a decrease depending on increased ratios of B_4C and Si_3N_4 by weight and found the lowest weight loss value in the Al7075/15%B_4C/2%Si_3N_4 material [24]. Furthermore, Arık H. studied the effects of SiC as a reinforcement component on the wear properties of aluminum-matrix composite materials. The author used PM as the production method for Al-SiC composite materials and the pin-on-disk method in the wear test. It was observed that the weight loss value decreased by 48.4% to 79.6% when SiC was added at 10% by weight to the matrix [25]. Aksöz S. and Bostan B. produced 10/20% B_4C-reinforced AA2014-matrix composite materials using the casting method and sintering at 600°C for 2 hours after casting and examined the effects of reinforcement ratios on wear behaviors. They found lower wear-related weight loss as a result of adding increased ratios of B_4C reinforcement and sintering. The lowest weight loss was observed in the composite material containing 20% B_4C that was sintered at 600°C for 2 hours [26].
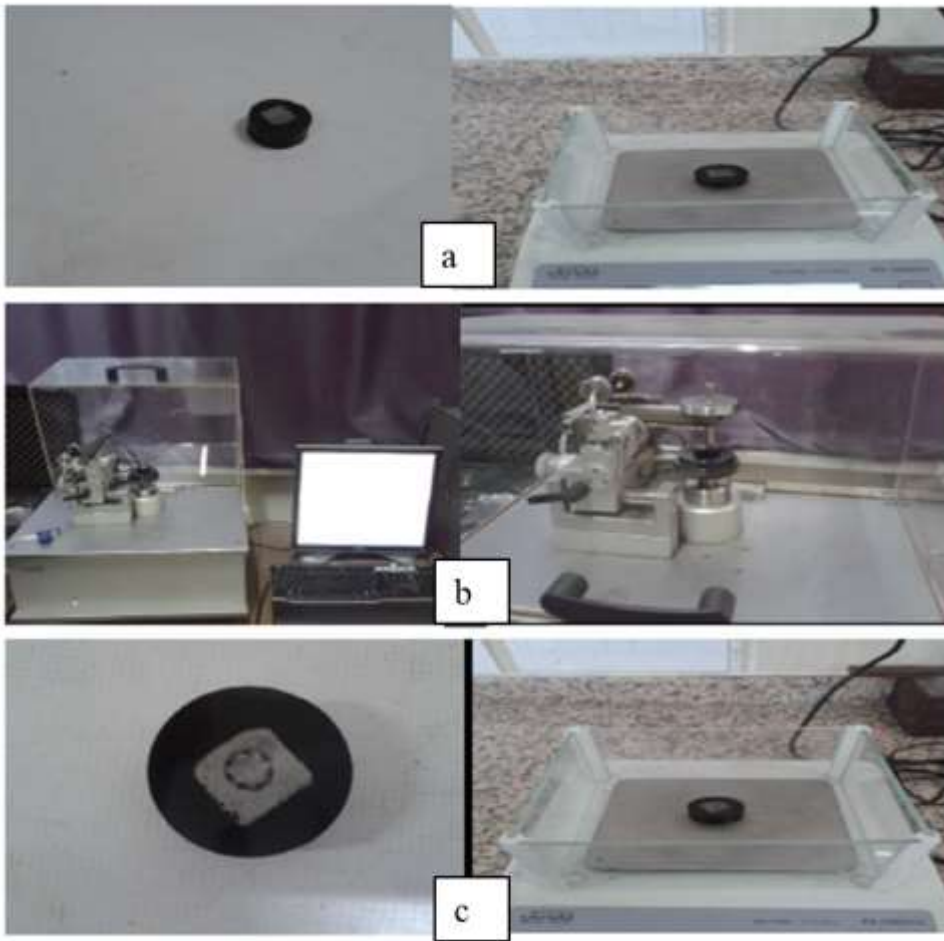
Figure 5. Wear tests of the composite specimens (a: Weighing before the test; b: Wear test; c: Weighing after the test).
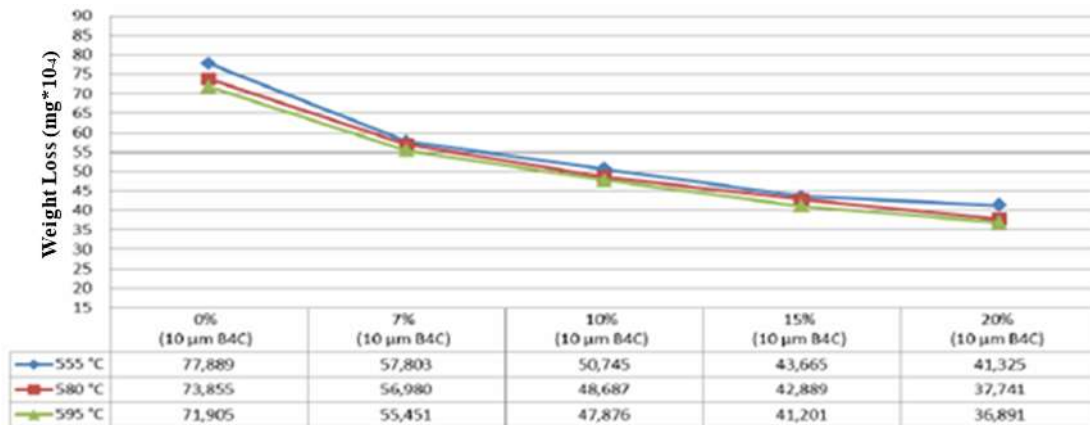

Figure 6. Changes in the weight loss values of AA2024 + 10 μm B_4C depending on temperatures and reinforcement ratios.
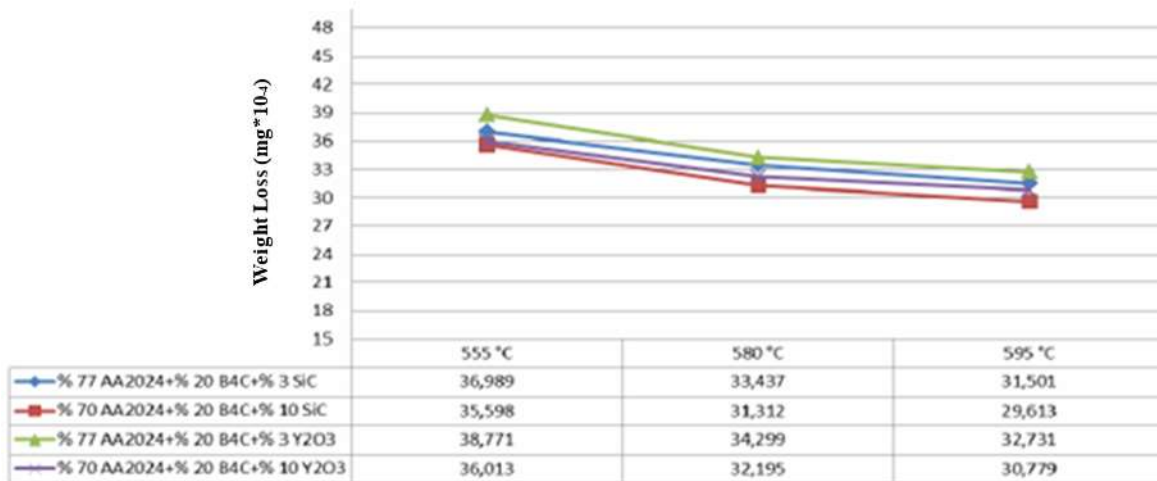
Figure 7. Changes in the weight loss values of AA2024+(B$_4$C+SiC) and AA2024+(B$_4$C+Y$_2$O$_3$) depending on temperatures and reinforcement ratios.

Figure 7 presents the changes in the weight loss values of AA2024+(B$_4$C+SiC) and AA2024+(B$_4$C+Y$_2$O$_3$) along with increased sintering temperatures. It is seen that with the increase in the sintering temperature, wear values decreased, and the AA2024+(B$_4$C+SiC) composite had higher wear resistance values in comparison to the AA2024+(B$_4$C+Y$_2$O$_3$) composite.

2.5 SEM

The microstructures of the specimens were examined using a JEOL JSM-6060 brand SEM device.
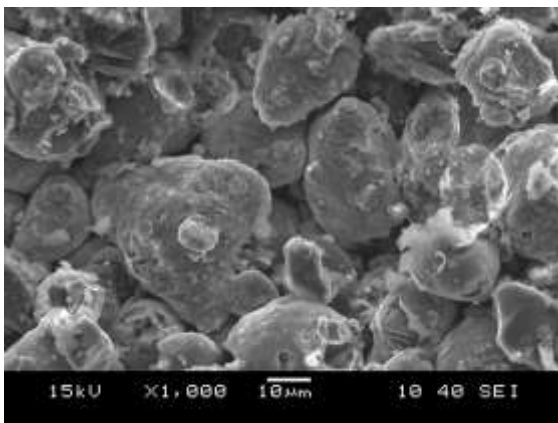

Figure 8. SEM image of 85%AA2024+15%B$_4$C (10 μm) sintered at 575°C (x1000).

Figure 9. SEM image of 77%AA2024+20%B$_4$C (22-49 μm) +3%SiC sintered at 575°C (x500).

It was observed in the microstructure of the 77%AA2024+20% B$_4$C (22-59 μm) +3% SiC composite shown in Figure 9 that the distributions of B$_4$C and SiC were generally homogeneous but occasionally non-homogeneous, and the structure was non-porous in general.

As seen in Figures 8 and 9, although both materials were sintered at the same temperature, the 77%AA2024+20% B$_4$C (22-59 μm) +3%SiC composite had a lower porosity value because a more compacted structure was obtained with the addition of SiC (10 μm).
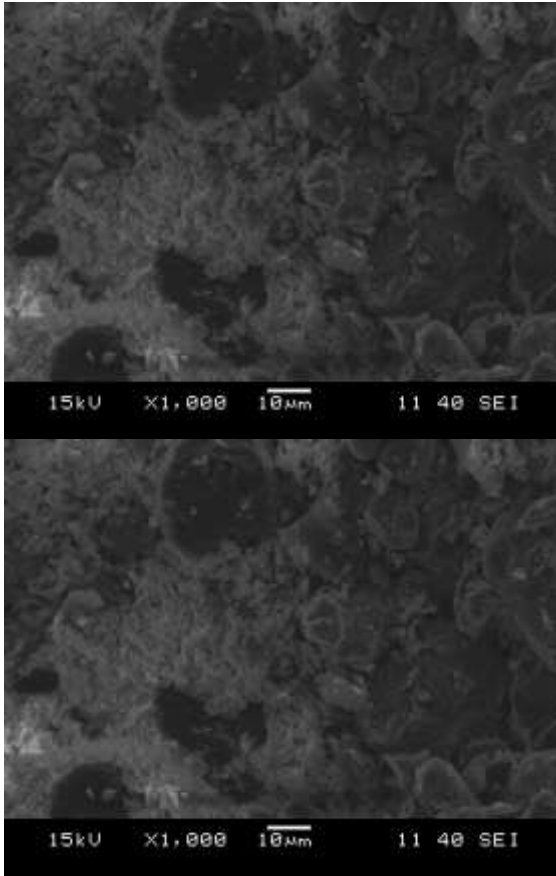
Figure 10. SEM image of 70%AA2024+20%B$_4$C (22-59 μm) +10%Y$_2$O$_3$ sintered at 575°C (x1000).

Figure 10 shows the microstructure of the composite that had lower porosity due to the more compacted structure that was obtained with the addition of 10 μm Y$_2$O$_3$.

3. Results

The conclusions made based on the results of the experiments that were conducted in this study are given below.

1- As the reinforcement particle ratio by weight increased, the hardness values of the composites increased, and in comparison to the unreinforced AA2024 matrix material, the hardness values of the composites were approximately 2.5 times higher.

2- The density values of the 10 μm B$_4$C-reinforced composites decreased along with increasing reinforcement ratios.

3- With the increase in the reinforcement particle ratio by weight, there was a decrease in the wear-related weight loss values of the composites.

4- The SEM examinations (Figures 9 and 10) showed lower porosity values depending on the addition of SiC (10 μm) and Y$_2$O$_3$ (10 μm) due to the more compacted structure that was obtained.

Author Contributions

Halit Doğan: He planned, designed and performed the analysis.
Yılmaz Mutlu: He designed the study, made the statistical analyzes and wrote the article.

Ethics

There are no ethical issues after the publication of this manuscript.

References

[1]. Herzallah H., Elsayd A., Shash A., Adly M.,; Effect of carbon nanotubes (CNTs) and silicon carbide (SiC) on mechanical properties of pure Al manufactured by powder metallurgy, j m a t e r r e s t e c h n o l . 2 0 2 0;9(2):1948–1954. https://doi.org/10.1016/j.jmrt.2019.12.027

[2]. Zhang J., Liu Q., Yang S., Chen Z., Liu Q., Jiang Z.,; Microstructural evolution of hybrid aluminum matrix composites reinforced with SiC nanoparticles and graphene/graphite prepared by powder metallurgy, Progress in Natural Science: Materials International 30 (2020) 192–199. https://doi.org/10.1016/j.pnsc.2020.01.024

[3]. Sharma A. K., Bhandari R., Pinca-Bretotean C.,; A systematic overview on fabrication aspects and methods of aluminum metal matrix composites, Materials Today: Proceedings 45 (2021) 4133–4138. https://doi.org/10.1016/j.matpr.2020.11.899

[4]. Fuse K., Badheka V., Patel V., Andersson J.,; Dual sided composite formation in Al 6061/B4C using novel bobbin tool friction stir processing, j o u r n a l o f m a t e r i a l s r e s e a r c h and technology 2 0 2 1 ; 1 3 : 1 7 0 9 e1 7 2 1. https://doi.org/10.1016/j.jmrt.2021.05.079

[5]. Devadiga U., Fernandes P.,; Taguchi analysis for sliding wear characteristics of carbon nanotube-flyash reinforced aluminium nanocomposites, Heliyon 7 (2021) e06170. https://doi.org/10.1016/j.heliyon.2021.e06170

[6]. Pul M. ve Baydaroğlu V., B4C/SiC katkılı alüminyum esaslı kompozitlerin mekanik özelliklerin incelenmesi ve balistik performanslarının modellenmesi, Politeknik Dergisi, 23(2): 383-392, (2020). https://doi.org/10.2339/politeknik.525011

[7]. Şenel M. C.,; Toz Metalürjisi Yöntemiyle Üretilen Saf Al ve Al-B4C, Al-Al2O3 Kompozitlerin Mekanik ve Mikroyapı Özelliklerinin Karşılaştırılması, GÜFBED/GUSTIJ (2020) 10 (3): 783-795. https://doi.org/10.17714/gumusfenbil.689359

[8]. Yang J., Chung D.D.L.,; Wear of bauxite-particle reinforced aluminum alloys", Composite Materials Research Laboratory,

Furnas Hall, State University of New York, Buffalo, NY 14260(U.S.A.), Wear, 135: 53-65 (1989). https://doi.org/10.1016/0043-1648(89)90095-1

[9]. Abenojar J.; Velasco F.; Martinez M.A.; Optimization of Processing Parameters for The Al + 10% B4C System Obtained by Mechanical Alloying, Journal of Materials Processing Technology 184(2007) 441–446. https://doi.org/10.1016/j.jmatprotec.2006.11.122

[10]. Saessı M., Alızadeh A., Abdollahı A.,; Wear behavior and dry sliding tribological properties of ultra-fine grained Al5083 alloy and boron carbide-reinforced Al5083-based composite at room and elevated temperatures, Trans. Nonferrous Met. Soc. China 31(2021) 74−91. https://doi.org/10.1016/S1003-6326(20)65479-6

[11]. Lakshmikanthan A., Prabhu T.R., Babu U. S., Koppad P. G., Gupta M., Krishna M., Bontha S.,; The effect of heat treatment on the mechanical and tribological properties of dual size SiC reinforced A357 matrix composites, j m a t e r r e s t e c h n o l . 2 0 2 0;9(3):6434–6452. https://doi.org/10.1016/j.jmrt.2020.04.027

[12]. Karakoc H., Ovalı İ, Dündar S., Çıtak R.,; Wear and mechanical properties of Al6061/SiC/B4C hybrid composites produced with powder metallurgy, j m a t e r r e s t e c h n o l . 2 0 1 9;8(6):5348–5361. https://doi.org/10.1016/j.jmrt.2019.09.002

[13]. Aherwar A., Patnaik A., Pruncu C. I.,; Effect of B4C and waste porcelain ceramic particulate reinforcements on mechanical and tribological characteristics of high strength AA7075 based hybrid composite, j m a t e r r e s t e c h n o l . 2 0 2 0;9(5):9882–9894. https://doi.org/10.1016/j.jmrt.2020.07.003

[14]. Boussebha H., Bakan S., Kurt A. O.,; Dynamic / thermochemical method: A novel approach in the synthesis of B4C powder, Open Ceramics 6 (2021) 100133. https://doi.org/10.1016/j.oceram.2021.100133

[15]. Abd-Elwahed M.S., Sadoun A.M., Elmahdy M.,; Electroless-plating of Ag nanoparticles on Al2O3 for enhanced mechanical and wear properties of Cu–Al2O3 nanocomposites, j m a t e r r e s t e c h n o l . 2 0 2 0;9(6):13749–13758. https://doi.org/10.1016/j.jmrt.2020.09.077

[16]. Balog M., Orovcik L., Nagy S., Krizik P., Nosko M., Oslanec P., Zifcak P.,; To what extent does friction-stir welding deteriorate the properties of powder metallurgy Al?, j m a t e r r e s t e c h n o l . 2 0 2 0;9(3):6733–6744. https://doi.org/10.1016/j.jmrt.2020.04.087

[17]. Hasan H., Ferhat G.,; B4C / Al Kompozitlerin Takviye Hacim Oranına Bağlı Olarak Abrasif Aşınma Davranışlarının İncelenmesi, SDU International Technologic Science, 2(1): 15-21, (2010). https://dergipark.org.tr/tr/pub/utbd/issue/25991/273754

[18]. Ergul E., Kurt H.I., Civi C., Eyici G., Wear Characteristics of Carbon Nanotube Reinforced Al2024 Composites, El-Cezerî Fen ve Mühendislik Dergisi 2020, 7(3); 1008-1016. https://doi.org/10.31202/ecjse.716287

[19]. Şenel M. C., Gürbüz M., Koç E.,; Toz Metalürjisi Metoduyla Üretilen Al-Si3N4 Metal Matrisli Kompozitlerin Mekanik Özelliklerinin İncelenmesi, Mühendis ve Makina Dergisi, cilt 59, sayı 693, s. 33-46, 2018. https://dergipark.org.tr/tr/pub/muhendismakina/issue/48384/612874

[20]. Şık A., Ertürk İ. ve Önder M., AA2024 Alüminyum Alaşımının Sürtünme Karıştırma Kaynağında Farklı Parametrelerin Mekanik Özelliklere Etkisinin İncelenmesi, Pamukkale Üniversitesi Mühendislik Bilimleri Dergisi Cilt 16, Sayı 2, 2010, Sayfa 139-147. https://dergipark.org.tr/en/pub/pajes/issue/20508/218316?publisher=pamukkale

[21]. Gündoğan K., Özsarı A.R.B.,; Basınçlı İnfiltrasyon Yöntemiyle Üretilen AA2024 ve AA6061 Matrisli, B4C ve SiC Takviyeli Kompozit Malzemelerin Mikroyapı, Mekanik ve Isıl İletkenlik Özelliklerine Basıncın Etkisi, UMAGD, (2019) 11(2), 657-669. https://doi.org/10.29137/umagd.540610

[22]. Pul M.,; Toz Metalurjisi Yöntemiyle Üretilen B4C+TiB2 Takviyeli Al 2024 Esaslı Kompozitlerde Takviye Miktarının Mekanik Özelliklere Etkisi, UMAGD, (2019) 11(1), 87-99. https://doi.org/10.29137/umagd.407488

[23]. Topcu İ, Dikici M., İpek C.; Seramik Takviyeli Alüminyum Esaslı Metal Matrik Kompozitlerin Aşınma Özelliklerinin İncelenmesi, Published in 6th International Symposium on Innovative Technologies in Engineering and Science 09-11 November 2018 (ISITES2018 Alanya – Antalya - Turkey). https://doi.org/10.33793/acperpro.01.01.91

[24]. Karakoç H., Toz metal Al7075/B4C/Si3N4 kompozit malzemelerin üretimi ve aşınma özelliklerinin incelenmesi, Politeknik Dergisi, 23(4): 1141-1151, (2020). https://doi.org/10.2339/politeknik.585813

[25]. Arık H.,; Investigation of Wear Properties of Al-SiC Composite Materials Produced by Powder Metallurgy Method, GU J Sci, Part C, 7(3): 741-754 (2019). https://doi.org/10.29109/gujsc.587637

[26]. Aksöz S., Bostan B.; AA2014/B4C MMK yapının döküm ve döküm sonrası sinterleme işlemleri ile üretiminin aşınma davranışlarına etkileri, BORON 3 (2), 132 - 137, 2018. https://doi.org/10.30728/boron.373140

Celal Bayar University Journal of Science

Statistical Analysis of Noise-induced Brain Electrical Activity of Employees in the Underground Mining Sector in the Soma Basin

Ayla Tekin[1] , Mustafa Oğuz Nalbant[1*] , Mustafa Orhan[1] , Fırat Tekin[1] , Fatih Suvaydan[1] ,
Kemal Berki[1] , Aslı Aydın Savran[2] , Sami Gümüş[2]

[1] Manisa Celal Bayar University, Soma Vocational School
[2] Soma Medigün Hospital
* mustafa.nalbant@cbu.edu.tr
* Orcid: 0000-0002-9311-2241

Abstract

In the mining sector, which requires a lot of attention, excessive noise pollution is encountered during the works due to the use of mining machines, and this is observed as one of the most important factors causing various problems for the personnel working in underground mining. The present study investigated the neurological effects of instantaneous noise exposure and exposure to noise on workers' health in the underground mining sector using electroencephalography (EEG) device. Firstly, the noises that underground workers are exposed to in different working areas were determined. One hundred people working or working in the mining industry were included in the study. Brain electrical activities of these people were measured at periodic intervals under the noise that occurred in the underground mine. Their relationship with occupational noise exposure was analyzed statistically. As a result of these measurements, the values collected in noise-free and noisy environments were compared.

Keywords: Noise Effect, Underground Mining, Occupational Health, Statistical Analysis, EEG.

1. Introduction

Today, rapidly developing technology includes many positive developments that will make life easier. However, these developments also have aspects that negatively affect human health. One such negative problem is noise. Noise is an important problem in all workplaces and is one of the effective parameters in the occurrence of occupational accidents [1]. The most important effect of noise on human health is on the hearing system [2]. In addition to negatively impacting hearing loss and verbal communication, noise can also lead to distress, cardiovascular disease, sleep disturbance, and even cognitive performance. Many studies have confirmed a direct relationship between increased noise levels and decreased cognitive performance [3-6]. As noted in the study of Rostam Golmohammadi et al., noise caused people to react more quickly due to higher stress levels compared to silence, and the noise was found to be a distraction for cognitive performance in occupational settings [7]. Distraction on employees is quite common. However, the issue of distraction

at worksites has not yet been adequately explored. Since distraction occurs due to reasons such as noise, moving vehicles, body discomfort, fatigue, depression, a wearable physiological device has been proposed to monitor the distraction of employees. It has been conducted a research to improve hazard identification performance by analyzing people's physical and physiological responses through wearable sensors. The basic logic in this research is that employees show unusual or abnormal reactions when faced with a danger [8-9]. Physical responses (eg walking and stepping) have been studied using wearable sensors and the relationship between the presence of hazards and changes in physical responses has been demonstrated [10-12]. Similarly, physiological responses (eg, eye movement, brain activity) derived from wearable sensors have also been investigated to elicit and identify hazards in the environment [13-14]. Electroencephalogram (EEG) is a diagnostic imaging technique used to obtain information about brain activities by detecting voltage changes created by neurons on the scalp cortical surface, and new technologies have made it

possible to obtain EEG data without any problems [15]. Because the brain activity is directly linked to people's cognitive processes [16], some studies have also analyzed patterns of brain electrical activity measured using EEG to predict cognitive states such as stress, attention, mental workload, and alertness [17-19]. A different study suggested using EEG to detect a person's mind wandering. The findings showed that EEG data from several electrodes could predict the intensity of mind wandering and contributed to the development of neurofeedback studies [20]. Jeon and Cai [21] investigated the feasibility of identifying construction hazards by developing an EEG classifier based on wearable experiments that can classify EEG signals associated with perceived hazards in a virtual reality (VR) environment. At the work of You Bo et al; investigated the effects of underground mining conditions (high temperature, high humidity, noise, etc.) on human health and safety. They used a memory test before and after exercise to examine the effects of mining conditions on the brain nerve activity of workers. However, to analyze the effect of temperature and humidity on workers' body blood pressure (including systolic pressure, diastolic pressure, and mean pressure), heart rate, respiratory rate, body temperature, body weight, typing speed, and memory level, a bedside monitor, and EEG device have been used. As a result of the study, it has been quantitatively and accurately analyzed that high temperature and high humidity in the mine have a detrimental effect on body physiology and labor productivity and that occupational health standards should be taken as a reference [22]. Önder, and Önder [23] in their study, they made statistical noise analysis in three main mining areas including lavavar, open pit and underground mine.

In summary, noise exposure is dangerous for occupational health, harms the perception of risk, and increases the psychophysiological burden. Since the noise of the machines in the mining industry is harmful, the focus of the present research is to evaluate the noise levels and analyze the physiological responses of the machines with a wearable EEG that can classify the EEG signals in the noise environment in which they operate.

2. Materials and Methods

In this study, an Electroencephalography (EEG) device was used to measure and analyze the electrical activities in the brain during exposure to noise of people who work or will work in the underground mining sector. Measurements were made on 100 people. Selected 100 people work in the mining company with 5500 personnel. Factors such as the fact that the people are male and

working in the underground area were taken into consideration during the selection.

2.1. Location of Measurements

Measurements were made in the underground mine training pit, where chain conveyor, belt conveyor, water discharge systems, and ventilation systems, which are constant source of noise in underground mining enterprises, are located. The underground training colliery where measurements were made is shown in Figure 1.

Figure 1. Underground Training Colliery where the study was carried out.

The noise levels of each noise source were measured with a calibrated PCE-430 brand noise measuring device as listed in Table 1 and the noise intensity was observed to vary between 84 -94 dBA.

Table 1. Noise Intensities of Underground Training Machines.

Noise Source	Noise Intensity (dB)
Chain Conveyor	94
Belt Conveyor	86
Water Disposal System	84
Ventilation	88

2.2. Participants

One hundred male volunteers who work and will work in mining enterprises in Soma, which has the highest quality lignite reserves in Turkey, were studied. In the light of the information obtained as a

result of the survey conducted with the workers, the characteristics of the workers were formed as in Table 2. In addition, all volunteer employees were subjected to audiometric tests with the AMPLIVOX 240 brand audiometer device and audiometric tests were applied to all-volunteer employees. As seen in Figure 2, workers whose hearing limit is below the sound produced by noise sources were not included in the experiment.

Table 2. Characteristics of the Worker Population.

Worker (N:100)			
Old (year)			
Mean ± SD	Min-Max	23,95 ± 5,26	19 - 49
Weight (kg)			
Mean ± SD	Min-Max	76,46 ± 16,85	55 - 115
Height (cm)			
Mean ± SD	Min-Max	176,68 ± 5,80	166 - 186

All volunteers accepted the use of personal data in academic studies and accepted that these data are sensitive data and they were informed that the results obtained are handled collectively with methods and purposes in accordance with scientific principles. Also, before the experiment, all participants were fully informed about the general experimental procedure and signed a consent form.
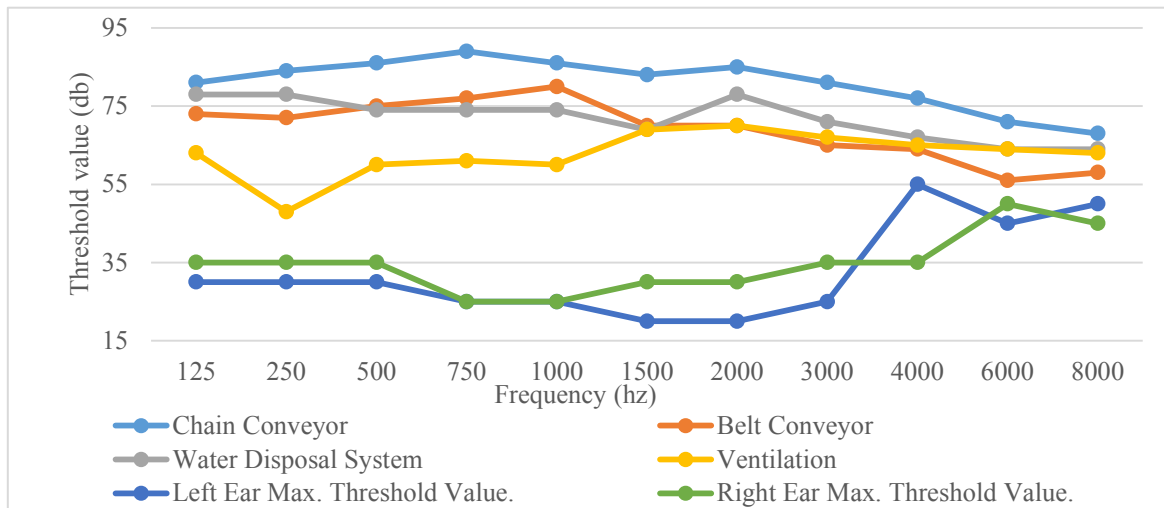

Figure 2. Comparison of noise intensity per frequency of noise sources and minimum hearing thresholds per frequency of participants.

2.3. Equipment and Measurements

A wearable physiological device has been proposed to monitor employee distractions. Instead of transmitting events between a single neuron, EEG records the total activity of thousands or millions of neurons as oscillatory activity [24]. EEG signals are mostly between 0.5-4 Hz Delta (δ), 4-8 Hz signals Theta (θ), 8-16 Hz signals Alpha (α), 16-32 Hz signals Beta (β), 32 Hz and The signals above are divided into five frequency bands as Gamma (γ). The band gaps of the EEG signals cause different success rates depending on the classification target. Thanks to the research in this field, the band gaps in which emotional states are active and the brain activities that are generally active can be grouped [25].

Figure 3. Electroencephalography Device

With the Contec KT88-3200 brand electroencephalography device shown in Figure 3, the brain electrical activities of the individuals were recorded separately before and after the operation of the machines that are the source of noise in the underground training colliery.

In the study, in order to examine the effect of noise on mine workers, measurements were taken from 100 people (males) who are working or will work in mining companies in the Soma basin, with the algorithm drawn in Figure 4.
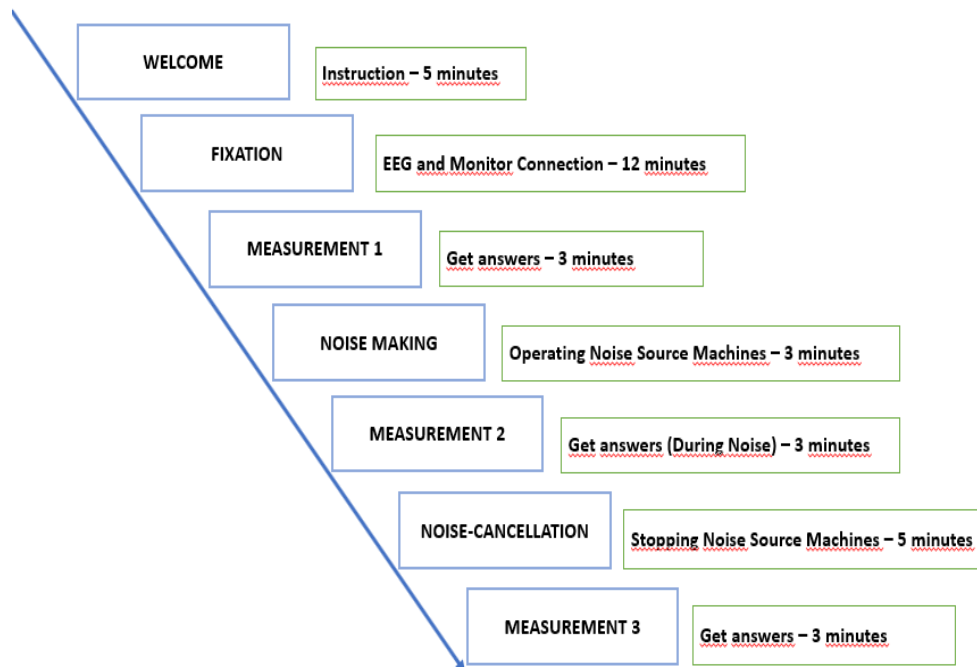

Figure 4. The procedure of each experimental personnel.

In order to examine the electrical activities of the brain in the measurement area prepared in the Underground Training Colliery, 16 EEG electrodes were connected to the places included in the box in the diagram given in Figure 4. In the first place, the signals of the person were recorded under the conditions when the systems called the 1st state were turned off. Then the person was exposed to the noise of the machines for a while. After the noise, the person was measured after the noise as the 2nd situation, and the data were recorded. After these measurements, the person rested for 5 minutes outside the Underground Training Colliery.

The rested person was taken back to the Underground Training Colliery to take the final measurements. The person was connected to the bedside monitor and EEG in the sitting position and the last measurements were taken. The following values were recorded in three cases.

- **1.Case:** In a noise-free environment, SYS, DIA, MEAN, HR, PR, SPO2, RR, and body temperature values were obtained with a bedside monitor, and Brain Electrical Activity Mapping with EEG.
- **2.Case:** SYS, DIA, MEAN, HR, PR, SPO2, RR, and body temperature values were recorded in a noisy environment.

- **3.Case**: After the noise, SYS, DIA, MEAN, HR, PR, SPO2, RR, and body temperature values were recorded and Brain Electrical Activity Mapping was performed with EEG.

2.4. Monitoring the Electrical Activities of the Brain with Electroencephalography Device

In this study, the positions of the measurement and reference electrodes on the skull were predetermined. Figure 5 shows this arrangement. For signal recording, 18 channels of 32-channel Electroencephalography (EEG) device, 2 of which are references, were used. EEG data were recorded by placing electrodes on the scalp. The electrodes are placed symmetrically to the brain regions. Before the measurement was taken, the electrodes were checked for wear. Then the electrodes were washed and disinfected with alcohol. Here, "Nasion" defines the front part of the head and "Inion" defines the back part. In the 10-20 system, odd-numbered electrodes identify the left side of the brain, and even-numbered electrodes identify the right side of the brain. The letters in front of the numbers are the abbreviations of the names of the relevant regions of the brain. (Fp = frontopolar; F = frontal; C = central; P = parietal; O = occipital; T = temporal). The brain regions where they are located

and their electrode nomenclature are as follows; on the frontal lobe (Fp1, Fp2), (F3, F4, Fz, F7, F8), on the temporal lobe (T7, C3, C4, T8), on the occipital lobe (O1, O2), on the parietal lobe (P7, P3, P4, P8) and on the central region (C3, C4). Electrical activity was recorded by reference to the ear reference electrodes (A1 and A2). 500 Hz as the sampling frequency for each channel. value is used.
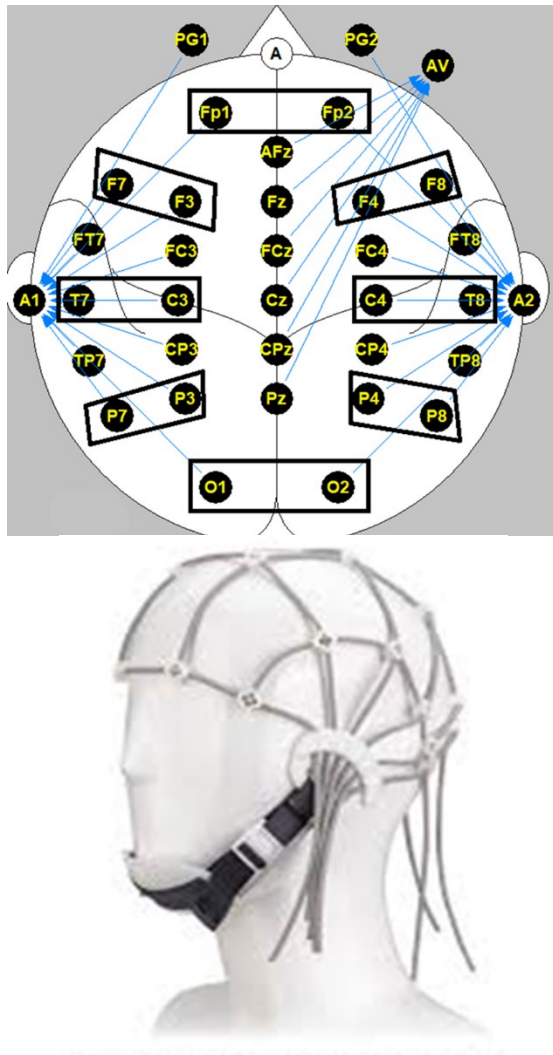

Figure 5. Electroencephalography Electrode Layout Diagram.

2.5. Statistical Analysis

The data obtained from the research were analyzed as dependent data in the SPSS statistical analysis program. Statistical analysis of the data, arithmetic mean and standard deviation (SD) were calculated according to the nature of each variable. Whether the data violated the assumption of normal distribution was checked using Kolmogorov-Smirnov's Lilliefors Significance Correction and Shapiro-Wilks Test. As a result of the controls, the tests of the workers and the scores they got from the

attitude scale were compared using the Parametric T-Test for Related Samples, and the Nonparametric T Test for Unrelated Samples and the Wilcoxon Test. While analyzing the data, the significance level (p) was taken as 0.05.

3.   Findings

In the present study, the effects of noise generated in underground mining on worker health were examined. During the study, the brain electrical activities of 100 people who work or will work in the mining sector were recorded for two different situations, and the data obtained in a noise-free environment and a noisy environment were compared, and the risk levels of noise and its effects on people were statistically analyzed.

3.1. Electroencephalography Results

At the measurement area prepared in the Underground Training , 16 EEG electrodes were connected to examine the brain's electrical activities to 100 volunteers who passed the audiometry test. In the first place, the signals of the people were recorded in the conditions when the systems called the 1st case were turned off. Afterward, people were exposed to the noise of machines for a while. After being exposed to noise, people rested outside the underground training for 5 minutes. The rested people were taken back to the underground training to take the final measurements, and in the 3rd case after the noise measurements were made and the data were recorded. EEG results of individuals were obtained as Numerical BEAM average values in microVolts for all frequency bands.

Statistical significance analyzes were performed using EEG signals recorded before and after noise. The results were created separately for the delta (0-4Hz), and theta (4-8Hz) bands of the EEG for each person. 16 electrode placements of each participant were examined. Case 1 and Case 3 values were compared for the Delta (δ) and Theta (θ) frequency bands with the highest electrical activity, and statistical analyzes of the remaining 61 individuals were made after the artifacts were filtered out.

When the values before noise (Case 1) and after (Case 3) were compared, no significant difference was observed in the values obtained from the Delta frequency bands (p>0.05, Table 3).

Similar to the delta band results, when the values before and after the noise were compared, there was no or very small change in the values obtained from the Theta frequency bands, and no significant difference was detected (p>0.05, Table 4).

Table 3. Table of Comparison of Delta Frequency Band Values of Volunteers in Before and After Noise Environments.

	Fp1_δ3	Fp2_δ3	F7_δ3	F3_δ3	F4_δ3	F8_δ3	T7_δ3	C3_δ3
	Statistical Test[a]							
	Fp1_δ1	Fp2_δ1	F7_δ1	F3_δ1	F4_δ1	F8_δ1	T7_δ1	C3_δ1
Z	-,798[b]	-,766[c]	-,383[c]	-,767[c]	-,600[b]	-,331[b]	-,366[b]	-,798[b]
Sig.	,425	,444	,701	,443	,548	,740	,715	,425
	C4_δ3	T8_δ3	P7_δ3	P3_δ3	P4_δ3	P8_δ3	O1_δ3	O2_δ3
	C4_δ1	T8_δ1	P7_δ1	P3_δ1	P4_δ1	P8_δ1	O1_δ1	O2_δ1
Z	-,250[c]	-,029[c]	-,891[b]	-,030[c]	-,430[b]	-,710[c]	-,941[b]	-,812[b]
Sig.	,802	,977	,373	,976	,667	,477	,347	,417

a: Wilcoxon Signed Ranks Test, b: According to positive ranks, c: According to negative ranks

Table 4. Table of Comparison of Volunteers' Theta Frequency Band Values in Before and After Noise Environments.

	Fp1_θ3	Fp2_θ3	F7_θ3	F3_θ3	F4_θ3	F8_θ3	T7_θ3	C3_θ3
	Statistical Test[a]							
	Fp1_θ1	Fp2_θ1	F7_θ1	F3_θ1	F4_θ1	F8_θ1	T7_θ1	C3_θ1
Z	-,662[b]	-,906[c]	-,807[c]	-1,20[c]	-,676[b]	-,751[c]	-,115[b]	-,792[c]
Sig.	,508	,365	,420	,227	,499	,453	,908	,428
	C4_θ3	T8_θ3	P7_θ3	P3_θ3	P4_θ3	P8_θ3	O1_θ3	O2_θ3
	C4_θ1	T8_θ1	P7_θ1	P3_θ1	P4_θ1	P8_θ1	O1_θ1	O2_θ1
Z	-1,07[c]	-1,38[b]	-,360[c]	-,284[c]	-,478[b]	-,086[b]	-,164[b]	-,254[c]
Sig.	,281	,167	,718	,776	,633	,931	,870	,799

a: Wilcoxon Signed Ranks Test, b: According to positive ranks, c: According to negative ranks

4. Discussion

The aim of this study is to determine the instantaneous noise exposure of workers exposed to noise in the mining sector and its effects on the body during noise exposure.

As a result of these measurements, the effects of the noise on the workers were observed by statistically comparing the values collected at the moment and after the noise exposure for the workers or volunteers who will work in underground mining.

When the neurological effects of the study were examined, the data obtained before and after the noise exposure in 6 frequency bands of 16 electrodes connected to the volunteers were analyzed and no significant difference was observed. Jinjing Ke et al. [26], in their study on the distraction of construction workers exposed to noise, concluded that although the noise group had a lower level of attention than the control group, there was no statistically significant difference. They concluded that this situation may be due to individual factors such as age, gender and noise sensitivity of the participants. In line with this view, they stated that the participants cared about

their performance during the experiment, they were willing to work harder, and they consciously controlled their attention levels to complete the task. In this study, which was conducted on underground mine workers or those who will work, it was concluded that the results did not differ significantly, due to similar individual effects.

5. Result and Suggestions

In this study, the effects of the noise that the workers who work or will work in the underground mining sector are exposed to in the working areas have been observed experimentally and the important results and suggestions to reduce these effects are as follows:

1.   Noise measurements were made in 4 sections of the underground mining training colliery within the Soma Vocational School of Manisa Celal Bayar University, which are a constant source of the noise. In the ambient noise measurements made, 94 dB(A) values were obtained in the section with the chain conveyor, 86 dB(A) in the section with the belt conveyor, 84 dB(A) in the section with the water discharge system, and 88 dB(A) in the section with the ventilation system. The daily noise exposure values were determined in the section where the chain conveyor was the most.

2.   Persons who work or will work in the underground training colliery were subjected to an audiometry test in a sound-insulated room and it was examined whether they could hear the noise intensity and frequency range revealed by the devices. Due to the fact that 4 out of 104 people could not hear the operating noise frequency threshold of the mentioned machines, they were not taken to the next measurements, and 100 people whose hearing ability was within the desired tolerances were taken to the Underground Training Colliery. Measurements were made for both ears at frequencies of 125, 250, 500, 750, 1,000, 1500, 2,000, 3,000, 4,000, 6,000, and 8,000 Hz. For the determination of hearing loss, 500, 1,000, 2,000, and 4,000 Hz frequency combination and 25 dB average hearing threshold value recommended in ISO-1999 and TS-2607: ISO 1999 standards were taken into consideration in the evaluation of the test results.

3.   In the measurement area prepared in the Underground Training Colliery, 16 EEG electrodes were connected to examine the brain's electrical activities to 100 volunteers who passed the audiometry test. In the first place, the signals of the people were recorded under the conditions when the systems called the 1st case were closed. Afterward, people were exposed to the noise of

machines for a while. After being exposed to noise, people rested outside the underground training for 5 minutes. The rested people were taken back to the underground training to take the final measurements, and in the 3rd case after the noise measurements were made and the data were recorded.

•   In the present work, EEG measurements were recorded using 16 electrodes placed (C3, C4, F3, F4, F7, F8, FP1, FP2, O1, O2, P3, P4, P7, P8, T7, T8) on the scalp using the Contec KT88-3200 brand electroencephalography device.

•   After the EEG measurements were made, artifact evaluations of the measurements were made and measurements containing too many artifacts were eliminated. After this elimination, 61 data remained.

•   In the EEG measurements of the participants, the digital BEAM data obtained before and after the noise exposure in 6 frequency bands (Delta, Theta, Alpha 1, Alpha 2, Beta 1, and Beta 2) of 16 electrodes were analyzed. The frequency bands for digital BEAM are Delta 1– 4 Hz, Theta 4 – 8 Hz, Alpha1 8-12 Hz, Alpha2 12 – 16 Hz, Beta1 16-24 Hz, and Beta2 24-32 Hz. When the before (Case 1) and after (Case 3) values were compared in the SPSS program analysis platform, no statistically significant difference was found as seen in Tables 2 and 3 ($P>0.05$). The main reasons for not finding a difference may be:

- Young workers participating in the experiment. Jinjing Ke et al. [26] emphasized in his study that this is likely.
- Awareness of the participants that they will be exposed to noise at the time of measurement.

As a result, in underground mines, noise-related physiological effects can be seen in workers who are exposed to noise, especially if they do not use personal protective equipment. For this reason, it is recommended that those who will work in unit areas with high ambient noise levels use personal protective equipment to reduce the noise level they are exposed to. In addition, it is recommended to provide training and inspections aimed at raising awareness among employees about the harmful effects of ambient noise on hearing and other physiological systems and reducing noise levels.

Employers are advised to evaluate risk factors by managing their employees' health examinations and health education, monitoring for significant hearing loss by having audiometry measurements at regular intervals and controlling noise measurements.

It is thought that the results of this study will be a guide for the people who work or will work in the mining sector and the sector representatives. The application of these findings is not only limited to

the mining sector but is important for any environment that requires constant attention in a noisy environment.

In the next study, the cardiovascular effects of noise will be discussed. It is also planned to take into account the age, weight, height and working time of the participants. In order to enrich the results of the study, it is planned to compare the measurements with a reference group.

Author contributions

All authors listed have significantly contributed to the development and the writing of this article.

Ayla TEKİN: Supervised the experimental work and the manuscript process.

Mustafa Oğuz NALBANT: Did literature review and prepared the manuscript

Mustafa ORHAN: Compiled study data.

Fırat TEKİN: Compiled study data.

Fatih SUVAYDAN: Compiled study data.

Kemal BERKİ: Compiled study data.

Sami GUMUS: Were involved in the analysis, interpretation of the data.

Aslı Aydın SAVRAN: Were involved in the analysis, interpretation of the data.

Acknowledgments

Ethics

There are no ethical issues after the publication of this manuscript.

References

[1]. Akbay, D, Altındağ, R, Şengün, N. 2019. Geleneksel Yöntemle Açılan Karayolu Tünellerinde Çalışanların Gürültü Maruziyetlerinin Değerlendirilmesi. *Politeknik Dergisi*. DOI: 10.2339/politeknik.495339.

[2]. Ikuharu M, Kazuhisa M, Shintaro T. 1997. Noise-Induced Hearing Loss in Working Environment and its Background, *Journal of Occupational Health*. 39(1), 5-17. DOI: https://doi.org/10.1539/joh.39.5.

[3]. Nassiri, P, Monazam, M, DehaghiFouladi, B, Abadi, LIG, Zakerian, A. 2013. The effect of noise on human performance: a clinical trial, *International Journal of Occupational and Environmental Health,* 4, pp. 87-95.

[4]. Monteiro, R, Tomé, D, Neves, P, Silva, D, Rodrigues, MA. 2018. Interactive effect of occupational noise on attention and short-term memory: a pilot study, *Noise Health*, 20, pp. 190-198.

[5]. Tekin, A. 2020. Noise Exposure Estimation of Surface-Mine- Heavy Equipment Operators Using Artificial Neural Networks . *Celal Bayar University Journal of Science* , 16 (4) ,

429-436. Retrieved from https://dergipark.org.tr/tr/pub/cbayarfbe/issue/58992/773051.

[6]. Sensogut C. 2007. Occupational Noise in Mines and Its Control – A Case Study, *Polish Journal of Environmental Studies*. 16(6):939-942.

[7]. Golmohammadi, R, Darvishi, E, Faradmal, J, Poorolajal, J, Aliabadi, M. 2020. Attention and short-term memory during occupational noise exposure considering task difficulty, *Applied Acoust*ics, 158 107065, https://doi.org/10.1016/j. apacoust.2019.107065.

[7]. Schmidt-Daffy, M. 2012. Velocity versus safety: impact of goal conflict and task difficulty on drivers' behaviour, feelings of anxiety, and electrodermal responses, *Transportation Research Part F: Traffic Psychology and Behaviour,* 15 319–332, https://doi.org/10.1016/j. trf.2012.02.004.

[9]. Ahn, CR, Lee, S, Sun, C, Jebelli, H, Yang, K, Choi, B. 2019. Wearable sensing technology applications in construction safety and health, *Journal of Construction Engineering and Management,* 145, 03119007, https://doi.org/10.1061/(asce)co.1943-7862.0001708.

[10]. Yang, K, Ahn, C.R. 2019. Inferring workplace safety hazards from the spatial patterns of workers' wearable data, *Advanced Engineering Informatics,* 41,100924, https://doi.org/ 10.1016/j.aei.2019.100924.

[11]. Kim, H, Ahn, CR, Yang, K. 2017. Identifying safety hazards using collective bodily responses of workers, *Journal of Construction Engineering and Management,* 143, 04016090, https://doi. org/10.1061/(ASCE)CO.1943-7862.0001220.

[12]. Kim, H, Ahn, CR, Yang, K. 2019. Validating ambulatory gait assessment technique for hazard sensing in construction environments, *Automation in Construction,* 98, 302–309, https://doi.org/10.1016/j.autcon.2018.09.017.

[13]. Jeon, J, Cai, H, Yu, D, Xu, X. 2020. Identification of Safety Hazards Using Wearable EEG, Construction Research Congress, 2020, *American Society of Civil Engineers,* Reston, VA, pp. 185–194, https://doi.org/10.1061/9780784482872.021.

[14]. Choi, B, Jebelli, H, Lee, S. 2019. Feasibility analysis of electrodermal activity (EDA) acquired from wearable sensors to assess construction workers' perceived risk, *Safety Science,* 115, 110–120, https://doi.org/10.1016/j.ssci.2019.01.022.

[15]. Olbrich, S, Mulert, C, Karch, S, Trenner, M, Leicht, G, Pogarell, O, Hegerl, U. 2009. EEGvigilance and BOLD effect during simultaneous EEG/fMRI measurement, *NeuroImage* 45, 319–332, https://doi.org/10.1016/j.neuroimage.2008.11. 014.

[16]. Zhai, J, Chen, X, Ma, J, Yang, Q, Liu, Y. 2016. The vigilance-avoidance model of avoidant recognition: an ERP study under threat priming, *Psychiatry Research,* 246, 379–386, https://doi.org/10.1016/j.psychres.2016.10.014.

[17]. Eoh, HJ, Chung, MK, Kim, SH. 2005. Electroencephalographic study of drowsiness in simulated driving with sleep deprivation, *International Journal of Industrial Ergonomics,* 35, 307–320, https://doi.org/10.1016/j.ergon.2004.09.006.

[18]. Aryal, A, Ghahramani, A, Becerik-Gerber, B. 2017. Monitoring fatigue in construction workers using physiological measurements, *Automation in Construction,* 82, 154–165, https://doi.org/10.1016/j.autcon.2017.03.003.

[19]. Ikenishi, T, Kamada, T, Nagai, M. 2013. Analysis of longitudinal driving behaviors during car following situation by

the driver's EEG using PARAFAC, *IFAC Proc,* Vol. 46, 415–422, https://doi.org/10.3182/20130811-5-US-2037.00023.

[20]. Kawashima, I, Kumano, H. 2017. Prediction of mind-wandering with electroencephalogram and non-linear regression modeling, *Frontiers in Human Neuroscience,* 11, pp. 1-10, https://doi.org/10.3389/fnhum.2017.00365.

[21]. Jeon, J, Cai, H. 2021. Classification of construction hazard-related perceptions using: Wearable electroencephalogram and virtual reality. *Automation in Construction, 132,* 103975.

[22]. Bo, Y, Chao, W, Ji, L, Huimin, L. 2014. Physiological responses of people in working faces of deep underground mines. *International Journal of Mining Science and Technology.* 24(5), 683-688, https://doi.org/10.1016/j.ijmst.2014.03.024.

[24]. Önder, S, Önder, M. 2018. Statistical Investigation of the Noise Levels in Coal Mining Industry. Eskişehir Osmangazi Üniversitesi Mühendislik ve Mimarlık Fakültesi Dergisi. 26(1), 30-35.

[24]. Bashashati, A, Fatourechi, M, Ward, RK, Birch, GE. 2007. A survey of signal processing algorithms in brain-computer interfaces based on electrical brain signals, *Journal of Neural Engineering,* 4, R32–R57, https://doi.org/10.1088/1741-2560/4/2/R03.

[25]. Zauner, A, Fellinger, R, Gross, J, Hanslmayr, S, Shapiro, K, Gruber, W, Müller, S, Klimesch, W. 2021. Alpha entrainment is responsible for the attentional blink phenomenon, *NeuroImage* 63 674–686, https://doi.org/10.1016/j. neuroimage.2012.06.075.

[26]. Ke, J, et al. 2021. Monitoring distraction of construction workers caused by noise using a wearable Electroencephalography (EEG) device. *Automation in Construction,* 125, 103598.